

# **The Development of the Miniature X-Ray Telescope μROSI**

A thesis accepted by the Faculty of Aerospace Engineering and Geodesy of the  
Universität Stuttgart in partial fulfilment of the requirements for the degree of  
Doctor of Engineering Sciences (Dr.-Ing.)

by

Lars Tiedemann

born in Hamburg

Main referee: Prof. Dr. rer. nat. Hans-Peter Röser  
Co-referee: Prof. Dott. Andrea Santangelo

Date of defence: 02 July 2014

Institute of Space Systems  
University of Stuttgart  
2014



# Preface

This thesis is the result of my work at the Max-Planck-Institut für extraterrestrische Physik (MPE) for the institute's high energy research group. My principal task at the MPE was the design of the X-ray camera and the camera cooling system for the eROSITA X-ray telescope, the primary scientific payload on board the Russian Spectrum-Roentgen-Gamma satellite (SRG). At the same time, I had the task to design the  $\mu$ ROSI miniature X-ray telescope.

The  $\mu$ ROSI project emerged in late 2007, when Dr. Peter Predehl, senior scientist in the MPE high-energy astrophysics research group, was approached by a group of amateur astronomers from the Max Valier observatory in Bolzano, Italy. Together with ambitious teachers from the Max-Valier technical high school (Gewerbeoberschule Max-Valier Bozen, GOB) they had the idea of developing a small satellite of about 10 kg and were looking for an astronomical payload. As a high energy astronomer, Dr. Predehl naturally proposed a miniature X-ray telescope. The idea was readily accepted as primary payload.

## Acknowledgements

I would like to take the opportunity to express my deepest gratitude to those people who made this thesis possible.

First of all, my most sincere appreciation and gratitude goes to my doctoral supervisor Prof. Röser for his patience, his guidance and invaluable advice as well as Prof. Andrea Santangelo for co-examining my thesis.

A special thank you goes to Dr. Peter Predehl for his ideas, discussions, counsel and for being the best boss imaginable.

Many thanks go to Elias Breunig, who started working on the  $\mu$ ROSI project when writing his study thesis about the development and qualification of the optical bench (Breunig, 2011b) (see section 8.2). Afterwards, he wrote his master's thesis about the superpolishing of the mandrels, which were essential for the manufacturing of the  $\mu$ ROSI mirror shells (Breunig, 2011a) (see section 7.4).

I would also like to thank Maria Fürmetz for her work on the thermal control subsystem. Her thermal analyses and her contribution to thermal hardware testing were essential for the whole project.

---

Furthermore, I thank Vadim Burwitz, Benedikt Menz, Gisela Hartner and the whole team at the PANTER X-ray test facility for testing and evaluating the first X-ray mirror shell; Martin Schlecker for his work on the mirror shell integration; Walter Kink, Siegfried Müller, Diogo Coutinho and Ziliang Zhang for their work on the  $\mu$ ROSI electronics; Stefan Czempiel and his workshop team for converting short-term requests into real hardware.

Also, many thanks go to Giuseppe Valsecchi and his team at Media Lario for producing the mirror shells without consideration.

Most of all, I thank my wife Annely for her constant support and love.

Lars Tiedemann  
München, August 2014

# Contents

<b>List of Tables</b>	ix
<b>List of Figures</b>	xi
<b>List of Acronyms</b>	xv
<b>Abstract</b>	xix
<b>Zusammenfassung</b>	xxi
<b>1 Introduction</b>	1
1.1 Project Description . . . . .	1
1.2 Scope of this Work . . . . .	2
1.3 Thesis Structure . . . . .	3
1.4 Contributions by Others . . . . .	3
<b>2 A Brief Introduction to X-Ray Astronomy</b>	5
2.1 X-Rays in the Electromagnetic Spectrum . . . . .	5
2.2 X-Ray Astronomy History and Missions . . . . .	6
2.3 Solar System X-Ray Sources . . . . .	16
2.4 Extrasolar X-Ray Sources . . . . .	18
<b>3 Max-Valier Satellite Mission</b>	21
3.1 Project Partners and Tasks . . . . .	21
3.2 Satellite Launch . . . . .	23
3.3 All Sky Survey . . . . .	24
3.4 Sun-Synchronous Orbit (SSO) . . . . .	27
3.5 Scanning Rotation . . . . .	30
<b>4 Instrumentation</b>	33
4.1 X-Ray Focussing Mirrors . . . . .	33
4.1.1 How To Focus X-Rays . . . . .	33
4.1.2 The Wolter Geometry . . . . .	35

## Contents

---

4.1.3	Mathematics of Wolter-1 Mirrors . . . . .	36
4.1.4	Mirror Performance . . . . .	39
4.1.5	Double Cone Approximation . . . . .	40
4.1.6	Nesting Mirror Shells . . . . .	43
4.1.7	Established Mirror Manufacturing Technologies . . . . .	43
4.2	X-Ray Detectors . . . . .	44
4.2.1	pnCCDs . . . . .	45
4.2.2	Detector Noise . . . . .	46
4.2.3	Silicon Drift Detectors . . . . .	48
4.3	Instrumentation for Small Satellites . . . . .	51
<b>5</b>	<b>µROSI Miniature X-Ray Telescope</b>	<b>53</b>
5.1	Introduction . . . . .	53
5.2	Telescope Sizing . . . . .	54
5.3	Preliminary Observation Simulation . . . . .	56
5.4	Objectives . . . . .	58
5.5	µROSI Subsystems . . . . .	59
5.6	Requirements . . . . .	60
5.7	Design Description . . . . .	67
5.8	Model Philosophy . . . . .	70
<b>6</b>	<b>µROSI Detector</b>	<b>73</b>
6.1	Filter Selection . . . . .	75
6.2	Detector Assembly Design Description . . . . .	76
<b>7</b>	<b>Mirror Module</b>	<b>79</b>
7.1	Mirror Parameters . . . . .	81
7.2	Effective Area . . . . .	83
7.3	Mirror MAIT Process . . . . .	86
7.4	Mandrel Manufacturing and Polishing . . . . .	89
7.5	Mirror EM Test . . . . .	93
7.5.1	Test Set-Up . . . . .	94
7.5.2	Focus Search . . . . .	95
7.5.3	PSF Measurement . . . . .	95
7.5.4	Supplementary Ray Tracing Simulation . . . . .	100
7.5.5	Effective Area of Mirror Shell #06 . . . . .	105
7.5.6	Results Summary . . . . .	105
7.6	Mirror Shell Integration . . . . .	106
<b>8</b>	<b>Structure</b>	<b>109</b>

8.1	Preliminary Design . . . . .	109
8.2	Structural Qualification Model (SQM) . . . . .	110
8.3	Final Design Description . . . . .	114
8.4	Summary . . . . .	115
<b>9</b>	<b>Thermal Control Subsystem</b>	<b>117</b>
9.1	Thermal Requirements . . . . .	117
9.2	TCS Design Description . . . . .	117
9.3	Latent Cold Storage (LCS) . . . . .	120
9.3.1	Storing Heat . . . . .	120
9.3.2	LCS Design . . . . .	122
9.3.3	Selecting and Testing the PCM . . . . .	124
9.4	Radiator . . . . .	129
9.4.1	Radiator Optimization . . . . .	129
9.5	Heat Pipe . . . . .	133
9.5.1	Working Principle . . . . .	133
9.5.2	Heat Pipe Manufacturing . . . . .	136
9.5.3	Working Fluid . . . . .	138
9.5.4	Heat Pipe Modelling . . . . .	143
9.5.5	Heat Pipe Testing . . . . .	144
9.6	In-Orbit Simulation . . . . .	144
9.7	TCS Summary . . . . .	147
<b>10</b>	<b>Electronics</b>	<b>151</b>
10.1	Electronics Breadboard Model . . . . .	151
10.2	Breadboard Test . . . . .	155
10.3	Electronics Engineering Model . . . . .	158
<b>11</b>	<b>Conclusion</b>	<b>159</b>
<b>A</b>	<b>Appendices</b>	<b>163</b>
A.1	Thermal Modeling . . . . .	163
A.2	Spectral Lines . . . . .	165
A.3	Technology Readiness Levels . . . . .	166
A.4	Parts List . . . . .	167
	<b>Bibliography</b>	<b>171</b>
	<b>Curriculum</b>	<b>177</b>



# List of Tables

1.1	Small satellite classification . . . . .	2
2.1	List of selected X-ray survey missions. . . . .	8
2.2	Comparison of current X-ray observatories. . . . .	9
5.1	$\mu$ ROSI initial design parameters. . . . .	55
5.2	Abbreviations for requirement verification methods . . . . .	60
5.3	List of requirements. . . . .	62
5.4	$\mu$ ROSI test matrix. . . . .	72
6.1	$\mu$ ROSI SDD detector properties. . . . .	74
6.2	Transmission of selected filters for different energies. . . . .	75
7.1	$\mu$ ROSI mirror shell parameters. . . . .	82
7.2	$\mu$ ROSI double cone focus parameters. . . . .	83
7.3	Calculated effective areas of $\mu$ ROSI mirror shells. . . . .	84
7.4	Results of mirror shell #06/01 PSF measurements. . . . .	97
7.5	$\mu$ ROSI mirror shell effective areas from ray-tracing simulation . .	104
7.6	Colour codings of ray-tracing simulation results . . . . .	104
7.7	Mirror shell #06 effective areas in [ $mm^2$ ]. . . . .	105
8.1	SQM vibration test program. . . . .	110
8.2	PSLV random vibration input spectrum . . . . .	113
9.1	Temperature limits of $\mu$ ROSI components. . . . .	117
9.2	PCM evaluation plan and expected behaviour of suitable PCM. .	125
9.3	Properties of 1-Octanol . . . . .	128
9.4	Heat capacities of 1-Octanol . . . . .	128
9.5	Radiator properties. . . . .	129
9.6	Results of radiator benchmark analysis. . . . .	130
9.7	Properties of ethane. . . . .	139
9.8	Coefficients for ethane properties as a function of the temperature. .	140
10.1	Detector breadboard best fit parameters . . . . .	156

*List of Tables*

---

A.1	Value ranges for different states in PCM modeling. . . . .	164
A.2	X-ray emission lines of selected elements in <i>keV</i> . . . . .	165
A.3	Technology Readiness Levels . . . . .	166
A.4	$\mu$ ROSI parts list. . . . .	167

# List of Figures

1.1	3D-Model of the Max-Valier Satellite . . . . .	4
2.1	X-ray radiation in the electromagnetic spectrum . . . . .	6
2.2	X-ray photography of Mrs. Röntgen's hand . . . . .	7
2.3	Diagram of the satellite layout of the HEAO-2 satellite . . . . .	10
2.4	The ROSAT satellite in flight configuration. . . . .	10
2.5	Illustration of the Chandra X-ray observatory . . . . .	11
2.6	Artist's impression of XMM-Newton . . . . .	12
2.7	Schematics of the Suzaku X-ray observatory. . . . .	13
2.8	Diagram of the NuSTAR X-ray observatory . . . . .	14
2.9	SRG Scientific payload: eROSITA, SXC and ART-XC on the Navigator platform. . . . .	15
2.10	The Sun in X-rays . . . . .	16
2.11	The Moon in soft X-rays . . . . .	17
2.12	X-ray image of the aurora borealis. . . . .	18
2.13	Example of a galactic X-ray source: The crab nebula . . . . .	19
3.1	Max-Valier Satellite project partners. . . . .	22
3.2	Accommodation of MVS and the Latvian Venta-1 satellite inside the VEGA payload fairing . . . . .	23
3.3	All-sky survey geometry . . . . .	25
3.4	ROSAT X-ray background map and exposure map . . . . .	26
3.5	Orbit altitude for Sun-synchronous orbits. . . . .	29
3.6	Scanning rotation of the $\mu$ ROSI telescope . . . . .	31
4.1	Optical properties of gold. . . . .	34
4.2	Critical grazing incidence angle $\alpha_t$ . . . . .	35
4.3	Schematic of Wolter-1 optics . . . . .	36
4.4	Wolter-1 geometry variables definition . . . . .	37
4.5	On-axis point spread functions of the three XMM-Newton instruments. . . . .	39
4.6	Off-axis point spread functions of XMM-Newton . . . . .	40
4.7	Double cone approximation. . . . .	42

4.8 Examples of different X-ray mirror systems. . . . .	44
4.9 Schematic of a frame-store pnCCD . . . . .	47
4.10 Energy resolution as a function of the photon energy . . . . .	48
4.11 Silicon Drift Detector working principle . . . . .	49
4.12 SSD energy resolution versus temperature and shaping time . . .	50
4.13 Silicon Drift Detector Droplet (SD <sup>3</sup> ) . . . . .	50
5.1 Simulated map of $\mu$ ROSI all-sky survey . . . . .	57
5.2 $\mu$ ROSI system block diagram . . . . .	61
5.3 Preliminary design of the $\mu$ ROSI telescope. . . . .	68
5.4 Explosion view of the $\mu$ ROSI telescope. . . . .	69
6.1 Transmission of selected filter materials . . . . .	76
6.2 Explosion drawing of the $\mu$ ROSI detector assembly. . . . .	77
6.3 $\mu$ ROSI detector assembly with dummy detector and filter cap . .	78
7.1 Section view of nested $\mu$ ROSI mirror shells. . . . .	80
7.2 Reflectivities and resulting effective areas for the $\mu$ ROSI mirror shells. . . . .	85
7.3 Mirror shells #01-06. . . . .	88
7.4 The $\mu$ ROSI superpolishing device. . . . .	90
7.5 Mandrel #06 initial state after diamond lathing, $R_q = 9.2 \text{ nm}$ . . .	91
7.6 Mandrel #06 after 10 h polishing with pitch, $R_q = 1.8 \text{ nm}$ . . . .	91
7.7 Mandrel #06 after fine polishing $R_q = 0.8 \text{ nm}$ . . . . .	91
7.8 Mandrel #06 after fine polishing, smaller sample areas . . . . .	92
7.9 Mirror shell #06/01 before integration into X-ray test adapter. . .	93
7.10 Schematics of the mirror test set-up in the PANTER facility . . .	94
7.11 Mirror shell #06 mounted in PANTER . . . . .	95
7.12 $\mu$ ROSI mirror shell #06 focus search results . . . . .	96
7.13 PSF analysis of mirror shell #06/01 at 0.28 keV (C-K <sub><math>\alpha</math></sub> ) . . . .	98
7.14 PSF analysis of mirror shell #06/01 at 1.49 keV (Al-K <sub><math>\alpha</math></sub> ) . . . .	99
7.15 Comparison of ray tracing simulation and PSF measurement of mirror shell #06 at C-K <sub><math>\alpha</math></sub> . . . . .	101
7.16 Comparison of ray tracing simulation and PSF measurement of mirror shell #06 at Al-K <sub><math>\alpha</math></sub> . . . . .	102
7.17 Updated simulation and PSF measurements of mirror shell #06 .	103
7.18 Schematics of $\mu$ ROSI vertical optical bench (VOB). . . . .	107
8.1 The $\mu$ ROSI SQM model on the shaker during vibration testing .	111
8.2 Comparison of simulation and measured frequency response of mirror module mass dummy . . . . .	112

8.3 The $\mu$ ROSI optical bench and cover after yellow chromating. . . . .	116
9.1 Explosion view of the $\mu$ ROSI thermal control subsystem. . . . .	119
9.2 Temperature-heat diagram during phase change. . . . .	120
9.3 Schematics of heat fluxes in a latent cold storage. . . . .	122
9.4 First LCS container prototype before welding. . . . .	124
9.5 PCM test setup in vacuum chamber . . . . .	126
9.6 Freezing curve of 1-Octanol. . . . .	127
9.7 Radiator benchmark analysis . . . . .	131
9.8 Photography of the $\mu$ ROSI radiator . . . . .	132
9.9 Heat pipe working principle. . . . .	133
9.10 Limitations of the $\mu$ ROSI heat pipe . . . . .	135
9.11 $\mu$ ROSI heat pipe. . . . .	137
9.12 Surface tension of ethane and ammonia . . . . .	141
9.13 Schematics of the $\mu$ ROSI heat pipe thermal model . . . . .	143
9.14 Test setup for the $\mu$ ROSI heat pipe test. . . . .	145
9.15 Temperature curve of test with $\mu$ ROSI heat pipe. . . . .	146
9.16 In-orbit simulation of the Max-Valier Satellite with the $\mu$ ROSI X-ray telescope. . . . .	149
10.1 $\mu$ ROSI EM electronics block diagram. . . . .	152
10.2 Development boards of the electronics BB model. . . . .	154
10.3 Test setup with sensor board version 3. . . . .	155
10.4 Multichannel analyzer output during detector breadboard testing	157
10.5 Detector breadboard test data with a gaussian fit curve . . . . .	157
10.6 Electronics EM boards during testing. . . . .	158



# List of Acronyms

$\mu$ ROSI	Micro Röntgen Satellite Instrument
AGN	Active Galaxy Nuclei
AIS	Automatic Identification System
AIT	Assembly, Integration and Testing
AMV	Amateurastronomen Max Valier
ASD	Acceleration Spectral Density
BB	Breadboard Model
BOL	Beginning of Life
CAD	Computer Aided Design
CCD	Charge-Coupled Device
CCHP	Constant Conductance Heat Pipe
CDR	Critical Design Review
CFRP	Carbon Fibre Reinforced Plastics
CMOS	Complementary Metal Oxide Semiconductor
COG	Center of Gravity
COTS	Commercial off-the-shelf
DOF	Degree of Freedom
EOL	End of Life
EM	Engineering Model
eROSITA	Extended Röntgen Survey with an Imaging Telescope Array
EQM	Engineering and Qualification Model
ESA	European Space Agency
EUV	Extreme Ultraviolet
FEM	Finite Element Method

## *List of Acronyms*

---

FET	Field Effect Transistor
FM	Flight Model
FOV	Field of View
FWHM	Full Width Half Maximum
GOB	Gewerbeoberschule <i>Max Valier</i> , Bolzano
GOM	Gewerbeoberschule <i>Oskar von Miller</i> , Merano
HEW	Half Energy Width
IR	Infrared
LCS	Latent Cold Storage
LEO	Lower Earth Orbit
MAIT	Manufacturing, Assembly, Integration and Testing
MD	Mass Dummy
MLI	Multi Layer Insulation
MPE	Max-Planck-Institut für extraterrestrische Physik
MVS	Max-Valier Satellite
NASA	National Aeronautics and Space Administration
NIR	Near Infrared
OHB	OHB System AG, Bremen
PCB	Printed Circuit Board
PCM	Phase Change Material
PDR	Preliminary Design Review
PEEK	Polyether Ether Ketone
PSD	Power Spectral Density
PSF	Point Spread Function
PSLV	Polar Satellite Launch Vehicle (Indian launch vehicle)
QM	Qualification Model
RASS	ROSAT All-Sky Survey
RASS-BSC	ROSAT All-Sky Survey Bright Source Catalogue
RASS-FSC	ROSAT All-Sky Survey Faint Source Catalogue
RMS	Root Mean Square

---

ROSAT	Röntgensatellit
SDD	Silicon Drift Detector
SDOF	Single Degree Of Freedom
SI	Système International (International System of Units)
SM	Structural Model
SNR	Supernova Remnant
SQM	Structural Qualification Model
SRG	Spectrum Röntgen Gamma
SSO	Sun Synchronous Orbit
TCS	Thermal Control System
TRL	Technology Readiness Level
UART	Universal Asynchronous Receiver Transmitter
UV	Ultraviolet
VCHP	Variable Conductance Heat Pipe
VEGA	Vettore Europeo di Generazione Avanzata (Advanced Generation European Carrier Rocket)
VIS	Visual Spectrum
VOB	Vertical Optical Bench
XMM	X-ray Multi-Mirror
XUV	Extreme Ultraviolet



# Abstract

Within the scope of this work, a unique miniature X-ray telescope is developed, manufactured and tested. The  $\mu$ ROSI (Micro Röntgen Satellite Instrument) telescope is the primary payload on board the South-Tyrolean nanosatellite Max-Valier. The satellite is developed by a team of South-Tyrolean amateur astronomers and technical schools with the support of the German space company OHB. The primary objective of the instrument is to conduct an all-sky survey and measure spectra of at least 100 bright sources in the soft X-ray bandwidth.

For the development of the telescope, the constraints for the satellite mission and the scientific objectives are elaborated. The scientific objectives are selected in such a way that the  $\mu$ ROSI mission fills a niche among the big X-ray telescopes. This is achieved by selecting the same F-number and energy range as the successful ROSAT telescope and using a silicon drift detector (SDD) with high spectral resolution. Thus, the extensive database compiled in the ROSAT all-sky survey bright source catalogue can be enriched by  $\mu$ ROSI with high resolution spectra.

Although the  $\mu$ ROSI telescope is smaller by a factor of 10 in focal length compared to ROSAT, it requires the same subsystems as a large X-ray telescope:

- the mirror module to focus the X-ray radiation,
- the detector module to convert the radiation into electronic signals,
- the structure to provide mechanical stability,
- the thermal control subsystem to maintain the temperatures in specified limits and
- the electronics subsystem for signal and data processing.

In the course of this work, all subsystems are designed and tested with different development models. Special attention is paid to the mirror subsystem as well as the detector cooling subsystem.

Due to the short wavelength of X-ray radiation, the mirrors need to have extremely smooth surfaces. In order to achieve this, the mirrors are manufactured by an electrogalvanic forming process, which requires highly polished mandrels. The complete mirror shell manufacturing process, including the manufacturing

## *Abstract*

---

and polishing of the mandrels, has been developed and verified by measuring one sample mirror shell in the PANTER X-ray test facility.

The detector cooling system is required as the spectral resolution of the detector depends on its temperature. In order to maintain a stable detector temperature in a low Earth orbit, the detector is connected to a specifically developed latent cold storage (LCS) which contains a phase change material. The LCS is connected to a radiator with a heat pipe making the whole system completely passive. All components for the thermal control system have been designed, manufactured and tested.

The structure of the telescope has been analysed, manufactured and tested with mass dummies in a random vibration test to verify its load capability and mechanical stability.

The detector module including the optical filter has been designed, manufactured and tested in a vacuum chamber to verify the integrity of the filter foil and the thermal properties of the detector housing.

The electronics required for retrieving signals and processing data from the detector module has been developed and tested using several breadboard models to verify the basic design functionality. A final X-ray test with a  $^{55}\text{Fe}$  X-ray source demonstrated the spectral resolution capabilities of the combined detector and electronics system.

# Zusammenfassung

Im Rahmen dieser Arbeit wird ein einzigartiges Miniatur-Röntgenteleskop entwickelt, gefertigt und getestet. Das  $\mu$ ROSI (Micro Röntgen Satellite Instrument) Teleskop ist die Hauptnutzlast auf dem Südtiroler Nanosatelliten Max-Valier. Der Satellit wird von einer Gruppe aus Südtiroler Amateurastronomen und technischen Schulen mit der Unterstützung der deutschen Firma OHB entwickelt. Das primäre Missionsziel des Instruments ist es, eine vollständige Himmelsdurchmusterung durchzuführen und dabei Spektren von mindestens 100 hellen Quellen im weichen Röntgenspektrum zu messen.

Für die Entwicklung des Teleskops werden zunächst die Rahmenbedingungen für die Satellitenmission und die wissenschaftliche Zielsetzung erarbeitet. Die wissenschaftlichen Ziele wurden so gesteckt, dass die  $\mu$ ROSI Mission eine Nische zwischen den großen Röntgenteleskopen ausfüllt. Dies wird erreicht, indem dieselbe F-Zahl und derselbe Energiebereich wie bei dem erfolgreichen ROSAT Teleskop verwendet wird und ein Silizium Drift Detektor (SDD) mit hoher spektraler Auflösung zum Einsatz kommt. Somit kann die umfangreiche Datenbank des ROSAT All-Sky Survey Bright Source Catalogue um hochauflösende Spektren erweitert werden.

Obwohl das  $\mu$ ROSI Teleskop um den Faktor 10 in der Fokallänge kleiner ist als ROSAT, benötigt es die gleichen Subsysteme wie ein großes Röntgenteleskop:

- das Spiegelmodul zur Fokussierung der Röntgenstrahlen,
- das Detektormodul zur Konvertierung der Strahlung in elektronische Signale,
- die Struktur zur Gewährleistung der mechanischen Stabilität,
- das Thermalkontrollsysteem zur Einhaltung der spezifizierten Temperaturgrenzen und
- das Elektronikssystem zur Signal- und Datenprozessierung.

Alle Subsysteme werden im Rahmen dieser Arbeit für das  $\mu$ ROSI Teleskop ausgelegt und mit verschiedenen Versuchsmodellen getestet. Besonderes Augenmerk liegt auf dem Spiegelsystem und dem Detektor-Kühlsystem.

## Zusammenfassung

Aufgrund der sehr kurzen Wellenlänge der Röntgenstrahlen benötigen die Spiegelschalen eine extrem glatte Oberfläche. Um diese zu erreichen, werden die Spiegel mit einem elektrogalvanischen Formprozess hergestellt, der extrem fein polierte Mandrels benötigt. Der komplette Fertigungsprozess der Spiegelschalen, inklusive Fertigung und Polieren der Mandrels wurde erfolgreich entwickelt und durch Messung einer Probeschale in der Röntgentestanlage PANTER verifiziert.

Das Detektor-Kühlsystem wird benötigt, da die spektrale Auflösung des Detektors von der Temperatur abhängig ist. Um die Detektortemperatur im niedrigen Erdorbit stabil zu halten, ist der Detektor mit einem eigens entwickelten Latentkältespeicher (LCS) verbunden, der ein Phasenübergangsmaterial enthält. Der LCS ist über eine Heat pipe mit einem Radiator verbunden, so dass das gesamte System komplett passiv arbeitet. Alle Komponenten des Thermalsystems sind erfolgreich entwickelt, gefertigt und getestet worden.

Die Teleskopstruktur wurde analysiert, gefertigt und mit Massendummies in einem Vibrationstest getestet, um die Lastaufnahme und die Stabilität der Struktur zu verifizieren.

Das Detektormodul inklusive des optischen Filters wurde designed, gefertigt und in einer Vakuumkammer getestet, um die Belastbarkeit der Filterfolie und die thermischen Eigenschaften des Detektorgehäuses nachzuweisen.

Die Elektronik, die für die Signalaufnahme vom Detektor und die weitere Datenverarbeitung benötigt wird, wurde entwickelt und mit mehreren Breadboard Modellen getestet, um die Funktionalität nachzuweisen. Ein abschließender Röntgentest mit einer  $^{55}\text{Fe}$  Quelle zeigte das spektrale Auflösungsvermögen des kombinierten Detektor-Elektronik Systems.

# 1. Introduction

## 1.1. Project Description

The  $\mu$ ROSI<sup>1</sup> miniature X-ray telescope was developed at the Max-Planck-Institut für extraterrestrische Physik (MPE) as the primary payload for the South-Tyrolean amateur satellite *Max-Valier* (MVS: Max-Valier Satellite). The project was initiated by a group of amateur astronomers from the Max Valier observatory (AMV: *Amateurastronomen Max Valier*) and ambitious teachers from the *Gewerbeoberschule Max Valier* located in Bolzano, Italy (GOB).

GOB found a range of project partners that contributed to the project. Among them the *Gewerbeoberschule Oskar von Miller* in Merano (GOM), as well as the Bremen based space company OHB System AG (OHB), that offered technical support for the satellite development and also secured the launch with a VEGA rocket from Kourou scheduled for 2014.

The MVS concept was first published in 2009 at the IAC Congress (Orgler et al., 2009). The satellite, announced as a nanosatellite of  $\sim 10\text{ kg}$ , has in fact a total mass of  $16\text{ kg}$ . According to the widely accepted<sup>2</sup> small satellite classification (see table 1.1), it could be also referred to as a microsatellite. However, within the scope of this work we will keep referring to it as a nanosatellite.

Figure 1.1 shows a 3D-model of the MVS nanosatellite with  $\mu$ ROSI payload. The satellite is based on the Quadsat platform developed by the University of Applied Sciences, Bremen. The spacecraft consists of solar panel and a cubic main structure that houses the satellite's electronics and serves as the structural interface to the launcher. The  $\mu$ ROSI X-ray telescope is mounted to the side of the main structure. The satellite is three-axes stabilized with one flywheel and magnetorquers.

Apart from the  $\mu$ ROSI miniature X-ray telescope the MVS payload comprises an AIS<sup>3</sup> experiment and a CMOS imaging camera.

The MVS primary mission objective is to perform an all-sky survey in the soft

---

<sup>1</sup>micro ROentgen Satellite Instrument

<sup>2</sup>See, for example, Fortescue et al. (2003) or Wikipedia:

[http://en.wikipedia.org/wiki/Miniaturized\\_satellite](http://en.wikipedia.org/wiki/Miniaturized_satellite)

<sup>3</sup>AIS: Automatic Identification System, a marine vessel identification system

Wet Mass	Classification
1 – 100 g	Femtosatellite
0.1 – 1 kg	Picosatellite
1 – 10 kg	Nanosatellite
10 – 100 kg	Microsatellite
100 – 500 kg	Minisatellite
500 – 1000 kg	Medium satellite
> 1000 kg	Large satellite

Table 1.1.: Small satellite classification. The term *small satellite* refers to satellites  $< 500 \text{ kg}$ .

X-ray bandwidth searching the whole sky for bright X-ray sources with an angular resolution of  $1^\circ$ . The X-ray data will be evaluated by the AMV together with students of the participating South Tyrolean schools GOB and GOM.

## 1.2. Scope of this Work

The objective of this thesis is the development of the  $\mu$ ROSI miniature X-ray telescope. The final result of this work should be a working piece of flight hardware which is ready for launch. This document attempts to give the reader a thorough understanding of the  $\mu$ ROSI payload, its design and the rationales that led to the final design. My role in this project has been manifold and truly interdisciplinary, ranging from optical, thermal, mechanical and MAIT<sup>4</sup> engineering to systems engineering and general project management.

The tasks I had to perform included the definition of scientific objectives for the  $\mu$ ROSI telescope and the elaboration of a basic instrument concept. Based upon this basic concept, the satellite mission had to be defined in close co-operation with the project partners GOB, GOM and OHB. This included the baseline selection of a suitable orbit and attitude control modes for the all-sky survey.

On the telescope system level, the basic optical parameters needed to be defined, so that the instrument meets the scientific objectives without exceeding the allocated mass and power budgets. Design decisions concerning the key components of the X-ray telescope had to be made: The detector had to be selected as well as the technology for the manufacturing of the X-ray focusing mirrors.

---

<sup>4</sup>MAIT: Manufacturing, Assembly, Integration and Testing

Before entering the detailed design phase, system level requirements for the telescope had to be formulated and subsystem level requirements had to be deduced. All components had to be designed in full detail according to the requirements and, finally, the system components had to be manufactured and verified with development tests.

### 1.3. Thesis Structure

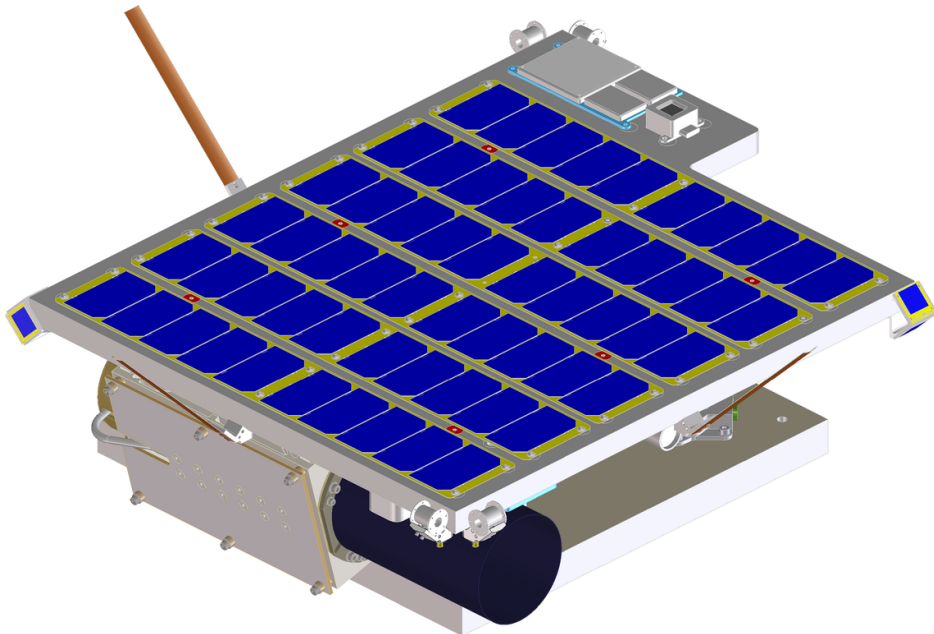
This thesis starts with a short introduction to X-ray astrophysics in chapter 2 describing in brief its history, significant X-ray astronomy missions and celestial X-ray sources. Chapter 3 describes in detail how the MVS spacecraft performs the all-sky survey. This includes a description of the selected sun-synchronous orbit (SSO) and the spacecraft rotation required for scanning the whole sky. Chapter 4 gives an overview of X-ray instrumentation, i.e. focusing mirrors and detectors for X-ray detection. Based on the existing instrumentation technology, a concept for the  $\mu$ ROSI telescope is presented in chapter 5. This includes the basic system design, the requirements, and the model philosophy. Then, the  $\mu$ ROSI subsystems are described in detail: the  $\mu$ ROSI detector (chapter 6), the mirror module (chapter 7), the structure (chapter 8), the thermal control subsystem (chapter 9) and the electronics (chapter 10). Chapter 11 draws the conclusion of the previous chapters and outlines the steps necessary to make MVS and  $\mu$ ROSI ready for launch.

### 1.4. Contributions by Others

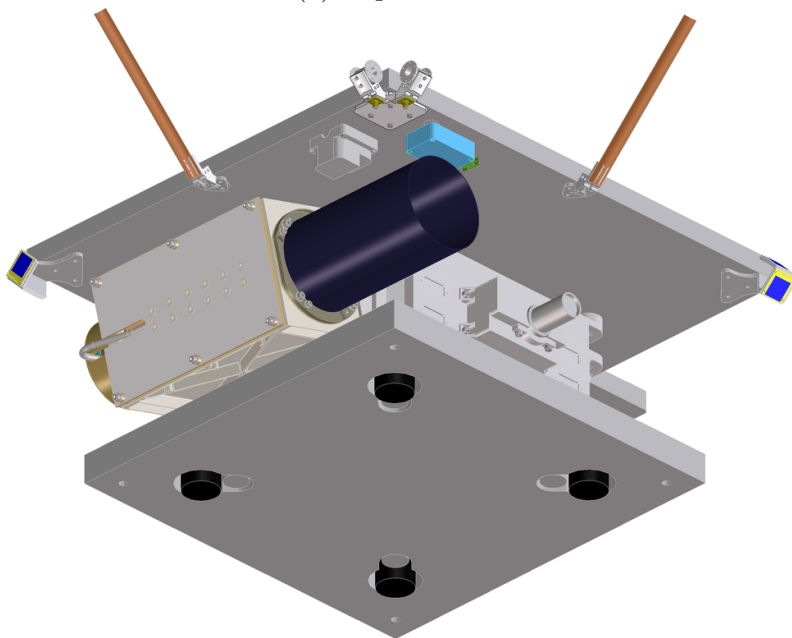
Developing an X-ray telescope requires expert knowledge in mechanical, optical, thermal and electronics engineering. Numerous people at the MPE have contributed to the development of  $\mu$ ROSI. Without their effort, this project would never have been possible. Elias Breunig started working on the  $\mu$ ROSI project when writing his study thesis about the development and qualification of the optical bench (Breunig, 2011b) (see section 8.2). Afterwards, he wrote his master's thesis about the superpolishing of the mandrels, which are essential for the manufacturing of the  $\mu$ ROSI mirror shells (Breunig, 2011a) (see section 7.4). The testing of the first mirror shell (section 7.5) was conducted at the MPE PANTER X-ray test facility by Vadim Burwitz and his team. Maria Fürmetz contributed to the thermal control subsystem (chapter 9) with her thermal analyses and her work on heat pipe filling and testing (Fürmetz, 2012). The electronics subsystem (chapter 10) has been designed, developed and tested by the MPE electronics group, namely Walter Kink, Diogo Coutinho, Siegfried Müller and Ziliang Zhang.

## *1. Introduction*

---



(a) Top left view



(b) Bottom left view

Figure 1.1.: 3D-Model of the Max-Valier Satellite in launch configuration mounted on the release adapter plate with four separation bolts (3D-model provided by GOB/OHB).

## 2. A Brief Introduction to X-Ray Astronomy

### 2.1. X-Rays in the Electromagnetic Spectrum

X-rays are a form of electromagnetic radiation just as infrared (IR), visible light (VIS), ultraviolet (UV) or gamma-radiation. While IR represents the cold, low energetic end in this sequence, X-rays are at the hot, high energetic end. The boundaries of the aforementioned bandwidths can be characterized by their wavelength  $\lambda$ , frequency  $f$ , energy  $E$  or temperature  $T$ . The relation between energy, frequency and wavelength are given by the Planck relation (see eq. (2.1)).

$$E = h f = \frac{h c}{\lambda} \quad (2.1)$$

The associated temperature can be derived with Wien's displacement law:

$$\lambda T = b \quad (2.2)$$

where

$c = 299,792,458 \frac{m}{s}$	Speed of light
$h = 6.62606957 \cdot 10^{-34} J \cdot s$	Planck constant
$= 4.135667516 \cdot 10^{-15} eV \cdot s$	
$b = 2.8977685 \cdot 10^{-3} m \cdot K$	Wien's displacement constant

Figure 2.1 shows a fraction of the electromagnetic spectrum from  $\sim 10 \mu m$  infrared to gamma-radiation. While the boundaries of the visible light are well confined, the boundaries between the other regimes are rather blurred. For instance, the transition between highly energetic ultraviolet and X-ray radiation is often called *extreme ultraviolet* (EUV or XUV). When describing IR, VIS or UV radiation, it is common to use the wavelength as characteristic dimension. For X-rays and gamma-rays, it is more convenient to use the energy level in electron volts [eV].

## 2. A Brief Introduction to X-Ray Astronomy

---

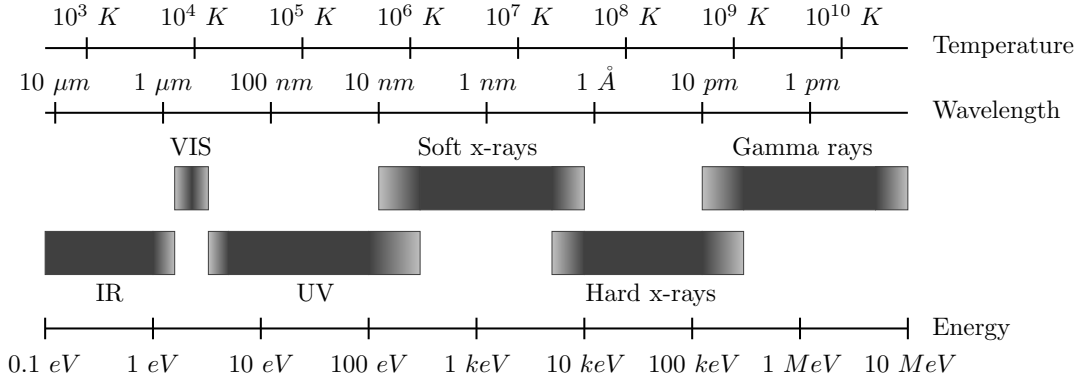


Figure 2.1.: X-ray radiation in the electromagnetic spectrum

X-ray radiation ranges from  $\sim 120 \text{ eV}$  to  $\sim 200 \text{ keV}$ . X-ray radiation itself is subdivided into low energetic *soft* X-rays and high energetic *hard* X-rays. The boundary between soft and hard X-rays is typically considered to be at  $\sim 10 \text{ keV}$  and in the scope of this work this value will be used to discern soft from hard X-ray radiation.

However, this is not a clearly defined convention. More important for the distinction of hard and soft X-rays than the energy level are the methods required for detecting them. The wavelength of hard X-rays is in the order of (or smaller than) an atomic diameter. Thus, hard X-rays have considerably higher penetration depths than soft X-rays. In effect, they cannot be focused by refraction or reflection. Instead, collimators or coded masks were required to achieve spatial resolution for energies  $> 10 \text{ keV}$ <sup>1</sup>.

Looking at the temperature scale in fig. 2.1, it becomes clear that soft X-ray radiation corresponds to temperatures from 1 to several tens of million  $K$ . X-ray astronomy thus reveals astrophysical processes involving extremely high temperatures.

## 2.2. X-Ray Astronomy History and Missions

X-rays were first discovered by Wilhelm Conrad Röntgen in 1895 when experimenting with vacuum tubes. The X-rays produced a visible image on a photo-sensitive plate and the photography depicting his wife's hand (see fig. 2.2) immediately suggested the practical use of X-rays for medical diagnosis. Röntgen's breakthrough discovery won him the very first Nobel Prize in physics in 1901.

---

<sup>1</sup>Multi-layer mirrors, such as the one used for the NuSTAR telescope, are capable of focusing



Figure 2.2.: X-ray photography of Mrs. Röntgen’s hand taken by Wilhelm Conrad Röntgen in 1895 showing her bones and her wedding ring (source: NASA).

In 1908, Rutherford, Geiger, and Harling published “An Electrical Method of Counting the Number of  $\alpha$  -Particles from Radio-Active Substances” introducing the first technique to measure ionizing radiation with a gaseous detector (Rutherford et al., 1908). Subsequently, ionizing radiation was measured in 1912 in the atmosphere by Hess and his team during several balloon experiments (Hess, 1912). The radiation was later identified as cosmic rays and Hess was awarded the Nobel Prize in physics in 1936 for his work.

The first X-ray experiments detecting X-ray radiation from the Sun was launched in 1949 under the direction of the U.S. Navy with a V2 rocket from White Sands missile range. In 1962, Scorpius X-1 was the first extrasolar X-ray source discovered by an X-ray detector mounted on an Aerobee 150 rocket which was originally intended to measure X-ray emissions from the Moon.

The UHURU mission conducted the first all-sky survey in the early 1970s. With its proportional counter detector behind a collimator, it was capable of measuring 339 X-ray sources. The next big leap was the use of focusing optics, so-called Wolter-1 telescopes (refer to section 4.1 for details about X-ray focusing optics) to increase the effective area. The HEAO-2 mission, later renamed *Einstein*, was

---

soft and hard X-rays using special multi-layer coatings.

## 2. A Brief Introduction to X-Ray Astronomy

---

the first mission featuring an imaging X-ray telescope. Its survey yielded almost 7000 X-ray sources with unprecedented angular resolution.

Mission	Year	Energy	Sources	Reference
UHURU	1970–1973	2–6	339	Forman et al. (1978) <sup>2</sup>
OSO-7	1971–1973	1–60	184	Markert et al. (1979) <sup>2</sup>
HEAO-1/A1	1977–1979	1–20	842	Wood et al. (1984) <sup>2</sup>
HEAO-1/A2	1977–1979	0.2–2.8	114	Nugent et al. (1983) <sup>2</sup>
HEAO-1/A4	1977–1979	13–180	40	Levine et al. (1984) <sup>2</sup>
HEAO-2 <sup>3</sup>	1978–1981	0.2–20	6816	Harris (1990)
ROSAT	1990–1999	0.1–2.4	145,060	Voges et al. (1999)
ASCA	1993–2000	0.7–10	104	Ueda et al. (1998)
RXTE	1995–2012	3–20	294	Revnivtsev et al. (2004)
SRG <sup>4</sup>	2014–	0.1–10	$> 3 \cdot 10^6$	Predehl et al. (2010)

Table 2.1.: List of selected X-ray survey missions. Energy ranges given in [keV].

ROSAT surpassed the results of *Einstein* by detecting some 150,000 sources. Its comprehensive sky coverage and precise measurement of the X-ray background radiation are unmatched until today.

The ROSAT all-sky survey (RASS) and the following ROSAT pointed observation phase completed in 1999 generated the most comprehensive database of X-ray sources. All detected sources are listed in “The ROSAT all-sky survey bright source catalogue” (RASS-BSC: Voges et al., 1999) and “ROSAT All-Sky Survey Faint Source Catalog (Voges+ 2000)” (RASS-FSC: Voges et al., 2000). A recent review of the scientific achievements of the RASS is given by Watson (2009) stressing the mission’s scientific achievements:

- mapping of the X-ray background,
- compilation of a large sample of clusters of galaxies enabling the assessment of the large-scale structure of the universe,
- measurement of the space density of active galactic nuclei (AGN) providing insight into their evolution processes,

<sup>2</sup>Reference given in “The ROSAT all-sky survey bright source catalogue” (Voges et al., 1999)

<sup>3</sup>Later renamed *Einstein*

<sup>4</sup>SRG = Spectrum Röntgen Gamma

- providing vast amount of X-ray emissions from stars throughout the H-R diagram giving insights into fundamental stellar properties and emission processes.

As of 2013, there are four large X-ray observatories in operation: Chandra, XMM, Suzaku and NuSTAR (see table 2.2). None of the telescopes currently in orbit performs an all-sky survey. The European XMM has the highest collecting area of all imaging X-ray telescopes and therefore allows to observe even the faintest sources. Chandra has an unprecedented angular resolution of 0.5 arcseconds enabling it to discern the finest features in an observation. The Japanese Suzaku mission has an extremely high energy range from low energetic soft X-rays up to gamma-rays. NuSTAR features a deployable mast to increase the focal length. With its special multi-layer coating on the focusing mirrors, NuSTAR is capable of achieving high resolution images up to energy levels of  $\sim 80 \text{ keV}$ .

In 2014, the Russian mission Spectrum-Roentgen-Gamma (SRG) with the German eROSITA telescope will be launched to, once again, perform an all-sky survey. The objective of this mission is to detect several millions of sources and at least 100,000 clusters of galaxies in soft X-rays. The vast amount of data is needed to learn more about the large scale structure of the universe and to discern theoretical models explaining the role of the dark energy in our universe. As SRG is intended as an instrument for an all-sky survey, its optical design is optimized for a high grasp, i.e. the product of FOV and effective area.

	Chandra	XMM	Suzaku	NuSTAR	SRG
Launch year	1999	1999	2005	2012	2015
Mass [kg]	4800	3800	1700	360	3000
Energy range [keV]	0.1 - 10	0.2 - 12	0.4 - 600	3 - 79	0.1 - 15
FOV	31'	30'	19'	10'	60'
Best resolution	< 0.5''	$\sim 6''$	< 1.5''	18''	25''
Max. eff. area [cm <sup>2</sup> ]	525	1304	1600	$\sim 1000$	1500
at [keV]	1.5	1.5	1.0	$\sim 10$	1.5
Focal length [m]	10	7.5	4.75	10.14	1.6
Outer diameter [m]	1.2	0.7	0.4	0.382	0.36
F-number [1]	8.333	10.714	11.875	26.545	4.444

Table 2.2.: Comparison of current X-ray observatories (launch of SRG is scheduled for 2015).

## 2. A Brief Introduction to X-Ray Astronomy

---

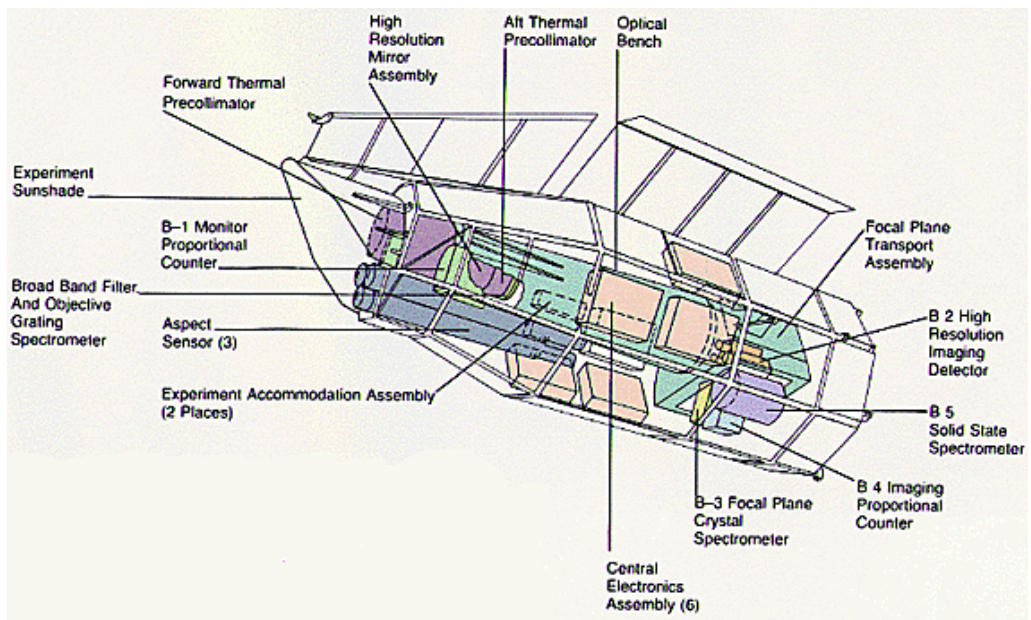


Figure 2.3.: Diagram of the satellite layout of the HEAO-2 satellite, also known as Einstein (source: NASA).

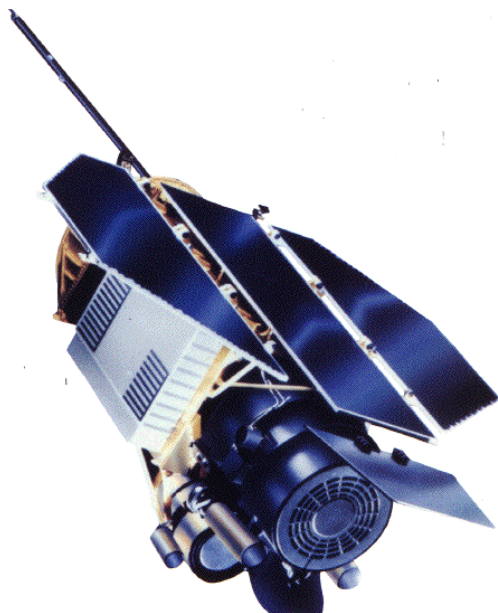


Figure 2.4.: The ROSAT satellite in flight configuration (source: MPE).

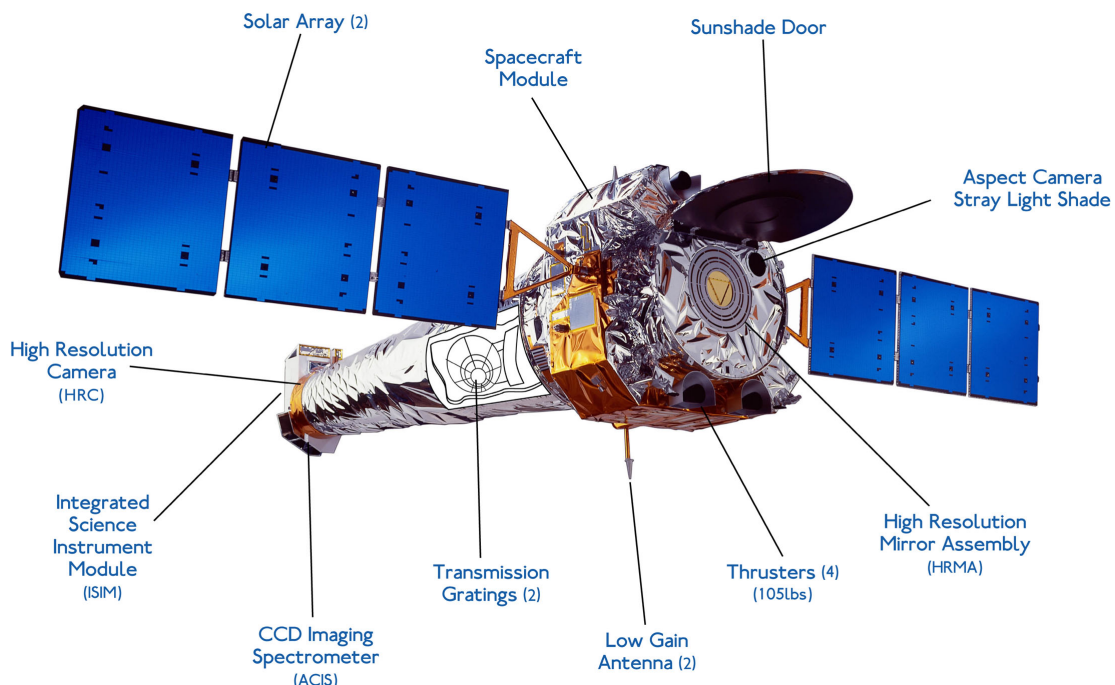


Figure 2.5.: Illustration of the Chandra X-ray observatory (source: NASA/CXC/SAO).

## *2. A Brief Introduction to X-Ray Astronomy*

---



Figure 2.6.: Artist's impression of XMM-Newton (source: ESA).

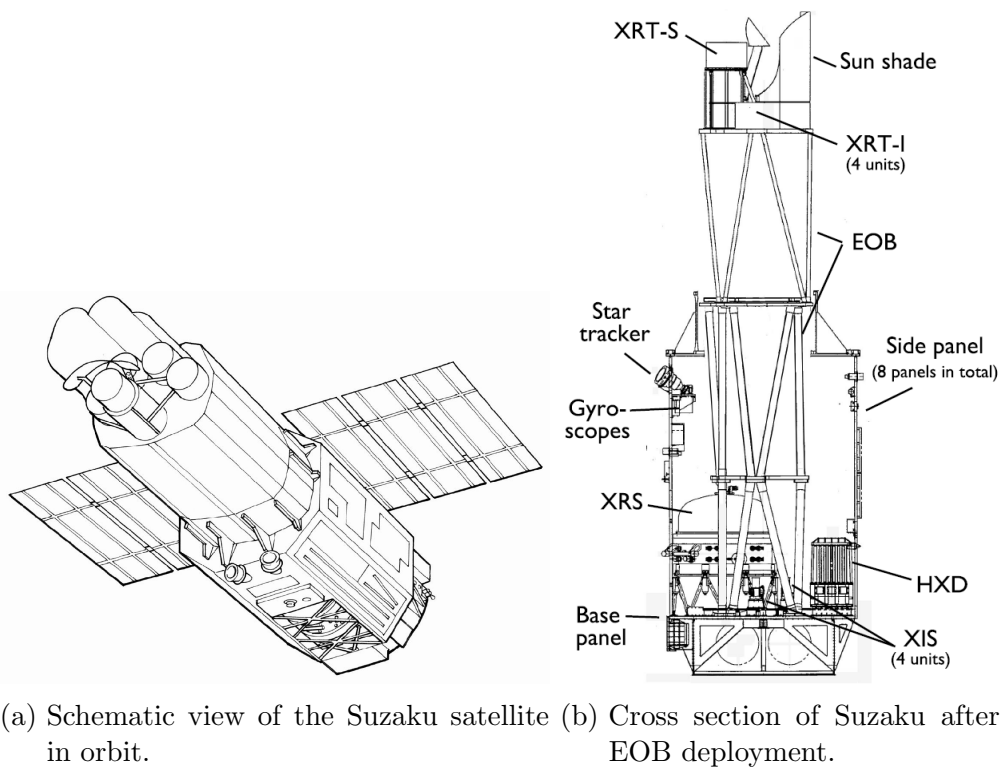


Figure 2.7.: Schematics of the Suzaku X-ray observatory (source: Mitsuda et al., 2007).

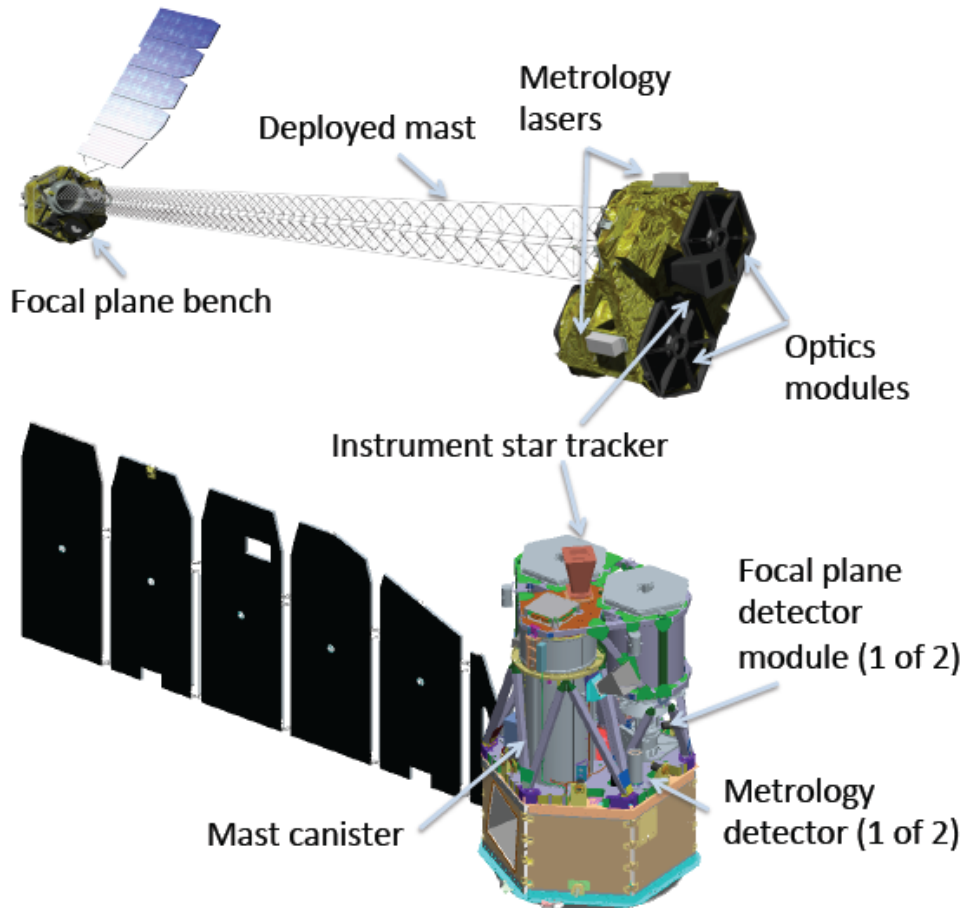


Figure 2.8.: Diagram of the NuSTAR X-ray observatory in the stowed (bottom) and deployed (top) configurations (Harrison et al., 2013).

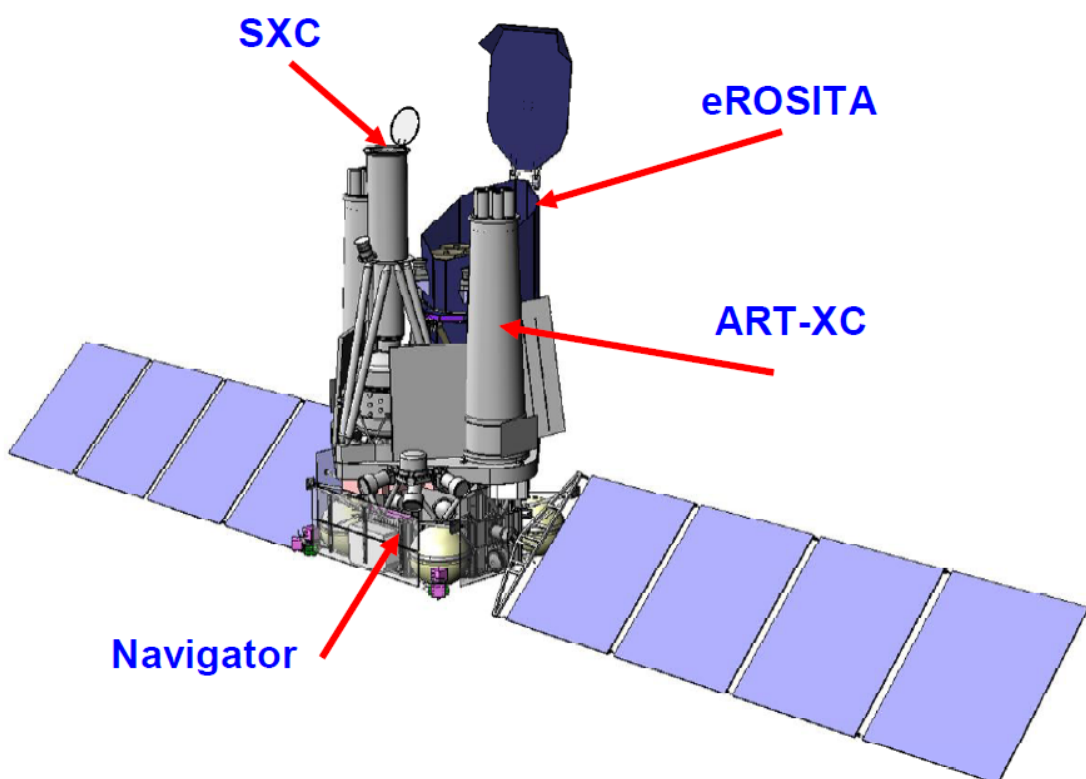
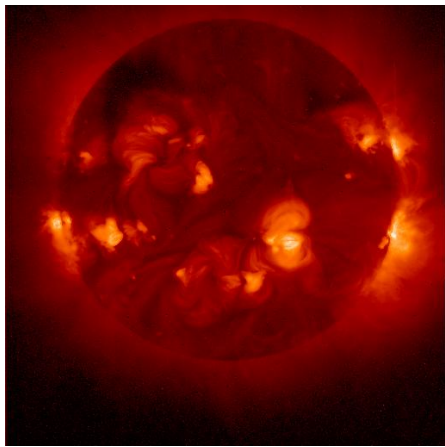


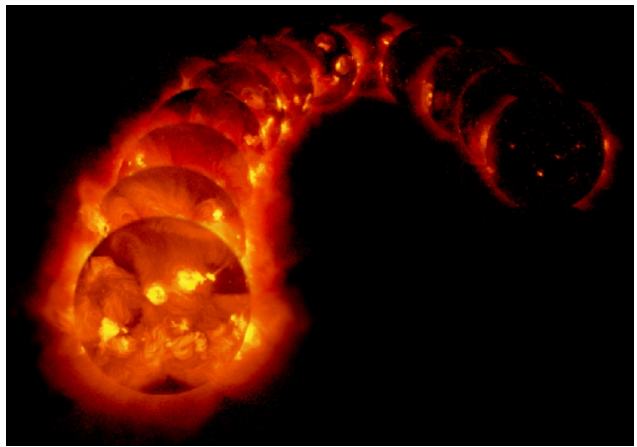
Figure 2.9.: SRG Scientific payload: eROSITA, SXC and ART-XC on the Navigator platform (source: Pavlinsky et al., 2008).

## 2.3. Solar System X-Ray Sources

In our solar system, the Sun is the most predominant primary X-ray source. While the Sun's outer surface with its  $6000\text{ K}$  is too cool to produce any X-ray radiation, the temperatures of the solar corona can reach several millions of degrees – hot enough to produce soft X-ray radiation. Solar X-ray radiation is transient, changing over timescales of decades (the solar cycle, see fig. 2.10) down to minutes with solar flares. Solar flares emit radiation over the full electromagnetic spectrum, from radio wavelengths to gamma rays.



(a) Solar soft X-ray emissions.



(b) The 11-year solar cycle in X-rays.

Figure 2.10.: The Sun in X-rays. Images from the Japanese Yohkoh mission (source: NASA).

The Sun also contributes to the luminosity of other solar system objects. X-ray radiation and charged particles from the Sun, predominantly H-ions, He-ions and electrons, are scattered or absorbed by almost any object in the solar system. These objects are therefore visible in X-rays with comparable appearance as in the optical. But as the overall X-ray radiation intensity of the Sun is considerably lower than in the optical, the objects are much fainter.

For example, the ROSAT telescope observed the Moon in soft X-rays (see fig. 2.11). According to Konrad Dennerl (in Trümper and Hasinger, 2008), this image shows three separate phenomena:

1. *Scattering of solar X-rays on the lunar surface at the Sunlit side*
2. *Shadowing of the diffuse cosmic X-ray background on the dark side*
3. *Excess X-rays at the dark side due to X-ray emission from the geocorona in the foreground*

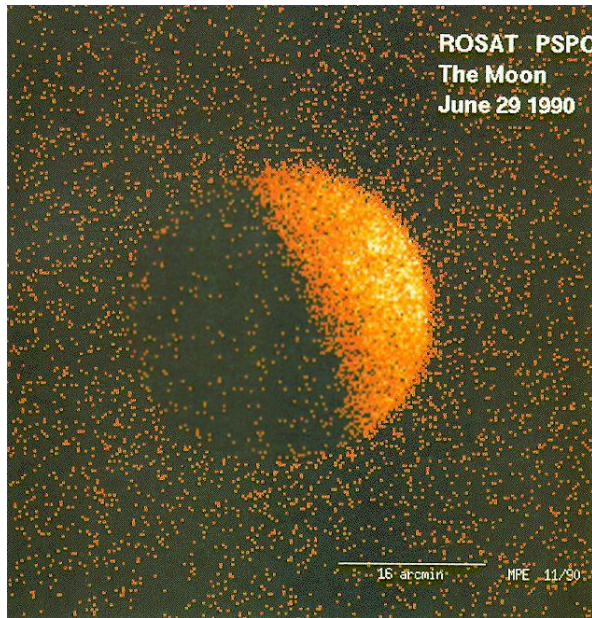


Figure 2.11.: The Moon in soft X-rays. Image from the ROSAT mission, printed in Trümper and Hasinger (2008), originally published in *Nature* (Schmitt et al., 1991)

These findings show the following:

1. The sun is the predominant source of X-rays in the solar system.
2. Any object scatters X-rays in a similar way as it scatters visible light (a half Moon in the visible also appears as a half Moon in X-rays).
3. There is a diffuse X-ray background radiation.
4. There is another background radiation source between Moon and Earth.

Other solar system objects, that have been observed in X-rays include Venus (Dennerl et al., 2002), Mars (Dennerl, 2002; Dennerl et al., 2006), Jupiter (Metzger et al., 1983) and comets (Lisse et al., 1996) among others. Bhardwaj et al. (2007b) give an overview of X-ray radiation from solar system objects.

The observation of comets (Lisse et al., 1996) in X-rays revealed the mechanism of charge exchange, which plays an important role in all areas of high energy astrophysics.

The Earth is also active in X-rays in several ways. The geocorona is visible in X-rays due to charge interactions between the solar wind and hydrogen. This way, the Earth's outermost atmosphere contributes to the X-ray background that is

## 2. A Brief Introduction to X-Ray Astronomy

---

visible from satellite platforms within the geocorona. This background radiation is visible in fig. 2.11 in the dark Moon regions (Dennerl, 2008).

Another process that contributes to the Earth's luminosity in X-rays is the magnetosphere. Electrons that are accelerated by the Earth's magnetic field emit bremsstrahlung when decelerated in the upper atmosphere. This effect is particularly present in the polar regions as measurements with the POLAR Earth observation mission revealed, mapping the Earth aurora in X-rays with the PIXIE instrument (Petrinec et al., 2000). The large X-ray observatory Chandra also measured the polar regions in soft X-rays (Bhardwaj et al., 2007a).

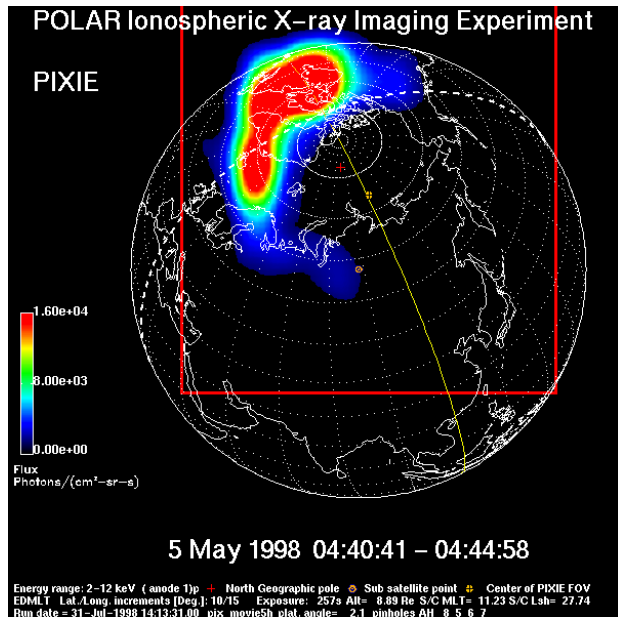


Figure 2.12.: X-ray image of the aurora borealis from the POLAR mission taken with the PIXIE instrument (source: NASA/GSFC).

The observation of Jupiter with the Einstein telescope between 0.2 and 3.0 keV (Metzger et al., 1983) revealed the more complex interaction of the Jovian magnetosphere with the solar wind and its orbiting moons Io, Europa and Ganymede.

## 2.4. Extrasolar X-Ray Sources

Galactic stellar sources are ubiquitous and the type of source is manifold – from cataclysmic variables (Verbunt et al., 1997; Ritter and Kolb, 2003), white dwarfs (Fleming et al., 1996), neutron stars (“The X-ray luminosity of rotation-powered neutron stars.”), OB-type stars (Berghofer et al., 1996) to late-type giants and

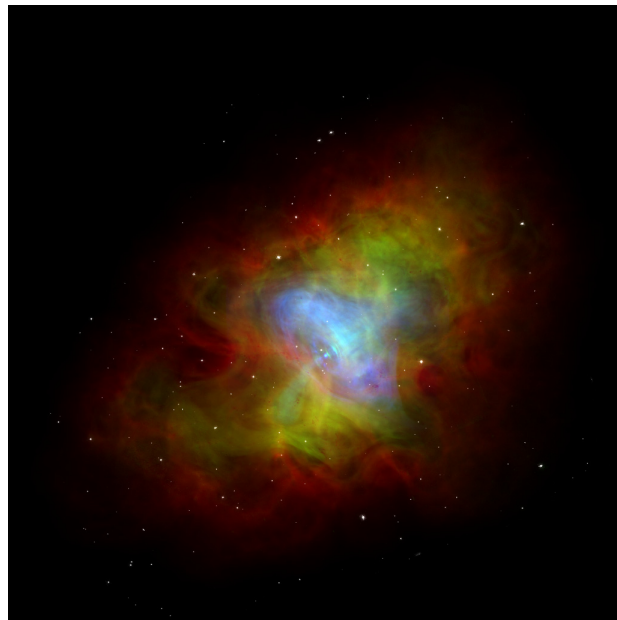


Figure 2.13.: Example of a galactic X-ray source: The crab nebula with its central pulsar. Composite image from radio (green), optical (red) and X-ray (blue) wavebands (source: Trümper and Hasinger, 2008).

supergiants (Hünsch et al., 1998). A cross-correlation of the RASS data with nearby star catalogues was performed by Hünsch et al. (1999). The brightest sources in our galaxy are accreting neutron stars and black holes, for example “Low Mass X-ray Binaries” (LMXB), which transfer vast amounts of energy in confined spaces. Supernova remnants (SNR) are the largest visible objects in the X-ray sky. SNR are the only type of source that is not variable.

Among the extragalactic sources are active galaxy nuclei (AGN) of various types (e.g., Bade et al., 1995), quasars and super-massive black holes in galaxy centers. All these sources are variable, unlike the most distant objects visible in X-rays, galaxy clusters (e.g., Briel and Henry, 1993; Vikhlinin et al., 1998; Rosati et al., 2002). These objects comprise thousands of galaxies and are the largest structures in the universe.



# 3. Max-Valier Satellite Mission

## 3.1. Project Partners and Tasks

The Max-Valier Satellite (MVS) project is a co-operation of South-Tyrolean schools *Gewerbeoberschule Max Valier* Bolzano (GOB), *Gewerbeoberschule Oskar von Miller* Merano (GOM), the amateur astronomer's club *Amateurastronomen Max Valier* (AMV), the space company OHB System AG Bremen (OHB) and the *Max-Planck-Institut für extraterrestrische Physik*, Garching (MPE). Figure 3.1 (Orgler et al., 2009) shows a map that shows the locations of the project partners. The Italian company Media Lario Technologies (MLT) contributes to the project by delivering the X-ray mirror shells free of charge.

The tasks and responsibilities of each of the aforementioned project partners are summarized below.

GOB:

- Power supply
- On-board data handling
- Attitude control electronics
- Structural manufacturing
- Operations

GOM:

- Telemetry and telecommand
- Antennas

OHB:

- Project management
- Systems engineering
- Project funding
- Structural and thermal design
- Launch
- Satellite integration
- Secondary payloads
  - AIS receiver
  - CMOS camera

### 3. Max-Valier Satellite Mission

---

AMV:

- Astronomical data analysis

MPE:

- X-ray telescope
- Telescope integration
- Satellite environment testing

MLT:

- X-ray mirror shells



Figure 3.1.: Max-Valier Satellite project partners (Orgler et al., 2009).

OHB is not only responsible for the systems engineering and the project management, which includes the co-ordination of the project partners, but also covers most of the funding. Each component is designed, developed and tested individually by the responsible partner. The complete satellite is integrated at the OHB facilities in Bremen. However, in order to avoid contamination of the extremely sensitive X-ray mirror surfaces, the  $\mu$ ROSI X-ray telescope is transported only if absolutely necessary. Thus, the satellite is integrated and transported to the

MPE facilities without the X-ray telescope. In the MPE cleanrooms, the  $\mu$ ROSI telescope will be integrated after the satellite has been outgassed properly. Then, the satellite undergoes the environmental tests at the MPE. These tests include random vibration test, thermal cycling, thermal balance test as well as functional tests.

## 3.2. Satellite Launch

The Max-Valier Satellite is scheduled for launch on a VEGA rocket in April 2014. The launch has been confirmed by Arianespace in June 2013 during the Paris Air Show in Le Bourget (Arianespace, 2013). The MVS nanosatellite is launched as one of two piggy-back payloads, the second being the Latvian Venta-1 nanosatellite. Both satellites are based on the same Quadsat platform developed by the University of Applied Sciences Bremen (Ventspils High Technology Park, 2012).

Figure 3.2 shows the accommodation of MVS and the Latvian Venta-1 satellite within the VEGA payload fairing. MVS and Venta-1 are both mounted directly on the conical section of the launch adapter underneath the adapter ring for the primary payload.

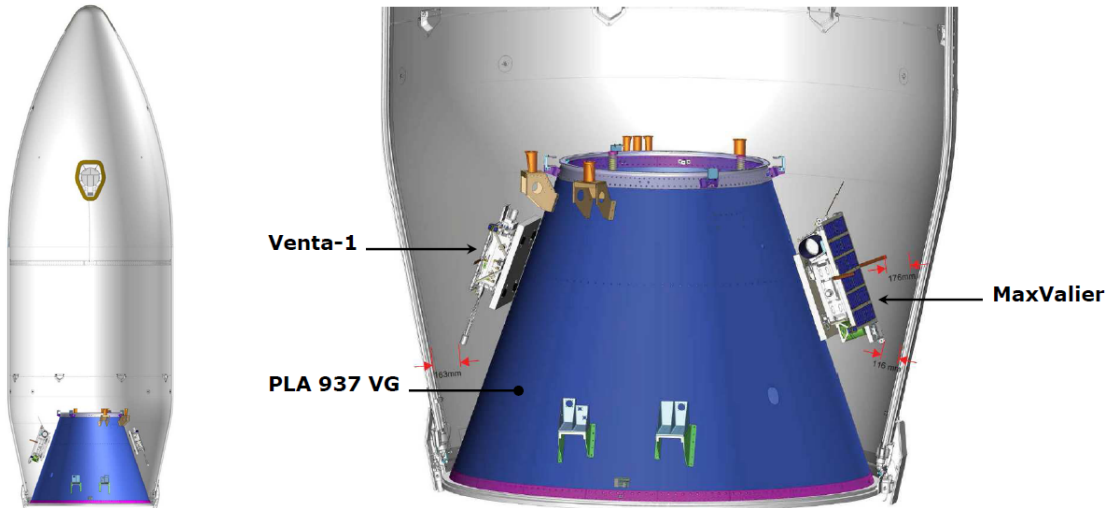


Figure 3.2.: Accommodation of MVS and the Latvian Venta-1 satellite inside the VEGA payload fairing (source: Arianespace, 2013). The primary payload is not shown in this image.

### 3. Max-Valier Satellite Mission

---

Due to the accommodation on the conical launch adapter, the piggy-back payload satellites are separated after the primary payload. The separation from the launcher is performed with four separation bolts that release the satellite perpendicularly to the mounting plate. The orientation of the satellites on the conical adapter has an impact on the final orbit of each satellite. Assuming that the primary payload is released in a circular orbit, both piggy-back payloads will be injected into an elliptical orbit due to the lateral orientation of the release adapter. However, as of July 2013, the exact release sequence is still under investigation by OHB and Arianespace.

## 3.3. All Sky Survey

Performing an all-sky survey means that the telescope scans the whole sky. For this purpose the telescope needs to rotate with an angular velocity  $\omega_s$  (see fig. 3.3). Thus, the telescope scans a swath with a width that matches its field of view (FOV)  $\Theta$  along one great circle of the sky. In order not to scan the same great circle again and again, the scanning plane needs to precess with a precession rate  $\omega_p$  so that, over time, the swaths cover the whole sky.

Figure 3.4a shows the exposure map of the ROSAT all-sky survey (RASS) in equatorial coordinates. This map gives a distribution of the time spent observing the sky. Clearly visible are the survey poles (bright blue regions) that are crossed by every scanning swath. As a result, the survey poles were observed with longer exposure time than the regions close to the ecliptic plane. The image also shows some gaps on the map (dark spots) that were observed only briefly. This was due to the fact that the ROSAT PSPC instrument was switched off when it crossed the South Atlantic anomaly (Voges et al., 1999) to avoid damage due to higher density of charged particles.

An ideal all-sky survey would equally distribute the exposure time over the whole sky. But the areas of deep exposure coincide with the precession axis, and the precession axis can not be changed arbitrarily. However, with a nutation of the precession axis, the areas of deep exposure could be widened up and the effect of high-highlighted regions in the exposure map can be reduced.

Assuming that the telescope is firmly mounted to the satellite, it is the satellite attitude control system's task to perform the manoeuvres required for the all-sky survey. The attitude accuracy is not required to be high. As the telescope scans the whole sky, a brief deviation of the scan path is acceptable as long as the actual orientation is known precisely. Thus, the spacecraft's attitude sensors shall be able to deliver information where the telescope was pointed with an accuracy of half of the field of view angle as a minimum requirement.

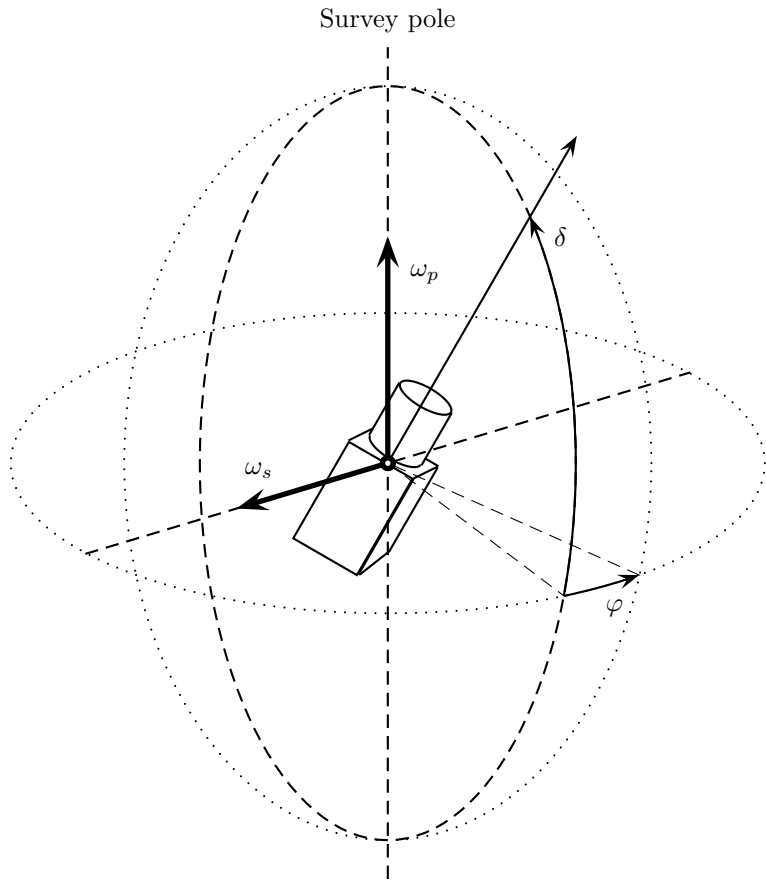
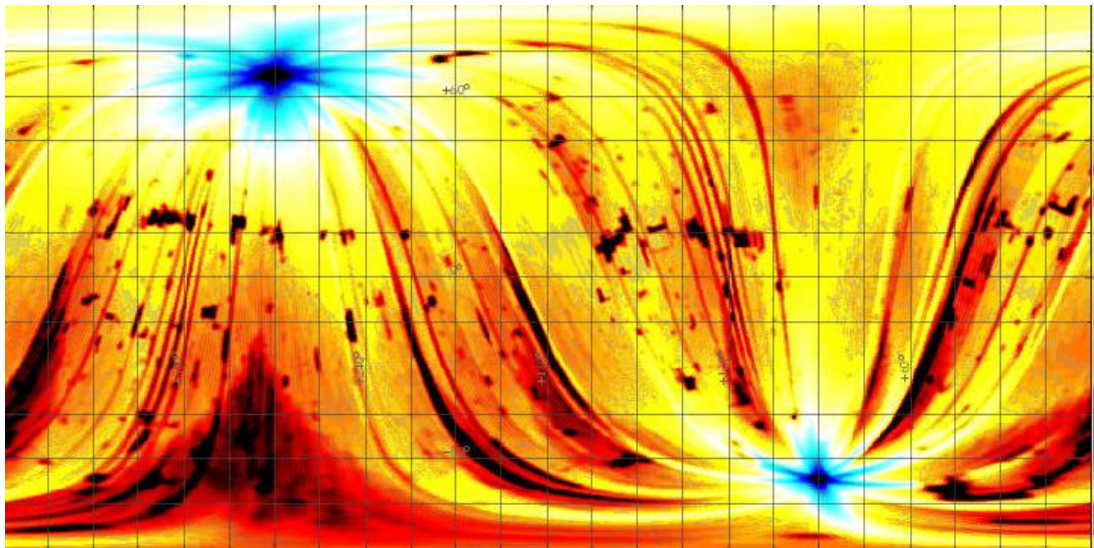


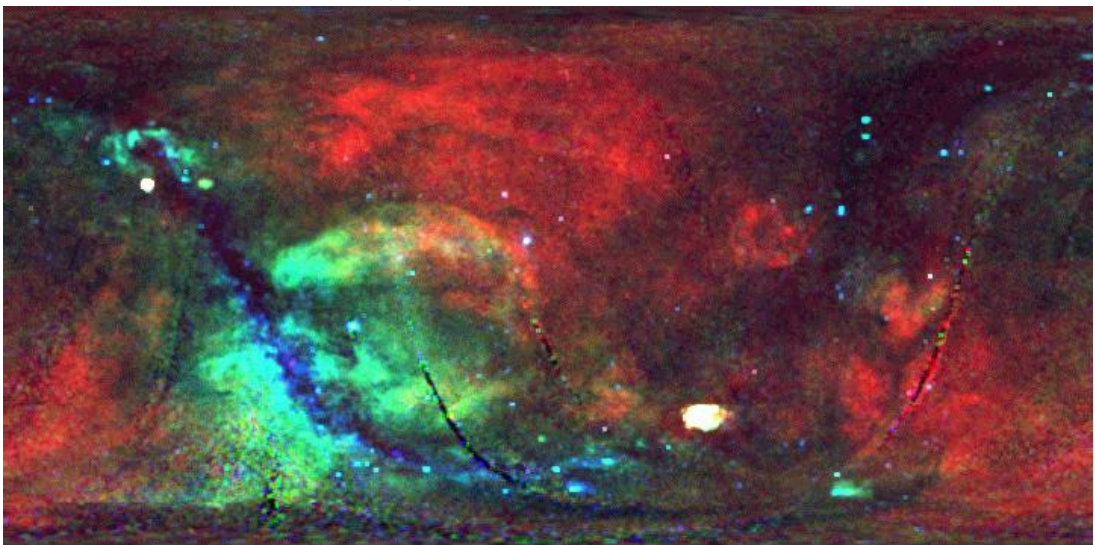
Figure 3.3.: All-sky survey geometry. The telescope boresight rotates around its scan axis with the angular velocity  $\omega_s$  describing a great circle in the sky for one full revolution. The scanning plane precesses around with a precession rate  $\omega_p$ .

### 3. Max-Valier Satellite Mission

---



(a) ROSAT exposure map



(b) ROSAT X-ray background radiation map

Figure 3.4.: X-ray background map (fig. 3.4b) and exposure map (fig. 3.4a) of the ROSAT all-sky survey in equatorial coordinates (Englhauser (images from 2001), Voges et al. (originally published by 1999)). The survey poles were observed with longer exposure times (blue regions in the exposure map), as they are crossed with every scanning great circle. The X-ray background map does not show point sources. It could be measured precisely due to the outstanding background rejection capabilities of the ROSAT PSPC detectors.

## 3.4. Sun-Synchronous Orbit (SSO)

Sun-synchronous orbits are a class of orbits that use the perturbations caused by the Earth oblateness to maintain a constant angle between the orbit plane and the Sun. This angle is often referred to as the  $\beta$ -angle. A constant  $\beta$ -angle has the great advantage that the solar panels of three-axis stabilized spacecraft continuously point towards the sun without the need for attitude changes or solar panel movements. Another characteristic of SSOs is that each geographical latitude is always crossed at the same local time.

In order to achieve a constant  $\beta$ -angle, the orbit plane needs to precess around the Earth with the same speed in which the Earth circles around the Sun. Expressed in figures, the orbit is perturbed so that the orbit plane precesses with an angular velocity of  $0.9856^\circ$  per day, summing up to a total  $360^\circ$  in one year.

If the  $\beta$ -angle is zero, the spacecraft ground track coincides with the day-night border. The ascending node is either passed at 0600 local time or at 1800 local time. As the spacecraft never enters the Earth's shadow, solar panels can work continuously. The temperatures of the spacecraft remain rather stable as it never enters the Earth shadow.

A SSO with an ascending node at 1200 or 2400 local time crosses the day-night border perpendicularly. The spacecraft is exposed to the Sunlight during a first day phase of the orbit and enters the Earth shadow during the eclipse phase of the orbit. Depending on the orbit altitude, the first phase comprises some 55 to 75% of the orbit time. The rapid change between the two phases is a major challenge for the thermal control of the spacecraft.

Other popular SSO orbits cross the ascending node at 0900 or 2100 local time, the so-called dusk-dawn orbits. They are particularly suited for Earth observation missions as the Earth below is illuminated by the Sun with low incidence angles. Objects on the ground cast long shadows which is helpful for certain Earth observation methods.

The deviations of the Earth from a perfect sphere is usually described in geopotential models. These models give an analytical approach do describe the actual gravitational field of the Earth with various terms  $J_i, C_i, S_i$ . The most dominant is the  $J_2$  term that specifies the oblateness of the Earth<sup>1</sup>. In effect, the gravitational forces on the satellite are larger at the equator than at the poles. This perturbation can be expressed as a momentum with the momentum vector originating in the Earth center and going through the ascending node. Due to the momentum of inertia of the satellite, the resulting perturbation is a precessing rotation with an angular velocity  $\Omega_{orbit}$  of the orbit plane.

---

<sup>1</sup>The diameter of the Earth at the equator is 12756 km and 12714 km at the poles.

### 3. Max-Valier Satellite Mission

---

$$\Omega_{orbit} = -2\pi \frac{J_2}{\mu_E p^2} \frac{3}{2} \cos i \quad (3.1)$$

where

$\Omega_{orbit}$	$\left[ \frac{\text{rad}}{\text{orbit}} \right]$	Precession rate of the ascending node
$J_2$	$= 1.7555 \cdot 10^{10} \text{ km}^5/\text{s}^2$	2 <sup>nd</sup> zonal coefficient in geopotential model
$\mu_E$	$= 398600.440 \text{ km}^3/\text{s}^2$	Gravitational constant of the Earth
$p$	$[\text{km}]$	Semi-latus rectum of the orbit
$i$	$[\text{rad}]$	Orbit inclination

With the orbit period  $P$  depending only on the semi-major axis  $a$

$$P = 2\pi \frac{a^{\frac{3}{2}}}{\sqrt{\mu_E}} \quad (3.2)$$

and assuming a circular orbit where  $p = a$ , eq. (3.1) can be rewritten with  $\Omega$  [ $\text{rad}/\text{s}$ ]

$$\Omega = \frac{\Omega_{orbit}}{P} \quad (3.3)$$

$$= -\frac{3}{2} \frac{J_2 a^{-\frac{7}{2}}}{\sqrt{\mu_E}} \cos i \quad (3.4)$$

Introducing the orbit altitude  $h_{orbit} = a - R_E$  and equalizing eq. (3.3) with the angular velocity of the Earth around the Sun

$$\Omega_E = 1.99106 \cdot 10^{-7} \frac{\text{rad}}{\text{s}} \approx \frac{2\pi}{365 \text{ days}} \quad (3.5)$$

the relation between the orbit altitude and the inclination can be expressed

$$\cos i = -\frac{2}{3} \frac{\Omega_E \sqrt{\mu_E} (h_{orbit} + R_E)^{\frac{7}{2}}}{J_2} \quad (3.6)$$

Figure 3.5 shows inclinations and orbit altitudes for circular SSOs. The inclination is strictly higher than  $90^\circ$  which means that the spacecraft trajectory is retrograde towards the Earth rotation. SSOs exist theoretically for orbit altitudes of up to  $6000 \text{ km}$ , but the most common SSOs are at altitudes between  $600$  and  $1000 \text{ km}$ .

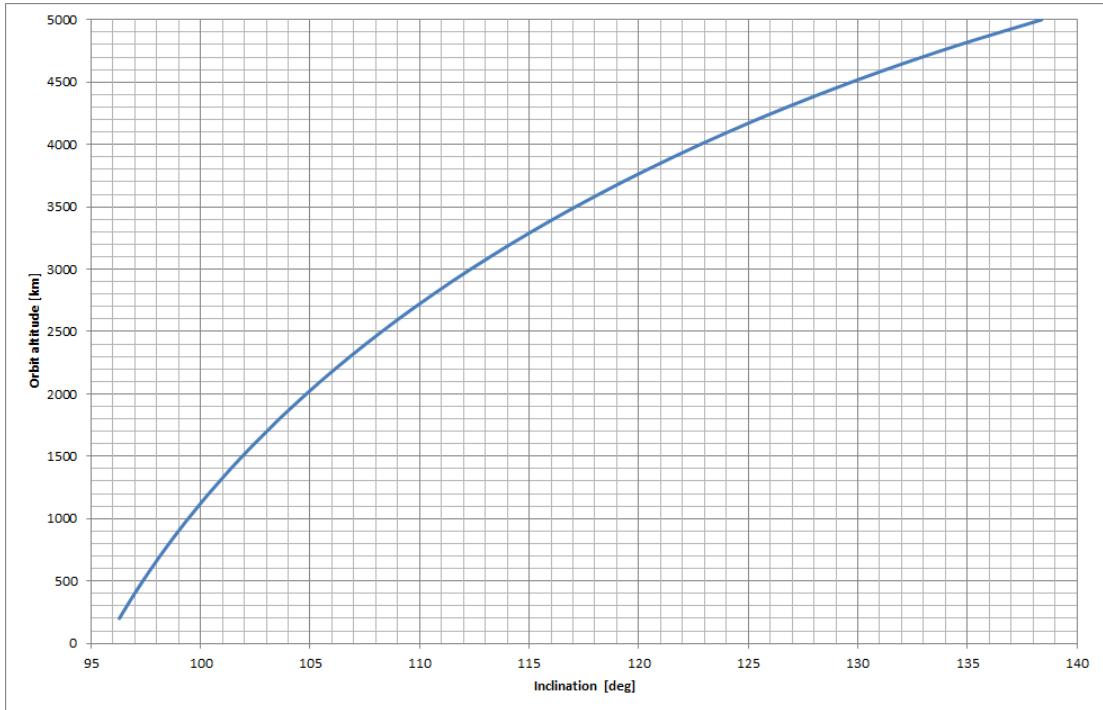


Figure 3.5.: Orbit altitude as a function of the inclination for Sun-synchronous orbits.

For the Max-Valier satellite mission, a SSO is the orbit of choice for two reasons. First, the solar panels can continuously generate electrical power without attitude changes. Secondly, the orbit precession helps to perform a full all-sky survey, if the scanning axis points towards the Sun (see section 3.5).

A small satellite mission such as Max-Valier is hardly able to select the orbit it is flying in. Instead, it is more likely to fly as a piggy-back payload and the prime customer determines the orbit. However, SSO have significant advantages for many satellite missions and chances are good to get a lift to a SSO.

The local time of the ascending node of the SSO is not relevant for the science case of the  $\mu$ ROSI telescope on board MVS. But, the local time has an impact on the thermal environment and on the availability of electrical power. The spacecraft and the telescope therefore should be designed for all types of SSOs.

### 3.5. Scanning Rotation

The solar panel, which is firmly mounted to the spacecraft, determines the attitude of the whole spacecraft. As the solar panel should always be pointed towards the Sun, the only degree of freedom for the spacecraft attitude is the rotation around the Sun vector. This rotational degree of freedom is used for the scanning rotation  $\omega_s$  (as shown in fig. 3.3).

The scanning rotation can be performed with almost any angular velocity. However, it should not be too fast so that observed X-ray sources in the sky do not get “smeared”. And it should also be not too slow so that the orbit precession creates dark streaks in the exposure map. An angular velocity that equals the orbit period is probably the most obvious selection. This way, the telescope could be continuously zenith pointed (see fig. 3.6a). The Earth would never be in the field of view, which is good for maximum time spent for observing the sky. However, the secondary mission goal requires observation of the Earth’s upper atmosphere in soft X-rays. This implies that the telescope should spin around the scan axis so that Earth horizon observations are possible.

Figure 3.6 shows the orbit plane and the telescope orientation during one orbit for different scanning rates. Figure 3.6a shows the above mentioned zenith pointing mode with a scan rate of one prograde revolution per orbit. In this mode no Earth horizon observations can be made. Figure 3.6b shows the same scanning velocity, but with retrograde rotation. This way, the Earth crosses the telescope’s field of view two times with four possible horizon observations. Increasing the scanning rotation velocity to two revolutions per orbit increases the number of possible Earth horizon observations to two for prograde rotation and six for retrograde rotation (see figures 3.6c and 3.6d).

For the zenith pointing mode the position of the Sun and the Earth, both the most dominant sources of thermal radiation, are stable as seen from the spacecraft. The Sun continuously shines on the solar panel and the Earth is always in the opposite direction of the telescope boresight. All other options depicted in fig. 3.6 yield varying view factors for the Earth. This circumstance has to be taken into account by the thermal analysis of the telescope.

The scanning rotation has an important influence on the telescope’s thermal environment. It does not determine whether or not the spacecraft enters eclipse, but it determines which parts of the spacecraft are pointed to Earth. However, as the final orbit is not yet fixed, precise recommendations can not be given as to how and when to change the scanning rotation.

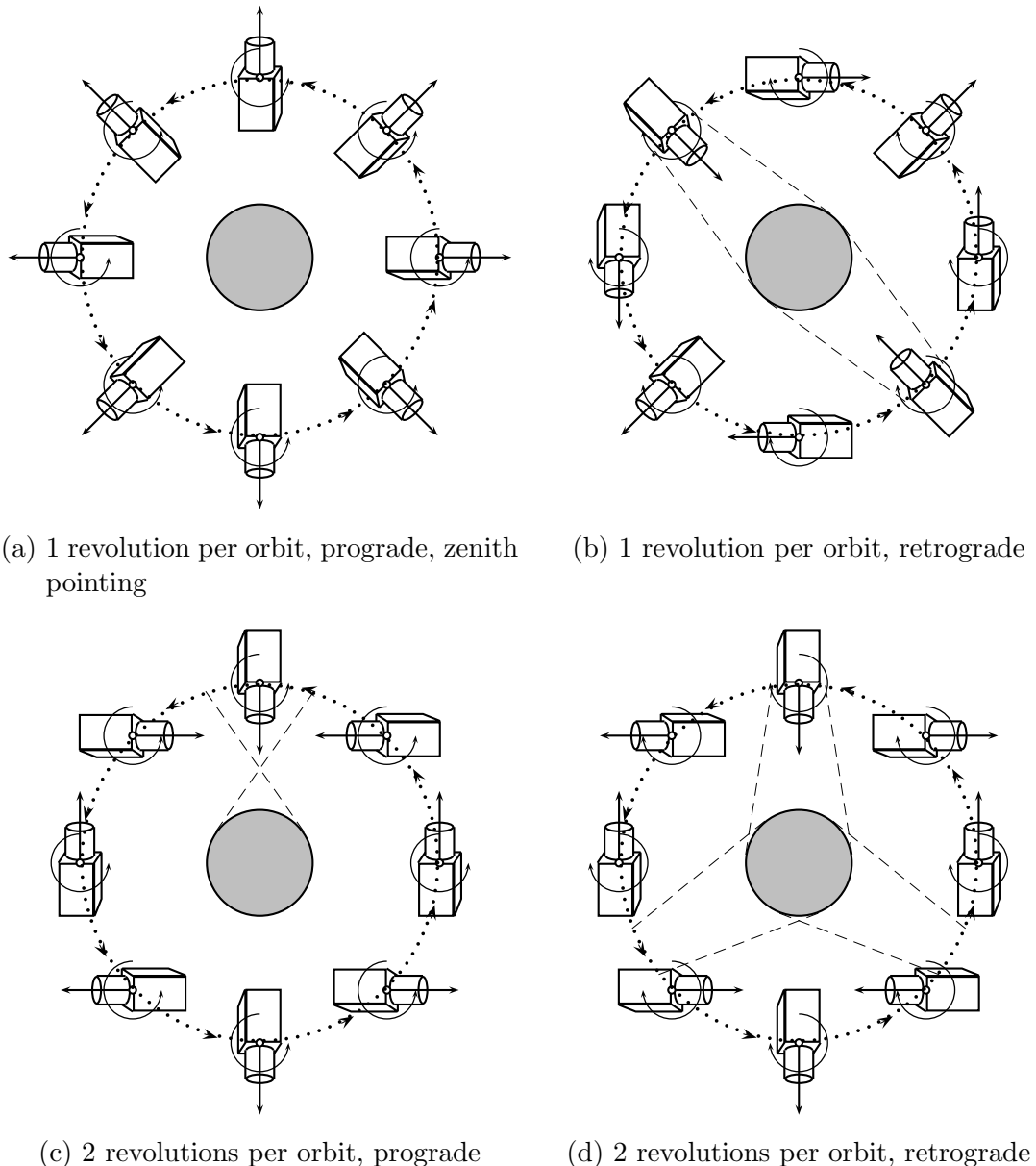


Figure 3.6.: Scanning rotation of the  $\mu$ ROSI telescope in the orbit plane. The dashed lines indicate possible Earth horizon observations.



# 4. Instrumentation

## 4.1. X-Ray Focussing Mirrors

In the middle of the 20th century, X-ray detectors had been in use for several decades in particle physics research. But, X-rays still could not be focussed imposing severe limits on X-ray telescope sensitivity. The main problem is that classical optical components used in the VIS and IR bandwidths, such as lenses, filters and mirrors, do not work in X-rays. Since optical material properties are functions of the wavelength, optical designs for X-ray telescopes are very different from visual telescopes. Section 4.1.1 gives a brief introduction to optical properties of X-rays.

In 1952, Wolter published his solution for focussing X-ray radiation (Wolter, 1952). Although his publication was specifically aimed at X-ray microscopy, the optical geometry he had proposed could also be used for X-ray astronomy. The Wolter geometries are described in detail in section 4.1.2.

### 4.1.1. How To Focus X-Rays

For optical or infrared bandwidths, numerous configurations of focussing optics exist. For X-rays, however, the situation is more complicated. Most materials are transparent to X-rays and refraction can be hardly observed. But there is a way to focus X-rays using total external reflection at small incidence angles.

The complex refraction index  $n$  helps to understand this phenomenon.

$$n = 1 - \delta - i\beta \quad (4.1)$$

$n$	[1]	Complex refraction index
$\delta$	[1]	Phase change coefficient
$\beta$	[1]	Absorption coefficient

The optical “constants”  $\beta$  and  $\delta$  are in fact functions of the wavelength. For materials with high atomic number  $Z$ , values for  $\beta$  and  $\delta$  are typically positive and in the order of  $10^{-6} \dots 10^{-3}$ . This means that the real part of  $n$  is slightly smaller than unity and refraction does not occur.

$$1 - \delta := 1 \text{ in vacuum}$$

$$1 - \delta < 1 \text{ for matter}$$

In fig. 4.1, the optical properties of gold are shown for energies from 0.1 keV to 30 keV for different incidence angles.

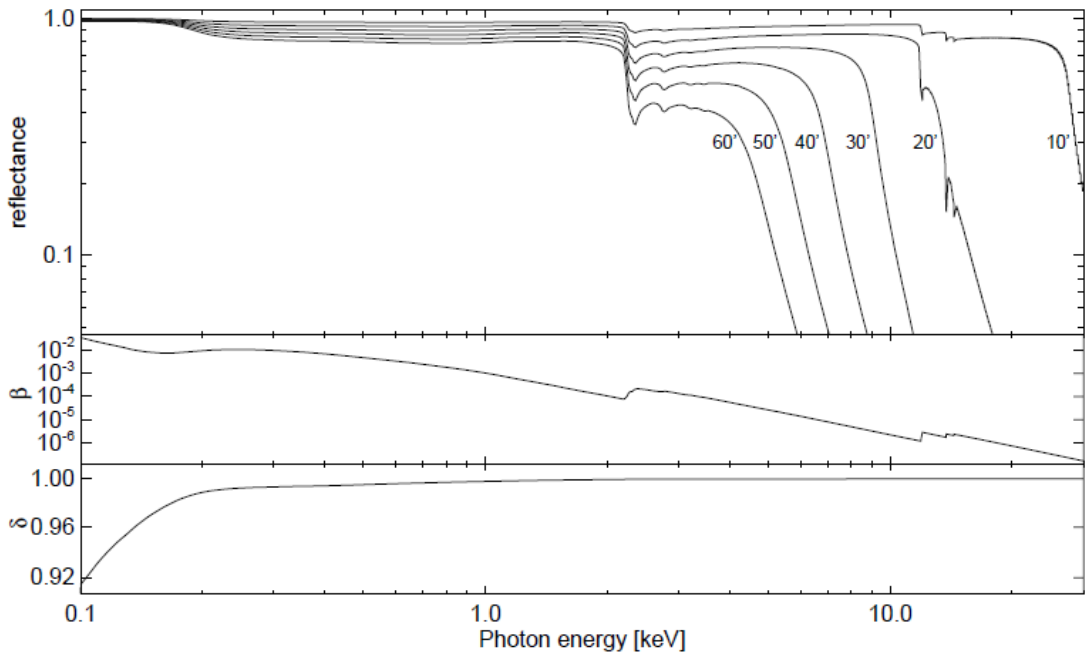


Figure 4.1.: Optical properties of gold for different grazing incidence angles between 0.1 keV and 30 keV (Trümper and Hasinger, 2008).

An effective and efficient way to focus X-ray radiation is to make use of total reflection under small incidence angles. Consider a plain boundary between two materials with different refractive indices with  $1 - \delta_1 > 1 - \delta_2$  as shown in fig. 4.2. When radiation hits the boundary, it is refracted. Under a certain small angle  $\alpha_t$ , however, radiation is refracted in such a way that it travels along the boundary. For smaller, grazing incidence angles  $\alpha < \alpha_t$ , total reflection occurs. The critical grazing incidence angle  $\alpha_t$  can be calculated using eq. (4.2).

$$1 - \delta = \cos \alpha_t \quad (4.2)$$

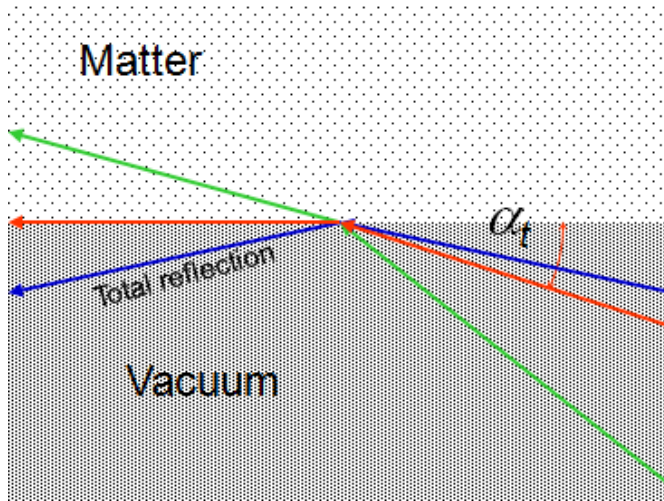


Figure 4.2.: The critical grazing incidence angle  $\alpha_t$ .

### 4.1.2. The Wolter Geometry

The publication of Wolter in 1952 presented for the first time a practical solution to focus X-ray radiation. Wolter could show that it is possible to focus X-rays compliantly with Abbe's sine condition using a mirror system with an even number of mirrors. He also suggested three possible configurations with two mirrors each (Wolter, 1952) of which the Wolter-1 configuration is most commonly used for X-ray astronomy.

The major advantage of the Wolter-1 configuration is that mirror shells can be nested coaxially to increase the effective area of the mirror system. If effective area is less critical, e.g. for solar X-ray telescopes, the more compact Wolter-2 configuration may be advantageous. Classical Wolter-1 and Wolter-2 configurations consist of a parabolic and a confocal hyperbolic mirror shell. Wolter-3 configurations consist of a paraboloid and an ellipsoid, but did not find any application in astronomy so far.

The most important properties can be summarized as follows: Wolter-1 optics consist of a parabolic primary mirror and a hyperbolic secondary mirror. Incoming radiation is reflected at small grazing incidence angles  $\alpha \leq \alpha_t$ . The aperture of a Wolter optic is a ring surface, i.e. the projected surface of the primary mirror normal to the optical axis. In the following, the Wolter-1 configuration will be investigated in more detail.

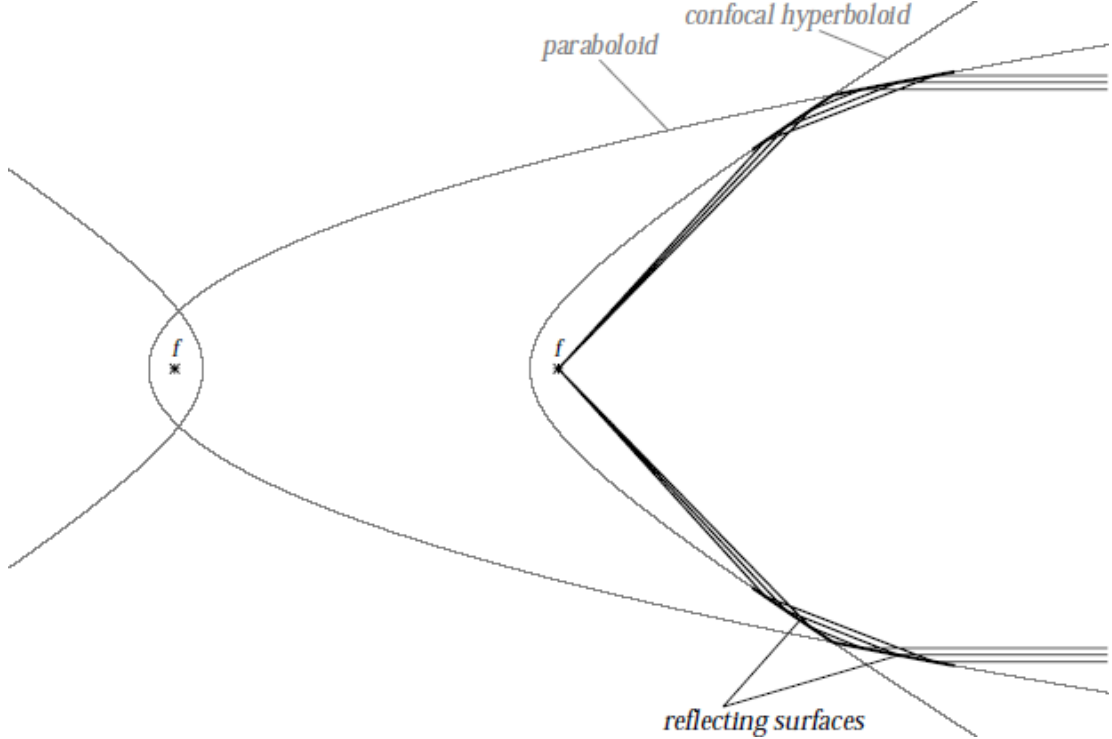


Figure 4.3.: Schematic of Wolter-1 optics (Trümper and Hasinger, 2008).

#### 4.1.3. Mathematics of Wolter-1 Mirrors

Figure 4.4 shows a cylindrical coordinate system  $(r, z)$  with the origin in the focus and the  $z$ -direction along the optical axis. The intersecting circle between the primary and secondary mirror is described by the coordinates  $(r_0, z_0)$ . The angles  $\alpha$  and  $\beta$  are the slope of the primary and secondary mirror respectively in  $(r_0, z_0)$ . The incidence angle  $\alpha$  for each mirror shell should not exceed the critical grazing incidence angle  $\alpha_t$  (see eq. (4.2)).

With the focal length  $f = z_0$  and the mirror radius  $r_0$ , the  $F$ -number is defined as follows:

$$F = \frac{f}{D_0} = \frac{z_0}{2 r_0} \quad (4.3)$$

The aperture area  $A$  of the mirror is given by eq. (4.4).

$$A = \pi (r_a^2 - r_0^2) \quad (4.4)$$

The largest deflection takes place at the smallest radius of the primary mirror at  $(z_0, r_0)$ . Thus, the incidence angle  $\alpha$  is defined here. The best reflecting efficiency

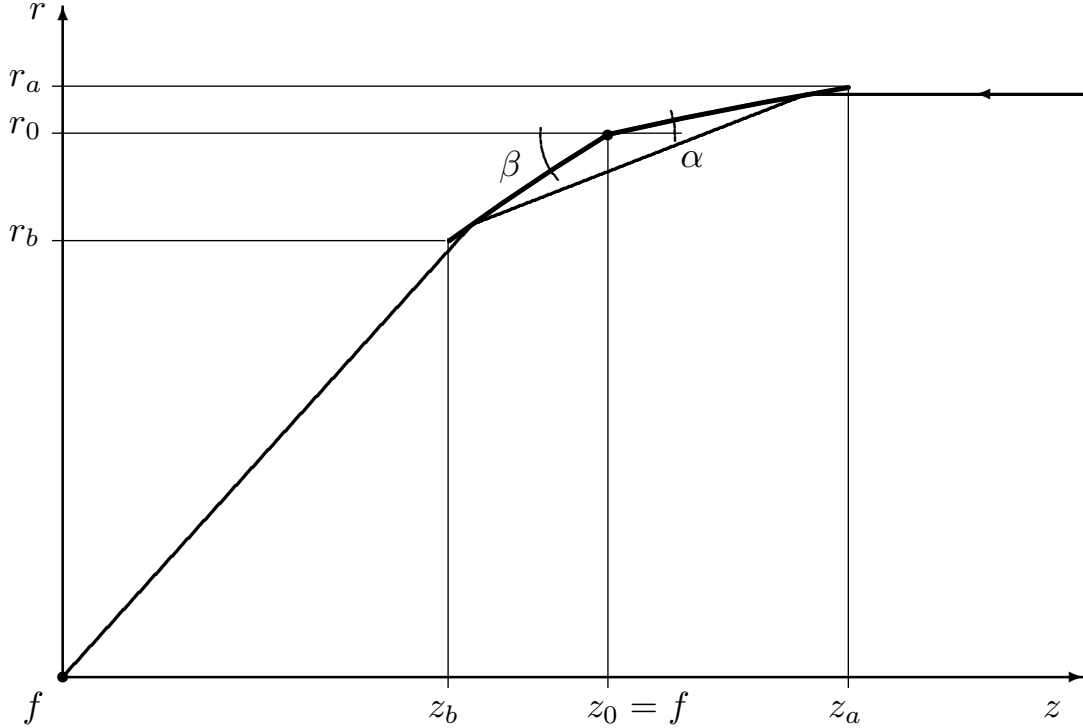


Figure 4.4.: Wolter-1 geometry variables definition

is achieved, when the ratio of grazing angles  $\zeta$  equals 1; in other words: when the reflecting angle of the primary and the secondary mirror are equal.

$$\zeta = \frac{\alpha}{\beta - 2\alpha} \quad (4.5)$$

$$\zeta = 1 \quad (4.6)$$

$$\Rightarrow \beta = 3\alpha \quad (4.7)$$

With this constraint the total deflection of the incoming radiation is  $4\alpha$ . Thus,  $\alpha$ ,  $r_0$  and  $z_0$  are related by eq. (4.8).

$$\tan(4\alpha) = \frac{r_0}{z_0} \quad (4.8)$$

With  $\alpha$ ,  $\beta$  known, the shape of the Wolter-1 mirrors are well defined for given  $(r_0, z_0)$ . The only free parameter is the length of the mirror shell given by eq. (4.9).

$$l = z_a - z_0 = z_0 - z_b \quad (4.9)$$

#### 4. Instrumentation

---

The length of the mirror shell  $l$  has no effect on the shape function. It is merely a cut-off value where the shape function ends.

Although the mirror shape is fixed, the assumptions made above are only valid for incident radiation that is parallel to the optical axis, i.e. for on-axis point sources.

There are numerous ways to define a suitable surface function depending on the selected science case (i.e. bandwidth, energy resolution, image resolution, on-axis versus off-axis properties etc.) as an optimum solution for the whole FOV. One possible general parametrization is given in eq. (4.10) (Burrows et al., 1992) for the primary mirror and eq. (4.11) for the secondary mirror.

$$r_a^2 = r_0^2 \cdot \sum_{i=0}^N a_i \cdot \left( \frac{z - z_0}{r_0} \right)^i \quad (4.10)$$

$$r_b^2 = r_0^2 \cdot \sum_{i=0}^N b_i \cdot \left( \frac{z - z_0}{r_0} \right)^i \quad (4.11)$$

The parameters  $a_i, b_i$  for usage in eqs. (4.10) and (4.11) for the classical Wolter-1 paraboloid-hyperboloid mirror shapes are:

$$\begin{aligned} N &= 2 \\ a_0 &= 1 \\ b_0 &= 1 \\ a_1 &= -2 \tan \alpha \\ b_1 &= -2 \tan \beta \\ a_2 &= 0 \\ b_2 &= 2 r_0 \frac{\tan \beta}{z_0 + \frac{r_0}{\tan 2\alpha}} \end{aligned}$$

The classical paraboloid-hyperboloid Wolter-1 mirrors have perfect on-axis properties, but worsening off-axis imaging properties. van Speybroeck and Chase give an empirical formula to estimate the off-axis RMS blur circle  $\sigma$  as a function of the off-axis angle  $\theta$  (van Speybroeck and Chase, 1972).

$$\sigma = \frac{\zeta + 1}{10} \frac{l}{f} \frac{2 \tan^2 \theta}{\tan \alpha} + 4 \tan \theta \tan^2 \alpha \quad (4.12)$$

Depending on the  $F$ -number and the FOV, off-axis errors are dominated either by spherical aberration or coma. Burrows et al. suggest a numerical approach to optimize higher order parameters  $a_i, b_i$  for  $N > 2$  to minimize the RMS spot size over the whole FOV (Burrows et al., 1992).

An effective, yet simple, way to improve the blur over the whole FOV is to move the detector slightly towards the mirror. This increases the on-axis blur, but reduces blurring over the total FOV. This solution has found practical use in various Wolter-1 optics, for example in the XMM telescope.

#### 4.1.4. Mirror Performance

All mirror performance parameters are functions of the energy. For example, the energy dependence of the reflectivity is shown in fig. 4.1. It is therefore useful to evaluate mirror performance parameters for discrete energies. Refer to table A.2 for a list of spectral lines.

The point spread function (PSF) characterizes the ability of the mirror to focus a point source in the detector plane. Incident radiation from a point source is scattered due to errors of the mirror surface from macroscopic figure errors to small scale errors in the micro roughness. The PSF is therefore a critical parameter for the spatial resolution. It is usually given for the half energy width (HEW) and/or the full width half maximum (FWHM) in units arc seconds.

Figure 4.5 shows the on-axis PSF for the three different instruments of the XMM-Newton X-ray telescope.

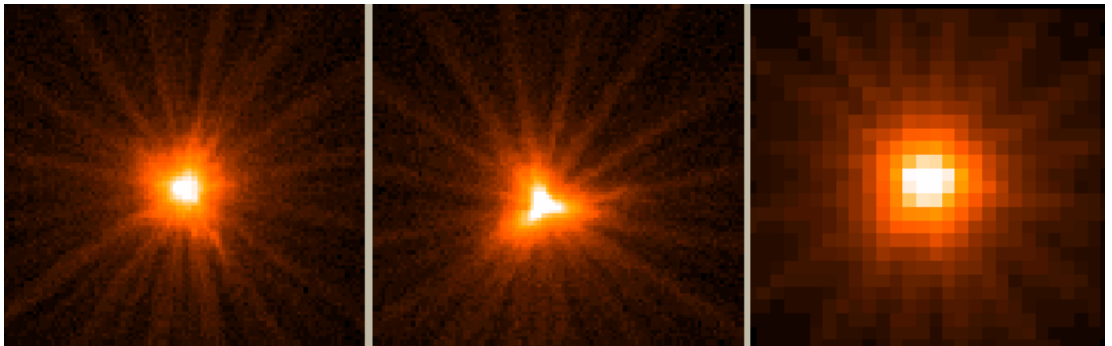


Figure 4.5.: On-axis point spread functions of the three XMM-Newton telescopes: MOS-1 (left), MOS-2 (middle) and pn (right) (source: ESA, 2012b).

The off-axis PSF differs from the on-axis PSF. With increasing off-axis angle  $\theta$  the point source appears to be smeared. Figure 4.6 shows the off-axis PSF of the XMM-Newton telescope depending on the position in the imaging field. The

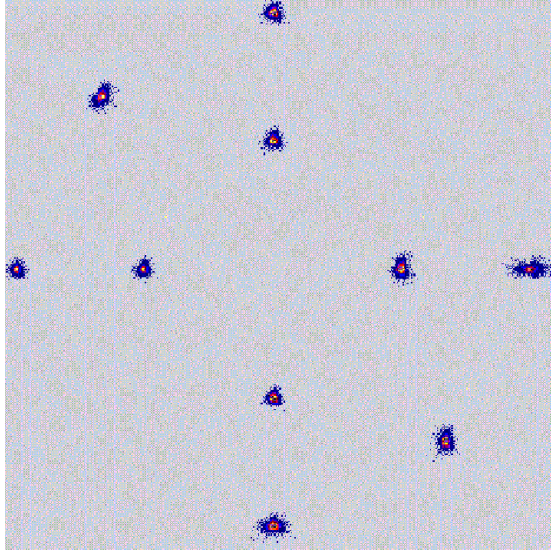


Figure 4.6.: Off-axis point spread functions of XMM-Newton (source: ESA, 2012b).

image is the result of calibration measurements conducted in the MPE's PANTER facility (refer to Burwitz et al., 2013, for more information about PANTER).

#### 4.1.5. Double Cone Approximation

A major simplification of the mirror geometry is the double cone approximation (see fig. 4.7). While Wolter-1 mirrors, in theory, have perfect on-axis imaging properties, the focus of an on-axis point source is always a disk. The imaging quality of double cone mirrors is therefore relatively poor compared to a Wolter geometry, but they are still capable of focusing X-ray radiation onto a spot.

The slope of the mirror surfaces in the  $r_0, z_0$  coordinate system is constant with the slope of the primary mirror given by eq. (4.8).

With  $\zeta = 1$  the slope of the secondary mirror is:

$$\beta = 3 \alpha \quad (4.13)$$

The surface function of a double cone can be expressed with the following parameters using eqs. (4.10) and (4.11):

$$\begin{aligned} n &= 2 \\ a_0 &= 1 \\ b_0 &= 1 \\ a_1 &= -2 \tan \alpha \\ b_1 &= -2 \tan \beta \\ a_2 &= \tan^2 \alpha \\ b_2 &= \tan^2 \beta \end{aligned}$$

This is a rather complex expression. It may be beneficial when comparing different shape curves, but a much more convenient way to describe the double cone surface function is simply by two linear functions eq. (4.14).

$$r(z) = \begin{cases} r_0 + \tan 3\alpha \cdot (z - z_0) & ; z \in [z_0 - l; z_0] \\ r_0 + \tan \alpha \cdot (z - z_0) & ; z \in [z_0; z_0 + l] \end{cases} \quad (4.14)$$

The actual focal length  $f'$  of a double cone mirror differs from the nominal focal length (see fig. 4.7) by the focal length offset  $\Delta f$ .

$$f' = \frac{\Delta f}{2} + f \quad (4.15)$$

$$\Delta f = \frac{r_b}{\tan 4\alpha} - f + l \quad (4.16)$$

The focus  $f'$  coincides with the smallest spot diameter  $d_{spot}$ .

$$d_{spot} = \Delta f \cdot \tan 4\alpha \quad (4.17)$$

The resolution  $u$  of the double cone can be calculated with the spot diameter and the actual focal length. The resolution  $u$  is usually given in units arcminutes or arcseconds.

$$u = \tan^{-1} \left( \frac{d_{spot}}{f'} \right) \quad (4.18)$$

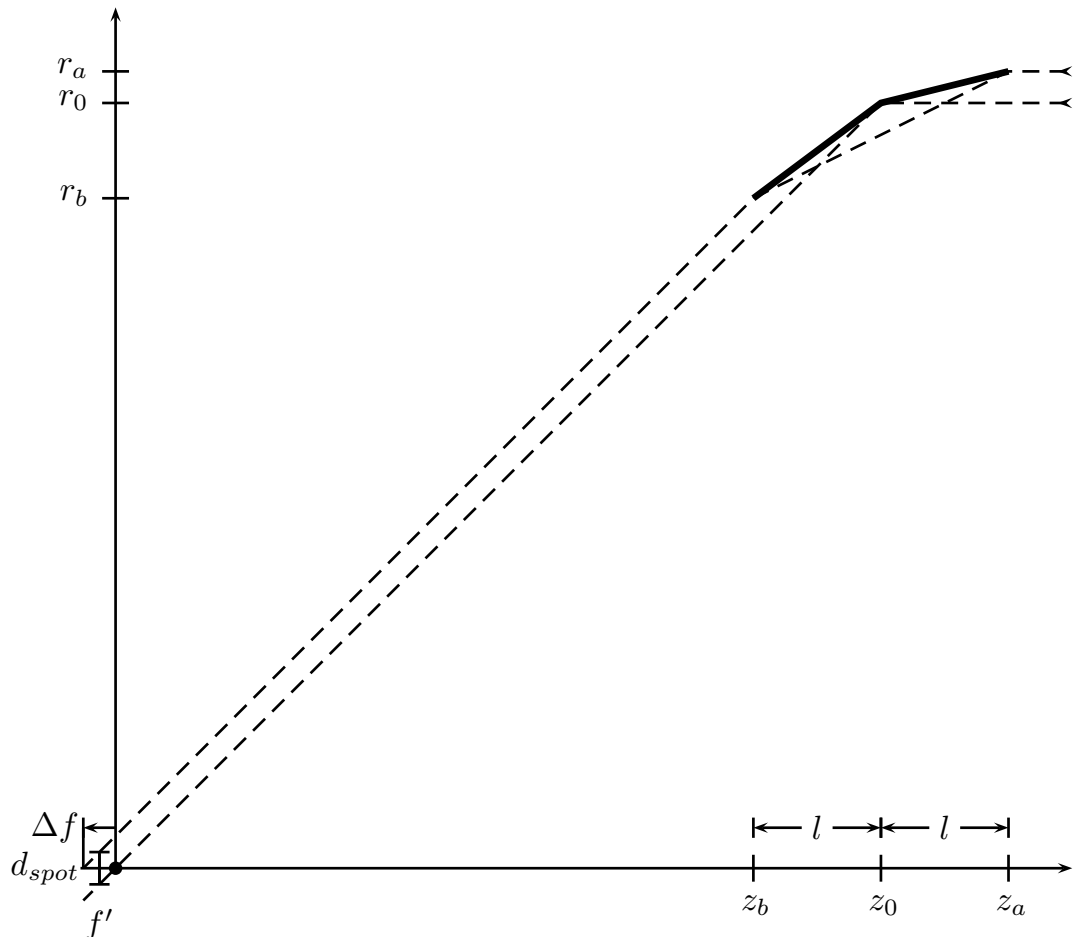


Figure 4.7.: Double cone approximation. Due to the constant slope angle of a double cone, reflected X-rays are parallel. The focal length of the double-cone is therefore longer by  $\Delta f/2$  and the focus is a disc with diameter  $d_{spot}$ .

#### 4.1.6. Nesting Mirror Shells

To increase the total area, several Wolter-1 mirror shells can be nested, so that a Wolter-1 mirror system comprises several mirror shells. The total aperture area of the mirror system is then the sum of the aperture areas of each mirror shell. Nesting thin walled mirror shells allows for a good filling factor while keeping the mirror system as compact as possible (see fig. 4.8 for examples of nested mirror shells).

Another advantage of nesting mirror shells is that the inner shells serve as aperture stops limiting the FOV and preventing single reflections (stray light reflected by the secondary mirror only).

#### 4.1.7. Established Mirror Manufacturing Technologies

As any other optical device, X-ray mirrors require high precision. The imaging quality is determined by macroscopic errors (misalignment, roundness, and slope errors) and micro-roughness. Since the wavelength of X-rays is shorter than visual by two to three orders of magnitude, the micro-roughness needs to be equally more precise. Improving the smoothness of mirror surfaces has long been the main driver for mirror manufacturing technologies. Today, micro-roughnesses of  $< 1 \text{ nm}$  can be achieved with established polishing techniques.

##### Polished Glass Mirrors

Glass has long been the preferred material for optical surfaces. Thick glass is ground, polished and coated to extremely smooth surfaces. The mirror of the Chandra X-ray telescope made from Zerodur glass achieves the best angular resolution ( $< 1 \text{ arcsec}$ ). After polishing, the reflective coating is applied on the mirror surface.

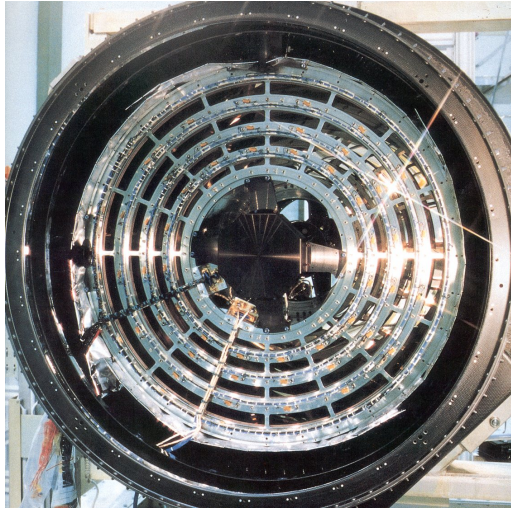
##### Electro-Galvanic Forming

Electro-galvanic formed (e-formed) mirrors are manufactured on a polished mandrel which is a negative form of the optical surface. The surface roughness of the mandrel directly influences the surface properties of the formed mirror shell. The mandrels are usually made from solid aluminium with a nickel surface.

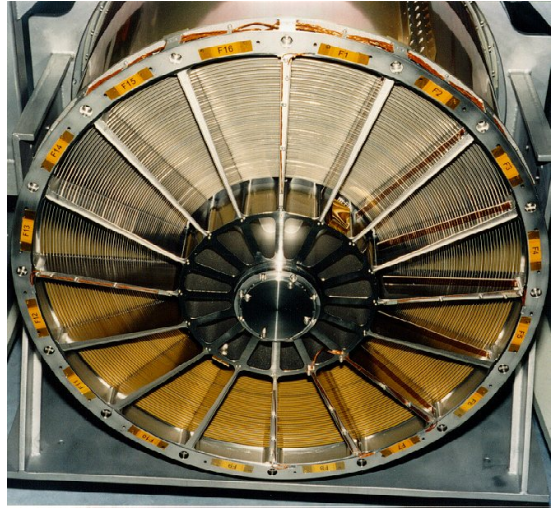
First, the optical surface coating material (typically gold) is vapor deposited on the mandrel. Then the mirror shell material (nickel) is deposited onto the gold in an electro-galvanic bath. By adjusting the currents in the galvanic bath and the time spent, the thickness of the mirror shells can be controlled. The finished

#### 4. Instrumentation

---



(a) The ROSAT mirror module consists of four nested Wolter-1 mirrors made from polished Zerodur glass with gold plating (image : MPE).



(b) One of the three XMM mirror modules comprising 58 nested mirror shells made from e-formed nickel (image : MPE).

Figure 4.8.: Examples of different X-ray mirror systems.

mirror shell is finally released from the mandrel and can then be integrated into a mirror support structure.

One major advantage of this process is that the mandrel can be used several times to replicate identical mirror shells. This way, telescopes may increase the total effective area by using several identical mirror modules.

## 4.2. X-Ray Detectors

Gaseous detectors were the first electronic instruments available for detecting X-rays. Large achievement in this area were made in the early and mid 20th century, primarily in the field of nuclear physics research. Proportional counters are gaseous detectors with a signal output that is proportional to the photon energy of the incidence radiation. They were originally developed for particle physics research and later specifically designed for space applications with great success. Imaging gas proportional counters used for instance on the X-ray satellites *Einstein* and ROSAT had a moderate energy resolution, good position resolution and still unexcelled time resolution and background rejection efficiency. With the upcoming of silicon based detectors, the use of gaseous detectors for high energy astronomy has practically come to an end. Large CCDs are now used on

all X-ray satellites delivering vast amounts of data with high spatial and spectral resolution.

Silicon has been used as detector material since the 1950s. One advantage of silicon is that an energy of only 3.7 eV is needed to create an electron-hole pair making it an ideal base material for detecting photons and particles over a wide bandwidth with high sensitivity. Today, fully depleted p-n junction silicon is the current state-of-the-art in X-ray detector technology. The working principle of fully depleted silicon detectors for X-ray detection was first published by Gatti and Rehak (Gatti and Rehak, 1983). Although the article concentrated on drift detectors (see section 4.2.3), the same basic principle applies for all silicon semiconductor detectors, such as CCDs.

Semiconductor detectors have some intrinsic advantages compared to gaseous detectors. Higher density of detector material ( $\rho_{Silicon}/\rho_{Gas} \approx 10^3$ ) yields higher quantum efficiency and lower required energy for generating an electron hole pair yields better energy resolution. However, gaseous detectors have an excellent background noise rejection capability with the application of anti-coincidence measures.

### 4.2.1. pnCCDs

The first space mission with a CCD for X-ray astronomy was the Japanese ASCA satellite launched in 1993. Chandra and XMM-Newton following in 1999 were also equipped with several CCD detectors as focal plane instruments. Other missions with CCDs are, for example, SWIFT and SUZAKU. CCDs for X-ray detection are used in many different areas, such as particle physics, quantum optics or material analysis. The typical bandwidth covered by CCD detectors is 0.1...15 keV, although pnCCDs are sensitive up to 30 keV with still  $\sim 20\%$  quantum efficiency.

Like CCDs for optical bandwidths, different architectures are possible: full frame, frame transfer or backside-illuminated with the same intrinsic advantages and disadvantages for each mode.

Full frame CCDs are highly sensitive devices with a simplistic, compact architecture. However, read-out and integration can only be conducted sequentially. With read-out times of  $\sim 2.6$  seconds (full-frame mode of XMM Epic MOS camera), full-frame CCDs are prone to pile-up if X-rays are detected during the read-out.

Frame transfer CCDs push the integrated charge to a dedicated read-out register and thus mitigate the problem of pile-up. However, the extra register makes the CCD larger, heavier (the read-out register must be shielded from irradiation), more complex and more sensitive to charge transfer losses.

Backside-illuminated CCDs receive the radiation from the side that does *not* have the pixel structure. Thus, the radiation is transported deep inside the bulk silicon, as seen from the illuminated side. Backside-illuminated CCDs are therefore less susceptible to radiation damages due to soft X-ray background radiation.

In fig. 4.9, the schematics of a backside-illuminated, fully depleted pnCCD is shown. CCDs of this type in frame-transfer configuration are used for the upcoming eROSITA X-ray telescope on board the SRG satellite.

Figure 4.9 shows the schematic cross-section through a CCD wafer along one read-out channel. The wafer consists of bulk n-silicon with both surfaces covered with a p<sup>+</sup> boron implant. The read-out anode is an n<sup>+</sup> phosphorous implant with an ohmic connection to the silicon bulk. Adjusting the voltages of the p<sup>+</sup> layers sets the depth of the potential minimum (shown on the right in fig. 4.9). Charges generated by incoming radiation are collected at the potential minimum (pixel well) close to the front side of the wafer with the pixel structure nearby. As the charges are transported in a depth of  $\sim 10 \mu m$ , pnCCDs have good radiation hardness.

### 4.2.2. Detector Noise

Detector noise has an impact on the energy resolution and is therefore a key parameter for the overall detector performance. The total noise is the squared sum of all equivalent noise charge contributions.

The Fano noise describes the effect that monochromatic radiation does not appear as a straight spectral line, but is rather visible as a narrow gaussian curve in the spectrum. It therefore imposes a hard limit to the energy resolution of the detector. Since Fano noise is proportional to the incident photon energy, it becomes dominant for energies  $> 1 \text{ keV}$  (see fig. 4.10).

Transmission noise describes the effect that each time the charge is transferred from one pixel to the next towards the read-out channel, a small fraction of that charge is lost due to inefficiencies. As charges are transported over the length of the CCD channel, charge transfer losses are dependent of the number of pixel transfers and the charge transfer efficiency (*CTE*). Pixels that are further away from the read-out anode will have higher transmission noise levels as these charges are transferred over more pixels. In effect, the transmission noise is not constant over the area of the CCD. With  $(1 - CTE) \approx 10^{-5}$ , transmission noise becomes relevant for large detectors with several hundreds of pixels per read-out channel. Furthermore, charge transfer efficiency degrades significantly over time.

Electronic noise takes into account the noise generated by the analogue front-end electronic components. It can be reduced by minimizing the read-out anode capacitance, lowering the leakage current and by optimizing the shape time con-

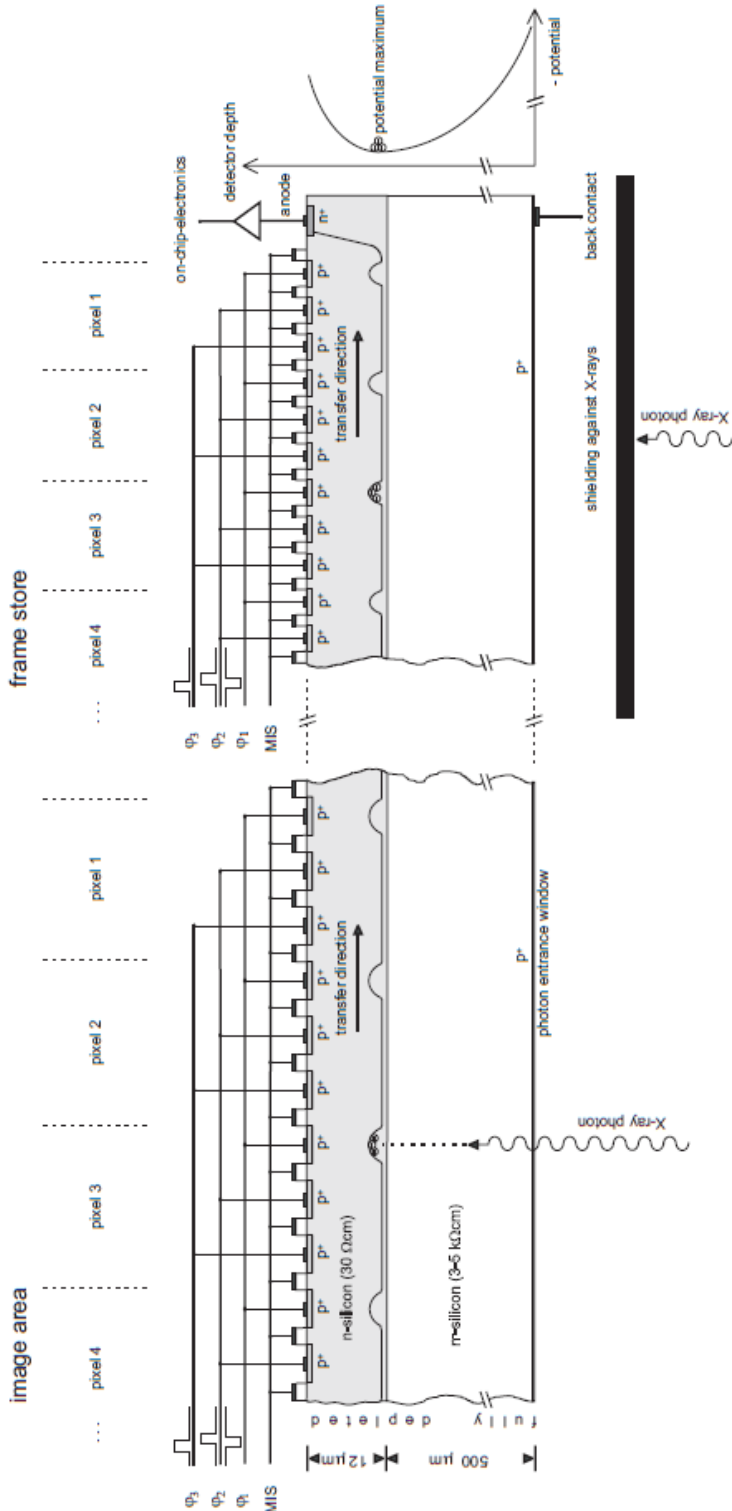


Figure 4.9.: Schematic of a frame-store pnCCD (Trümper and Hasinger, 2008; Meidinger et al., 2003).

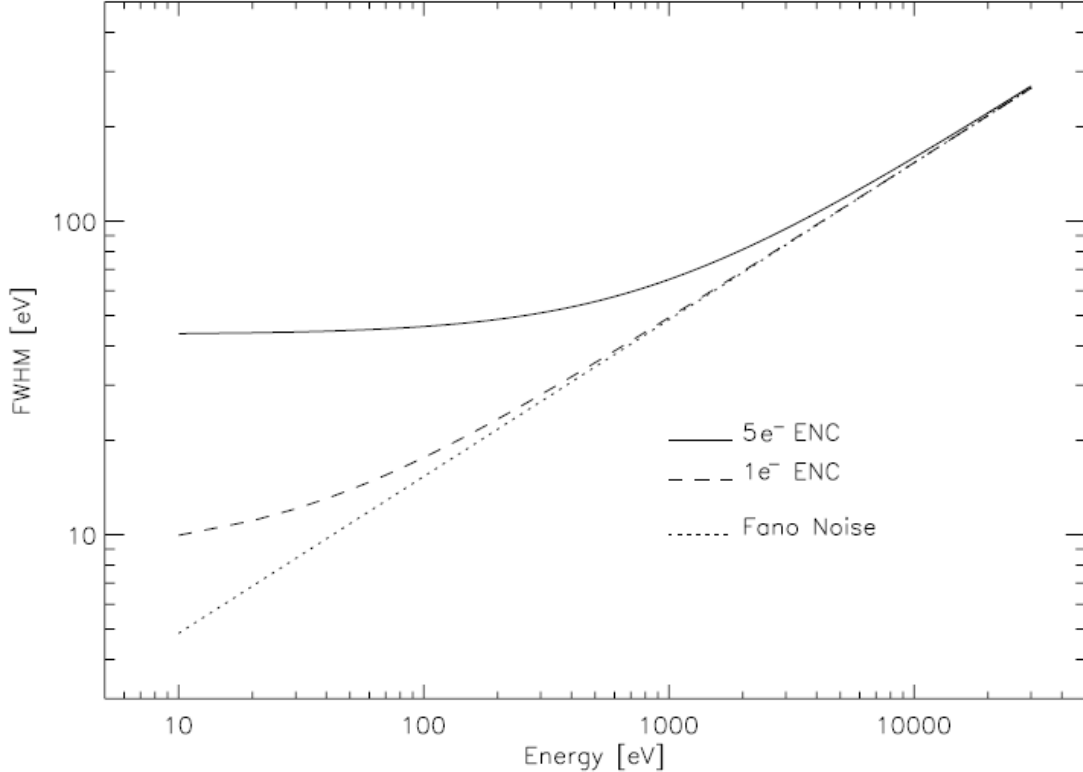


Figure 4.10.: Energy resolution as a function of the photon energy for low ( $1e^-$ ) and high ( $5e^-$ ) electronic noise. The fano noise contribution is dominant for high energies, the electronic noise for lower energies (Trümper and Hasinger, 2008).

stant and filter function. Another important contribution to the electronic noise comes from the detector temperature. State-of-the-art pnCCDs have electronic noise of  $\sim 2 e^-$  at readout speeds of  $< 1 \mu s$  and operating temperatures of  $-60^\circ C$ .

### 4.2.3. Silicon Drift Detectors

The concept of modern fully depleted silicon drift detectors (SDDs) was first introduced by Gatti and Rehak in 1983 (Gatti and Rehak, 1983). This publication anticipated the lateral charge transfer through semiconductors parallel to the sensitive area. This concept is used in SDDs as well as in thick CCDs.

Figure 4.11 shows the basic configuration of a SDD with integrated FET amplifier. It consists of monolithic  $n^-$  silicon with high resistance. An electric field parallel to the detector surface transports charges generated by incoming X-ray

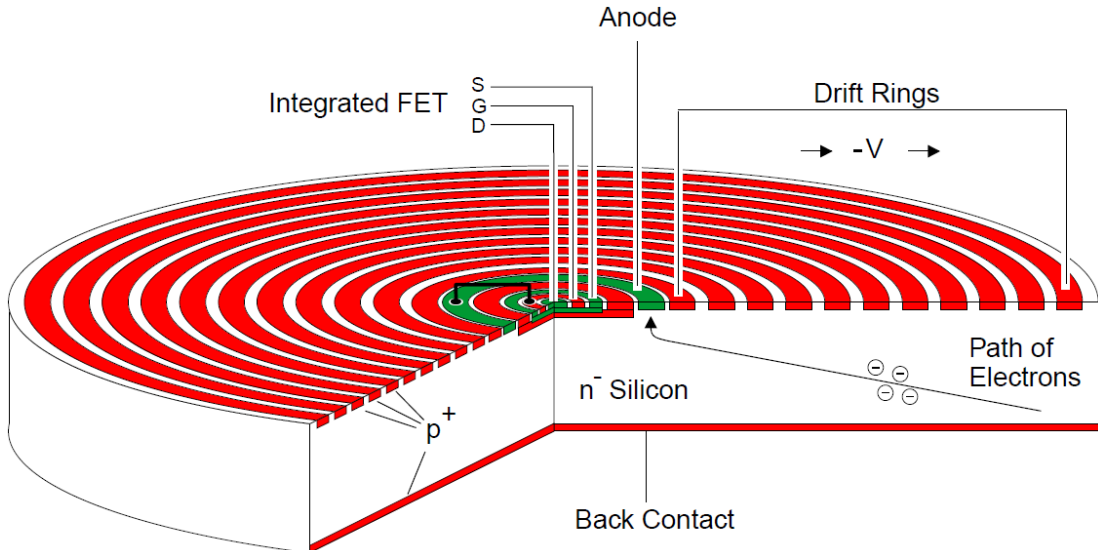


Figure 4.11.: Silicon Drift Detector working principle (Eggert et al., 2003).

photons to the anode, which is located in the center close to the on-chip amplifier.

Due to the centered read-node concept, the capacitance is not dependent on the sensitive area size. Thus, high read-out frequencies and excellent spectral resolutions can be achieved with SDDs. Equipped with a peltier element for cooling, SDDs can be operated at or close to room temperature with good energy resolution (see fig. 4.12). However, this requires additional electrical power for cooling.

The most recent generation of SDDs are the so-called *Silicon Drift Detector Droplets* (SD<sup>3</sup>, see fig. 4.13). To reduce background noise, the position of the on-chip amplifier is shifted from the center towards the rim of the SDD. By placing a circular collimator in front, the amplifier is protected from direct irradiation. The peak to background ratio is thus increased significantly. Due to its shape, the capacitance of the amplifier can be optimized, additionally reducing the noise (Lechner et al., 2004).

#### 4. Instrumentation

---

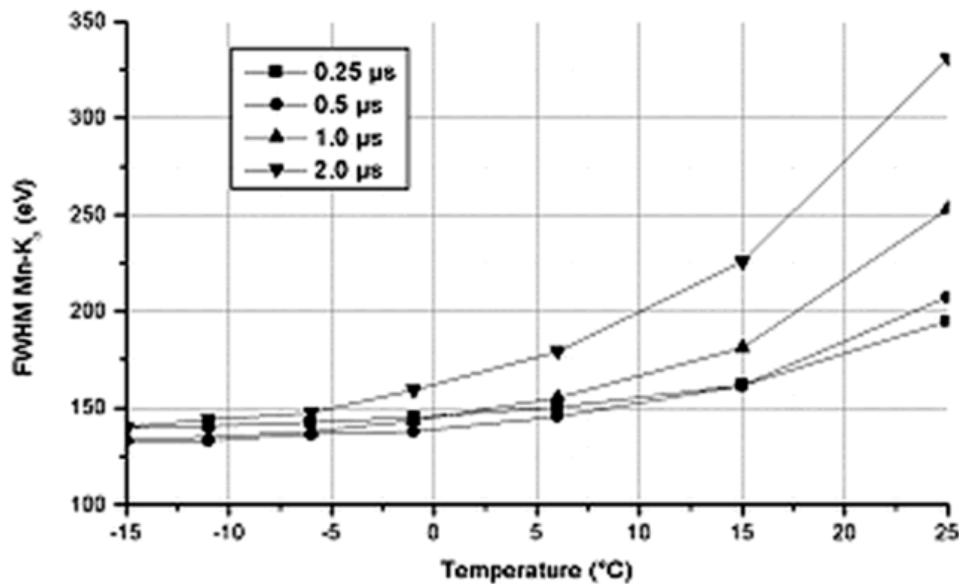


Figure 4.12.: SDD energy resolution versus temperature and shaping time (source: PNSensor GmbH, <http://www.pnsensor.de>)

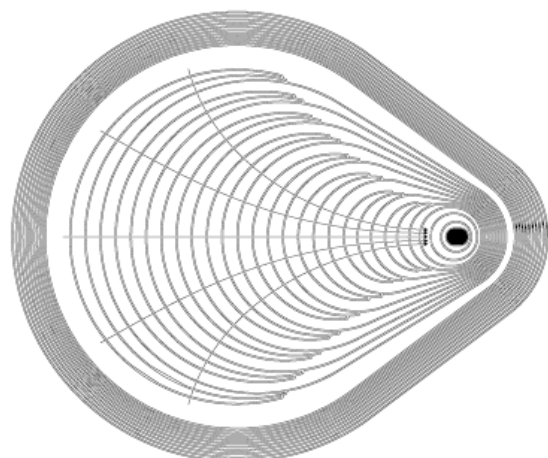


Figure 4.13.: Silicon Drift Detector Droplet (SD<sup>3</sup>) (Lechner et al., 2004). The black region is the readout anode with on-chip amplifier.

## 4.3. Instrumentation for Small Satellites

Since the launch of HEAO-2 (*Einstein*), the use of Wolter-1 grazing incidence focusing mirrors is common practice. Over the past 40 years this has led to a constant increase in effective area of X-ray telescopes. One major design driver for X-ray instruments is the mirror substrate material. The material directly influences the thickness and the optical precision of the mirror shell. While polished glass mirrors achieve the best precision (e.g. Chandra), their relatively high thickness limits the effective area. Additionally, the mass of a thick glass mirror is significantly higher than that of thinner e-formed nickel shells. Current research in mirror manufacturing technology for X-ray telescopes concentrates on silicon pore optics (Collon et al., 2010; Willingale et al., 2013) and slumped glass foils (Friedrich et al., 2006; Ghigo et al., 2012). The major difference to “conventional” technologies is that X-ray mirrors from silicon pore optics or slumped glass are always segmented. This means that several mirror sectors are assembled to form an axially symmetric mirror. However, both technologies require more research until being ready for usage in a space mission (estimated TRL  $\leq 4$ )<sup>1</sup>.

Since the introduction of CCD detectors into X-ray astronomy instrumentation, the development of gaseous detectors has de facto come to an end. They have been replaced by CCD detectors that deliver high spatial and spectral resolution. SDDs are based on the same working principle as CCDs enabling them to deliver spectral resolution comparable to current state-of-the-art CCDs. SDDs have been used on Mars and Lunar rovers for mineral analysis. Both detector types can be therefore considered space-proven (estimated TRL  $\geq 8$ )<sup>2</sup>.

Due to their high spatial resolution, CCDs are the first choice if the focusing optics is capable of delivering enough photons with sufficiently small point spread. Presuming that small satellite X-ray telescopes have limited effective area, they are hardly able to work well with high resolution CCDs. Thus, SDDs are well suited for small X-ray telescopes as they do not require high throughput focusing optics and are less complex electronically.

The selection of the optical components for the  $\mu$ ROSI telescope has been limited to established technologies with high TRLs in order to save development time and costs. The  $\mu$ ROSI mirror is therefore made from e-formed nickel using the same technology that is currently used for the eROSITA mirror shells. The infrastructure required for the manufacturing and measurement of the shells is available and has demonstrated its effectiveness. More importantly, the company

---

<sup>1</sup>Component and/or breadboard validation in laboratory environment, compare table A.3

<sup>2</sup>Actual system completed and “Flight qualified” through test and demonstration (ground or space), compare table A.3

#### *4. Instrumentation*

---

Media Lario Technologies (MLT), who is responsible for the eROSITA mirror manufacturing, agreed to provide the mirror shells for  $\mu$ ROSI free of charge.

Presuming that the telescope will not have a high aperture area, a commercially available SDD is selected for the  $\mu$ ROSI telescope. With just one pixel, the read-out electronics is much more simplistic and requires less power than a CCD solution. Relinquishing spatial resolution also allows to use the double cone approximation instead of a real Wolter-1 shape.

# 5. **$\mu$ ROSI Miniature X-Ray Telescope**

## 5.1. Introduction

The miniature X-ray telescope  $\mu$ ROSI on board the Max-Valier Satellite opens up a window to the high energy universe for amateur astronomers. It is the first X-ray telescope specifically designed for a nanosatellite in the  $10\ kg$  class. This circumstance makes it a novelty and at the same time imposes some serious constraints in terms of mass, power consumption and budget.

The primary mission objective of the Max-Valier Satellite already has been mentioned in section 1.1 (p. 1):

The MVS mission objective is to perform an all-sky survey in the soft X-ray bandwidth searching the whole sky for bright X-ray sources with an angular resolution of  $1^\circ$ .

This definition is the starting point for designing the  $\mu$ ROSI telescope. For the  $\mu$ ROSI telescope design process, the following approach has been used. Before detailing the scientific objectives, the size of the telescope is determined using a similarity approach (see section 5.2). From the similarity we can also deduce a preliminary simulation of the sources that are observable during the all-sky survey (see section 5.3). In the following, the scientific objectives are defined in more detail (section 5.4). Then, the subsystems of the  $\mu$ ROSI telescope are defined (section 5.5) and the requirements for all subsystems are established (section 5.6). The chapter concludes with the final design description (section 5.7) and the presentation of the model philosophy used for developing the telescope (section 5.8).

## 5.2. Telescope Sizing

The telescope size is mainly driven by the focal length  $f$  and the  $F$ -number, which is the relation between  $f$  and the aperture diameter  $D_0$  (see eq. (4.3) on p. 36). The focal length defines the distance between the Wolter mirrors and the detector and is therefore a reference for the overall telescope dimensions, while the  $F$ -number is a key parameter for the telescope design.

Most X-ray telescopes have  $F$ -numbers around 10 and a FOV around  $30'$  (see table 2.2). In order to achieve a higher FOV, the  $F$ -number needs to be lower. For example, the SRG satellite with the eROSITA telescope has an  $F$ -number of 4.4 and a FOV of  $60'$ . But the  $F$ -number not only influences the FOV. It also has an impact on the energy range of the telescope. This is due to the difference in the reflecting angle. Using eqs. (4.3) and (4.8) (see p. 36), the relation between the  $F$ -number and the reflecting angle  $\alpha$  is given.

$$2F = \frac{1}{\tan(4\alpha)} \quad (5.1)$$

Equation (5.1) shows that larger  $F$ -numbers yield lower reflecting angles  $\alpha$ . The reflecting angle always needs to be smaller than the critical grazing incidence angle  $\alpha_t$  (see section 4.1.1). Lower energies allow for higher reflecting angles (lower  $F$ -number), while higher energies require lower angles (higher  $F$ -number).

In summary, the  $F$ -number needs to be selected carefully to match the specific science case. An all-sky survey requires a larger FOV and therefore a lower  $F$ -number than a pointed observation with high spatial resolution. Concentrating on the low energy range of the soft X-ray bandwidth allows for very low  $F$ -numbers. For instance, ROSAT had an  $F$ -number of 3 for its all-sky survey in the energy range  $0.1 - 2.4 \text{ keV}$  (see table 2.1), while SRG with  $F = 4.44$  targets for  $0.1 - 10 \text{ keV}$  for its survey. However, choosing the  $F$ -number as low as possible has some very practical advantages. Higher angles yield higher aperture areas per shell length and also increase the pitch between nested mirror shells.

A simple way to determine the telescope size is to use the  $F$ -number of a previous space mission with similar scientific objectives in terms of FOV and energy range. The telescope size, i.e. the focal length  $f$  and the aperture diameter  $D_0$ , then can be derived by applying a scale factor  $SF$ .  $f$  and  $D_0$  scale linearly with  $SF$ .

$$F_1 = F_2 \quad (5.2)$$

$$\frac{f_1}{f_2} = \frac{D_1}{D_2} = SF \quad (5.3)$$

The scale factor is also useful to roughly estimate some more telescope parameters. Assuming that the aperture area scales with the diameter, the effective area scales with  $SF^2$ . Furthermore, assuming a similar telescope mass per volume, the telescope mass can be estimated with  $SF^3$ .

$$\frac{A_{eff_1}}{A_{eff_2}} \approx SF^2 \quad (5.4)$$

$$\frac{M_1}{M_2} \approx SF^3 \quad (5.5)$$

Now, the X-ray telescope which serves as a template needs to be chosen and the scale factor  $SF$  needs to be set.

The ROSAT telescope was chosen for several reasons. First, the ROSAT all-sky survey (RASS) is the most comprehensive database of X-ray sources in the sky. This has the advantage that the existing data set of the RASS-BSC (Voges et al., 1999) can be used as a basis for comparative studies. Secondly, the ROSAT energy range is well suited for small telescopes. The ultra-soft X-ray bandwidth allows for small  $F$ -numbers which in turn yields larger effective areas per mirror shell making the mirror system more compact and lightweight.

	Scale	ROSAT	$\mu$ ROSI	
F-number	1	3	3	
Aperture	10	80 cm	80 mm	
Focal length	10	240 cm	240 mm	
Effective area	$10^2$	$1000 \text{ cm}^2$ $500 \text{ cm}^2$ $400 \text{ cm}^2$ $350 \text{ cm}^2$	$\sim 1000 \text{ mm}^2$ $\sim 500 \text{ mm}^2$ $\sim 400 \text{ mm}^2$ $\sim 350 \text{ mm}^2$	at 0.1 keV at 0.28 keV at 1.0 keV at 1.25 keV
Mass	$10^3$	2400 kg	$\sim 2.4 \text{ kg}$	

Table 5.1.:  $\mu$ ROSI initial design parameters derived from scaling down the ROSAT telescope by a factor of  $SF = 10$  using eqs. (5.2) to (5.5). ROSAT effective area values taken from (Briel et al., 1996).

The scale factor was set to  $SF = 10$ . With this value, the initial design parameters for the  $\mu$ ROSI telescope can be determined using eqs. (5.2) to (5.5). The results are listed in table 5.1.

The effective area of the  $\mu$ ROSI telescope can be estimated to be  $\sim 400 \text{ mm}^2$  compared to ROSAT's  $400 \text{ cm}^2$  maximum effective area at  $1.0 \text{ keV}$  (Briel et al., 1996). These values are, of course, very coarse estimates. They do not take into account any differences in mirror manufacturing technique which might yield even higher effective areas. Nevertheless, these values can be considered a minimum estimate.

The  $\mu$ ROSI mass is estimated to be  $\sim 2.4 \text{ kg}$ . For a  $10 \text{ kg}$  nanosatellite like MVS, a mass fraction of  $\sim 25\%$  for the main payload seems to be reasonable value. As with the effective area, the mass estimation is only a rough estimate. At this early stage, it is hard to predict, whether the final mass of the telescope is higher or lower than this estimate. Thus, this figure should be used with a margin of at least 25% resulting in a mass estimation of  $3.0 \text{ kg}$  including margin.

### 5.3. Preliminary Observation Simulation

With the relation between  $\mu$ ROSI and ROSAT given, it is already possible to roughly predict the capabilities of the  $\mu$ ROSI telescope. The RASS-BSC lists all bright X-ray sources with their respective count rates. With the relation between the effective areas given, and assuming equal detector quantum efficiency, the count rates can be scaled to the  $\mu$ ROSI dimensions. Figure 5.1 shows the result of this initial simulation. Even though the influence of the detector has been neglected in this first simulation, it shows that the  $\mu$ ROSI telescope is capable of detecting  $> 100$  X-ray sources. Moreover, the brightest extra-solar X-ray source in the sky, Scorpius X-1, that was too bright to be observed by ROSAT, can now be detected with  $\mu$ ROSI. This, however, is not shown in the simulation, since Sco X-1 is missing in the ROSAT data.

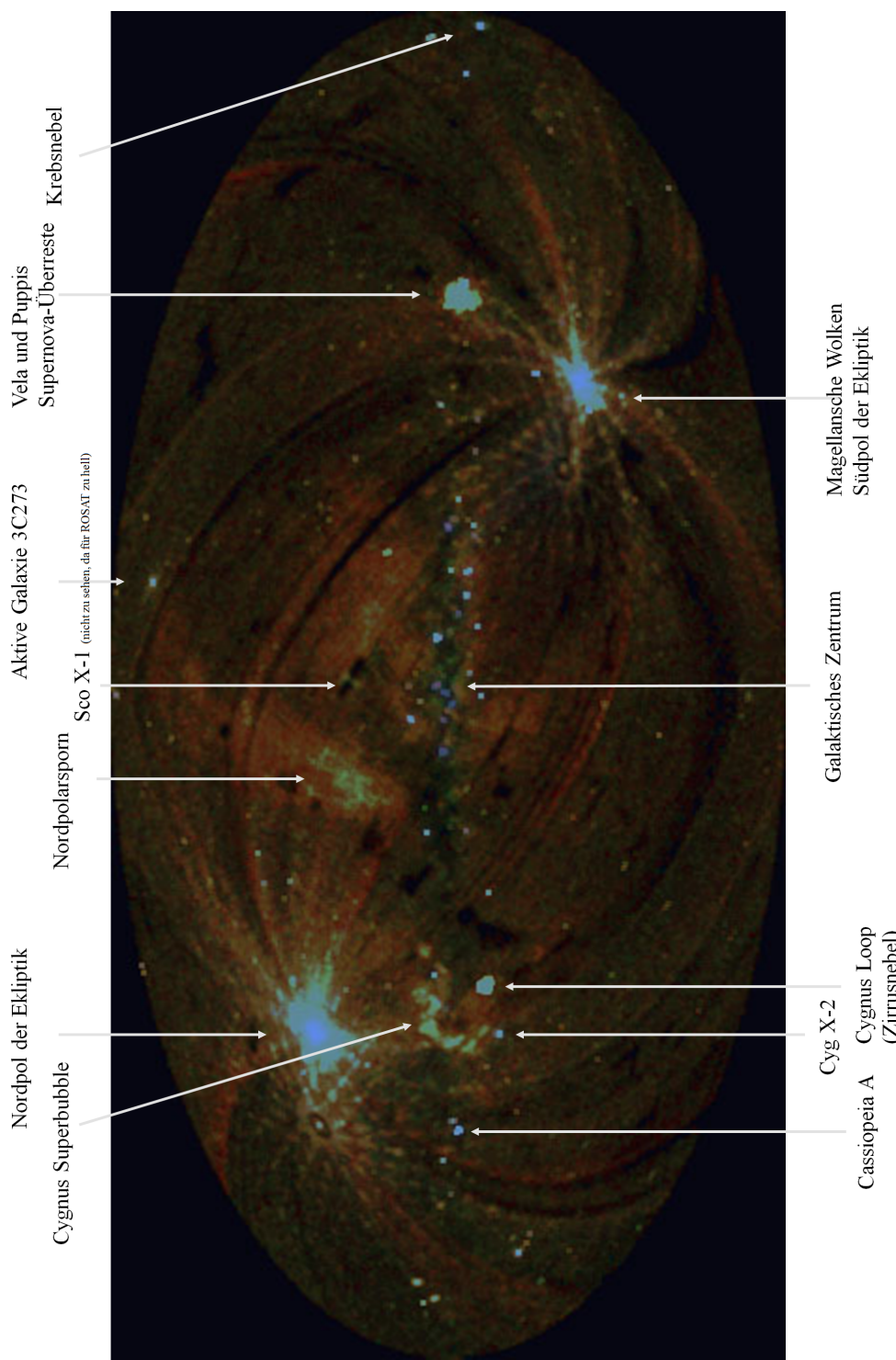


Figure 5.1.: Simulated map of  $\mu$ ROSI all-sky survey (Aitoff projection in galactic coordinates). Blue color indicates hard X-rays, red color indicates soft X-rays. Intensities are not normalized to the exposure time, so that the observation poles appear brighter. Exposure times are assumed as shown in fig. 3.4a.

## 5.4. Objectives

Since the basic dimensions of the  $\mu$ ROSI telescope are determined and a first simulation confirmed that the instrument is able to observe  $> 100$  bright sources, the mission objectives need further specification.

The simulation outlined in fig. 5.1 shows that the amount of observable targets is  $> 100$  and this figure shall be the minimum goal for the MSV all-sky survey with the  $\mu$ ROSI telescope.

The color coding in fig. 5.1 is consistent with the energy resolution provided by the RASS-BSC. ROSAT's PSPC instrument used for the all-sky survey had a FWHM energy resolution of 24% at 1.0 keV and around 27% at 1.5 keV (Briel et al., 1996). The approximation for the PSPC energy resolution is given in eq. (5.6).

$$\left( \frac{\Delta E}{E} \right)_{FWHM} = 0.43 \left( \frac{E}{0.93 \text{ keV}} \right)^{-0.5} \quad (5.6)$$

With a suitable detector, the  $\mu$ ROSI telescope could enrich the all-sky map with a finer energy resolution. With state-of-the-art semiconductor detectors energy resolutions of  $< 3\%$  are possible when operated at low temperatures (Strüder and Meidinger, 2008). The low temperature required for operating the detector needs to be stable and should be achieved by passive cooling only.

A detector with good energy resolution grants the opportunity to measure spectra and possibly detecting some elementary absorption line in the soft X-ray bandwidth (see table A.2 on p. 165 for a list of spectral lines). The scanning geometry outlined in section 3.5 allows for observing the Earth horizon during the all-sky survey, possibly measuring the O<sub>2</sub> line at 0.5 keV in the ionosphere.

The all-sky survey takes half a year to complete. During six months, the scanning axis (refer to section 3.3 p. 24) precesses by 180° and the observed great circles cover the whole sky. However, a full year is allocated for the all-sky survey to allow for covering possible blank streaks that were missed out in the first half year. Reasons for missing out a streak can be numerous, e.g. obstruction due to the proximity of the Earth, satellite safe modes due to solar flares, delays in sending data to the ground station etc. After finishing the survey, the telescope can be used for pointed observations. Long exposure times on a specific target can reveal transient sources (refer to sections 2.3 and 2.4), possibly alerting larger X-ray telescopes to observe unexpected events.

Apart from its scientific purpose,  $\mu$ ROSI is also used as a technology demonstrator. In order to achieve the low operational temperature of the detector with minimum of power consumption, a passive cooling system similar to the camera cooling system originally designed for the eROSITA telescope (Fürmetz et al., 2008; Tiedemann et al., 2008) is anticipated. During its first development phase,

eROSITA was scheduled to fly in a low Earth orbit (LEO). In order to achieve the operational temperature of the X-ray detector CCDs of  $-90^{\circ}\text{C}$  a passive cooling system was designed. The X-ray cameras were connected to the radiators by specifically developed low power, low temperature heat pipes. To keep the low temperature stable, a latent cold storage (LCS) filled with a phase change material (PCM) was included in the cooling system. In the course of the eROSITA project, the mission scenario changed from a LEO orbit to a quasi-halo orbit around the Lagrangian point L2 rendering the LCS obsolete. However, early tests with laboratory LCS containers were promising and  $\mu$ ROSI was identified as an ideal platform for in-orbit testing of such a passive cooling system.

In brief, the objectives of the  $\mu$ ROSI project can be summarized as follows:

1.  $\mu$ ROSI is planned to perform an all-sky survey in the soft X-ray bandwidth.
2. The system shall be capable of detecting at least one hundred bright X-ray sources.
3. The energy resolution of the detector shall be sufficient to measure spectra and discern absorption lines in the soft X-ray bandwidth.
4. The scan geometry of the all-sky survey allows to investigate X-ray absorption in the Earth's ionosphere in soft X-rays as secondary mission goal, potentially observing the O<sub>2</sub> line at 0.5 keV.
5. The telescope can be used for pointed observations of selected targets in a second mission phase, potentially detecting transient sources and being able to alert large X-ray telescopes for further investigation.
6. The telescope detector is cooled by a completely passive cooling system that ensures low, constant temperature using a phase change material to enhance energy resolution for technology demonstration.

## 5.5. **$\mu$ ROSI Subsystems**

The key components of any X-ray telescope are the detector unit and the X-ray focusing optics. The fundamentals governing those two subsystems have been discussed in chapter 4 and some constraints applying specifically to the  $\mu$ ROSI X-ray focusing optics have been mentioned in this chapter. However, an X-ray telescope requires more than just a detector and a focusing mirror. The detector requires electrical power, and the detector signals need to be processed. For this purpose, an electronics subsystem is required. Additionally, the detector

performance is temperature dependent and it therefore requires a thermal control subsystem. Finally, all the aforementioned components need to be mounted into a structure that also provides a mechanical interface to the satellite. In summary, the  $\mu$ ROSI telescope design is broken down into the following subsystems:

1. The mirror module
2. The detector module
3. The structure or optical bench
4. The thermal control subsystem
5. The electronics subsystem

All these subsystems are described in full detail in chapters 7 to 10.

Figure 5.2 shows the  $\mu$ ROSI system block diagram visualizing the interfaces between the subsystems and the environment. The interface types are labelled as follows:

E Electrical interface

M Mechanical interface

R Thermal radiation

Electrical and mechanical interfaces both include thermal conduction.

## 5.6. Requirements

Before detailing the design, a list of requirements is needed. Table 5.3 contains the requirements for each subsystem. The last column contains information on the verification method for each requirement. The meaning of these abbreviations is listed in table 5.2.

Verification	Description
A	Analysis
D	Design
I	Inspection
T	Test

Table 5.2.: Abbreviations for requirement verification methods used in the *Verification* column in the requirements list (table 5.3).

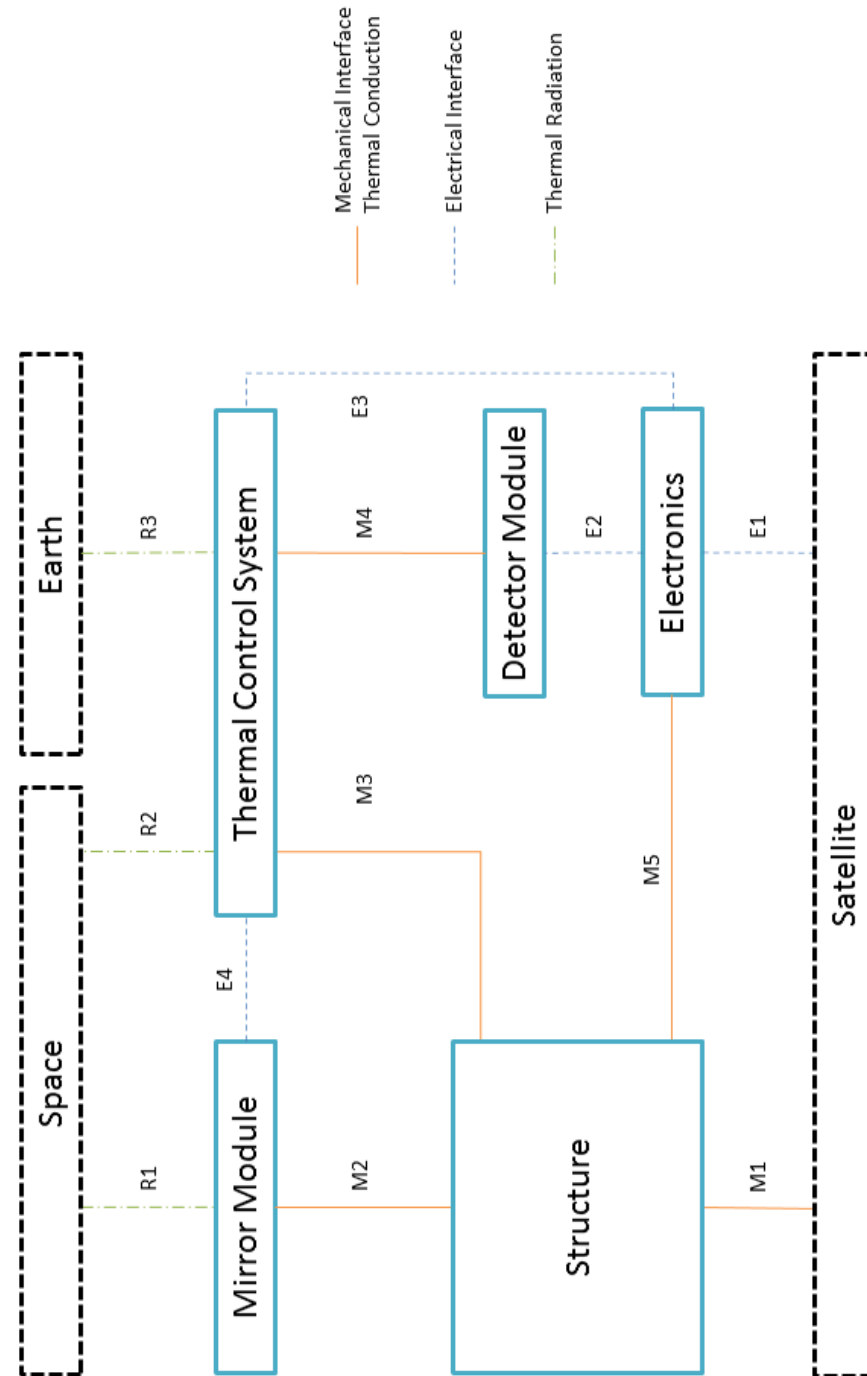


Figure 5.2.:  $\mu$ ROSI system block diagram with interface identifiers.

Table 5.3.: List of requirements.

No.	Requirement Parameter / Description	Verif
<b>Req. 1</b>	<b>Mirror Module Requirements</b>	
Req. 1.1	Focal Length $f = 240mm$	A, T
Req. 1.2	Nominal Aperture $D_{mirror_{nominal}} = 80mm$	D
Req. 1.3	Number of mirror shells $N_{shells} = 12$	I
Req. 1.4	Mirror surface material The mirror surface shall be made of gold (Au)	I
Req. 1.5	Mirror shell material The mirror shells shall be made of Nickel (Ni)	I
Req. 1.6	Mirror shell thickness The mirror shell thickness shall be $t_{mirror} = 0.3mm$ for all mirror shells.	I
Req. 1.7	Surface roughness The root mean square surface roughness shall be smaller than $1.0nm$ RMS	T
Req. 1.8	Mirror shell manufacturing method The mirror shells shall be manufactured by electro-galvanic forming	D
Req. 1.9	Effective area The effective area of the mirror system shall be $> 30cm^2$	A, T
Req. 1.10	Field of View $\Theta = 1^\circ$	T
Req. 1.11	Half energy width $0.5^\circ$	T

No.	Requirement Parameter / Description	Verif
Req. 1.12	Mirror shell shape  The primary and secondary mirrors shall be conical. Primary and corresponding secondary mirror are made of one piece.	I
<b>Req. 2</b>	<b>Detector Module Requirements</b>	
Req. 2.1	Energy resolution  The energy resolution of the detector at $0.3keV$ shall be $< 200eV$	T
Req. 2.2	Detector sensitivity bandwidth  The detector shall be sensitive in a bandwidth from $0.1keV \dots 10keV$	T
Req. 2.3	Detector Type  The detector shall be a Silicon Drift Detector (SDD)	D
Req. 2.4	Optical filter  The detector shall be equipped with an optical filter.	D
Req. 2.5	Filter material  The filter shall be made of $200nm$ polyimide (PI) foil and shall be coated with $100nm$ aluminium (Al).	D
Req. 2.6	Straylight  The detector housing shall be designed to prevent optical straylight from reaching the detector.	T
Req. 2.7	Venting  The detector housing shall be designed to allow venting when exposed to vacuum without damaging the filter foil.	D
Req. 2.8	Cleanliness  The detector and all components close to the detector shall be handled in clean environment corresponding to a cleanroom class 1000 or better.	I

## 5. $\mu$ ROSI Miniature X-Ray Telescope

---

No.	Requirement Parameter / Description	Verif
<b>Req. 3</b>	<b>Structure Requirements</b>	
Req. 3.1	Mechanical interfaces  The structure shall provide mechanical interfaces between all major components and to the satellite structure.	D
Req. 3.2	Mechanical loads  The structure shall provide sufficient load capability for... <ul style="list-style-type: none"><li>• static loads</li><li>• thermal loads</li><li>• sinusoidal loads</li><li>• random vibration loads</li><li>• shock loads</li></ul>	A, T
Req. 3.3	Structure is optical bench  The structure serves as optical bench. It shall maintain the focal length under all circumstances.	D
Req. 3.4	Accommodation of electrical interface  The structure shall provide a feed-through for the electrical interface between the telescope and the satellite.	D
Req. 3.5	Thermal insulation  The structure shall be thermally insulated from the spacecraft and from the surrounding environment.	A, T
Req. 3.6	Mass  The total mass of the telescope shall not exceed $M_{Total} \leq 3.0\text{kg}$	A, I
Req. 3.7	Center of gravity  The center of gravity shall be within the optical bench structure and within the spacecraft interface mounting points.	A

No.	Requirement Parameter / Description	Verif
Req. 4	<b>Thermal Control Subsystem Requirements</b>	
Req. 4.1	Nominal detector temperature $T_{detector,nominal} \leq -12^\circ\text{C}$	A, T
Req. 4.2	Detector temperature stability The operational detector temperature shall be stable within $\pm 0.5^\circ\text{C}$ .	A, T
Req. 4.3	Latent cold storage (LCS) The detector temperature shall be maintained stable under all circumstances by a latent cold storage.	D
Req. 4.4	Phase change material The latent cold storage shall be filled with a phase change material (PCM). The phase change temperature shall of the selected PCM shall be consistent with req. 4.1.	D
Req. 4.5	Heat capacity The heat capacity of the PCM shall be large enough to maintain the required detector temperature over one full orbit under all circumstances.	A, T
Req. 4.6	LCS heater The LCS shall be equipped with a resistive heater.	I
Req. 4.7	Mirror heater The mirror system shall be equipped with a resistive heater.	I
Req. 4.8	Radiator Heat dissipation shall be achieved by a radiator surface.	D
Req. 4.9	Radiator insulation The radiator shall be thermally insulated from the structure and all other components except for the heat pipe.	A, T

## 5. *μROSI* Miniature X-Ray Telescope

---

No.	Requirement Parameter / Description	Verif
Req. 4.10	Heat pipe  The radiator shall be thermally connected to the LCS by a constant conductance heat pipe (CCHP).	D
Req. 4.11	LCS insulation  The LCS shall be thermally insulated from the structure.	A, T
Req. 4.12	Temperature sensors  The temperature of critical components shall be measured in-orbit and included in the house-keeping data.	D
Req. 4.13	PCM compatibility  The phase change material (PCM) shall be compatible with the selected container (LCS) material, i.e. it shall not degrade or alter its physical properties or chemical composition due to contact with the container walls, and it shall not change alter the container material or surface.	D
Req. 4.14	PCM safety  The phase change material (PCM) shall be safe to handle under normal laboratory conditions with standard laboratory equipment, i.e. it shall not be toxic, explosive or hazardous.	D
<b>Req. 5</b>	<b>Electronics Requirements</b>	
Req. 5.1	Temperature sensors  The electronics subsystem shall provide interfaces to the temperature sensors of the Thermal Control Subsystem	D
Req. 5.2	Heaters  The electronics boards shall provide means to control the heaters of the Thermal Control Subsystem.	D

No.	Requirement Parameter / Description	Verif
Req. 5.3	Flexlead  The detector shall be connected to the main board with a flexlead cable.	D
Req. 5.4	Shielding  The power converters on the Power Board shall be shielded with a metal casing.	D
Req. 5.5	Power consumption  The total power consumption of the system shall be $P_{Total} \leq 3.0W$ .	D
Req. 5.6	Satellite interface  The electronics subsystem shall provide an electrical interface to the satellite.	D
Req. 5.7	Housekeeping Data  The electronics subsystem shall provide means to store housekeeping data and transmit these data to the satellite.	D
Req. 5.8	Scientific Data  The electronics subsystem shall provide means to store scientific data and transmit these data to the satellite.	D
Req. 5.9	Telecommand  The electronics subsystem shall be able to receive and process commands via the satellite interface (see req. 5.6)	D

## 5.7. Design Description

The preliminary design of the  $\mu$ ROSI telescope had a structure with a square cross-section with the mirror module and the detector module mounted to both sides of the structure (see fig. 5.3). The detector is cooled by a latent cold storage (LCS) which is connected to a radiator with a heat pipe. The electronics are mounted inside the structure.

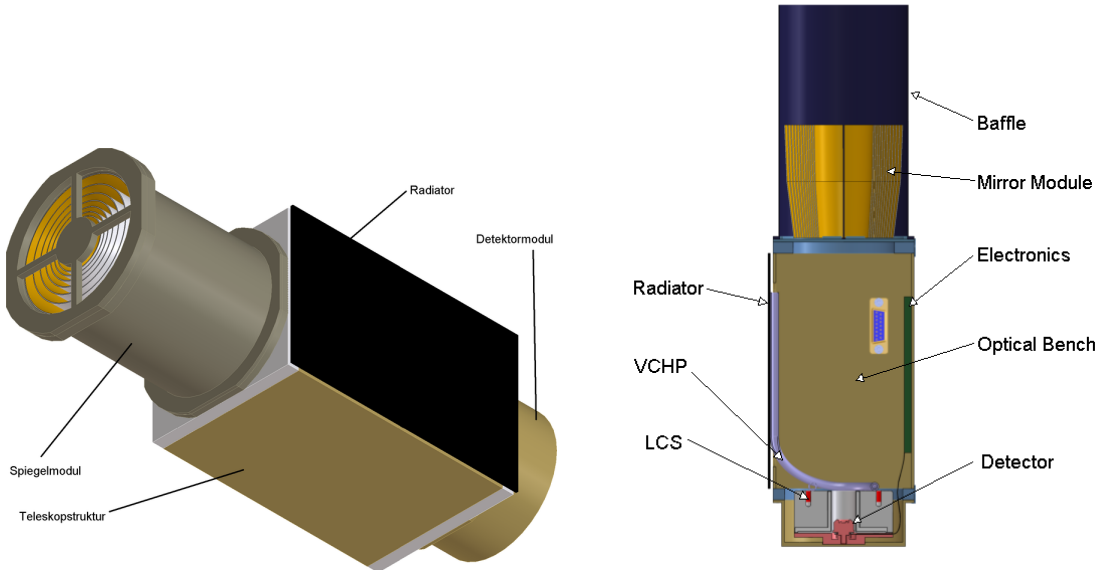


Figure 5.3.: Preliminary design of the  $\mu$ ROSI telescope. The basic configuration of the telescope and all major components remained unchanged until the final design.

The basic configuration of the telescope remained unchanged throughout the project, but the design details were updated several times. At this point, the final design of the  $\mu$ ROSI telescope is anticipated, before presenting each subsystem in full detail in the subsequent chapters.

Figure 5.4 shows an explosion view of the telescope design. The 12 nested mirror shells are mounted on a titanium mechanical interface and screwed on top of the optical bench. The optical and thermal baffle, a CFRP tube, prevents stray light from entering the mirror system and reduces thermal losses due to radiation. On the bottom side of the telescope is the detector module, which is mounted on the latent cold storage (LCS) for thermal stability. The LCS is mounted to the optical bench with a glass filled PEEK insulator. The aluminium heat pipe provides the thermal interface to the radiator, which is mounted on the back side of the telescope on thermally insulating bushings. The front side of the optical bench is the side that is mounted to the satellite with four M5 screws. A removable cover provides access to the inside of the optical bench, where the electronics is accommodated.

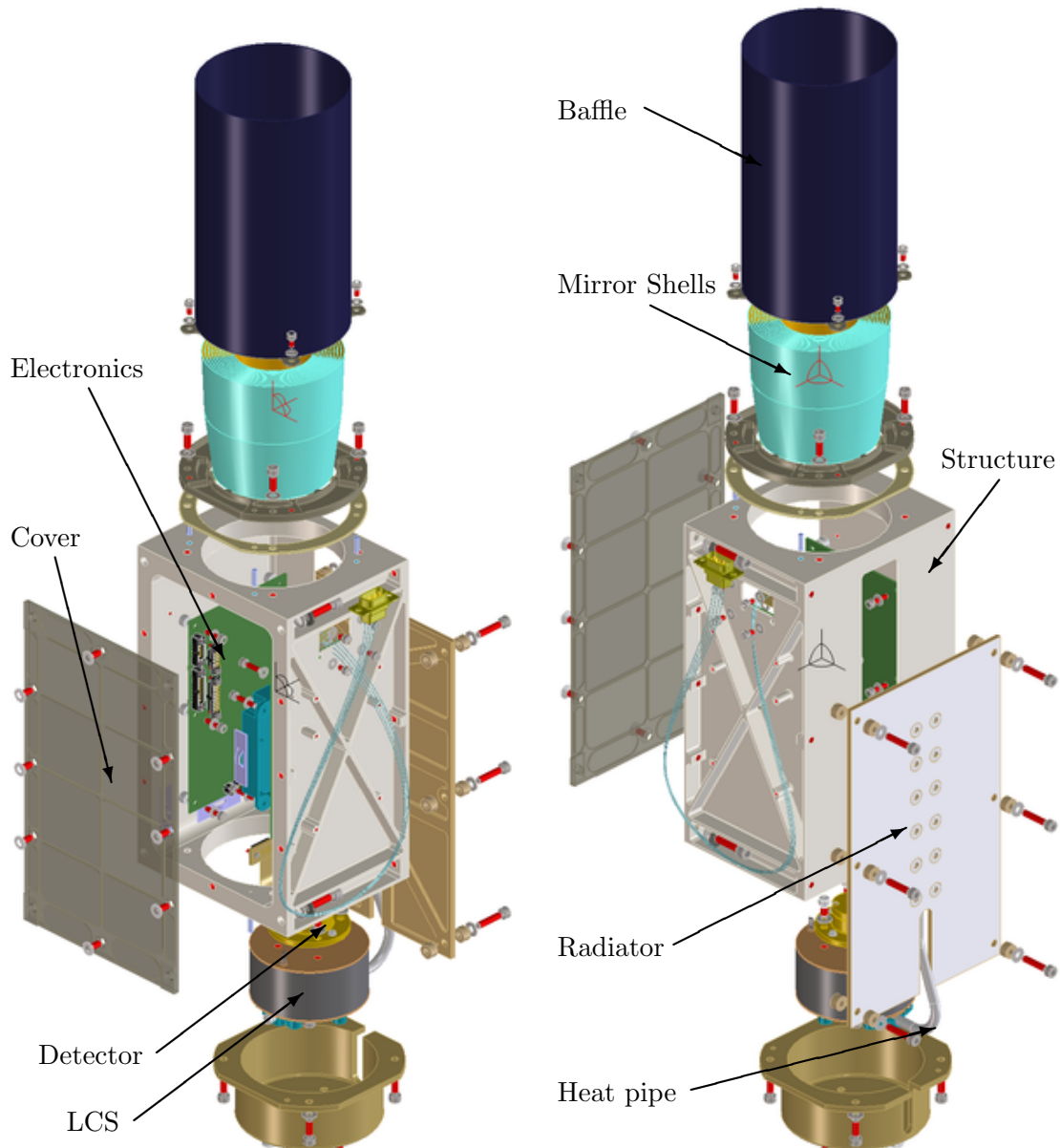


Figure 5.4.: Explosion view of the  $\mu$ ROSI telescope. The 12 nested mirror shells are protected against optical stray light with a CFRP baffle. The radiator is mounted with thermal insulators facing into space away from the satellite. A heat pipe connects it to the LCS unit on which the detector is mounted. The electronics is mounted inside the structure and is accessible via a removable cover plate. The structure is made of solid aluminium.

## 5.8. Model Philosophy

In the course of the  $\mu$ ROSI project various models are used for different purposes. The model philosophy corresponds to many large space missions with different models for qualification and flight. The reason for this effort is that the QM and EM model can be later used in the MPE X-ray test facilities. Table 5.4 lists the model types for all subsystems.

Model	Description
MD	Mass Dummy
SM	Structural Model
BB	Breadboard Model
EM	Engineering Model
QM	Qualification Model
FM	Flight Model

The final goal is to manufacture, integrate and test the final Flight Model (FM) of the whole telescope system. That is the real hardware that is actually integrated into the satellite and then flown into space. The FM test program includes the whole range of environmental test (i.e. vibration test, shock test, thermal balance and thermal cycling test), functional and performance tests.

The Qualification Model (QM) is identical to the FM. The QM is a demonstrator model that shows the capabilities of the overall system. With successful completion of the QM test campaign the telescope system design is completely verified. The test programs of the QM and FM are identical. However, the QM test levels are higher than those used for the FM to give the whole design some extra margin. The QM may also serve as a flight spare model after completing the QM test program.

The Engineering Qualification Model (EQM) is rather a work in progress than a fix set of parts assembled together. The purpose of the EQM is to conduct functional tests and to check all subsystem interfaces. Then, it is being upgraded, so it becomes the QM. The idea of the EQM is that critical parts, such as the Detector or the Mirror are integrated as non-critical Engineering Models (EM) first. And, after completion of all functional tests, are replaced by the fully flight-like QM models. For example, the Electronics EM is used for integrated system tests in the EQM before being replaced by the QM.

The Structural Qualification Model (SQM) is used for the structural verification of the overall system design. It includes mostly Structural Models (SM) or

Mass Dummies (MD). Section 8.2 gives more details on this model. SM are mechanically similar to the final design, whereas MD usually are aluminium blocks milled to match the mass properties.

Breadboard Models (BB) are used for development and evaluation tests on subsystem or component level only. Special focus is on the evaluation of the electronics with various BB models.

Component	Development tests	SQM vibration test	EQM functional tests	QM test campaign	FM test campaign
<b>Structure</b>					
Optical Bench		SM	QM	QM	FM
Cover		SM	QM	QM	FM
<b>Detector</b>					
Silicon Drift Detector	EM		SM	QM	FM
Filter Foil	EM		EM	QM	FM
Detector Housing	EM		EM	QM	FM
<b>Mirror</b>					
Mirror Shells	EM	MD		QM	FM
Spider		SM	EM	QM	FM
Baffle		SM	QM	QM	FM
<b>Thermal Control System</b>					
Latent Cold Storage	EM	MD	QM	QM	FM
Radiator		SM	QM	QM	FM
Heat pipe		SM	QM	QM	FM
LCS-Interface		SM	QM	QM	FM
<b>Electronics</b>					
Flexlead Cable			EM	QM	FM
Main Board	BB	SM	EM	QM	FM
Power Board	BB		EM	QM	FM

Table 5.4.:  $\mu$ ROSI test matrix.

## 6. **$\mu$ ROSI Detector**

The requirements for the  $\mu$ ROSI telescope were formulated in such a way, that the telescope can perform its designated scientific mission with only an angular resolution of  $1^\circ$  (see reqs. 1.10 to 1.11). For the detector this means that only one “pixel” is needed. Thus, the detector type is easily chosen. CCDs can be ruled out, as we do not need the angular resolution given by large number of pixels and for their complexity. Gaseous detector are also not suitable, as they do not have the high energy resolution required for the  $\mu$ ROSI telescope.

The detector used for the  $\mu$ ROSI miniature X-ray telescope is a commercial off-the-shelf (COTS) product provided by the Munich based company pnDetektor. This company is a spin-off of the Max-Planck-Institut semiconductor laboratory which has a world-wide reputation for its scientific X-ray detectors. The SDDs offered by pnDetektor are used for scientific or industrial applications and have space heritage being used on the NASA Mars rovers Spirit and Opportunity and on ROSETTA (Klingelhöfer et al., 2007).

For the  $\mu$ ROSI project, and for later use in test facilities at the MPE, a total number of six silicon drift detectors (SDD) of type SD3-20-128pnW were delivered. Two of them feature a Beryllium entry window and four have an open cap. Table 6.1 lists the basic properties of the SDDs.

The sensitive area is restricted by an internal collimator to a circular area with  $4.6\text{ mm}$  diameter. This circumstance yields rather comfortable requirements for the mirror system. The full field of view needs to be focussed on the sensitive area, but there is no need to match a certain pixel size except the collimator area.

The SDD is operated in single-photon-counting mode. This means that the detector is read out every  $1\text{ }\mu\text{s}$ . Photons that are detected during one read-out cycle are transmitted to the electronics as analogue signal. The electronics is then responsible for analogue-digital converting and data processing.

---

Type	SD3-20-128pnW
Material	High ohmic ultra-pure FZ-Silicon
Active thickness	$450 \pm 20 \mu m$
Active area	$20 mm^2$
Chip area	$64 mm^2$
Entrance window	pn Window
Mounting	TOX housing
Collimator	internal
Housing cap	open / $8 \mu m$ Be DB+ window
Depletion voltage	$-110 V$
Back voltage	$-97 \dots -107 V$
Energy resolution	$128.0 eV$ at Mn-K $\alpha$ ( $5.90 keV$ ) $T = -20 ^\circ C$
Signal-to-noise ratio	$14 \cdot 10^3$ at Mn-K $\alpha$ ( $5.90 keV$ ) $2 \cdot 10^3$ Counts per second Parallel beam on $4.6 mm$ collimator

---

Table 6.1.:  $\mu$ ROSI SDD detector properties.

## 6.1. Filter Selection

As the SDD is sensitive in the visible spectrum (VIS), the built-in entry window serves as a filter to prevent optical (stray-) light from reaching the detector surface. The SDDs without an entry window need to have a custom filter. This needs to be developed especially for this purpose, but has one critical advantage: the freedom to choose a suitable material or combination of materials for the intended X-ray energy bandwidth.

The optimum filter material has a high transmission rate in the X-ray bandwidth and a low transmission in the visible spectrum. The following materials were investigated:

- Beryllium (Be),  $8 \mu m$  thickness  
is the standard entry window material used in SDD production by pnDetector.
- Polyimide (PI, C<sub>22</sub>H<sub>10</sub>N<sub>2</sub>O<sub>5</sub>),  $0.2 \mu m$  thickness  
is available in extremely thin foils that can be coated with a thin Aluminium coating for optical opacity.
- Aluminium (Al),  $0.1 \mu m$  thickness  
is a thin coating on a PI substrate foil.
- Polyimide  $0.2 \mu m$  + Aluminium (Al)  $0.1 \mu m$   
is used as filter material for the eROSITA mission. A thin layer of aluminium is vapour deposited on a polyimide substrate.

Henke et al. provide a comprehensive online database where transmission values for different materials can be retrieved (see fig. 6.1). The values for the aluminium coated polyimide foil are obtained by multiplying the values for polyimide  $0.2 \mu m$  and aluminium  $0.1 \mu m$ . Table 6.2 lists the result for selected spectral line energies.

Table 6.2.: Transmission of selected filters for different energies.

	Photon energy [keV]					
	0.28	0.93	1.25	1.49	1.74	2.98
PI $0.2\mu m$ + Al $0.1\mu m$	0.3891	0.8740	0.9424	0.9638	0.9017	0.9755
Be $8.0\mu m$	0.0000	0.3331	0.6367	0.7622	0.8449	0.9686
PI $0.2\mu m$	0.9202	0.9090	0.9588	0.9743	0.9835	0.9965
Al $0.1\mu m$	0.4229	0.9616	0.9829	0.9892	0.9169	0.9788

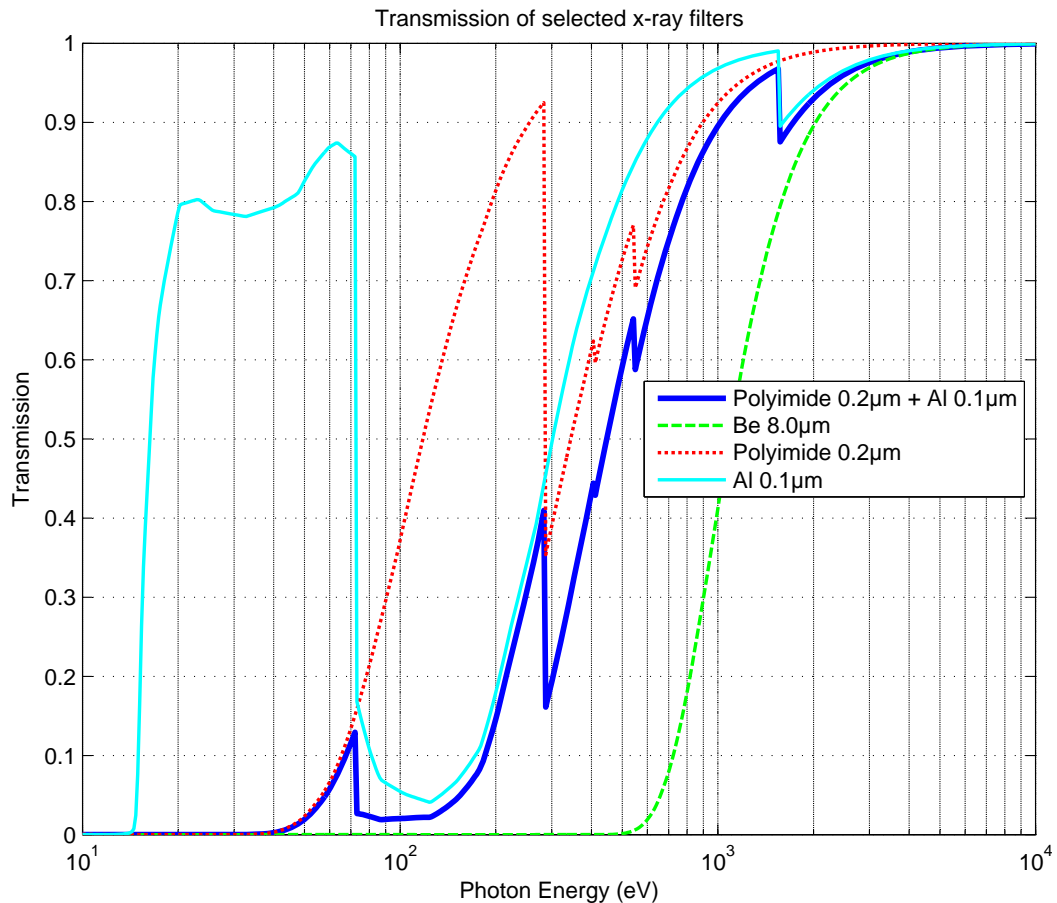


Figure 6.1.: Transmission of selected filter materials. Data for Be, polyimide and Al retrieved from Henke et al. (1993).

The aluminium coated polyimide foil is the best choice for the  $\mu$ ROSI filter. It allows good transmissions in the relevant spectral lines while still being opaque in the visible spectrum.

## 6.2. Detector Assembly Design Description

The  $\mu$ ROSI detector assembly is shown in fig. 6.2. The SDD detector (Pos. 8) comes packaged inside a TO-8 metal casing with a M4 bolt thread at the end. The flexlead cable connects the SDD's 16 pins with the main board via a Harwin miniature plug connector. The detector mounting plate (Pos. 2) can be rotated to adjust the lateral alignment of the flexlead after the detector is screwed into it.

## 6.2. Detector Assembly Design Description

---

The retention ring (Pos. 5) then clamps the detector mounting to the detector shroud (Pos. 3) and prevents further rotation. An o-ring (Pos. 9) is placed around the SDD's TO-8 casing for lateral centering and light sealing. A venting light seal ring (Pos. 6) is placed on top and holds the o-ring in position. The filter foil (Pos. 1) is adhered into the filter cap (Pos. 4) which is screwed on top of the detector shroud pressing the light seal onto the o-ring. The venting light seal is black anodized and features a groove that allows air to escape from between the SDD and the filter foil without allowing light to reach the detector. This is an extremely important feature, since the filter foil is likely to rupture during the rocket start phase, if the enclosed air could not escape freely.

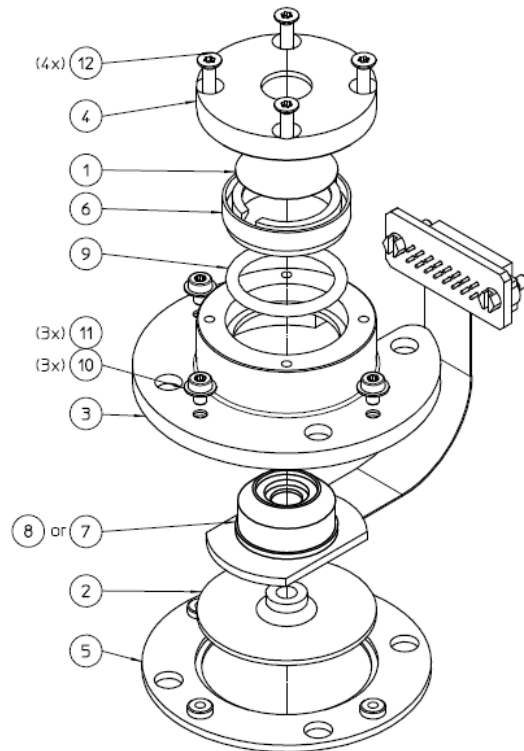


Figure 6.2.: Explosion drawing of the  $\mu$ ROSI detector assembly.

The complete detector assembly is mounted on top of the latent cold storage. The detector mounting has a fit that ensures centered alignment. It also provides a large contact surface and short distance to the detector for best thermal conduction.

## *6. $\mu$ ROSI Detector*

---

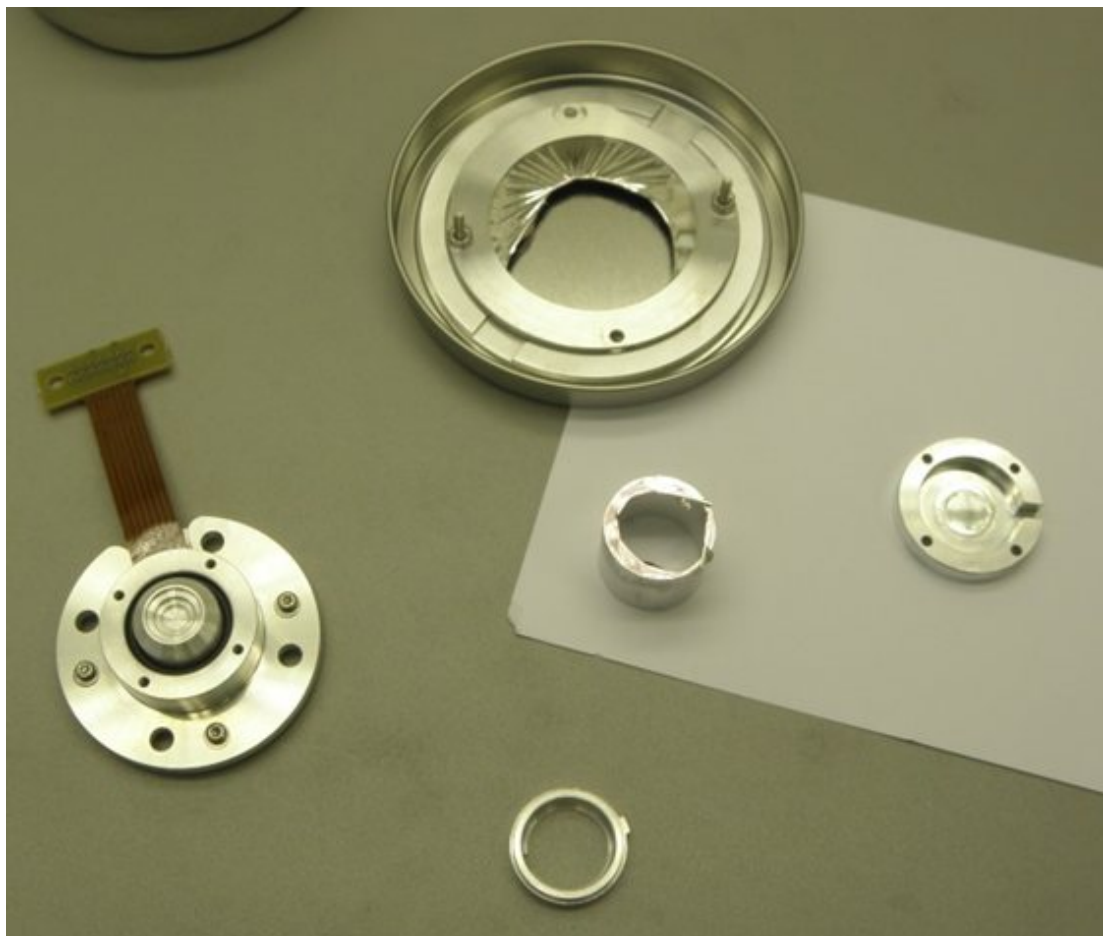


Figure 6.3.:  $\mu$ ROSI detector assembly with dummy detector and filter cap. The SDD dummy made from solid aluminium is already mounted in the casing (left). The filter was cut out from a larger filter foil (center top) and adhered inside the filter cap (right).

## 7. Mirror Module

The mirror module, together with the detector, is the heart of the whole telescope. Since the detector is a “one-pixel” silicon drift detector (SDD), the mirror only needs to focus as much X-ray radiation onto the detector surface as possible. Of course, scattering needs to be low to mitigate losses. But there is no requirement for good imaging properties to match a specific pixel size.

The  $\mu$ ROSI mirror module therefore comprises  $N = 12$  nested double-cone mirror shells. It is shown later, that this simplification is sufficient.

The mirror shells themselves are made of Nickel by electro-galvanic forming (or e-forming) using the same manufacturing process as the mirror of the large X-ray telescope eROSITA. Choosing this process has several critical advantages:

- **Technology readiness**

The manufacturing process is well understood and is currently ongoing for the eROSITA mirror shells at the facilities of the Italian company Media Lario. Since the XMM mirror shells were also manufactured by e-forming, the TRL level of 7 can be assessed (compare table A.3, p. 166).

- **Quality**

The produced mirror shells have excellent imaging properties with a resolution down to  $15 \text{ arcsec}$ .

- **Knowledge**

The persons involved in the eROSITA mirror manufacturing and verification process are either working for the MPE or for a sub-contractor.

Although mirror shells made of slumped glass are currently under development at the MPE, this technology needs more research and development to supply a first demonstrator mirror system.

The development of the  $\mu$ ROSI mirror subsystem foresees a mirror engineering model (EM) (see section 7.5). The EM consists of one mirror shell #06 that is manufactured and tested in the X-ray test facility PANTER (see Freyberg et al., 2008, for information about the PANTER capabilities) to verify the manufacturing process from the very start to the final X-ray measurement. Optical measurements support the process, but cannot be used for the verification due to the huge difference in wavelength between optical and X-ray.

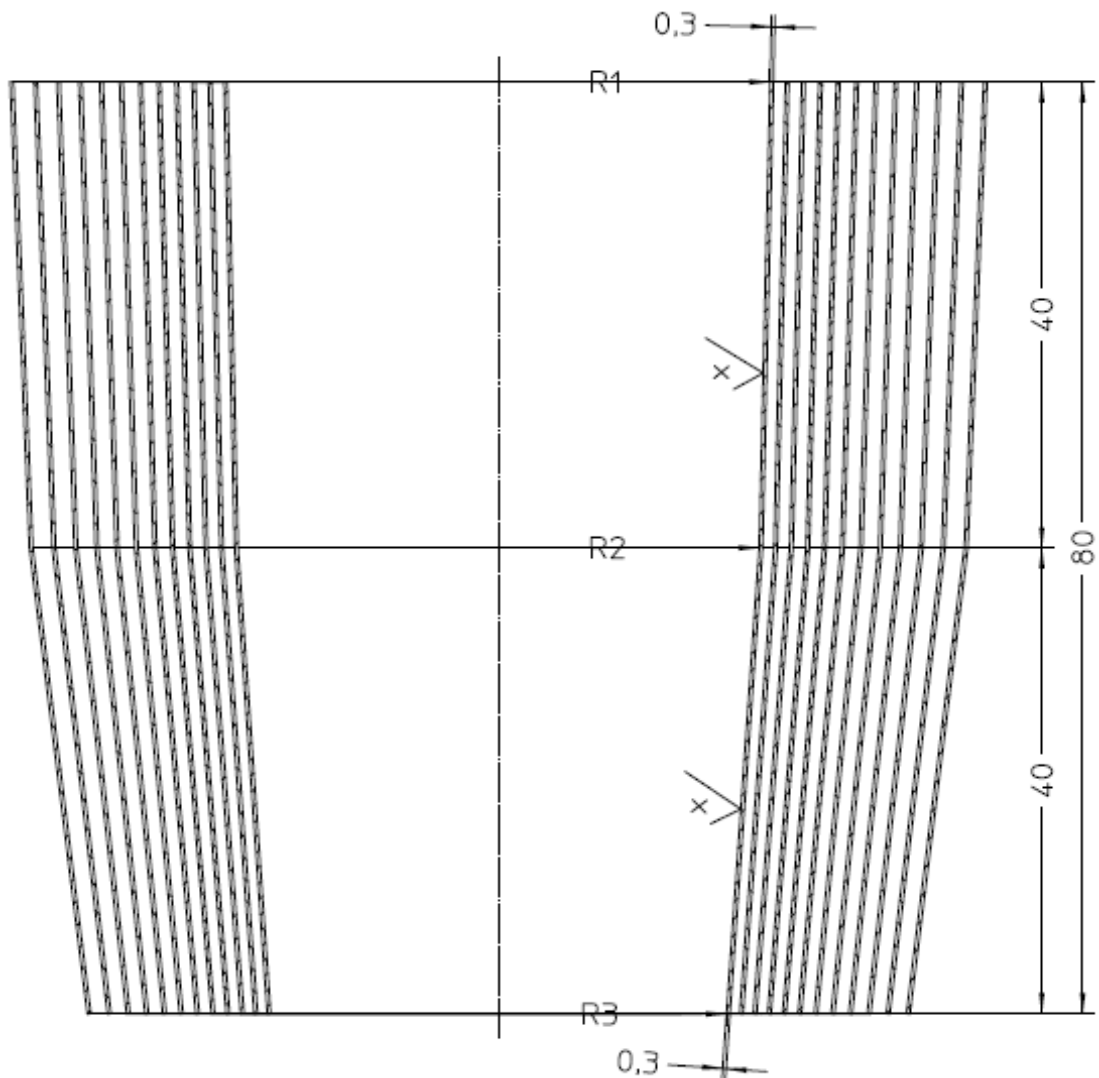


Figure 7.1.: Section view of nested  $\mu$ ROSI mirror shells.

## 7.1. Mirror Parameters

The mirror design parameters, chiefly the focal length  $f$  and the nominal diameter  $D_0$  define the basic dimensions as well as the optical performance. From these basics, the dimensions for each mirror shell is derived.

The  $\mu$ ROSI mirror module has the same  $F$ -number as the successful ROSAT space telescope. Its nominal aperture diameter  $D_0$  and focal length  $f$  are reduced by a factor of 10:

$$\begin{aligned} f &= 240 \text{ mm} \\ D_0 &= 80 \text{ mm} \\ \Rightarrow F &= 3 \end{aligned}$$

The reason for choosing this specific  $F$ -number can be understood when looking back at eq. (4.8). The grazing incidence angle  $\alpha$  is only dependent on the  $F$ -Number. At the same time, the reflectance for larger angles  $\alpha$  significantly decreases and is a function of the photon energy (see fig. 4.1). Thus, the  $F$ -number has a direct influence on the observable energy bandwidth.

As  $\mu$ ROSI and ROSAT are both performing an all-sky survey in the soft X-ray bandwidth, choosing the same  $F$ -number guarantees that the data of the  $\mu$ ROSI telescope can be well compared to and correlated with the ROSAT database.

The mirror shell thickness  $t$  should be as small as possible in order to reduce the area shaded by the mirror shell itself. This parameter is dominated by the manufacturing process and the required mirror shell stability. When the electrogalvanically formed Nickel shell is released from the mandrel, the shell with the previously deposited gold surface needs to be separated from the mandrel. The release is facilitated by cooling the aluminium mandrel so that the difference in thermal expansion between aluminium ( $\lambda_{Al} = 23.1 \cdot 10^{-6} K^{-1}$ ) and nickel ( $\lambda_{Ni} = 13.4 \cdot 10^{-6} K^{-1}$ ) eases the separation of mandrel and mirror shell. During this process, a lot of stress is induced on the shell, potentially leading to a deformation of the mirror shell.

Experience from Media Lario as the supplier for the eROSITA mirror shells have revealed, that a thickness of  $t = 0.3 \text{ mm}$  proved to be a good compromise between low shell thickness and mechanical stability. However, for small diameter mirror shells like the inner  $\mu$ ROSI mirror shells, even a shell thickness of  $0.2 \text{ mm}$  is feasible without deformation upon release. Thus, the base mirror shell thickness for the outer six out of twelve mirror shells was set to  $t = 0.3 \text{ mm}$  and for the remaining inner six shells a thickness of  $0.2 \text{ mm}$  was selected.

The mirror shell length  $l$  of the  $\mu$ ROSI mirror shells is constant. Other X-ray telescopes have non-constant mirror shell lengths to increase the geometric area

## 7. Mirror Module

---

#	$\alpha$ [°]	$r_0$ [mm]	$r_a$ [mm]	$r_b$ [mm]	$t$ [mm]	$A$ [mm <sup>2</sup> ]
01	2.366	40.000	41.652	35.020	0.3	366.35
02	2.260	38.186	39.765	33.430	0.3	331.67
03	2.159	36.448	37.956	31.907	0.3	300.01
04	2.061	34.781	36.221	30.447	0.3	271.11
05	1.968	33.184	34.558	29.047	0.3	244.75
06	1.878	31.653	32.965	27.706	0.3	240.61
07	1.792	30.185	31.437	26.421	0.2	217.79
08	1.709	28.779	29.973	25.189	0.2	196.97
09	1.630	27.431	28.569	24.009	0.2	177.99
10	1.554	26.139	27.224	22.877	0.2	160.68
11	1.481	24.901	25.935	21.793	0.2	144.91
12	1.411	23.714	24.699	20.754	0.2	138.00
$\Sigma$						2790.84

Table 7.1.:  $\mu$ ROSI mirror shell parameters. The calculated area  $A$  takes into account shaded areas from the mirror mounting structure.

of the inner shells. This approach requires a sloped mechanical interface and is therefore not supported for the  $\mu$ ROSI mirror module. Table 7.1 lists the shape parameters for all 12  $\mu$ ROSI double cone mirror shells.

Now that the mirror parameters are fixed, the double-cone approximation can be checked using eqs. (4.15) to (4.18). The values for the spot diameter  $d_{spot}$ , focal length offset  $\Delta f$  and the resolution  $u$  are calculated for each mirror shell. The value for all mirror shells is obtained with a weighted average using the effective area values from table 7.1.

Table 7.2 shows the results of the  $\mu$ ROSI double cone approximation parameters. The focal length is larger by  $\Delta f/2 = 5.08\text{ mm}$ . Thus, the focal length of the  $\mu$ ROSI mirror module is  $f' = 245.08\text{ mm}$ .

The spot diameter is  $d_{spot} \leq 1.69\text{ mm}$  and approximately  $1.38\text{ mm}$  for all mirror shells. This value is sufficiently small as the  $\mu$ ROSI detector has an aperture diameter of  $4.6\text{ mm}$ . The double cone approximation is therefore compatible with the selected detector.

The resolution of the double cone mirror system is  $19.36\text{ arcmin}$ . This value is smaller than the specified  $30\text{ arcmin}$  that are required in req. 1.11.

#	$\Delta f$ [mm]	$d_{spot}$ [mm]	$u$ [arcmin]
01	10.12	1.69	23.66
02	10.11	1.61	22.57
03	10.10	1.53	21.52
04	10.09	1.46	20.52
05	10.08	1.39	19.56
06	10.08	1.33	18.64
07	10.07	1.27	17.77
08	10.06	1.21	16.93
09	10.06	1.15	16.13
10	10.05	1.09	15.36
11	10.05	1.04	14.62
12	10.04	0.99	13.92
	10.08	1.38	19.36

Table 7.2.:  $\mu$ ROSI double cone focus parameters calculated with eqs. (4.15) to (4.18). Values for all mirror shells are obtained with a weighted average using the effective areas from table 7.1.

The calculated values prove that the double cone approximation is sufficient for the  $\mu$ ROSI telescope.

## 7.2. Effective Area

As already discussed in section 4.1.4, the effective area is an important parameter to quantify the mirror performance. The effective area is calculated for each mirror shell. Vignetting is neglected, which means that the calculated effective area is only valid for on-axis observations. Thus, the incidence angle is also fixed.

The aperture area for each mirror shell is already given in table 7.1. The only parameter left is the reflectivity for the selected surface material as a function of the energy and the incidence angle.

The reflectivity  $\rho$  has to be multiplied by 2 to take into account both reflections, at the primary mirror and the secondary mirror. The telescope was designed so that the incidence angle of the primary mirror equals the angle on the secondary. Thus, the effective area is calculated with eq. (7.1)

$$A_{eff} = 2 \cdot \rho \cdot A \quad (7.1)$$

Figure 7.2 shows the reflectivity of gold for selected energies and an assumed surface roughness of  $1.5\text{nm RMS}$  as a function of the incidence angle. The second plot shows the incidence angle for each mirror shell (compare  $\alpha$ -values in table 7.1). The next plots show the resulting reflectivity and the calculated effective area for the same spectral lines as above. The results are also summarized in table 7.3. The effective area depends on the observed energy. Table 7.3 and fig. 7.2 show how large mirror shells hardly contribute to the total effective area for high energies despite their larger geometric area. This effect is directly linked to the incidence angle and the reflectivity. The total effective area for all 12 mirror shells is  $> 1000 \text{ mm}^2$  for C-K ( $0.28 \text{ keV}$ ) and still  $> 400 \text{ mm}^2$  for Si-K ( $1.74 \text{ keV}$ ).

#	Photon Energy [ $\text{keV}$ ]					
	0.277	0.930	1.254	1.487	1.740	2.984
01	121.39	69.21	56.73	31.16	3.54	0.0002
02	115.71	69.34	60.30	39.16	7.68	0.0004
03	109.95	68.82	62.58	45.60	14.80	0.0010
04	104.14	67.75	63.72	50.34	23.74	0.0025
05	98.34	66.20	63.89	53.48	32.20	0.0059
06	100.91	70.03	68.94	60.19	42.35	0.0146
07	95.17	67.87	67.83	61.12	47.60	0.0326
08	89.52	65.43	66.15	61.04	50.90	0.0706
09	83.98	62.76	64.02	60.16	52.62	0.1487
10	78.58	59.92	61.53	58.65	53.08	0.2996
11	73.35	56.96	58.78	56.66	52.58	0.5738
12	72.18	57.00	59.04	57.40	54.28	1.0801
$\sum$	1143.22	781.29	753.52	634.96	435.37	2.2298

Table 7.3.: Calculated effective areas of  $\mu$ ROSI mirror shells in  $\text{mm}^2$ . The total effective area is  $> 1000 \text{ mm}^2$  for C-K ( $0.28 \text{ keV}$ ) and still  $> 400 \text{ mm}^2$  for Si-K ( $1.74 \text{ keV}$ ). For energies  $> 2 \text{ keV}$  the effective area significantly decreases.

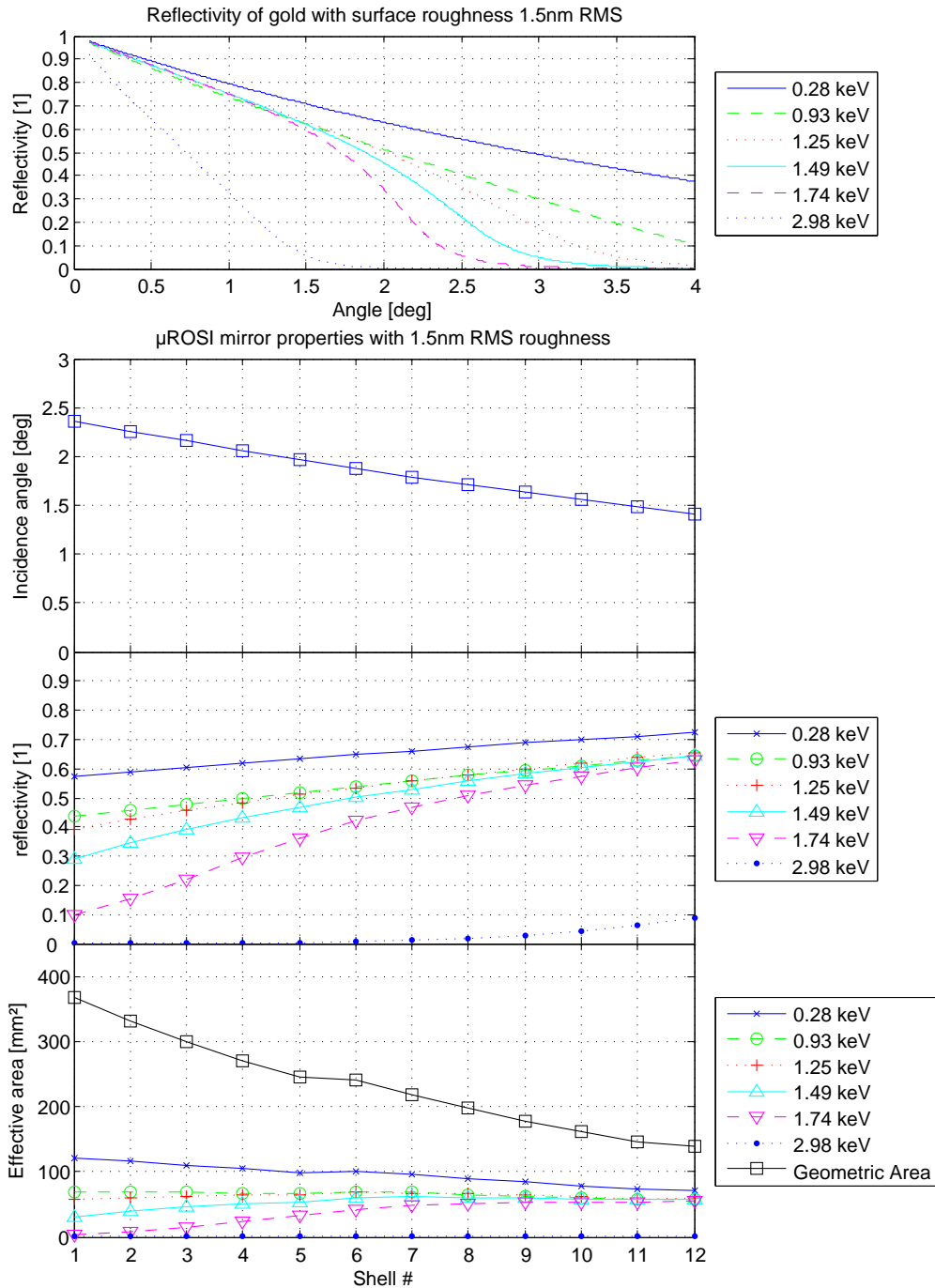


Figure 7.2.: Reflectivities and resulting effective areas for the  $\mu$ ROSI mirror shells. The discontinuity in the effective area curve is due to the step in the mirror shell thickness from  $0.3\text{ mm}$  for shells #01-06 and  $0.2\text{ mm}$  for #07-12.

### 7.3. Mirror MAIT Process

The manufacturing, assembly, integration and testing of the mirror module is one of the most critical processes in the whole project. The process involves many different sub-processes making it very complex, and thus, prone to errors. If the output of the process does not comply with the requirements, i.e. the mirrors do not perform as planned, the whole scientific mission is endangered. In order to reduce the risk of failure in the long chain of processes, it was attempted to use established sub-processes and rely on suppliers with proven good practice experience wherever possible.

The mandrel manufacturing was done by the company LT-Ultra that also provides the mandrels for the eROSITA mirror shells. The mandrel polishing could not be outsourced easily without significant costs, so that this sub-process was performed at the MPE (see section 7.4).

The mirror shell production was left to the company Media Lario that also manufactures the eROSITA mirror shells. The mirror shell integration again would be completed at the MPE (see section 7.6).

Finally, the testing of the integrated mirror is done at MPE's PANTER X-ray test facility which has the technical equipment and the experience to reliably conduct X-ray tests.

The complete electro-galvanic manufacturing process is a sequence with the following sub-processes:

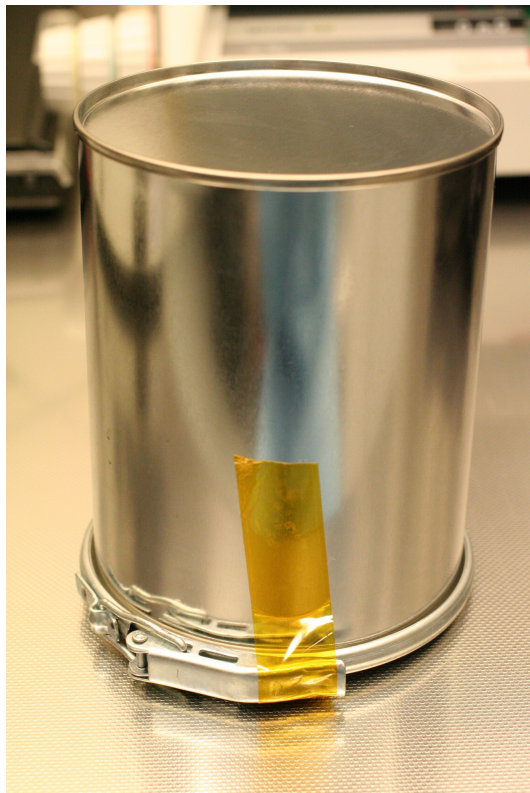
1. Mandrel manufacturing
  - a) Double-cone lathing from aluminium
  - b) Nickel coating
  - c) Diamond lathing to optical precision
2. Mandrel polishing
  - a) Coarse polishing
  - b) Fine polishing
3. Mirror shell production
  - a) Gold depositing on mandrel
  - b) Nickel depositing on gold coating
  - c) Mirror shell separation from mandrel
4. Mirror shell integration

- a) Adjustment of shell to optical axis
  - b) Focal length adjustment
  - c) Adhesive bonding to mirror spider
  - d) Outgassing
5. Mirror system testing
- a) Measurement of effective area
  - b) Measurement of point spread function
  - c) Focal length measurement

Figure 7.3 shows the first mirror shells #01 through #06 after transport to the MPE. For transportation the shells were stacked upside down and retained inside a stainless steel container.

## *7. Mirror Module*

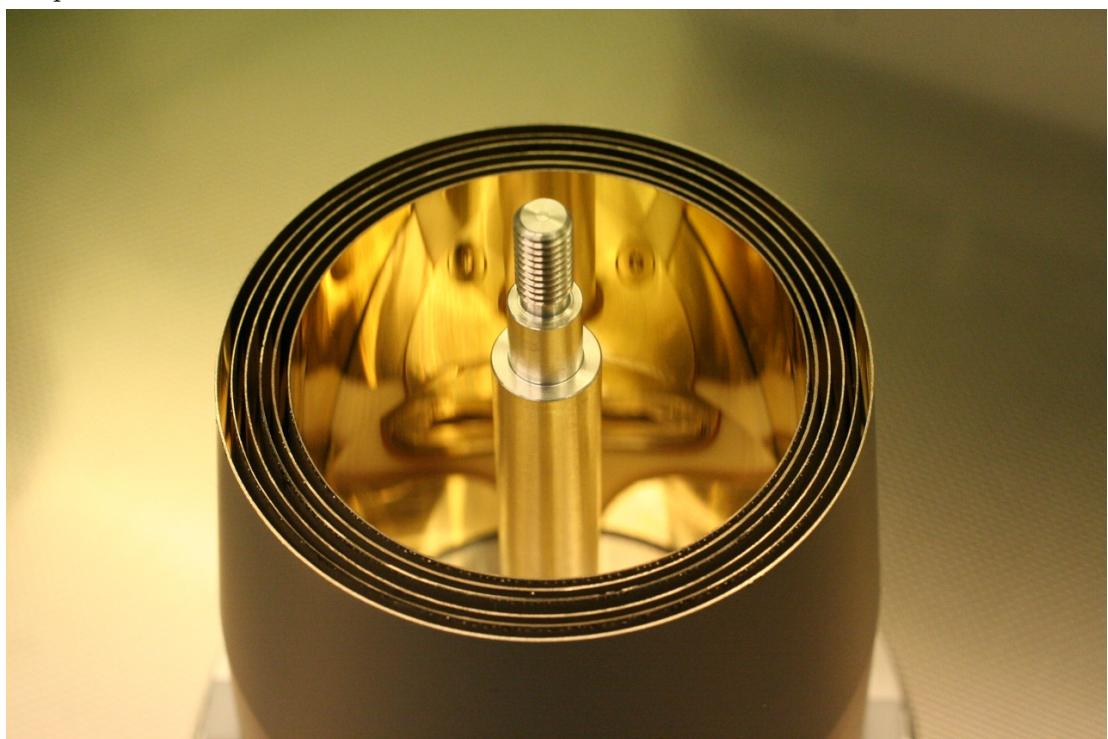
---



(a) Container used for mirror shell trans-  
portation



(b) Mirror shells retaining device



88 (c) Stacked mirror shells #01-06 with the retaining rod in the center

Figure 7.3.: Mirror shells #01-06.

## 7.4. Mandrel Manufacturing and Polishing

The mandrels are the key components of the whole mirror manufacturing process. They determine the dimensions of the final mirror surface from its largest scales (*shape*) down to the smallest scales (*micro roughness*).

The first step in the manufacturing process of the mandrels is done by the German company LT-Ultra. It has vast experience in manufacturing mandrels for X-ray telescopes, e.g. for the large X-ray telescope eROSITA. First, the mandrels are lathed from solid aluminium to double-cone shape. Then, they are coated with pure nickel. Finally, the nickel surface is diamond-lathed to optical (VIS) precision in shape and roughness. The micro-roughness now is smaller than  $R_q < 15 \text{ nm}$  as guaranteed by LT-Ultra.

The second and most critical step is the polishing of the mandrels. The mandrels are polished by the MPE with a special polishing machine that has been developed for this purpose by Elias Breunig (see fig. 7.4). Within the scope of his work he could show that the mandrel polishing process achieved good surface micro roughness and developed a method for quantifying the micro roughness of the mandrels with an interferometer.

Figure 7.5 shows the surface of mandrel #06 after diamond lathing. The image is the result of an interferometric measurement which was used to quantify the surface roughness of the mandrels throughout the polishing process (see Breunig, 2011a, for details). The vertical structure is the typical groove pattern for lathed surfaces. The actually measured surface roughness of  $R_q = 9.2 \text{ nm}$  is well below the specification.

Figure 7.6 shows the same mandrel surface after coarse polishing. The diamond lathing groove pattern is just still visible, but does not contribute much to the overall roughness. Instead, grooves made by the polishing tools themselves are dominant. This is a clear signal to begin fine polishing.

Figure 7.7 shows the surface after fine polishing. The surface looks much more even and the measured roughness of  $R_q = 0.8 \text{ nm}$  corresponds to this impression. The following fig. 7.8 shows four smaller sample areas of the same mandrel to evaluate the micro roughness on smaller area scales.

Using an optical interferometer is an effective way to pre-characterize the roughness of the mandrels. This way, it is possible to monitor the polishing process effectively with the same measurement method. However, the method has its intrinsic disadvantages. As the optical wavelength of the interferometer is by a factor of 1000 larger than the required micro-roughness, the measurement device is physically at its limits. Another disadvantage is that the interferometric measurement does not yield absolute values.

## 7. Mirror Module

---

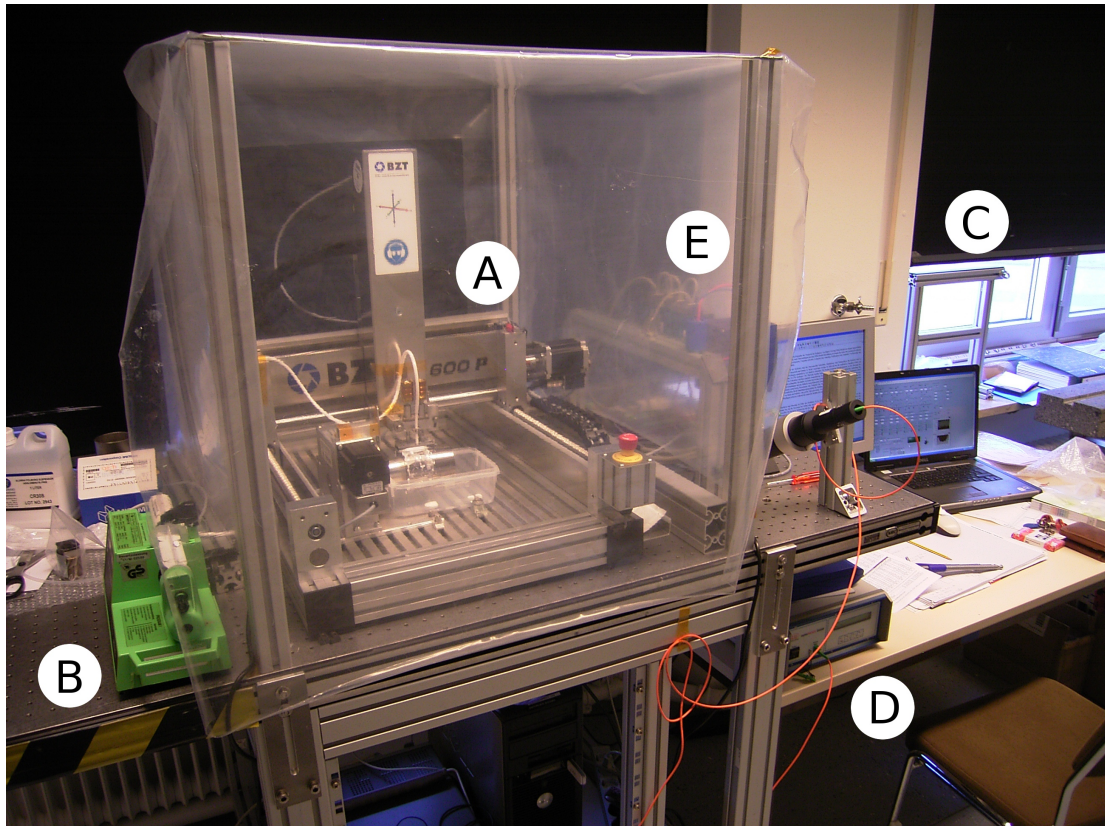


Figure 7.4.: The  $\mu$ ROSI superpolishing device (source: Breunig, 2011a).

- A: Linear axes portal with attached polishing head and rotation unit with mounted mandrel.
- B: Feed pump for the polishing agent.
- C: Control computer with LabView software.
- D: Achromatic distance sensor for machine adjustment.
- E: Electronics rack with power supply and control electronics.

## 7.4. Mandrel Manufacturing and Polishing

---

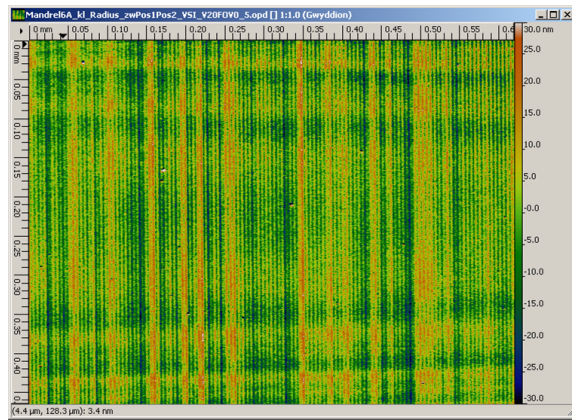


Figure 7.5.: Mandrel #06 initial state after diamond lathing,  $R_q = 9.2 \text{ nm}$ .

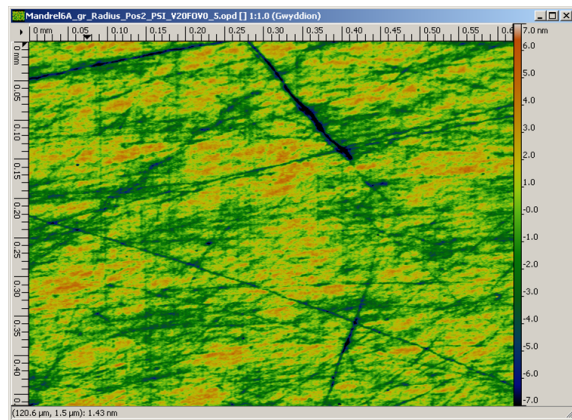


Figure 7.6.: Mandrel #06 after 10 h polishing with pitch,  $R_q = 1.8 \text{ nm}$ .

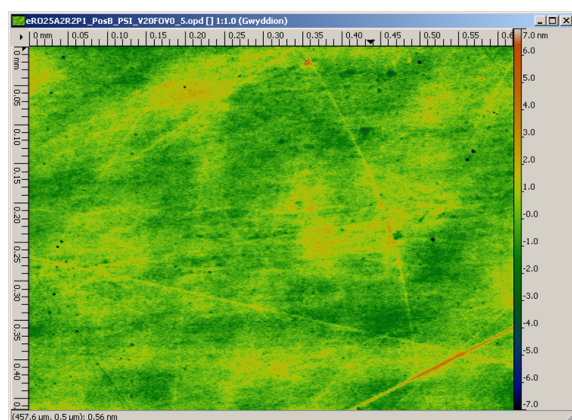


Figure 7.7.: Mandrel #06 after fine polishing  $R_q = 0.8 \text{ nm}$ .

## 7. Mirror Module

---

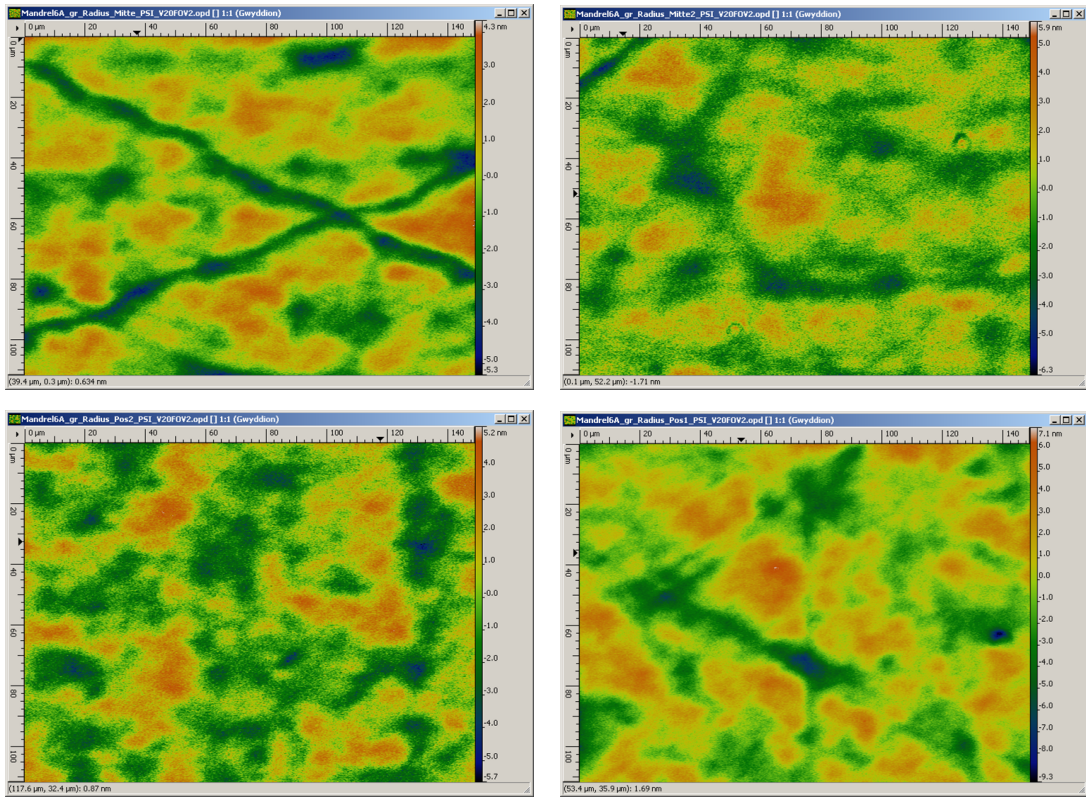


Figure 7.8.: Mandrel #06 after fine polishing, smaller sample areas. Measured RMS surface roughness  $R_q = 1.3\text{nm}, 1.4\text{nm}, 1.5\text{nm}, 1.8\text{nm}$  (top-left, top-right, bottom-left, bottom-right).

## 7.5. Mirror EM Test

The objective of the Mirror EM test is to verify the optical properties of the  $\mu$ ROSI X-ray mirror shells and the complete production process. This includes everything from manufacturing the mandrels, polishing of the mandrels, electro-galvanic replication of the mirror shells to integrating the shell into the test adapter. For this purpose the mandrel #06 was polished to 1.7 nm RMS roughness and a first single mirror shell was replicated from it by Media Lario.

The reason for selecting mirror shell #06 is simply because it is right in the middle in terms of size and effective area and for this reason is best representative for all other mirror shells. Figure 7.9 shows the first EM mirror shell #06/01 before integration into the test adapter.

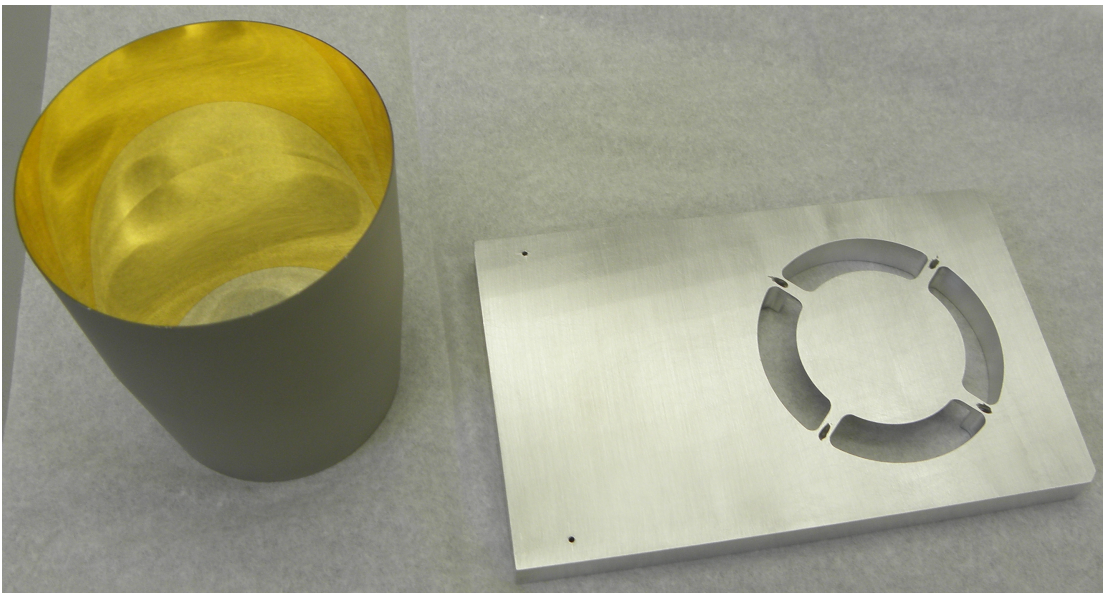


Figure 7.9.: Mirror shell #06/01 before integration into X-ray test adapter.

After integrating the mirror shell into the test adapter, its X-ray optical properties were tested in the X-ray test facility PANTER. The following tests were performed:

- Focus search
- In-focus measurements at Mg-K and Al-K
- Effective area measurements
- Deep in-focus measurement at Al-K and C-K

## 7. Mirror Module

---

- Off-axis in-focus measurements

These tests address all mirror requirements that are verified by testing listed in req. 1 (see p. 62). Refer to Menz et al., 2012 for a full test report. In the following, the most important results from this test are summarized here.

### 7.5.1. Test Set-Up

Figure 7.11 shows the mirror shell #06 in the PANTER test facility before testing. This unique facility features a vacuum chamber with a length of more than 130 m. On one end of the evacuated tunnel, a radioactive source is placed in front of a target. Depending on the target's material, X-ray radiation of specific spectral lines travel through the long chamber. Table A.2 contains the X-ray emission lines of selected materials.

On the other end of the PANTER tunnel, a large vacuum test chamber is situated where the test specimen is placed in front of a set of X-ray cameras. The mirror and the cameras are placed on separate manipulators to allow for various test set-ups.

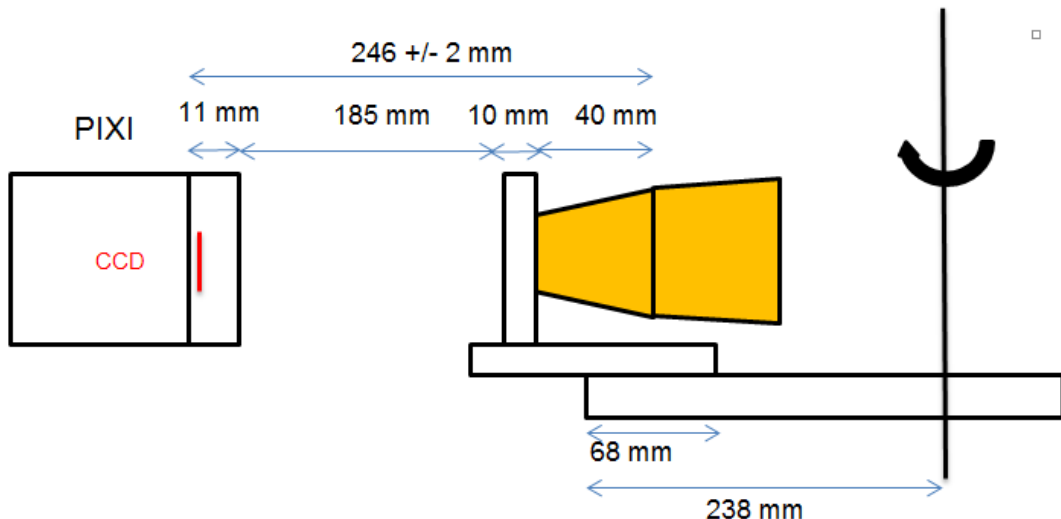


Figure 7.10.: Schematics of the mirror test set-up in the PANTER facility (source: Menz et al., 2012).

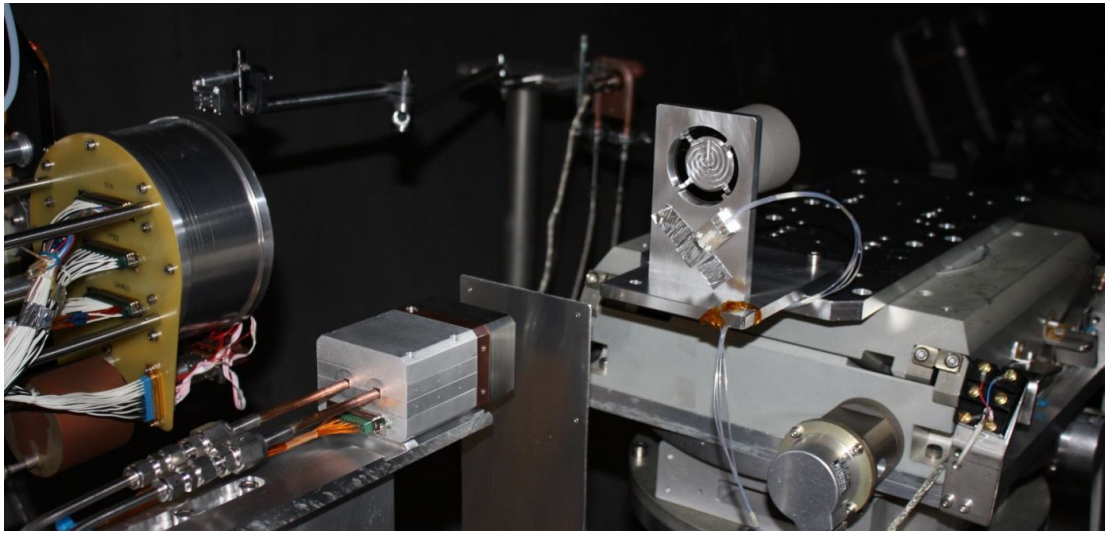


Figure 7.11.: Mirror shell #06 mounted in PANTER (source: Menz et al., 2012).  
The mirror shell (right) and the X-ray cameras (left) are mounted on separate manipulators.

### 7.5.2. Focus Search

After coarse positioning the mirror shell on the manipulator with regard to focus and optical axis the focus can be determined more precisely. The test beam on the end of the 130 m long evacuated tunnel simulates an on-axis point source. Now, the manipulator with the PIXI X-ray camera and the manipulator with the mirror shell are moved relatively so that the point spread function (PSF) of the resulting image is minimum (see fig. 7.12). This way, the focus of the mirror shell #06/01 was determined as  $f_{06/01} = 246 \pm 2 \text{ mm}$ .

### 7.5.3. PSF Measurement

The point spread function (PSF) of a mirror shell is a measure to quantify the ability of the X-ray optics to focus a point source onto a point in the focal plane.

One important parameter of the PSF is the half energy width (HEW). The HEW is determined by the ring integral  $\oint(r)$  as a function of the radius  $r$  in which 50% of the incident energy is detected in the focal plane (top diagram in figs. 7.13 and 7.14). Together with the focal length, the ring integral radius is then converted into an angle measure given in arc seconds or arc minutes. Accordingly, the 90% width (90%W) can be obtained for the radius in which 90% of the intensity is detected.

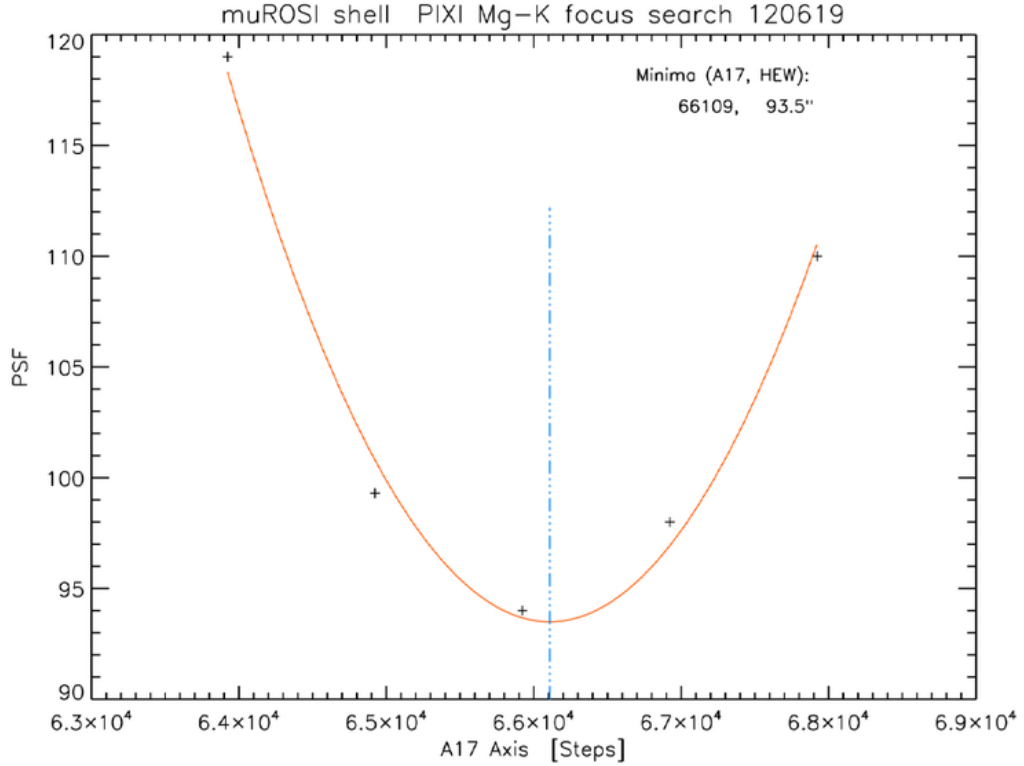


Figure 7.12.:  $\mu$ ROSI mirror shell #06 focus search results (source: Menz et al., 2012).

Another important parameter of the PSF is the scatter fraction  $\psi$ . The scatter fraction is determined using the  $1 - \phi$  intensity diagrams (see bottom diagrams in figs. 7.13 and 7.14). As the  $\phi$  is a measure how much intensity is concentrated within the ring integral radius, the  $1 - \phi$  value is evidence for the intensity that is *not* detected within the radius. It can be therefore used to analyse the scatter fraction. The assumption is that scattering is determined by the surface roughness and that it leads to large deflections. Figure 7.13 reveals that the intensity follows an almost linear trend for radii  $> 1500 \mu m$ . Assuming that this linear trend is due to a constant scattering, the intersection of straight trend line with the vertical axis at  $r = 0$  gives the percentage of scattering.

With the scatter fraction  $\psi$  known, the surface roughness can be estimated using eq. (7.2). With the test results of the mirror shell #06,  $\sigma$  can be calculated only for low energies, i.e. for C-K $_{\alpha}$  spectral line. As the PSF measurements for higher energies were dominated by scattering (and not by reflection), these results

could not be used to deduce the surface roughness.

$$\sigma = \frac{\lambda}{4\pi \alpha} \sqrt{-\ln \left(1 - \frac{\psi}{2}\right)} \quad (7.2)$$

- $\sigma$  [m] Surface roughness
- $\lambda$  [m] Wavelength of the X-ray measurement
- $\alpha$  [rad] Reflection angle
- $\psi$  [1] Scattering fraction

Spectral line	C-K $_{\alpha}$	Mg-K $_{\alpha}$	Al-K $_{\alpha}$
Energy	0.28 keV	1.25 keV	1.49 keV
HEW	698 arcsec	630 arcsec	510 arcsec
90%W	1746 arcsec		
Scatter fraction	14.94%		27.12%
Surface roughness	3 nm		

Table 7.4.: Results of mirror shell #06/01 PSF measurements.

## 7. Mirror Module

---

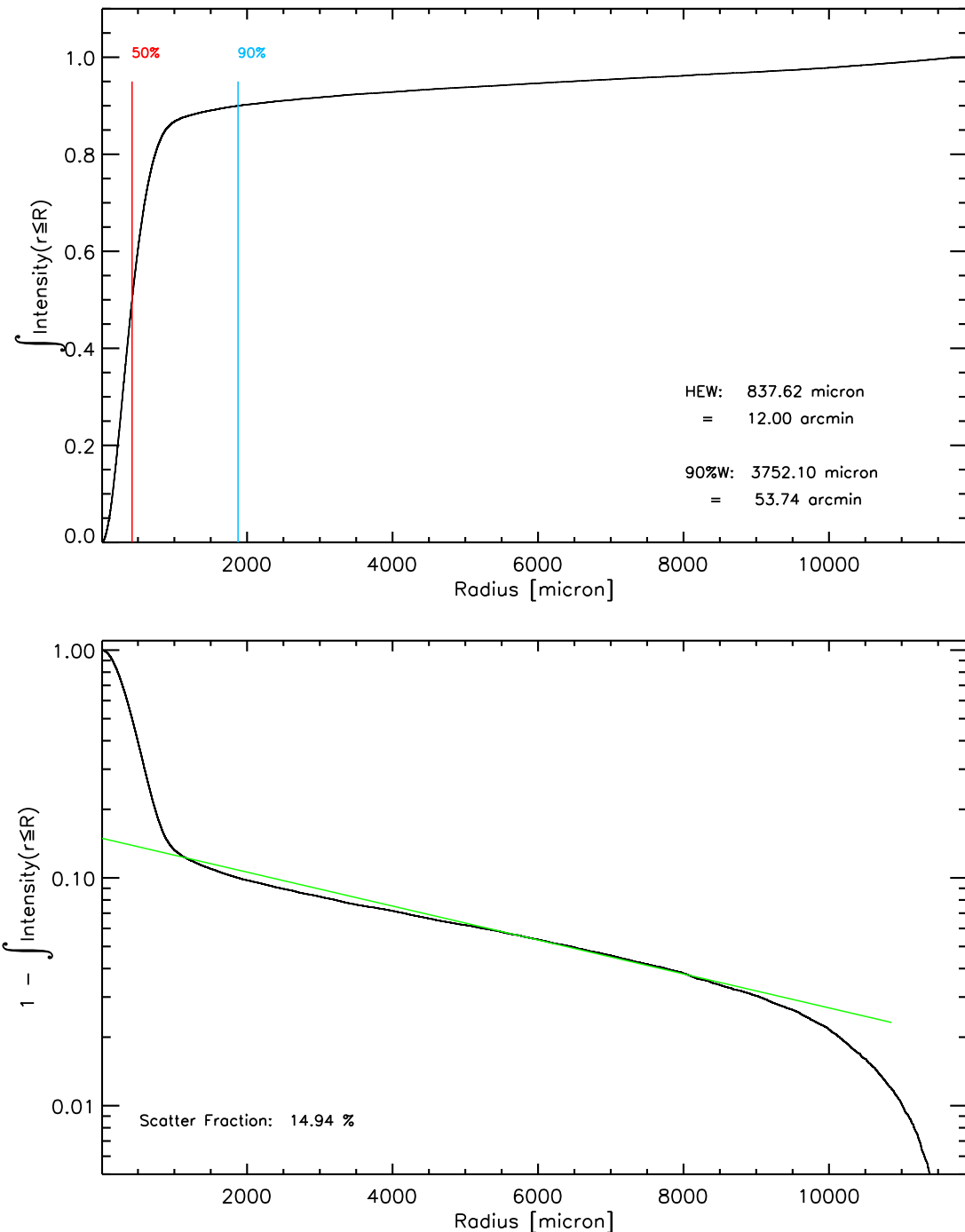


Figure 7.13.: PSF analysis of mirror shell #06/01 at 0.28 keV (C-K $\alpha$ ) (source: Menz et al., 2012).

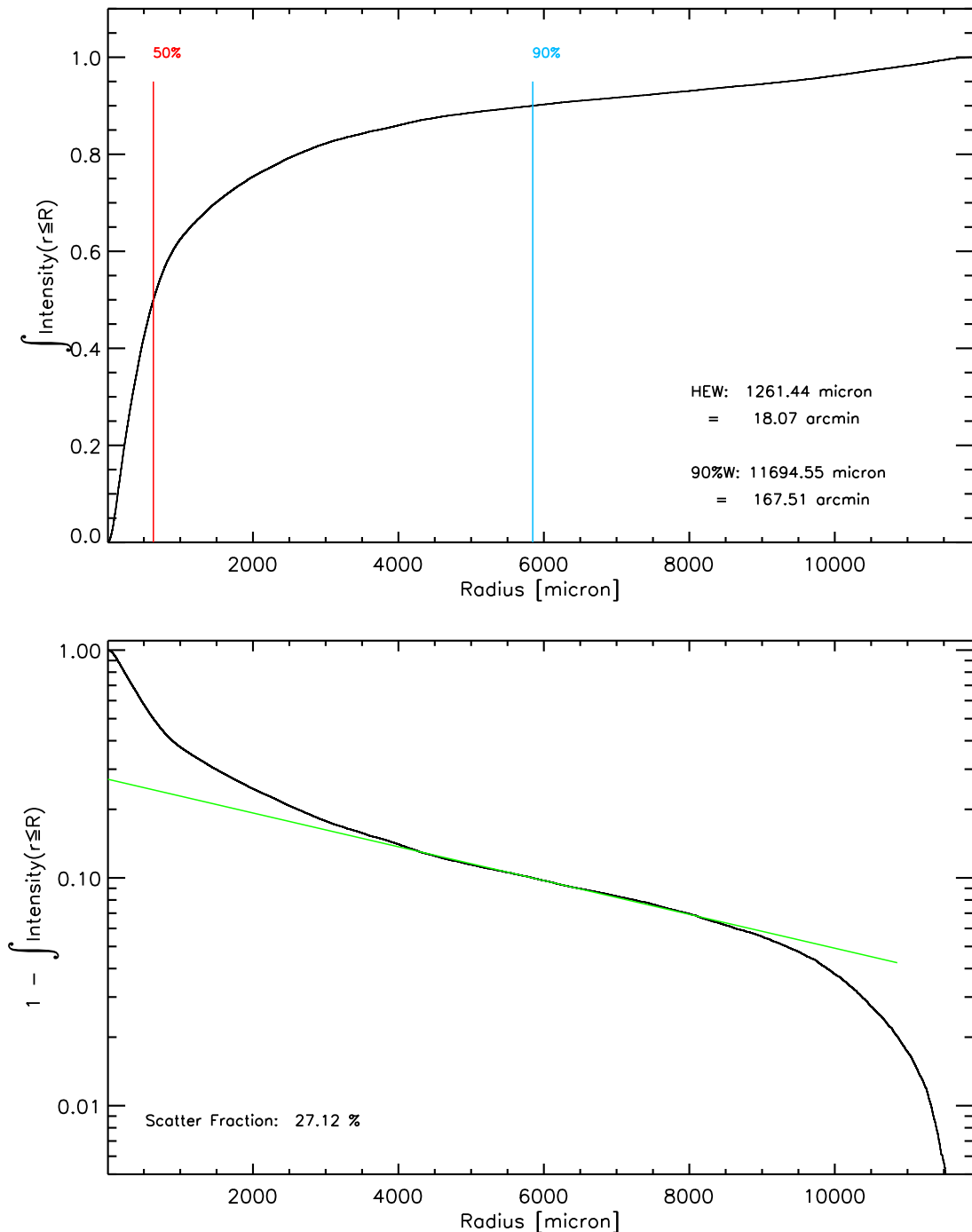


Figure 7.14.: PSF analysis of mirror shell #06/01 at 1.49 keV (Al-K $\alpha$ ) (source: Menz et al., 2012).

#### 7.5.4. Supplementary Ray Tracing Simulation

It is common practice to simulate the X-ray tests with ray tracing software. This helps to fully understand the results and to predict the mirror performance also for energy levels which were not tested.

The first ray tracing simulation was conducted before the X-ray test campaign in the PANTER facility. For this simulation, a surface roughness of 1 nm RMS was assumed. Figures 7.15 and 7.16 show the results of the first simulation (left) next to the PSF measurements (right). The color coding of the measurements represents the intensity, while the colors of the simulation have a different meaning. One major advantage of ray tracing simulations is the knowledge of the path of each individual photon. It is possible to separate photons by origin. Table 7.6 lists the color codings. Green dots in figures 7.15 and 7.16 represent “good” photons that are reflected from paraboloid and hyperboloid. Other photons are “bad” photons that are either single reflections or scattered. Single reflections are deflected by different angles and are therefore not in focus. The result is a characteristic ring artefact. Ray tracing simulations are very important for understanding measurement results, as the distinction of “good” from “bad” photons is not possible for measurements. Another result of the ray tracing simulation is the effective area. Table 7.5 lists the effective area results from ray tracing with an assumed surface roughness of 1 nm RMS.

After the first PSF measurements were conducted with mirror shell #06, the surface roughness was determined more precisely. Figure 7.17 shows a comparison of the simulation with the PSF measurements. The simulation assumed a surface roughness of 3 nm RMS as it was deduced from the C-K $\alpha$  measurements. Simulation and measurement are well consistent. This simulation also takes into account the installation orientation of the mirror shell: the test adapter is rotated by 45.

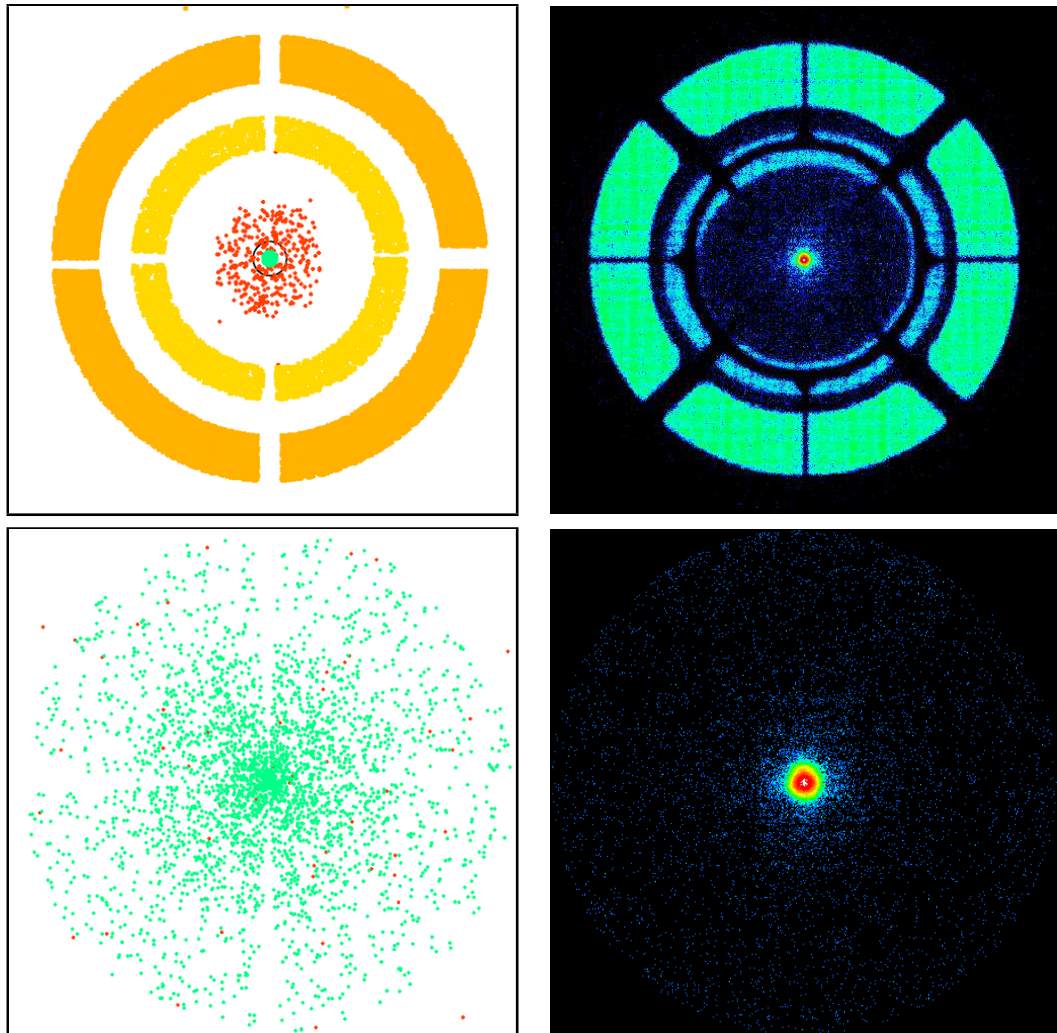


Figure 7.15.: Comparison of ray tracing simulation (left) and PSF measurement of mirror shell #06 at 0.28 keV (C-K $\alpha$ ). The simulation was conducted before measurement with an assumed surface roughness of 1 nm RMS.

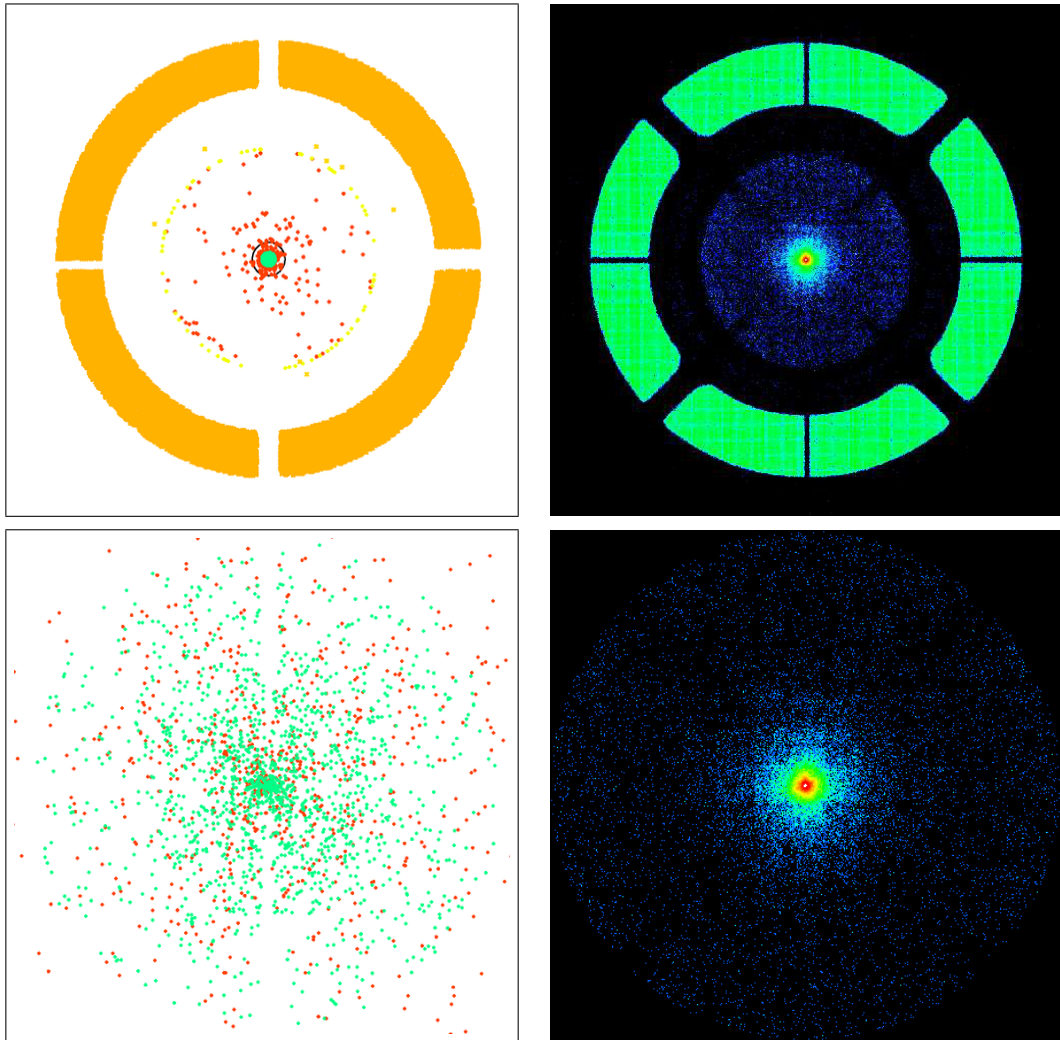


Figure 7.16.: Comparison of ray tracing simulation (left) and PSF measurement of mirror shell #06 at 1.49 keV (Al-K $\alpha$ ). The simulation was conducted before measurement with an assumed surface roughness of 1 nm RMS.

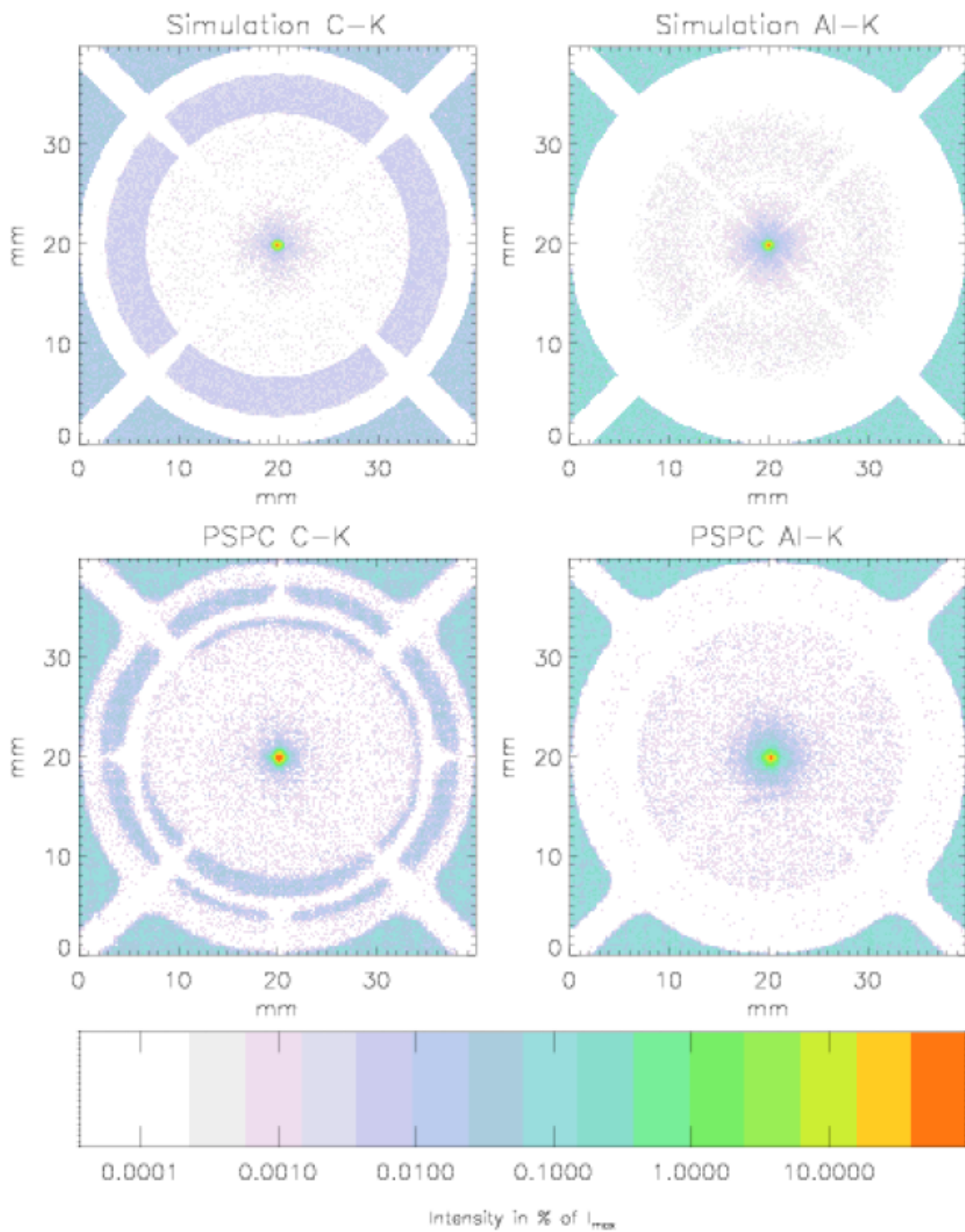


Figure 7.17.: Updated simulation (top) and PSF measurements (bottom) of mirror shell #06 with measured surface roughness of 3 nm RMS.

#	Photon energy [keV]					
	0.28	0.93	1.25	1.49	1.74	2.98
1	125.70	88.83	76.74	48.13	9.18	0.05
2	117.97	89.04	79.70	56.00	16.44	0.07
3	112.22	86.97	80.78	62.93	27.66	0.06
4	106.47	84.26	80.34	67.01	38.55	0.10
5	98.89	80.19	79.36	68.43	47.67	0.19
6	93.67	77.38	76.60	69.82	53.36	0.38
7	88.22	73.69	73.24	67.94	56.97	0.54
8	81.17	69.78	70.69	67.63	58.12	0.92
9	75.80	66.19	66.34	63.66	57.46	1.36
10	70.52	63.33	62.86	60.31	55.83	2.17
11	66.12	57.63	59.00	56.40	54.58	3.44
12	60.18	54.26	54.50	52.89	50.99	4.69
$\Sigma$	1096.91	891.56	860.15	741.16	526.82	13.98

Table 7.5.:  $\mu$ ROSI mirror shell effective areas in [ $mm^2$ ] from ray-tracing simulation calculated with 1nm RMS micro roughness.

Color coding	Description	Angle
Green	Double reflection	$4\alpha$
Dark yellow	Single reflection paraboloid	$2\alpha$
Bright yellow	Single reflection hyperboloid	$6\alpha$
Red	Scattering	

Table 7.6.: Colour codings of ray-tracing simulation results (compare figs. 7.15 and 7.16).

### 7.5.5. Effective Area of Mirror Shell #06

The effective area was determined first by several methods: calculation (section 7.2), simulation (section 7.5.4), and finally by X-ray measurement. Table 7.7 summarises the effective area for selected spectral lines. The measured values for lower energies  $< 0.93 \text{ keV}$  is higher than anticipated by calculation or simulation and is lower for high energies. This result is attributed to the high scatter fraction that was observed for higher energies (27% for  $1.49 \text{ keV}$  compared to 15% for  $0.28 \text{ keV}$ , see figs. 7.13 and 7.14) in the X-ray test. The scattering is also responsible for the relatively large deviation of calculation, simulation and measurements.

	Photon energy [keV]			
	0.28	0.93	1.49	1.74
Calculation	102.39	71.99	63.34	46.96
Simulation	93.67	77.38	69.82	53.36
Measured	98.8	81.5	61.2	39.0

Table 7.7.: Mirror shell #06 effective areas in [ $\text{mm}^2$ ].

### 7.5.6. Results Summary

The test of mirror shell #06 at the PANTER X-ray test facility provided sufficient data to evaluate the mirror shell. The measured focal length (req. 1.1) and HEW (req. 1.11) coincide well with the predictions. However, the PSF measurements show a scattering fraction of 15% at  $0.28 \text{ keV}$  and 27% at  $1.49 \text{ keV}$ . These values are higher than expected and suggest that the surface roughness of the mirror shell is not as low as expected. The scattering is likely responsible for the reduction of effective area, especially at higher energies (compare table 7.7). The fact that the effective area measured at  $0.93 \text{ keV}$  is higher than expected can not easily be explained. However, this is a typical behaviour of the detectors used at the PANTER X-ray test facility at  $0.93 \text{ keV}$  that has been observed many times before (Burwitz and Menz, 2013).

In order to quantify the actual surface roughness of the mirror shell #06, the ray-tracing simulation has been updated with an assumed surface roughness of  $3.0 \text{ nm}$  (fig. 7.17). These simulations are consistent with the measurements. The optical interferometer measurements of the mandrel #06, however, suggested a surface roughness of  $\sim 1.5 \text{ nm}$  (fig. 7.8). The discrepancy in surface roughness has two potential sources:

1. The mandrel surface and the mirror surface do not have the same roughness. This means that the mirror does not one-to-one reproduce the mandrel surface.
2. The measurements of the mandrel (VIS interferometry) and of the mirror (X-ray) yield different results, due to the different wavelength used for both measurements. It is possible that certain effects that are not observable with the VIS measurements are “visible” in X-rays.

A possible way to resolve the aforementioned deviation in surface roughness would be to measure the mirror shell and the mandrel with a profilometer as it is used for characterizing the eROSITA mandrels at Media Lario (Vernani et al., 2011). This instrument is capable of measuring the roundness, the profile accuracy and the surface roughness in 2D and 3D. With a grid of measurement points for the mandrel, ray-tracing simulations become very precise and it is possible to evaluate the surface in the spatial frequency domain. This method potentially reveals surface waves on the mandrel that need to be re-polished.

This diagnosis process is effective, yet time consuming and expensive as it involves many iterations of polishing, optical and X-ray measurements. A more pragmatic solution is to improve the mandrel polishing with the existing measurement methods and this way try to minimize the surface roughness, and, as result, also minimize the reduction in effective area. This would mean that the surface roughness requirement (req. 1.7) has to be revised and additional effort has to put into the mandrel polishing process.

## 7.6. Mirror Shell Integration

For the integration of all 12 mirror shells into the mirror module a special integration facility is required. Its main purpose is to verify the correct co-alignment of all mirror shells and to determine the focal length. After aligning the mirror shell it is then integrated permanently into the support structure, the so-called spider. The design of the mirror module requires an integration order starting with the largest mirror shell #01 down to the smallest #12.

For this purpose, a collimated light beam of  $> \phi 82\text{ mm}$  is needed, as this is the maximum diameter of the largest mirror shell. Parallel light is the only way to simulate a light source with  $\infty$  distance. In fig. 7.18 the working principle of the vertical optical bench (VOB) is shown. The monochromatic laser light source is dispersed and then collimated with optical lenses. Aperture masks are placed in front of the mirror. There are separate aperture masks for the inner and the outer diameter for all 12 mirror shells and each paraboloid and hyperboloid - 48

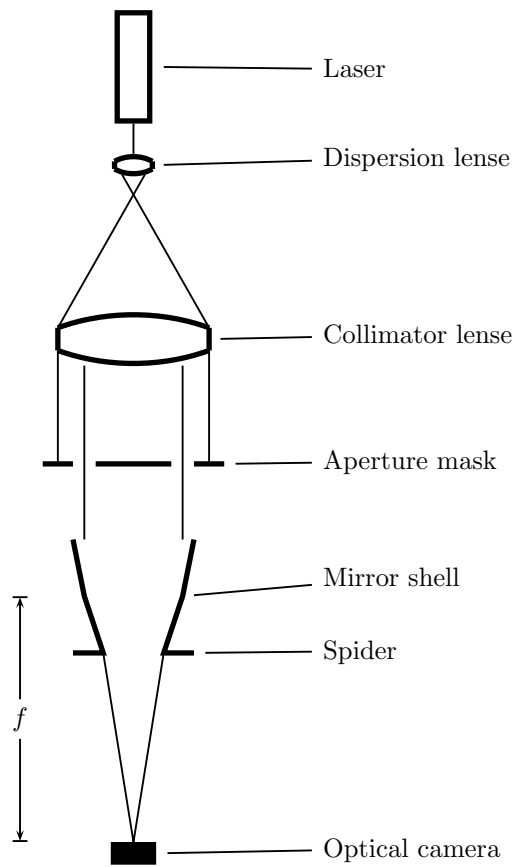


Figure 7.18.: Schematics of  $\mu$ ROSI vertical optical bench (VOB).

masks in total. Combining one mask for the inner diameter and one for the outer diameter, each mirror shell can be illuminated individually or in combination with other neighbouring (already integrated) mirror shells. The optical camera is used to determine the focal length of each mirror shell.



# 8. Structure

## 8.1. Preliminary Design

The structure of μROSI is the linking element between all other subsystems. Its main task is to provide the mechanical interface to the satellite and to maintain the required alignment between the optical components - most importantly between the mirror module and the detector unit. For this reason it is often also referred to as the “optical bench” of the telescope.

During the preliminary design phase (refer to fig. 5.3), the configuration of the telescope and the general dimensions have been determined. Yet, the materials and manufacturing methods as well as the detailed dimensioning were still an open issue. A study thesis conducted by Elias Breunig (Breunig, 2011b) identified the frame plates to which the detector and the mirror are mounted as the design drivers. For these, he elaborated different structural configurations:

- Solid aluminium
- Solid aluminium with milled recesses
- Aluminium sandwich

For the four side panels the options were:

- Solid panel plates
- Milled panels
- Aluminium sandwich panels
- CFRP sandwich panels

The evaluation of these options with regard to mass, ease of manufacturing, precision and costs revealed that the best solution is a structure milled from a solid block of aluminium in one piece (Breunig, 2011b). Although this approach is more expensive and more time consuming to manufacture, it also has several advantages. There are no mechanical interfaces in between any structural parts that need to be designed and tested individually. And, more importantly, the

interfaces for the mirror module and the detector assembly are co-aligned with machine precision. No additional alignment procedure is required. The monolithic aluminium structure with its good thermal conductivity also guarantees low thermal gradients over the whole telescope.

## 8.2. Structural Qualification Model (SQM)

For the structural qualification model (SQM), the findings of the preliminary design was used and a detailed design with mass dummies for all other telescope components was created. The design was thoroughly analyzed using FEM software. Finally, the SQM was subjected to vibration testing with good results (Breunig, 2011b). The vibration test proved that the structural design was capable to fulfill all mechanical requirements, particularly req. 3.2.

The mechanical loads applied on the SQM during vibration testing were derived from the PSLV (the Indian *Polar Satellite Launch Vehicle*) input spectrum (see table 8.2). This launcher was at that time the designated launch vehicle for the Max-Valier Satellite.

Test	Load	Frequency	Duration
Sinus low level	0.5 g	5 ... 2000 Hz	2 Oct/min
Sinus load run	3.75 g	5 ... 100 Hz	2 Oct/min
Sinus low level	0.5 g	5 ... 2000 Hz	2 Oct/min
Random low level	1.69 g RMS	see table 8.2	1 min
Random load run	6.71 g RMS	see table 8.2	2 min
Sinus low level	0.5 g	5 ... 2000 Hz	2 Oct/min
Shock	+50 g		10 ms
Shock	-50 g		10 ms
Sinus low level	0.5 g	5 ... 2000 Hz	2 Oct/min

Table 8.1.: SQM vibration test program.

Figure 8.2 shows a comparison of the frequency response measured during SQM vibration testing and the prediction of the FEM model. The curve shows the response of the SQM mirror module in Y-direction. The plot shows that the measurements are in good correlation with the predictions.

With successful completion of the vibration test, the basic design of the structure was verified. However, Breunig mentioned two structure related issues that

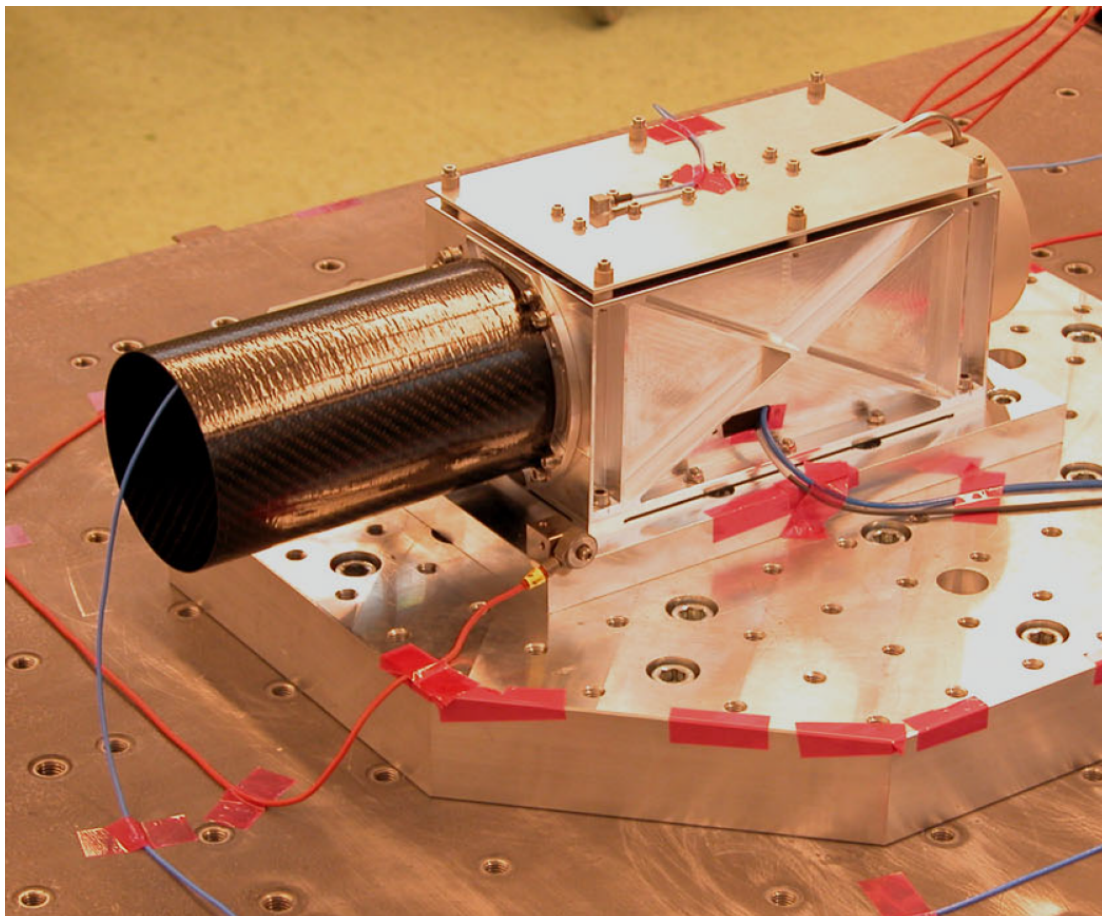


Figure 8.1.: The  $\mu$ ROSI SQM model on the shaker during vibration testing. The model and the test adapter are equipped with various accelerometers.

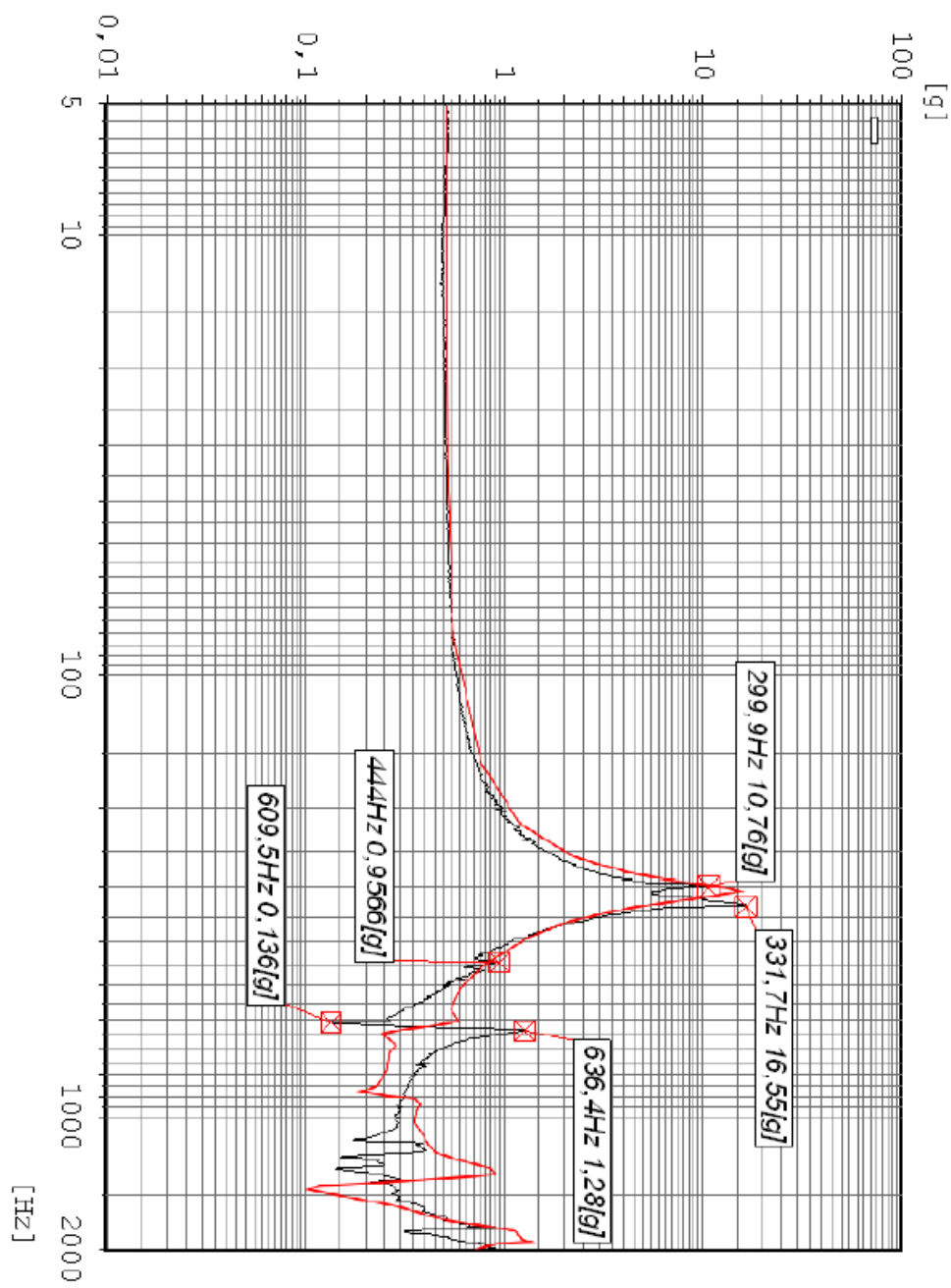


Figure 8.2.: Comparison of simulation (red) and measured (black) frequency response of SQM mirror module mass dummy (source: Breunig, 2011b).

Frequency [Hz]	Load run [ $g^2/Hz$ ]	Low level [ $g^2/Hz$ ]
20	0.002	$1.26 \cdot 10^{-4}$
110	0.002	$1.26 \cdot 10^{-4}$
250	0.034	$2.15 \cdot 10^{-3}$
1000	0.034	$2.15 \cdot 10^{-3}$
2000	0.009	$5.69 \cdot 10^{-4}$

Table 8.2.: PSLV random vibration input spectrum used for SQM testing, duration: 120 s.

should be resolved:

- Review of interface screws between the  $\mu$ ROSI telescope and the satellite
- Rework of the mechanical interface to electronics PCB

The review of the interface screws is a recommendation that is based on the screw stability analysis conducted by Breunig. The analysis revealed that the four M5 A2-70 stainless steel screws have a small margin of safety, so that the interface to the satellite might not have sufficient contact pressure to maintain a friction fit connection against shear stress. This suspicion could not be proven with the vibration test and a review of the screw analysis revealed that very conservative assumptions were made, i.e. pessimistic thread friction coefficients and shear stresses were applied to only one screw instead of all four. Nevertheless, the issue was addressed by using helicoil thread inserts to reduce thread friction and replacing the stainless steel screws with high strength titanium screws to allow for higher screw torque and, thus, for higher contact pre-tension. Additionally, the screws are equipped with spring washers. The spring washers provide force to the screw head to prevent loosening.

The mechanical interface of the PCB has been reworked completely. The problem was that the PCB was mounted to the cover of the optical bench - a relatively thin aluminium plate that is screwed to the optical bench to gain access to the inside of the optical bench. The resonance frequency of the cover and the PCB were too close to each other, so that an interference of frequencies could possibly yield too high loads on the PCB during launch or vibration testing. However, a rework of the PCB interface was not only necessary from a mechanical point of view, but also for reasons of electromagnetic compatibility. The power supply

section of the electronics was removed from the PCB to a separate power supply board. With two PCB boards on board  $\mu$ ROSI instead of one, the mechanical interface also needed to be changed. The solution was to mount the boards to the inside of the optical bench on the two opposing sides. The side walls are very stiff and provide a solid basis for mounting the PCBs. The side walls only needed some additional screw threads and the PCB required some standoffs.

With these modifications, the final design of the structure was complete.

### 8.3. Final Design Description

The final design of the  $\mu$ ROSI structure is almost identical to the SQM model (see section 8.2). The mechanical interface to the satellite consists of four M5 screws in a rectangular  $197 \times 113\text{ mm}$  pattern. The interface for the mirror module and the detector assembly are very similar. Both have four M4 threads in a circular pattern and two alignment pins to precisely mount the mirror and the detector. As the structure is milled from solid aluminium, both interfaces are co-aligned with machine precision.

The bottom side that is facing the satellite is closed by a cover plate. Removing the cover plate allows for accessing the interior of the optical bench where the electronics PCBs are mounted.

All aluminium parts are yellow chromated. Hard anodizing was deemed unfavourable as it makes the metal surface electrically isolating. Yellow chromated aluminium parts are electrically conductive which is required for electrical grounding of all parts.

Another change to the SQM model has been made for the attachment of the cover and the radiator. In the SQM model these attachments were through holes with screw and nut. Now there are threads cut into the structure. All threads of size M4 or larger are reinforced with Helicoil<sup>1</sup> bronze thread inserts. These inserts have the advantage of increasing the effective diameter of the thread and thus reducing the resulting pressure in the surrounding material. The bronze material has the advantage of reducing friction and wear on the thread surfaces, especially when used in aluminium with stainless steel screws. The Helicoils used in this project are not self-locking.

---

<sup>1</sup>*Helicoil* is a trade name for a range of commercially available thread inserts distributed by the company Böllhoff <http://www.boellhoff.com>

## 8.4. Summary

The performed SQM vibration test showed that the structure is capable of providing the mechanical stability as required in req. 3.2 under static, sinusoidal, random vibration and shock loads. Thermal loads and insulation (req. 3.5) are tested in a thermal cycling test, which is planned within the scope of the qualification programme performed with the telescope QM model. The design changes between the SQM and the telescope final design have been made ensuring the validity of the SQM test. No masses were added to any components and the design has been changed with care in order not to reduce mechanical stiffness.

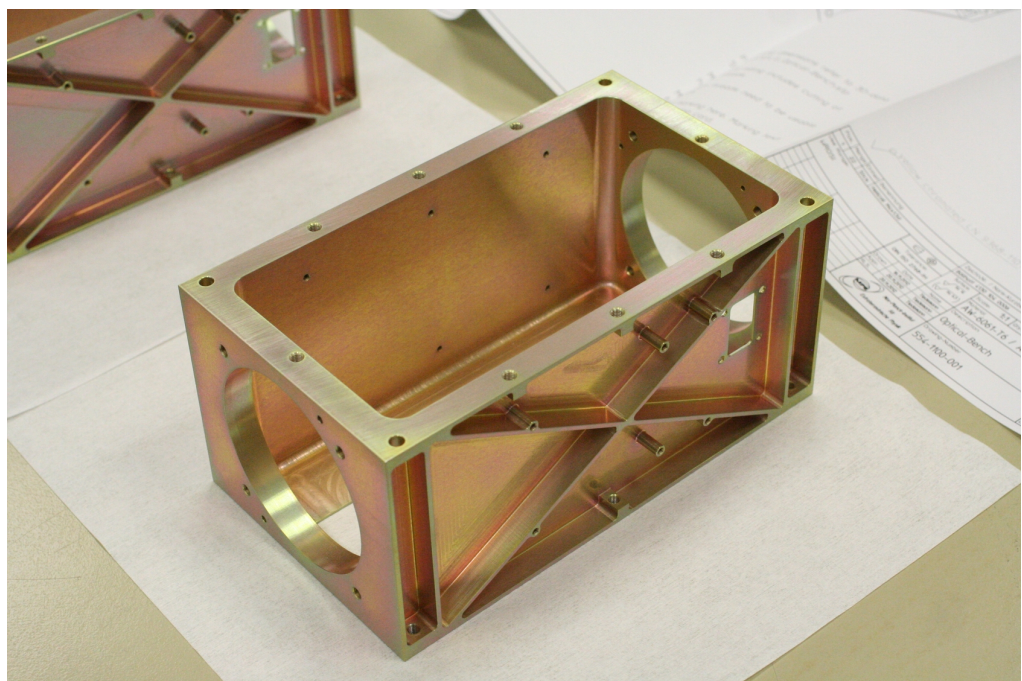
The mass requirements (reqs. 3.6 and 3.7) have been analysed using the CAD 3D-model of the telescope. The masses of the mass dummies used in the SQM have been designed with sufficient margin. However, the margin was not necessary as the final design mass is  $2.5\text{ kg}$ , which is well below the required  $3.0\text{ kg}$ . The center of gravity and moments of inertia have been communicated to GOB/OHB for the development and testing of the spacecraft attitude control system. After vibrating the SQM, the model was shipped to GOB for fit checks with the satellite structure.

The detailed design of the structure has been checked in a design review which concluded that all design requirements (requirements marked with “D”, reqs. 3.1, 3.3 and 3.4) are fulfilled. The mechanical interfaces (req. 3.1) are documented in the manufacturing drawing and tolerated according to their needs. The co-alignment of the mirror module and the detector module mounted on opposite sides of the structure is ensured by dowel bolts to meet req. 3.3. The position tolerance of these bolts is very low ( $< 0.02\text{ mm}$ ) and depends only on the machine precision of the milling machine. An additional adapter ring between the mirror module and the structure allows to adjust the focal length, if this should be required (see section 4.1.5 for an explanation, why the focus is not very precise).

The interface to the satellite has been reviewed in more detail (see p. 113). The design change included replacing the stainless steel screws by titanium screws of the same size and adding spring washers to increase the contact pressure. The applied changes have been accepted without further testing, since the vibration test already has been successful. The structure also provides an opening for the electric cable feedthrough (req. 3.4).

## *8. Structure*

---



(a) Optical bench



(b) Cover

Figure 8.3.: The muROSI optical bench and cover after yellow chromating.

# 9. Thermal Control Subsystem

## 9.1. Thermal Requirements

The μROSI Thermal Control Subsystem (TCS) manages the temperatures of all telescope components. The main task is to maintain the temperatures in the specified limits.

Component	Operating		Non-operating	
	min	max	min	max
Structure	+10	+35	-100	+80
Mirror Module	+10	+35	+10	+35
Detector	-18	-14	-40	+50
Electronics	+15	+35	-40	+50

Table 9.1.: Temperature limits of μROSI components.

## 9.2. TCS Design Description

The most critical components in the telescope when it comes to temperatures are the detector and the mirror. The components of the thermal control subsystem are:

- Radiator
- Heat pipe
- Latent cold storage
- Multi-layer insulation foil
- Heaters
- Temperature sensors PT-100

## *9. Thermal Control Subsystem*

---

The detector requires low, very stable temperatures to achieve best spectral resolution. The detector is therefore cooled passively with a dedicated radiator. The radiator is mounted on the optical bench with thermal insulating spacers. The outward surface is painted white, the inward surface is covered with multi-layer-insulation (MLI) foil.

Heat is transported to the radiator via a constant conductance heat pipe. The heat pipe tube is an extruded aluminium profile with grooves. The profile was developed by the MPE for the eROSITA camera cooling system (Fürmetz, 2012). Several heat pipes have already been manufactured and tested at the MPE during the eROSITA qualification campaign. However, using the same heat pipe profile for  $\mu$ ROSI and flying the heat pipe in space would again raise the technological readiness of this product before the eROSITA telescope is launched. Thus, the small miniature X-ray telescope serves as a technology demonstrator for the full-size eROSITA telescope.

A latent cold storage (LCS) provides the thermal/mechanical interface between the heat pipe and the detector to provide the necessary temperature stability at the detector while the radiator temperature changes during the spacecraft orbit. A heater is applied on the LCS to prevent the PCM from complete freezing.

The mirror is subject to thermal stress and deformation with its high view factor to the cold space background. One resistive heater is applied on the mirror interface structure to heat the mirror shells in case the temperature is too low.

Figure 9.1 shows an explosion view of the  $\mu$ ROSI TCS subsystem. The LCS is a cylindric container that is mounted to the optical bench with a thermal insulator. It provides a screw interface for the detector assembly. The bent heat pipe connects the LCS thermally to the radiator. The radiator has a cut-out to allow the heat pipe to over-shoot. This is necessary to bypass the optical bench structure (not shown in fig. 9.1). In this configuration the  $\mu$ ROSI TCS can be completely assembled and tested including the detector assembly, if required. For testing, the whole assembly can be tilted so that the bended heat pipe can be tested horizontally to avoid gravitational effects within the heat pipe.

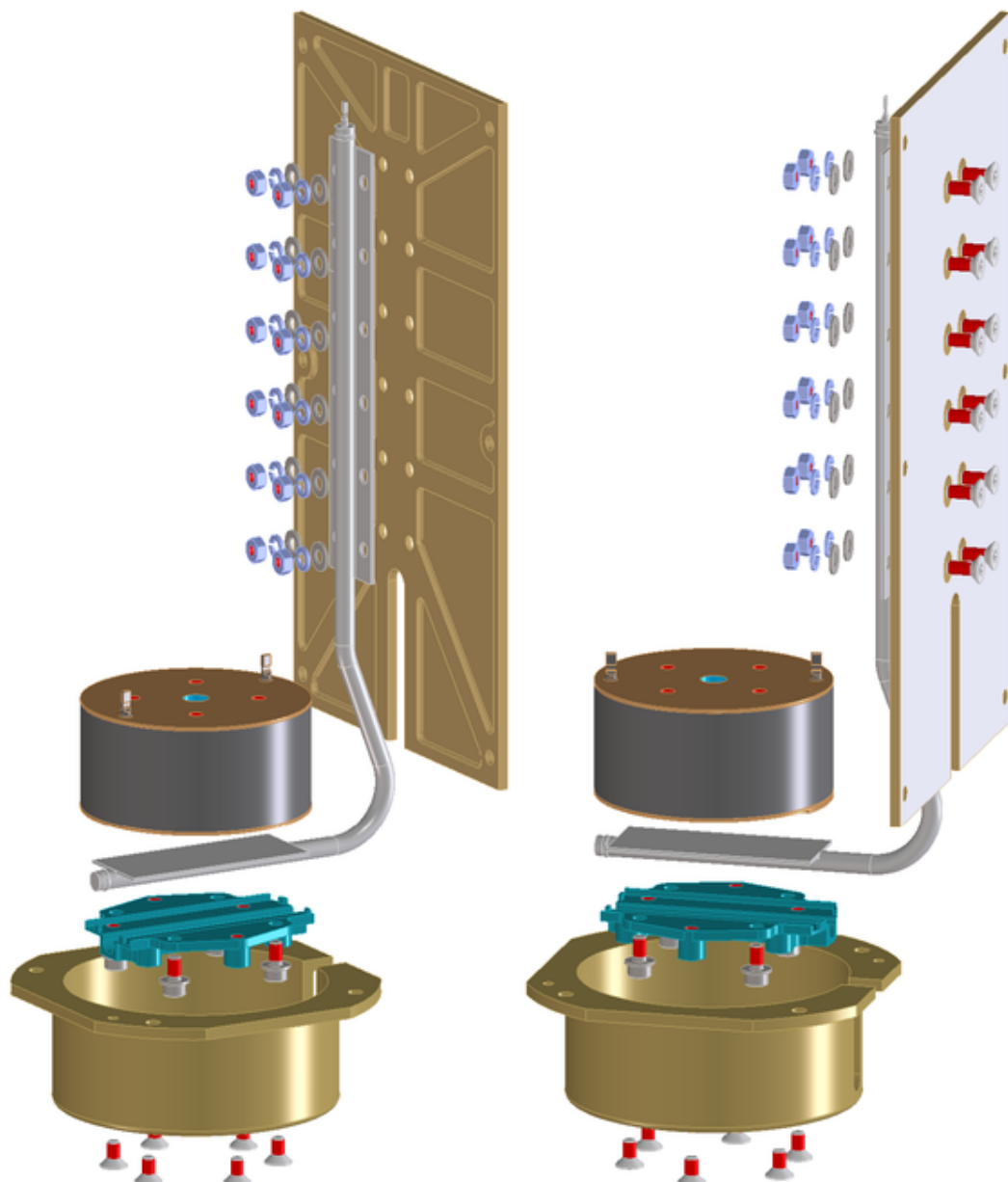


Figure 9.1.: Explosion view of the μROSI thermal control subsystem.

## 9.3. Latent Cold Storage (LCS)

### 9.3.1. Storing Heat

A latent heat storage is basically a container filled with a phase change material (PCM) that has a phase change at the desired stable temperature (see fig. 9.2). Excessive heat can be stored using the latent heat of fusion  $\Delta H$  during a phase change from liquid to solid at temperature  $T_S$ . The material used in a LCS is called a *phase change material* (PCM). During the phase change the temperature remains constant until the material has completely changed its state. And the stored energy then is:

$$Q_S = m_{PCM} \cdot \Delta H \quad (9.1)$$

$T_S$	[K]	Phase change temperature
$Q_S$	[kJ]	Stored energy
$\Delta H$	$\left[ \frac{kJ}{kg} \right]$	Latent heat of fusion
$m_{PCM}$	[kg]	PCM mass

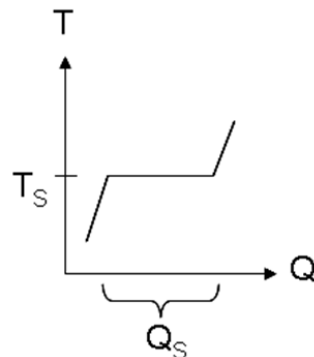


Figure 9.2.: Temperature-heat diagram during phase change.

Latent heat storages are widely used in space applications with operating temperatures typically ranging from  $+20^{\circ}\text{C}$  to  $+50^{\circ}\text{C}$ . Typical PCMs for these temperatures are:

- Paraffins
- Salts
- Fatty acids

In 2008 a concept for a cooling system for the eROSITA cameras at  $-80^{\circ}\text{C}$  was published at the ICES conference in San Francisco (see Fürmetz et al., 2008; Tiedemann et al., 2008) which included a *latent cold storage* (LCS)<sup>1</sup>. At that time eROSITA was still planned as a LEO mission. This implied high temperature changes at the radiators while the camera temperature was required to be stable within  $\pm 0.5^{\circ}\text{C}$ . The  $\mu\text{ROSI}$  telescope was intended as a technology demonstrator for a low temperature LCS. Meanwhile, the eROSITA mission is scheduled for a flight to Lagrangian point L2 some  $1.5 \cdot 10^6 \text{ km}$  from Earth opposite from the Sun. With no Earth albedo radiation and very stable thermal conditions the LCS concept is obsolete.

However, for any LEO mission with high temperature differences due to Earth shadow, albedo and direct Sun exposure on the one hand, and stable low temperature requirements on the other hand, latent cold storages might be the thermal component of choice. The advantages are stunning:

- **Temperature stability**

Temperature stability of  $T_S \pm 0.5^{\circ}\text{C}$  are feasible.

- **No power**

A LCS requires no electrical power to maintain a stable temperature.

- **Scalability**

The stored thermal energy is proportional to the PCM mass.

- **Reversibility**

The phase change is 100% reversible without degradation.

- **Unlimited lifetime**

Low leak rates provided, the lifetime of a LCS is practically unlimited.

The silicon drift detector used for  $\mu\text{ROSI}$  also requires stable, low temperatures in order to achieve a good spectral resolution. And, as the available power on board a micro satellite is always a rare asset, it was decided to design the  $\mu\text{ROSI}$  telescope with a LCS cooling system.

---

<sup>1</sup>The term *latent cold storage* is physically not quite correct. To be precise, it should be named *latent heat storage*. But, as the operating temperature of this specific device is below  $0^{\circ}\text{C}$ , it is more intuitive to speak of a *latent cold storage*.

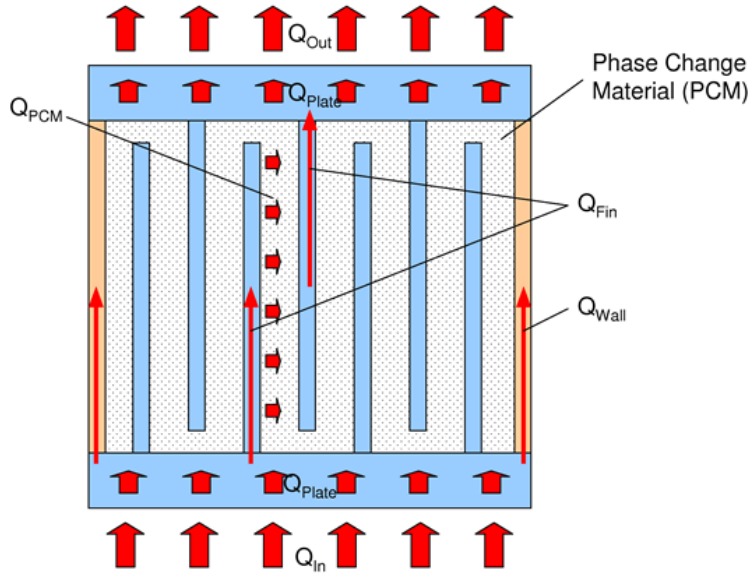


Figure 9.3.: Schematics of heat fluxes in a latent cold storage.

### 9.3.2. LCS Design

A good LCS Design should satisfy the following requirements:

- Vacuum-tight PCM containment with low leak rates
- High internal volume
- Low heat losses
- Two separate mechanical interfaces
- Minimum thermal conduction between mechanical interfaces
- Maximum heat exchange between mechanical interfaces and PCM

The demand for low losses and high internal volume would suggest a spherical shape. A sphere always has the lowest surface area per unit volume. But realizing a mechanical interface on a sphere is rather difficult, so that a cylindrical shape seems to be the best compromise.

Figure 9.3 shows the heat fluxes in a LCS container. To achieve good thermal conduction between the flat interface surfaces and the PCM, fins protrude from the top and bottom. Heat flux through the cylinder wall  $Q_{wall}$  should be minimized to improve the heat exchange between the interface plates and the PCM.

This can be achieved by reducing the wall thickness or increasing the cylinder length.

The width and height of the fins should be designed to *not* inhibit thermal conduction. A baseline for this criteria can be formulated by relating the heat flux through the fin  $\dot{Q}_{Fin}$  and the heat flux through the PCM  $\dot{Q}_{PCM}$  and introducing a margin of safety  $MS \geq 0$ .

$$\frac{\dot{Q}_{PCM}}{\dot{Q}_{Fin}} = MS + 1 \geq 1 \quad (9.2)$$

For space applications, natural convection effects in the heat transfer between fin and PCM can be neglected. With the thermal conductivities  $\lambda_{Fin}$  and  $\lambda_{PCM}$  of the fin material and the PCM respectively,  $\dot{Q}_{Fin}$  and  $\dot{Q}_{PCM}$  can be calculated as follows:

$$\dot{Q}_{Fin} = \lambda_{Fin} \frac{w \cdot l}{h} \Delta T \quad (9.3)$$

$$\dot{Q}_{PCM} = \lambda_{PCM} \frac{h \cdot l}{s} \Delta T \quad (9.4)$$

where  $h$  is the fin height,  $w$  is the fin width,  $l$  is the fin length and  $s$  is the spacing between one pair of opposing fins. Inserting the equations above into eq. (9.2) yields a first estimate for fin sizing:

$$\frac{h}{w} = \sqrt{(MS + 1) \frac{\lambda_{Fin} \cdot s}{\lambda_{PCM} \cdot w}} \quad (9.5)$$

Figure 9.4 shows the main parts of the first latent cold storage prototype made from aluminium AlMgSi1. The plates and fins were milled in a single piece to achieve optimum thermal conductivity. The  $\varnothing 100 \text{ mm}$  cylinder wall is only  $1 \text{ mm}$  thick and was welded to the plates. Threaded through holes in one plate could be used for filling and venting. Screw caps with teflon PTFE washers were used for sealing the filling holes. This way, different PCMs could be tested easily. The LCS was equipped with heaters and temperature sensors.



Figure 9.4.: First LCS container prototype before welding.

### 9.3.3. Selecting and Testing the PCM

Any PCM for use in a latent heat storage has a long list of requirements to fulfill:

- **Melting temperature**

The melting temperature  $T_S$  of the PCM should be compliant with thermal control subsystem requirements.

- **High latent heat of fusion**

$\Delta H$  should be high to keep the required PCM mass  $m_{PCM}$  low (eq. (9.1)).

- **Good thermal conductivity**

The thermal conductivity  $\lambda_{PCM}$  should be high for good temperature exchange and quick response.

- **High nucleation rate**

High nucleation rate means quick initial freezing without the need for supercooling below  $T_S$ .

- **Complete reversibility**

Freezing and melting shall be reversible over many cycles without degradation of  $T_S$  or  $Q_S$ .

- **Chemical stability**

The PCM shall be chemically stable in space environment (e.g. no polymerization due to radiation).

- **Non-hazardous**

The PCM shall be easy and safe to handle (e.g. non-toxic, non-flammable, non-explosive).

- **Material compatibility**

The PCM shall be compatible with the container material (i.e. non-corrosive, non-reactive).

The required melting temperature of  $-15^{\circ}\text{C}$  limited the choice of possible PCMs dramatically. The only promising candidate with a suitable melting temperature is 1-Octanol. Other possible materials would require changes in the latent cold storage working temperature. Thus, 1-Octanol would be the first choice if it proves the other requirements can be met as well. A strong emphasis is on testing the material for its planned purpose, which means testing it with a latent cold storage in the laboratory and verifying its properties and good freezing/melting properties.

Figure 9.5 shows the test setup with  $\mu$ ROSI LCS laboratory version. The LCS is mounted onto a cold plate which is cooled with a stirling cooler (not visible). On top of the LCS are two temperature sensors PT-100 and a resistive heater. The LCS is wrapped with MLI before closing the vacuum chamber to minimize parasitic temperature losses due to radiation. The mean PCM temperature is the arithmetic mean of top and bottom LCS plate temperatures due to the symmetric thermal conductivities.

The PCM was deemed suitable if the melting temperature could be verified and the material showed the expected behavior. The heating curve should ideally resemble the plot in fig. 9.2.

Evaluation step	Cooler	Heater	Temperature
Initial cooling	const.	off	gradual decline
Freezing	const.	off	discontinuity
Melting	off	const.	discontinuity
Phase Transition	varying	varying	const.

Table 9.2.: PCM evaluation plan and expected behaviour of suitable PCM.



Figure 9.5.: PCM test setup in vacuum chamber with LCS laboratory version.

The LCS is mounted onto a cold plate which is cooled with a stirling cooler (not visible). On top of the LCS are two temperature sensors PT-100 and a resistive heater.

The latent heat of fusion  $\Delta H$  can be measured by completely freezing the PCM and heating the LCS with constant heater power  $P$ . The time required to completely melt the PCM times the heater power then equals  $\Delta H$ .

Figure 9.6 shows the freezing of 1-Octanol with the test configuration as shown in fig. 9.5. The PCM is initially melted and cooled by the stirling cooler. The freezing process starts where the LCS temperature shows a small local minimum. The temperature of this local minimum is slightly below the nominal phase change temperature. Once the freezing process starts, the temperature recovers to the melting temperature and remains almost constant until the material is completely frozen.

This hysteresis effect is widely known as supercooling. It is a common behaviour for most pure substances (Sharma and Sagara, 2005). The hysteresis in the temperature curve can be used to determine precisely the point of initial freezing. The supercooling temperature is approximately  $-1.3^{\circ}\text{C}$ , which is suf-

### 9.3. Latent Cold Storage (LCS)

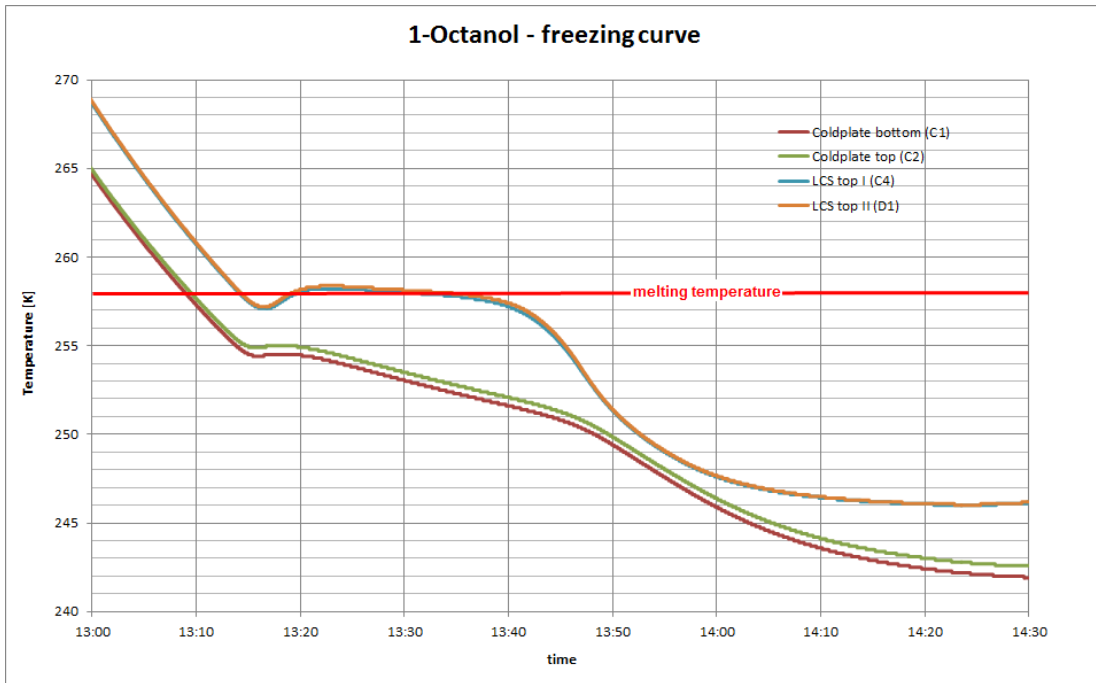


Figure 9.6.: Freezing curve of 1-Octanol.

ficiently low for the  $\mu$ ROSI LCS performance. During the freezing process the temperature remains stable within 1 °C. In summary, 1-Octanol is chosen as the phase change material in the  $\mu$ ROSI thermal control subsystem. The following tables 9.3 and 9.4 list the physical properties of 1-Octanol.

Property	Symbol	Value
Chemical formula		C <sub>8</sub> H <sub>18</sub> O
Melting temperature	$T_m$	258 K <sup>(a)</sup>
Molar mass	$M$	130.23 $\frac{g}{mol}$ <sup>(b)</sup>
Latent heat of fusion	$\Delta H$	25.13 $\frac{kJ}{mol}$ <sup>(c)</sup>
Density	$\rho$	830 $\frac{kg}{m^3}$ <sup>(b)</sup>

Table 9.3.: Properties of 1-Octanol. <sup>(a)</sup> measured data, <sup>(b)</sup> Wikipedia, <sup>(c)</sup> (source: van Miltenburg et al., 2003).

$T$ [K]	$c_{p,s}$ $\left[\frac{J}{mol \ K}\right]$	$T$ [K]	$c_{p,l}$ $\left[\frac{J}{mol \ K}\right]$
170	147.0	258	274.9
180	152.9	260	276.0
190	158.8	270	283.0
200	165.1	280	290.6
210	171.7	290	300.0
220	178.1	298	308.1
230	184.6	300	310.1
240	191.1	310	320.6
250	197.6	320	331.9
258	203.1	330	343.5

Table 9.4.: Heat capacities of 1-Octanol  $c_{p,s}$  for the solid phase and  $c_{p,l}$  for the liquid phase (data from: van Miltenburg et al., 2003).

## 9.4. Radiator

The purpose of the radiator is to provide a heat sink for the detector cooling system. It is connected to the LCS by a constant conductance heat pipe (see section 9.5). The radiator is mounted to the optical bench on six thermally insulating PEEK bushings on the side opposite of the satellite interface. The heat pipe is mounted on its back side, facing the optical bench. The outward surface is coated with white paint MAP SG121FD. It has a good  $\alpha/\varepsilon$  value while providing less absorption than black paint. These optical properties ensure that the radiator temperature remains below 30 °C even if the radiator was exposed to direct Sunlight.

Property	Value
Surface area	266 cm <sup>2</sup>
$\alpha$	0.2
$\varepsilon$	0.88
Average thickness	2 mm

Table 9.5.: Radiator properties.

### 9.4.1. Radiator Optimization

The radiator back side has milled recesses to reduce the mass of the radiator while providing good mechanical stiffness. In the preliminary design the radiator had a constant thickness of 2 mm. For the final design a benchmark analysis of the radiator panel without the mounted heat pipe was conducted. The goal of this benchmark was to find a geometry for the recesses that provides a smooth temperature distribution comparable to the constant thickness design, with roughly the same mass, but with higher mechanical stiffness to vibration loads.

Table 9.6 gives a brief summary of the results of the benchmark analysis. Two design iterations were completed, but only the first and the final analysis results are shown here. The overall thickness of the radiator increased by 50% while the mass was raised only by 4 g (j2.8%) due to the milled recesses.

To evaluate the temperature distribution across the radiator surface, both designs were subjected to the same thermal loads. The average temperature across the radiator surface changed only by 0.5 °C from the preliminary version to the final version. Figures 9.7a and 9.7b show the temperature distribution with isother-

## 9. Thermal Control Subsystem

---

mal lines. Both distributions show similar patterns with a maximum temperature difference of  $< 1^\circ\text{C}$  across the radiator surface for both designs.

An eigenfrequency analysis was conducted to compare the dynamic behaviour of both designs. Figures 9.7c and 9.7f show the first two modes of the initial design and the final design respectively. The first eigenfrequency of the final design is 650 Hz compared to 543 Hz for the initial design, which is an increase by 20%. Similarly, the second eigenfrequency of the final design is 22% higher than the initial design. Eigenmodes 1 and 2 contribute to  $> 70\%$  of the effective masses. This percentage remains constant for both preliminary and final design (see figures 9.7g and 9.7h). The effective mass fraction of the second eigenmode could nonetheless be reduced to  $< 6\%$ . This means that for the final design less than 6% of the radiator mass which means only about 9 g of material contribute to the second eigenmode. In effect, the number of critical eigenmodes with a mass fraction of  $> 10\%$  could be reduced to one.

	Preliminary design	Final design
Thickness	2 mm	3 mm
Recesses	no	yes
Mass	139 g	143 g
Mean temperature	$-32.2^\circ\text{C}$	$-31.7^\circ\text{C}$
Heat pipe influx	1.7 W	1.7 W
Structure heat influx	1.0 W	1.0 W
Eigenmodes $> 10\%$	54% / 543 Hz 19% / 619 Hz	66% / 650 Hz 6% / 754 Hz

Table 9.6.: Results of radiator benchmark analysis.

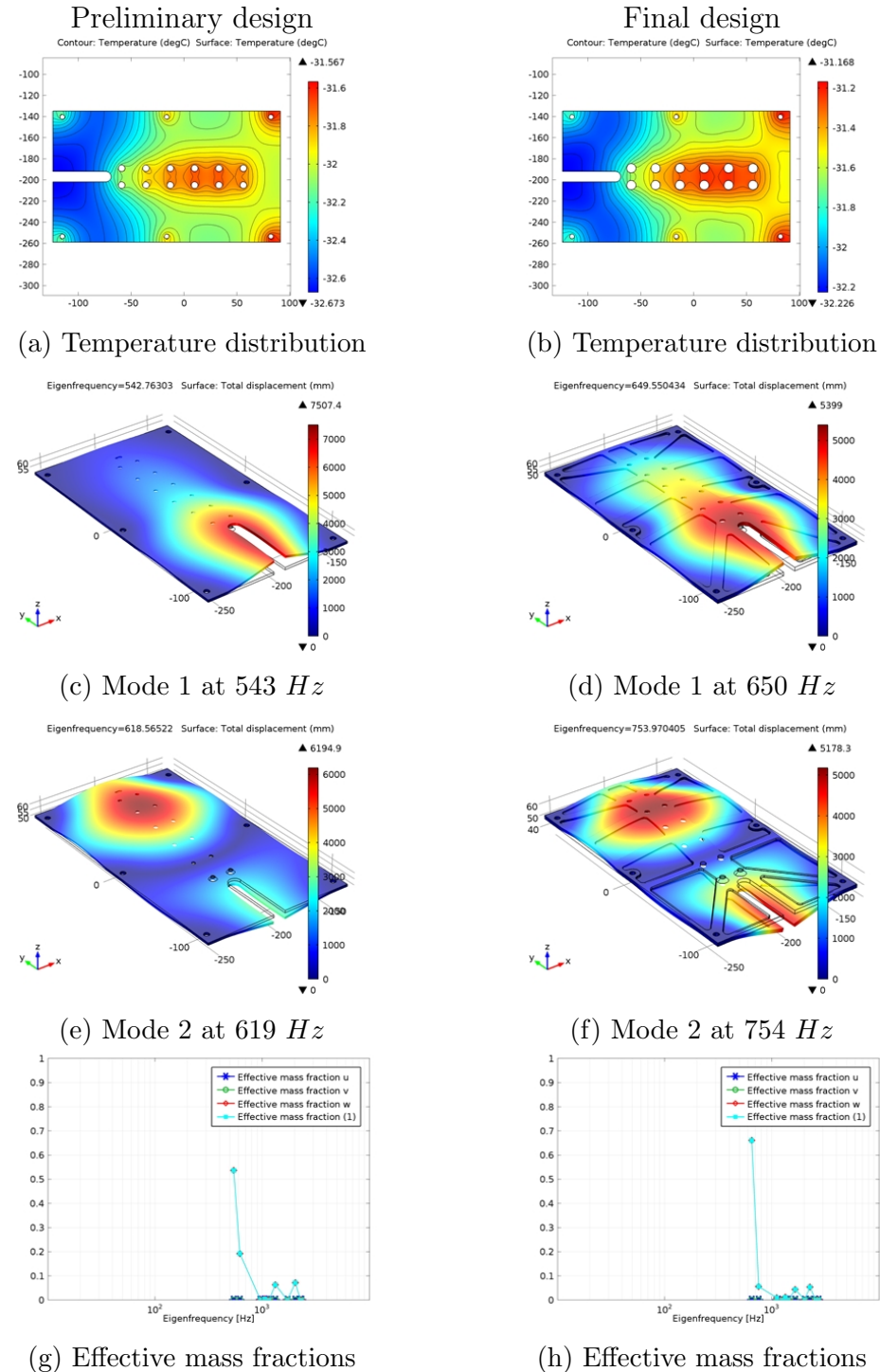
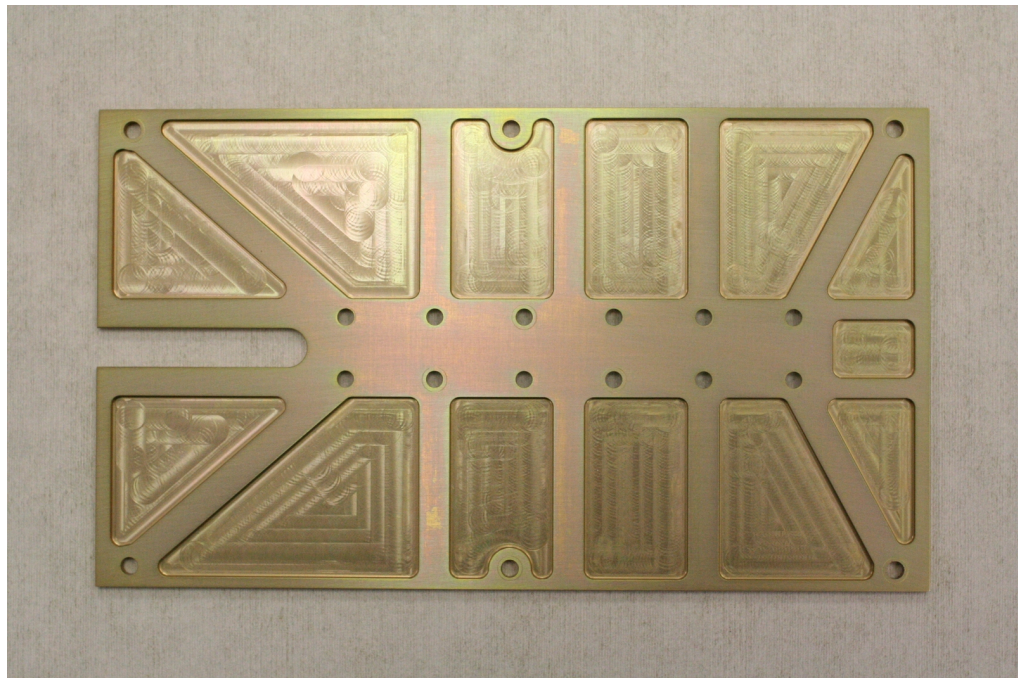


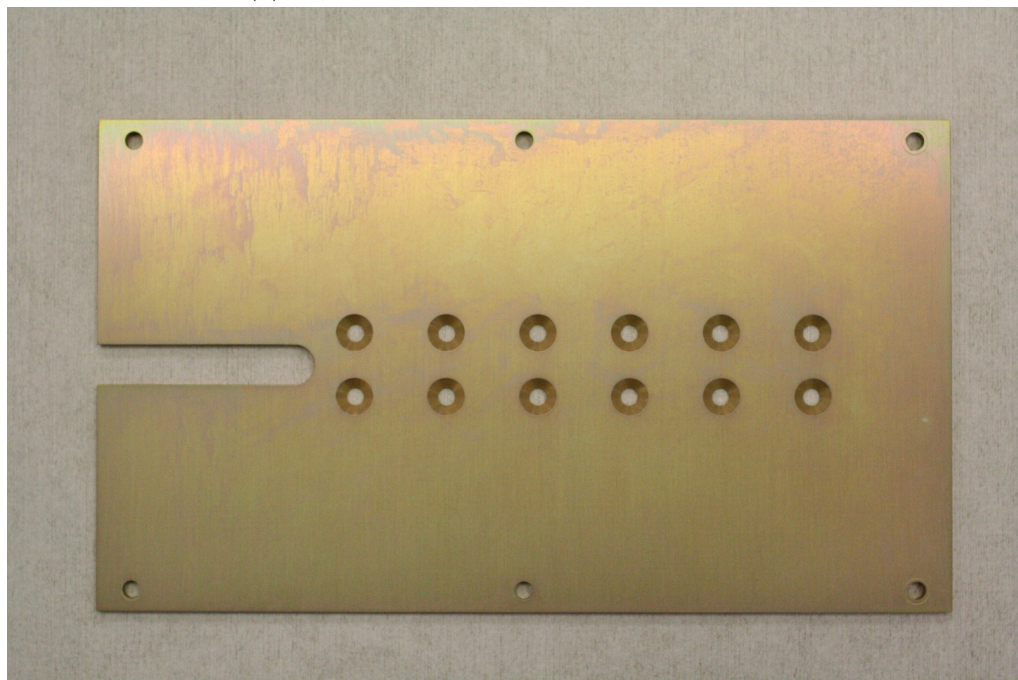
Figure 9.7.: Radiator benchmark analysis comparing the preliminary design (constant thickness, left) with the final design (with milled recesses, right).

*9. Thermal Control Subsystem*

---



(a) Radiator backside with milled recesses



(b) Radiator front side before painting

Figure 9.8.: Photography of the μROSI radiator after yellow chromating and before painting with white paint MAP SG121FD.

## 9.5. Heat Pipe

The heat pipe connects the radiator with the LCS container. It is made from an extruded aluminium profile with internal grooves (see fig. 9.11a). This profile was designed for the eROSITA camera cooling system. The experience gathered with the design, manufacturing and testing of the eROSITA heat pipes is very important for successfully designing, manufacturing and testing the heat pipe for the  $\mu$ ROSI telescope.

### 9.5.1. Working Principle

Heat pipes are closed tubes filled with a working fluid. They are capable of transporting heat over large distances with minimum temperature gradients by using phase transition heat transfers. The working fluid at the hot side of the heat pipe is evaporated and condensed at the cold side. The hot and cold sides are therefore called the *evaporator* and the *condenser* respectively.

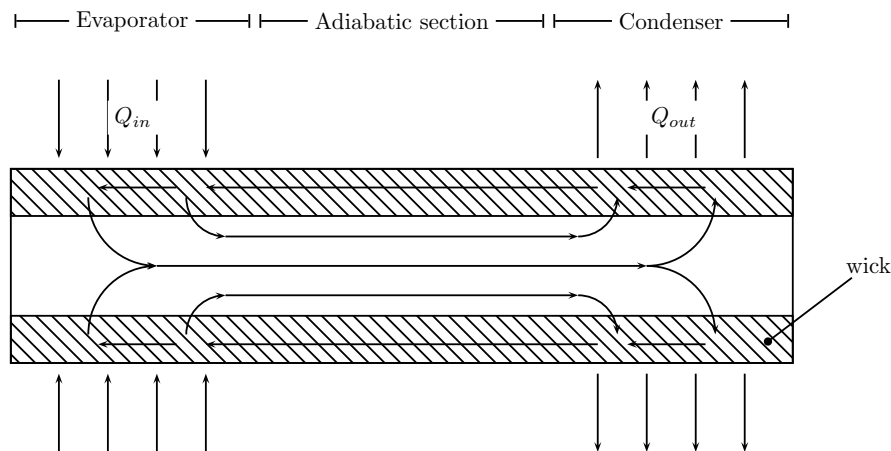


Figure 9.9.: Heat pipe working principle.

The working fluid inside the heat pipe is in a saturated state and strictly follows its saturation pressure curve. The gaseous phase flows from the evaporator to the condenser and the condensed phase flows in the opposite direction. The  $\mu$ ROSI heat pipe has small capillary grooves that transport the condensed phase with capillary pressure.

This process works only under certain conditions. In the following, a brief summary of the limitations are explained. Detailed explanation along with analytical methods to calculate each limitation can be found in Faghri, 1995.

### Capillary Limit

The capillary pressure in the heat pipe grooves is the driving force for the fluid flow inside the heat pipe. It needs to be higher than the sum of all pressure drops along the liquid-vapor path. Pressure drops occur at the liquid-vapor interfaces and along the path due to fluid friction, wall friction and gravity.

The capillary pressure  $p_{cap}$  determines the ability of the heat pipe to “pump” the liquid phase of the working fluid against the wall friction or gravity.

$$p_{cap} = \frac{2\sigma \cos \theta}{r_{eff}} \quad (9.6)$$

$$\Rightarrow p_{cap,max} = \frac{2\sigma}{r_{eff}} \quad (9.7)$$

where

$p_{cap}$	[Pa]	Capillary pressure
$\sigma$	[N/m]	Surface tension
$\theta$	[rad]	Wetting angle
$r_{eff}$	[m]	Effective pore radius

While the effective pore radius is determined by the heat pipe geometry, the surface tension of ethane is temperature dependent. Faghri (1995) give a comprehensive overview of how to determine the effective pore radius for different heat pipe types. To estimate the maximum capillary pressure  $p_{cap,max}$ , the wetting angle  $\theta$  can be neglected.

### Boiling Limit

If the wall temperature is too high, the fluid might boil in the wick. This can severely affect the fluid flow. In extreme cases the wick might even dry out locally causing a local pressure increase which counteracts the normal fluid flow. Thus, the boiling limit is typically a steep curve at the right edge in the  $Q / T$  diagram.

### Sonic Limit

If the flow rates in the liquid or in the vapor reach sonic speeds, the fluid flow friction increases drastically. In effect, the fluid flow is slowed down due to friction. The sonic limit can be reached at frozen startup conditions due to the temperature dependence of the speed of sound.

## Entrainment Limit

The heat pipe is limited by entrainment when high vapor velocities lead to a significant interaction with the liquid phase. Liquid is torn into the vapor stream and does not reach the evaporator.

## Viscous Limit

The viscous limit can be observed for heat pipes that operate below their normal operating temperatures. The vapor flow in the heat pipe is dominated by viscous forces and the vapor pressure at the end of the condenser drops to zero. The viscous limit is therefore also known as the vapor pressure limit.

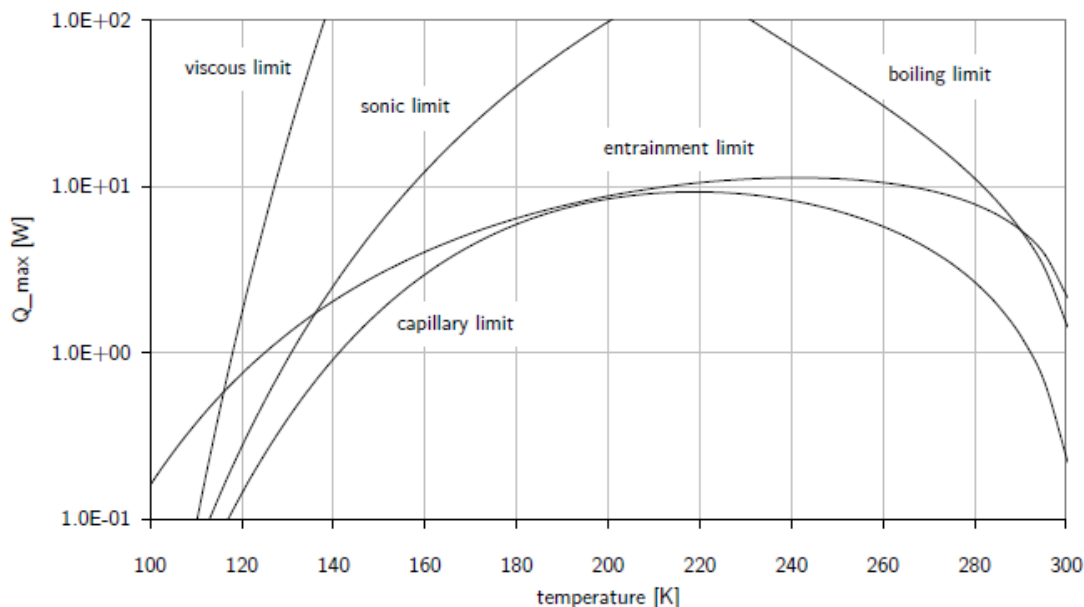


Figure 9.10.: Limitations of the  $\mu$ ROSI heat pipe. Calculated by Fürmetz (2012, p. 43) for the eROSITA camera heat pipes.

The extruded aluminium profile used for the  $\mu$ ROSI is the same that is used for the eROSITA camera heat pipes which has been thoroughly tested and comprehensively evaluated by Fürmetz (2012) with the working fluid ethane. Figure 9.10 shows the theoretical limitations (i.e. the maximum transferable heat power) of the eROSITA /  $\mu$ ROSI heat pipe as a function of the working temperature. The  $\mu$ ROSI heat pipe is capillary limited over the whole temperature range. This is chiefly due to the relatively low

## *9. Thermal Control Subsystem*

---

Other limitations that are not shown in fig. 9.10 are briefly described in the following.

### **Condenser Limit**

Heat pipes are condenser limited when the condenser is not able to provide enough cooling power. Non-condensable gases in the heat pipe can also limit the condenser cooling capability. Non-condensable gases like nitrogen are used in variable conductance heat pipes (VCHP). If the condenser temperature rises, the N<sub>2</sub> in the condenser expands and blocks a larger fraction of the condenser. Thus, VCHPs have a passive, automatic cooling power adjustment (see Fürmetz, 2012, for an example of a VCHP design).

### **Continuum Flow Limit**

Micro heat pipes or heat pipes that are operated at extremely low temperatures can be limited when the vapor is in the free molecular state.

### **Frozen Startup Limit**

If the heat pipe temperature is below the working fluid freezing temperature, the working fluid sublimates from frozen to vapor state. It may occur that the vapor re-sublimates in the adiabatic section. In effect, the evaporator dries out, as there is no fluid circulation.

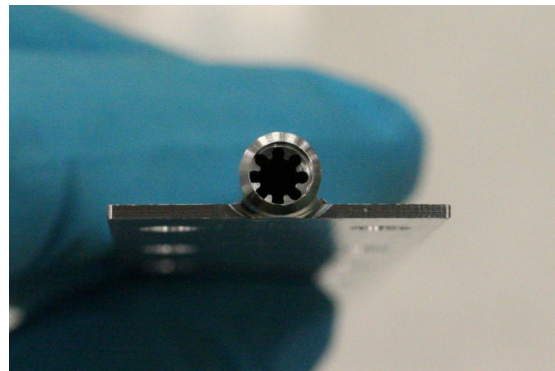
## **9.5.2. Heat Pipe Manufacturing**

The main body of the μROSI heat pipe consists of the heat pipe tube (see fig. 9.11a). This tube needs some end caps to keep the working fluid inside. Then, the working fluid needs to be filled into the heat pipe. For this purpose, a thin capillary tube is welded into one of the two end caps. The capillary tube is equipped with a standard Swagelok 1/4" fitting<sup>2</sup> for connecting it to the filling station. When the heat pipe is filled, the capillary tube is squeezed, cut and welded tight.

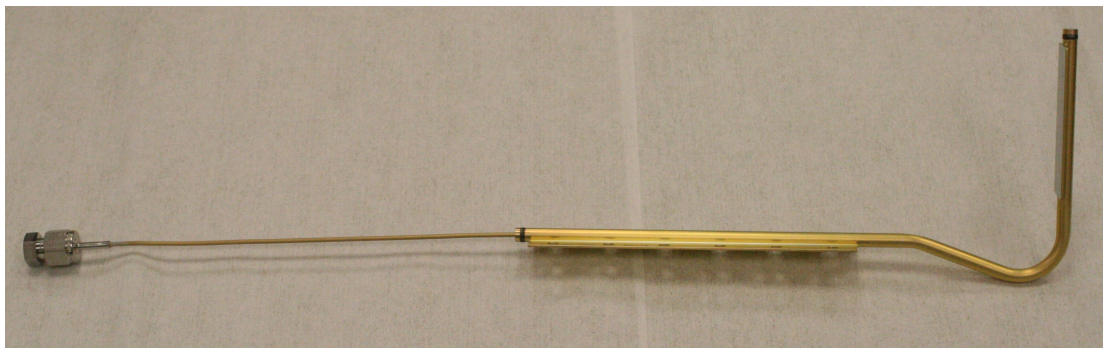
The following list gives a brief overview of how complex the manufacturing process is. The heat pipe profile used for the μROSI heat pipe was developed for the eROSITA camera cooling system and has been tested successfully. The complete manufacturing and testing process is known and all tools and facilities required are available.

---

<sup>2</sup>Swagelok is a manufacturer of fluid and gas fittings.



(a) μROSI heat pipe tube before welding the end caps and capillary tube.



(b) μROSI heat pipe with capillary tube and swagelok fittings before filling.

Figure 9.11.: μROSI heat pipe.

1. Profile manufacturing (aluminium extrusion)
2. Tube manufacturing
  - a) Removing superfluous flanges (milling)
  - b) Tube bending
  - c) Precise milling of remaining flanges
  - d) Drilling of flange bores
  - e) Drilling bores for end caps
3. End cap manufacturing
4. Cutting to length of capillary tube
5. Cleaning of parts

## *9. Thermal Control Subsystem*

---

6. Gluing Swagelok  $\frac{1}{4}$ " fitting to capillary tube
7. Laser welding tube, end caps and capillary tube
8. Helium leakage test
9. Surface treatment (yellow chromating)
10. Installing the heat pipe into the filling station
11. Filling with working fluid
  - a) Evacuating heat pipe
  - b) Weighing heat pipe
  - c) Filling with working fluid
  - d) Weighing heat pipe with working fluid
12. Heat pipe testing
13. Squeezing the capillary tube tight
14. Cutting and welding the capillary tube
15. Acceptance testing

Figure 9.11b shows the  $\mu$ ROSI heat pipe flight model after yellow chromating and before filling. The assembly underwent helium leak testing with a measured leak rate of  $1.1 \cdot 10^{-10} \text{ mbar l s}^{-1}$ . The Swagelok fitting at the end of the thin capillary tube will be connected to a hand-operated shut-off valve to keep the working fluid inside the heat pipe after filling. After successfully testing the heat pipe, the capillary tube is squeezed, cut and welded tight. This process has been developed for the eROSITA camera heat pipes using the same heat pipe profile.

### **9.5.3. Working Fluid**

The working fluid used in the  $\mu$ ROSI heat pipe is the same that is used for the eROSITA camera heat pipes: ethane. Table 9.7 lists the physical properties of ethane.

Other ethane properties are defined as parametrized function eq. (9.8). The parameter values  $a_i$  can be obtained from table 9.8.

$$F(T) = \exp \left\{ a_0 + a_1 T + a_2 T^2 + a_3 T^3 + a_4 T^4 + a_5 T^5 \right\} \quad (9.8)$$

Property	Symbol	Value	Condition
Chemical formula		C <sub>2</sub> H <sub>6</sub>	
Molar mass		30.07 $\frac{g}{mol}$	
Melting temperature	$T_m$	89.9 K	1 atm
Boiling temperature	$T_b$	184.6 K	1 atm
Vapor pressure	$p_v$	38.453 bar	21.1 °C

Table 9.7.: Properties of ethane.

### Ethane versus Ammonia

In Faghri (1995, Table 1.1, p.21) ethane is listed as a common heat pipe fluid with a useful temperature range from 150 ... 240 K. The nominal working temperature of the  $\mu$ ROSI heat pipe is  $-15^{\circ}\text{C} = 258\text{ K}$  which is determined by the latent cold storage. The temperature range is  $-30 \dots +30^{\circ}\text{C} = 243 \dots 303\text{ K}$ . Now, one could ask why ethane was selected when the nominal operating temperature range is not within the useful temperature range of the working fluid. Ammonia seems to be the better option since it has a useful temperature range of 213 ... 373 K. Figure 9.12 also seems to favour ammonia over ethane. It shows the surface tension ethane and ammonia as a function of the temperature. The surface tension is critical for the capillary pressure in the heat pipe (see eq. (9.6)). It is the driving force to overcome the pressure drops in the heat pipe. Both working fluids have increasing surface tension with lower temperatures, but the temperature range is different. In the range between 243 ... 303 K ammonia has a higher surface tension than ethane. This means that the expected capillary pressure is higher and the capillary limit allows for a wider temperature range, especially to higher temperatures. The heat transfer capability (i.e. the maximum transferable heat  $Q_{max}[W]$ ) is expected to be higher, and the efficiency (i.e. the temperature gradient  $\Delta T$ ) is expected to be lower for ammonia. So again, if ammonia is expected to have a higher  $Q_{max}$  and better efficiency, why would you not use ammonia instead of ethane?

First,  $Q_{max}$  is irrelevant for the  $\mu$ ROSI heat pipe. With a maximum transferable heat power of  $< 2\text{ W}$  the  $\mu$ ROSI heat pipe is low power heat pipe. Ethane and ammonia both can transport this little amount of heat at the designated working temperature of 258 K (refer to fig. 9.10).  $Q_{max}$  is high enough and there is no need for more.

Second, the efficiency of the heat pipe is *almost* irrelevant. Ammonia would be able to transport the same amount of heat with less temperature gradient or with

Property	Unit	$a_0$	$a_1$	$a_2$	$a_3$	$a_4$	$a_5$
$p_v$	$10^5 \cdot Pa$	3.2181	$2.5604e-2$	$-2.0481e-4$	$-1.6186e-6$	$1.1732e-8$	$1.9164e-10$
$h_{fg}$	$\frac{kJ}{kg}$	5.7153	$-1.3766e-2$	$-2.6378e-4$	$-3.8474e-6$	$-2.9487e-8$	$-8.7228e-11$
$\rho_l$	$\frac{kg}{m^3}$	6.0252	$-5.5940e-3$	$-5.4609e-5$	$-5.7691e-7$	$-4.0348e-9$	$-1.1902e-11$
$\rho_v$	$\frac{kg}{m^3}$	3.8345	$2.9745e-2$	$-1.0357e-5$	$1.6498e-6$	$1.8172e-8$	$1.0060e-10$
$\mu_l$	$10^{-7} \cdot \frac{Ns}{m^2}$	6.4915	$-6.1186e-3$	$5.8535e-5$	$5.1235e-7$	$2.7979e-9$	$-3.7143e-12$
$\mu_v$	$10^{-7} \cdot \frac{Ns}{m^2}$	4.4479	$3.6435e-3$	$-1.6045e-5$	$-3.3600e-7$	$-3.8411e-9$	$-1.3189e-11$
$\lambda_l$	$\frac{W}{m \cdot K}$	-2.5644	$-7.0141e-3$	$-2.1420e-5$	$-4.5965e-7$	$-6.1947e-9$	$-2.4827e-11$
$\lambda_v$	$\frac{W}{m \cdot K}$	-3.9900	$7.0307e-3$	$-2.4476e-5$	$-8.7918e-7$	$-1.1320e-8$	
$\sigma$	$10^{-3} \cdot \frac{N}{m}$	$1.9473e-1$	$-9.3444e-2$	$-1.7344e-3$	$-1.8129e-5$	$-9.1194e-8$	$-1.6900e-10$
$c_{p,l}$	$\frac{kJ}{kg \cdot K}$	1.2471	$1.0319e-3$	$-3.4135e-5$	$-7.0981e-7$	$-6.2492e-9$	$-1.9064e-11$
$c_{p,v}$	$\frac{kJ}{kg \cdot K}$	5.0629	$2.2657e-3$	$9.9616e-7$	$-3.3084e-8$	$-3.3254e-10$	$-8.7290e-13$

Table 9.8.: Coefficients  $a_i$  for ethane properties as a function of the temperature for use with eq. (9.8) (values taken from Faghri, 1995, Table A.42, p.824).

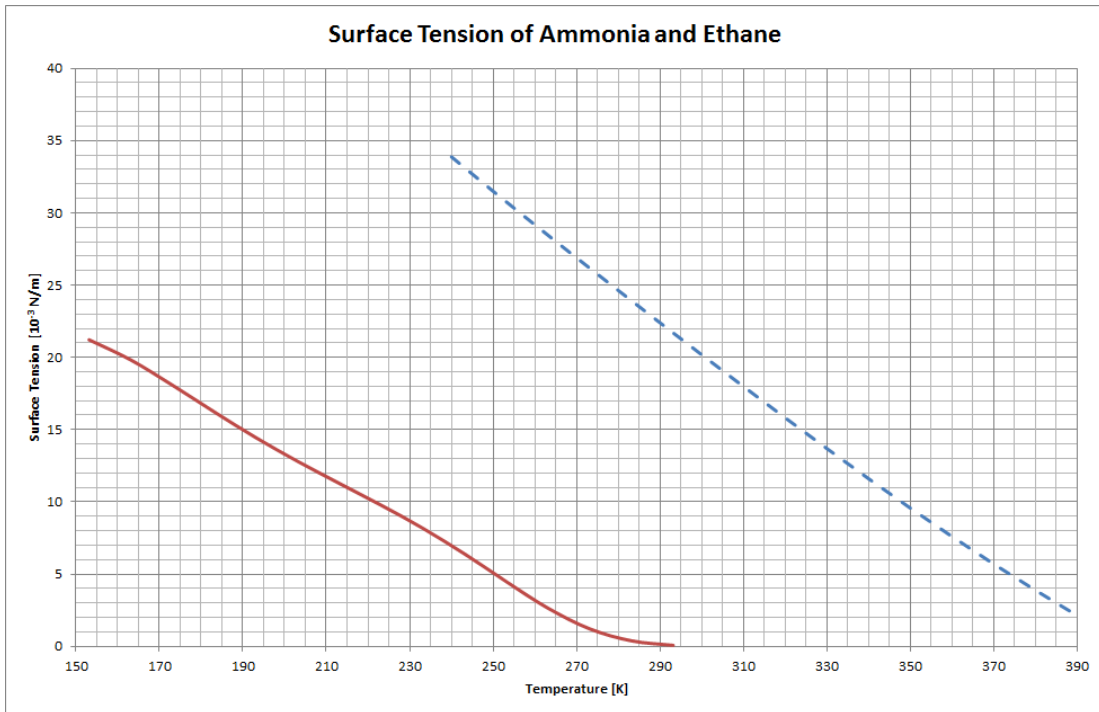


Figure 9.12.: Surface tension of ethane (red, solid) and ammonia (blue, dotted) as a function of the temperature (Temperature functions according to Faghri, 1995, Appendix A).

the same gradient, but with a smaller heat pipe. Well, a smaller heat pipe sounds great as this would mean less mass, but designing a smaller heat pipe profile is by far too expensive and time-consuming. However, a smaller temperature gradient would be a nice benefit indeed. But, at  $2\text{ W}$  the temperature gradient is  $\approx 1\text{ K}$  even with ethane (Fürmetz, 2012). Thus, reducing the  $\Delta T$  simply has no large impact for low power heat pipes.

Third, ethane stops working at exceedingly high temperatures. As can be seen in fig. 9.12, the surface tension of ethane is close to zero at  $290\text{ K}$ . This means that ethane can not provide capillary pressure for temperatures higher than  $290\text{ K}$ . This can also be seen in fig. 9.10 where the capillary limit curve suggests a maximum working temperature of slightly more than  $300\text{ K}$ . In other words, the  $\mu$ ROSI heat pipe will not work for temperatures significantly higher than room temperature whereas the same heat pipe filled with ammonia would continue to work even to temperatures around  $370\text{ K}$ . Using ammonia as a working fluid, higher temperatures at the radiator would heat up the latent cold storage more than with ethane. Ethane provides a natural power-off switch when

## *9. Thermal Control Subsystem*

---

the radiator temperature exceeds  $300\text{ K}$ , but it allows lower temperatures and that is exactly what we want for the  $\mu$ ROSI detector cooling system.

### 9.5.4. Heat Pipe Modelling

Modelling phase transitions, velocities, pressure gradients and capillary pressure effects in heat pipes in full detail is a very complex task. For the  $\mu$ ROSI thermal model a more simple approach is used.

The model as shown in fig. 9.13 consists of an evaporator node (E), a condenser node (C) and a vapour node (V). The nodes along the heat pipe are wall nodes that represent a cross section of the heat pipe. The vapour node is massless and connected to all wall nodes by a linear thermal resistance that simulates the heat exchange due to condensation or evaporation. The wall nodes are connected to their neighbours to take into account the thermal conductivity of the heat pipe tube. The evaporator and the condenser are connected to wall nodes with a thermal conductivity representing the temperature gradient across the heat pipe section to the mounting flanges which are the thermal-mechanical interfaces.

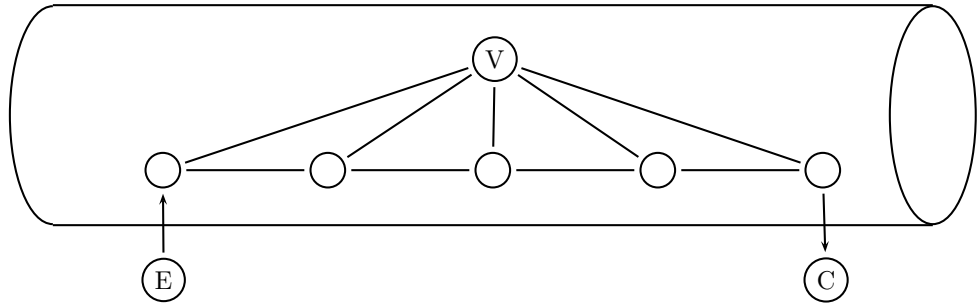


Figure 9.13.: Schematics of the  $\mu$ ROSI heat pipe thermal model. (E) evaporator node, (C) condenser node, (V) vapour node.

The thermal modelling of the interaction between the vapour node and the wall nodes is crucial for predicting the heat pipe performance. The thermal coupling here represents the heat exchange due to condensation or evaporation which is the key feature of any heat pipe. Faghri, 1995 gives a formula to estimate the heat transfer coefficient  $h_\delta$  at the liquid-vapour interface.

$$h_\delta = \frac{q_\delta}{T_v - T_l} = \left( \frac{2\alpha}{2 - \alpha} \right) \left( \frac{h_{fg}^2}{T_v v_{fg}} \right) \sqrt{\frac{M_v}{2\pi R_u T_v}} \left( 1 - \frac{p_v v_{fg}}{2 h_{fg}} \right) \quad (9.9)$$

## 9. Thermal Control Subsystem

---

$h_\delta$	$\left[\frac{W}{m^2 K}\right]$	Heat transfer coefficient at liquid-vapour interface
$q_\delta$	$\left[\frac{W}{m^2}\right]$	Heat exchange per unit area
$T_v$	[K]	Vapour temperature
$T_l$	[K]	Liquid temperature
$\alpha$	[1]	Empirical filling factor
$h_{fg}$	$\left[\frac{J}{kg}\right]$	Latent heat of evaporation
$v_{fg}$	$\left[\frac{m^3}{kg}\right]$	Change of specific volume from liquid to vapour
$M_v$	$\left[\frac{kg}{mol}\right]$	Molar mass
$R_u$	$\left[\frac{J}{mol K}\right]$	Universal gas constant
$p_v$	[Pa]	Vapour pressure

### 9.5.5. Heat Pipe Testing

The  $\mu$ ROSI heat pipe uses the same aluminium cross-section that is used the eROSITA camera cooling heat pipes. The heat pipe was designed for operation at very low temperatures with ethane as a working fluid.

Figure 9.14 shows the test setup for the  $\mu$ ROSI heat pipe. The condenser is mounted horizontally on an adapter plate to exclude gravitational effects. The adapter is mounted onto a cold plate inside a vacuum chamber for testing. The evaporator is equipped with a resistive heater that simulates the thermal load. During the test, the cold plate is temperature controlled with a stirling cooler and resistive heaters. The evaporator heater power is stepped up from 0 W in +1 W steps until the heat pipe power transport capability is reached.

Figure 9.15 shows the logged temperature curves at a cold plate temperature of 250 K. This test has been repeated for several different cold plate temperatures. It shows that the heat pipe is capable of transporting up to 5 W of heat power with a temperature gradient  $\Delta T < 9$  K and the temperature gradient for the calculated heat load of 1 W (detector dissipation plus parasitics) is  $\Delta T < 2$  K.

## 9.6. In-Orbit Simulation

In order to verify the design of the  $\mu$ ROSI thermal control subsystem, an in-orbit thermal analysis was conducted. Figure 9.16 shows the temperature distribution of  $\mu$ ROSI telescope in the planned sun-synchronous low Earth orbit. The orbit plane normal is assumed perpendicular to the Sun vector ( $\beta$ -angle is 90°). This orbit is the worst-case orbit for the TCS, as the temperature gradients on the

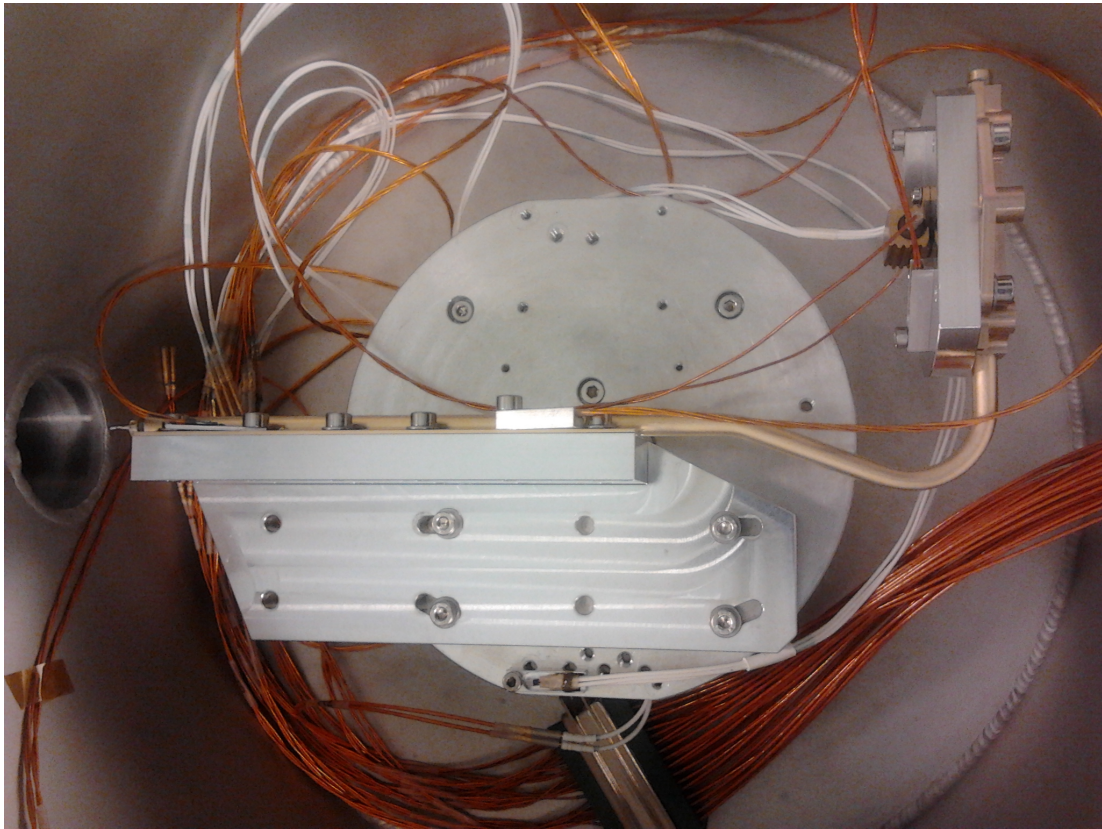


Figure 9.14.: Test setup for the  $\mu$ ROSI heat pipe test. The heat pipe is mounted horizontally inside a vacuum chamber to exclude gravitational effects (Tiedemann et al., 2013).

$\mu$ ROSI radiator are most extreme. This is due to the fact that the satellite spends more time in eclipse than in other SSO orbits.

The Max-Valier satellite is modeled assuming a stable temperature of  $20^{\circ}\text{C}$ . However, shading effects of the solar panel are taken into account as well as parasitic heat loads within the  $\mu$ ROSI telescope. The detector heat dissipation was assumed to be  $0.5\text{ W}$  and the electronics heat dissipation  $1.5\text{ W}$ .

As a result, the radiator temperatures vary between  $-5^{\circ}\text{C}$  and  $-30^{\circ}\text{C}$ , which equals  $-17.5 \pm 12.5^{\circ}\text{C}$ . This allows a medium temperature gradient of  $2.5^{\circ}\text{C}$  between the radiator and the LCS in order to maintain the stable temperature of  $-15^{\circ}\text{C}$ . The simulation has shown that this temperature gradient provides enough heat rejection for the detector thermal load and parasitics.

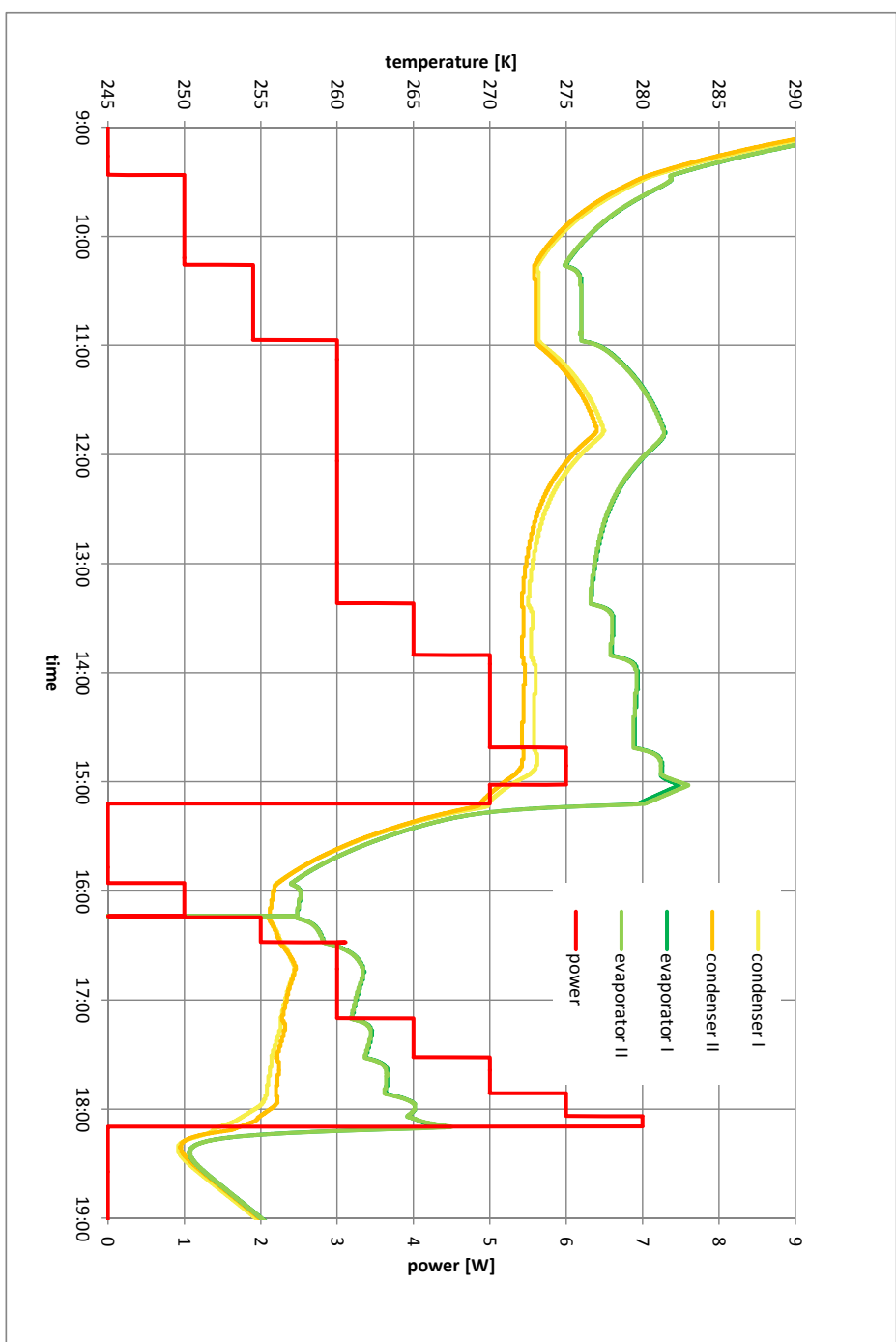


Figure 9.15.: Temperature curve of test with  $\mu$ ROSI heat pipe at a stable condenser temperature of  $250\text{ K}$  (Tiedemann et al., 2013).

## 9.7. TCS Summary

The principal purpose of the thermal control subsystem is to ensure the detector temperature remains stable at the specified temperature (reqs. 4.1 and 4.2). In order to achieve this with a minimum of electrical power, a completely passive system has been designed following a passive, low power design philosophy.

The LCS (req. 4.3) provides the temperature stability by means of a PCM (req. 4.4), which was selected to meet the desired temperature. A temperature difference of  $\sim 2^{\circ}\text{C}$  between the PCM melting temperature and the detector operating temperature has been foreseen to allow some margin for thermal interface resistance and parasitic heat loads.

The LCS has been designed, manufactured and tested with 1-Octanol to verify that the desired interface temperature is achieved and remains stable within the specified limits. The PCM melting temperature has been measured to be  $-15^{\circ}\text{C}$  as indicated by the data sheet. The measured temperature stability at the detector interface of the LCS was  $\leq 1.0^{\circ}\text{C}$  fulfilling req. 4.2 which required  $\pm 0.5^{\circ}\text{C}$ .

PCM safety (req. 4.14) is ensured as long as precautions indicated by the safety data sheet are observed. The compatibility of the PCM with the container material (req. 4.13) has been verified with a separate dummy container that showed no deterioration of the internal surface after containing the PCM for more than one year. Additionally, the PCM used in the laboratory version of the LCS has been re-tested after one year of storage without any degradation of melting temperature or temperature stability around the melting point.

The radiator (req. 4.8) provides the heat sink for the detector cooling system. Its design has been optimized for best mechanical stability and low mass while ensuring a smooth surface temperature distribution (see section 9.4.1). The radiator insulation (req. 4.9) is provided by composite bushings between the structure and the radiator panel. However, the radiator insulation has not yet been verified by testing as required in req. 4.9. The complete TCS will be tested during the telescope qualification test campaign. The same applies to the LCS insulation (req. 4.11).

The heat pipe that connects the LCS with the radiator (req. 4.10) has been tested successfully so that the medium temperature difference between the radiator and the LCS is  $< 2^{\circ}\text{C}$ . The heat pipe showed that it able to transport up to 5 W of heat which provides sufficient margin as the nominal heat load is 1.5 W including parasitics.

The complete TCS has been analysed with an in-orbit simulation in fulfil-

## *9. Thermal Control Subsystem*

---

ment of all requirements demanding analytical verification (reqs. 4.1, 4.2, 4.5, 4.9 and 4.11). The analysis shows that the TCS is capable of maintaining a stable, cold detector temperature in the assumed sun-synchronous orbit. The heat capacity of the PCM provides enough margin even in the SSO that has the largest temperature gradients.

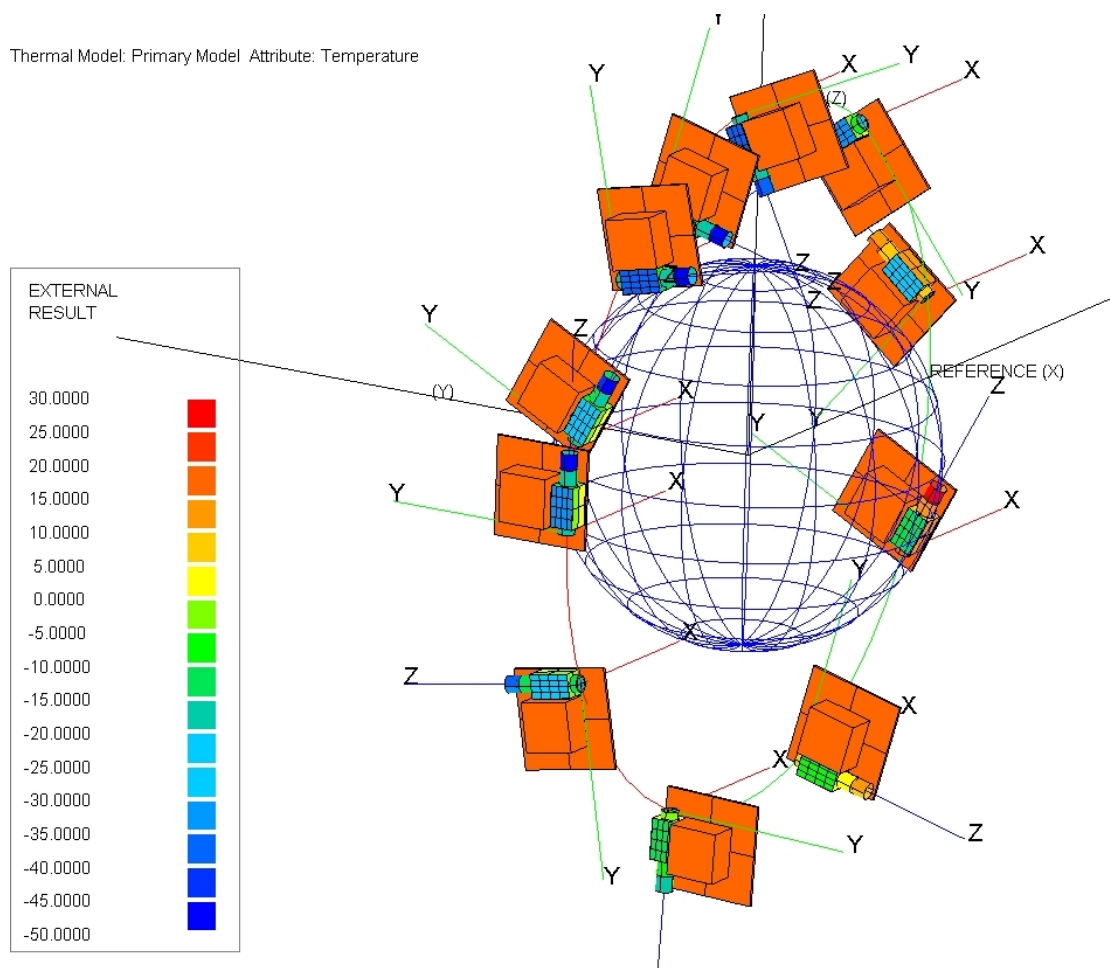


Figure 9.16.: In-orbit simulation of the Max-Valier Satellite with the  $\mu$ ROSI X-ray telescope. The color coding shows the temperature distribution over one orbit (Tiedemann et al., 2013).



# 10. Electronics

The  $\mu$ ROSI electronics consists of two separate PCBs, the Power Board and the Main Board. The Power Board is connected to the satellite with a standard D-SUB connector. Only four pins are used, 2 for the power supply and 2 for the UART interface.

1. +14V power supply
2. power return
3. UART TX
4. UART RX

## 10.1. Electronics Breadboard Model

The first version of the  $\mu$ ROSI electronics was the Breadboard (BB) model. Its purpose was to verify the energy resolution capability of the detector. The most challenging task in this context is the analogue detector signal processing. The BB comprises four separate boards for different purposes:

- **The high voltage board**  
converts 12V input voltage to  $-130V$  high voltage for the detector.
- **The power supply board**  
converts 12V input voltage to voltages required by all other components ( $+6V$ ,  $-6V$ ,  $+5V$ ,  $+10V$ ,  $-15V$ ).
- **The sensor board**  
provides the electrical interface to the detector unit and pre-processes the analogue detector output signals.
- **The processor board**  
converts analogue sensor signals to digital and processes them.

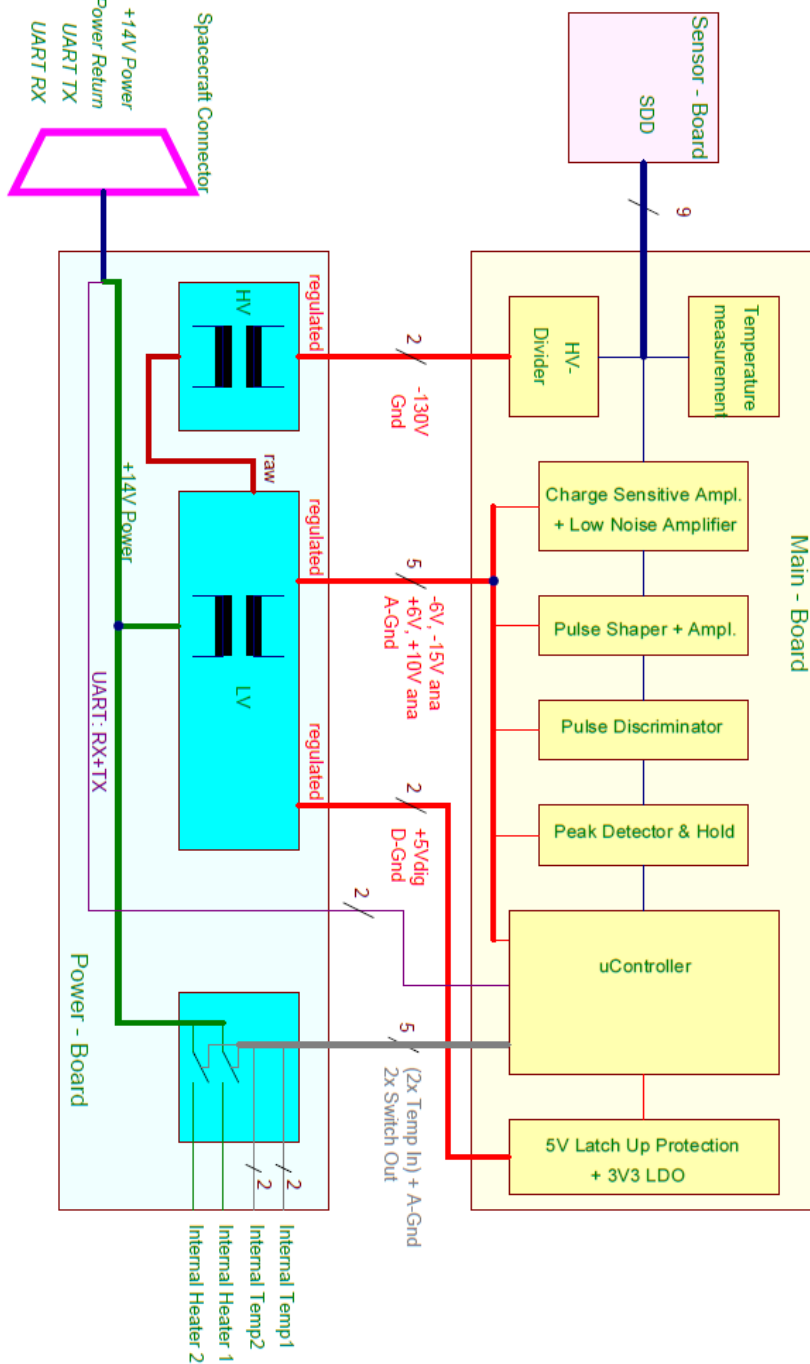
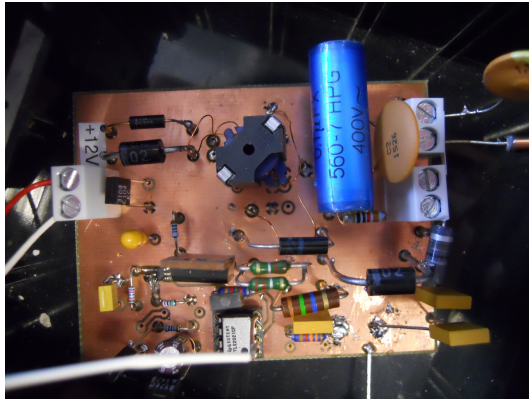


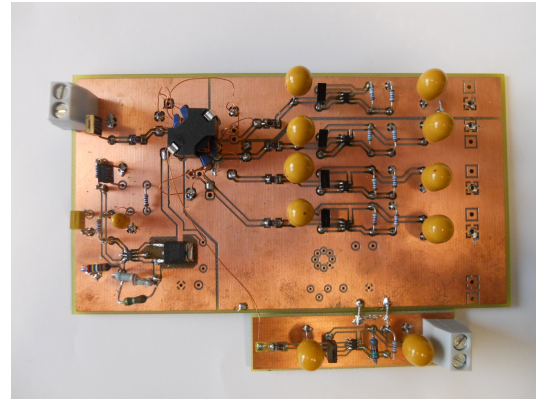
Figure 10.1.:  $\mu$ ROSI EM electronics block diagram.

Implementing the different tasks on separate boards allowed for redesigning one component without the need to change the other components. Likely, the power supply and high voltage supply board were implemented once and were operated with all revisions of the detector board.

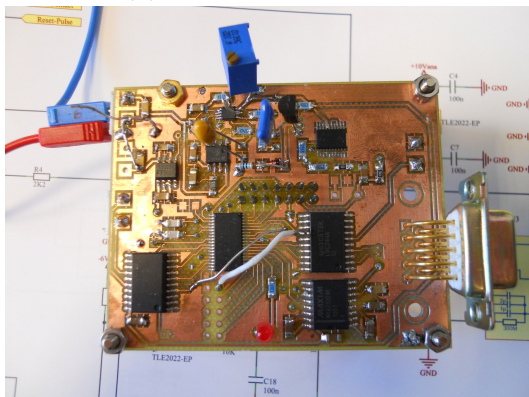
The detector board experienced the most design changes. The first version featured the charge sensitive pre-amplifier, a critical part for the charge detection. The second version already featured a signal shaper and a peak-and-hold detection circuitry.



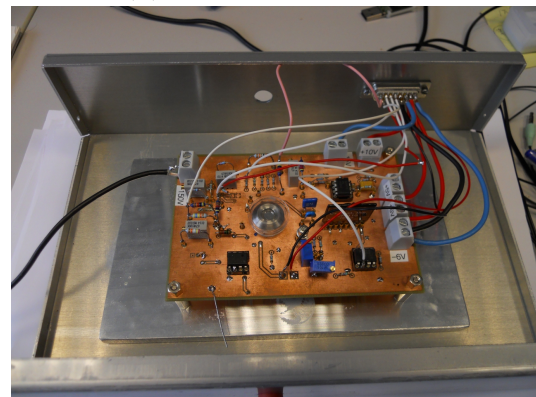
(a) High voltage board



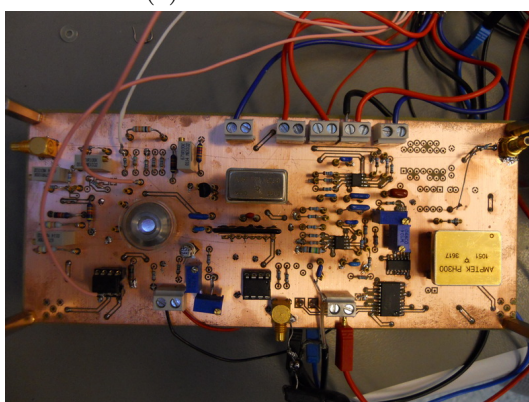
(b) Power supply board



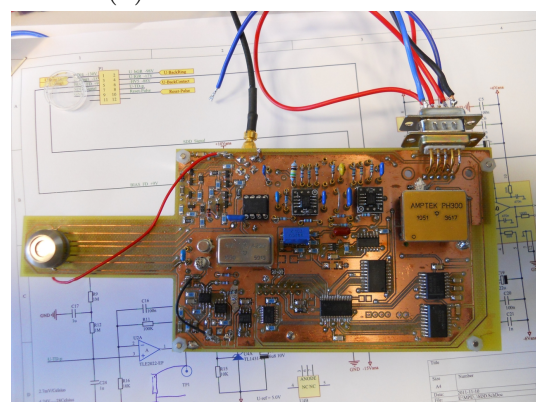
(c) Processor board



(d) Sensor board version 1



(e) Sensor board version 2



(f) Sensor board version 3

Figure 10.2.: Development boards of the electronics BB model.

## 10.2. Breadboard Test

The purpose of the detector breadboard test was to demonstrate the energy resolution capabilities of the electronics.

Figure 10.3 shows the test setup with the electronics BB model with the detector breadboard model. Not shown in the image is the power supply board and the high voltage board. The detector is cooled down to  $-20^{\circ}\text{C}$  with gaseous nitrogen and exposed to an iron-55 ( $^{55}\text{Fe}$ ) radioactive source for X-ray detection. The test was conducted in the electronics laboratory at the MPE inside a stainless steel box.

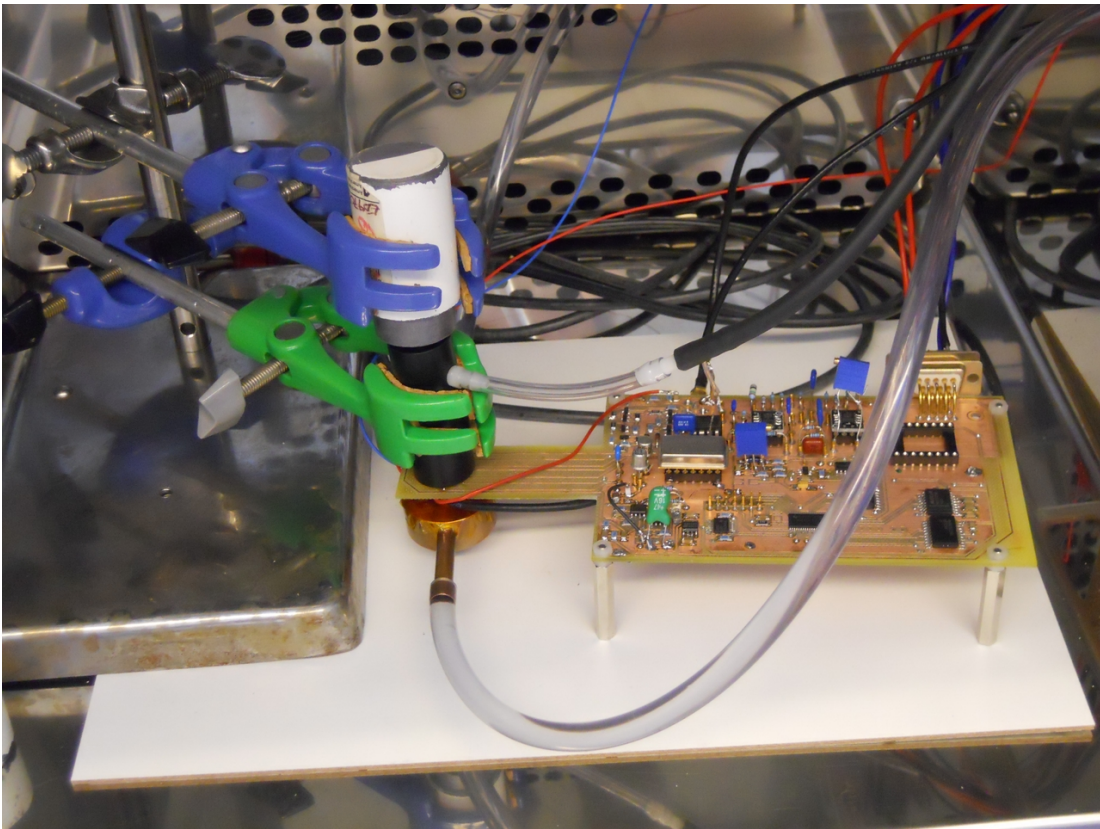


Figure 10.3.: Test setup with sensor board version 3.

At this time, the software for digitally processing the measured data was not yet fully implemented. As previously mentioned, the main focus of this test was to verify the analogue signal processing in the signal chain from the SDD detector to the AD converter on the breadboard electronics. The test data were obtained from oscilloscope measurements. The test data showed clearly two well shaped

peaks in the spectrum (see fig. 10.4). Two gauss curves were generated to best fit to those peaks. With the energies of the peaks known (they are predetermined by the  $^{55}\text{Fe}$  source), the x-axis could then be transformed to energy values. The result of the gauss fit curves together with the measured data is shown in fig. 10.5.

The general formula used for the gauss fit curves is given by eq. (10.1). Best fit parameters are obtained numerically by minimizing the sum of the squared errors.

$$f(x) = \frac{\text{Peak}}{\sigma\sqrt{2\pi}} \cdot e^{-\frac{1}{2}\left(\frac{x-\mu}{\sigma}\right)^2} \quad (10.1)$$

With the curve parameters the full width half maximum  $FWHM$  value of each peak can be calculated using eq. (10.2). The  $FWHM$  is a measure for the energy resolution of the detector and electronics system.

$$FWHM = 2\sqrt{2\ln 2} \sigma \quad (10.2)$$

The results are summarized in table 10.1.

Parameter	Energy	
	5.9 keV	6.5 keV
$\mu$	297.360	328.817
$\sigma$	3.570	3.888
$Peak$	39000	8003
$FWHM$	8.407	9.155
$FWHM [eV]$	158	172

Table 10.1.: Detector breadboard best fit parameters for gauss fit curves and  $FWHM$  values.

In summary, the electronics BB model proved the capability of the analogue circuitry to obtain signals from the detector and process them accordingly. The detector was able to measure X-ray radiation and delivered good energy resolution together with the electronics BB. The system's energy resolution was measured with 158 eV and 172 eV at 5.9 keV and 6.5 keV respectively. These values are well below the required 200 eV. The digital post-processing of the measured data still needs to be implemented and tested with the engineering model.

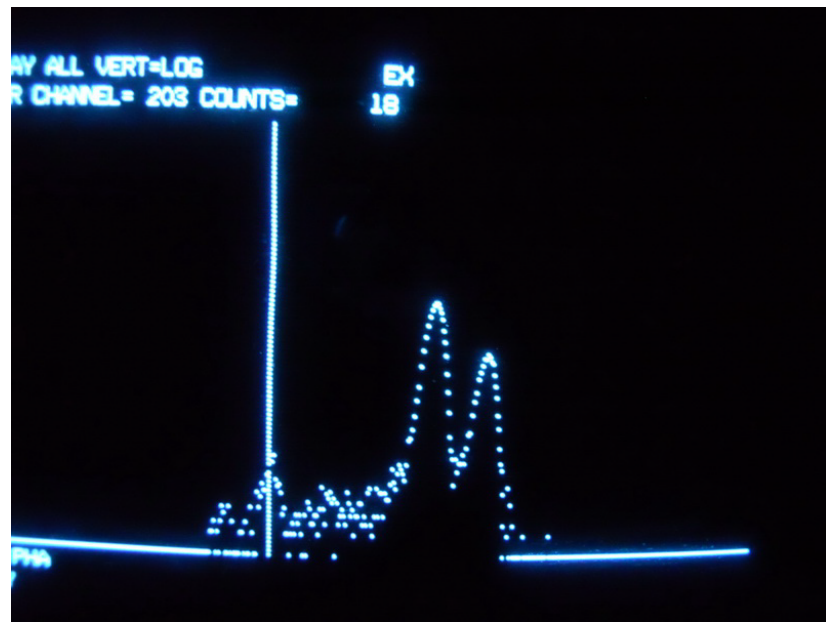


Figure 10.4.: Photography of multichannel analyzer output during detector breadboard testing (logarithmic y-axis).

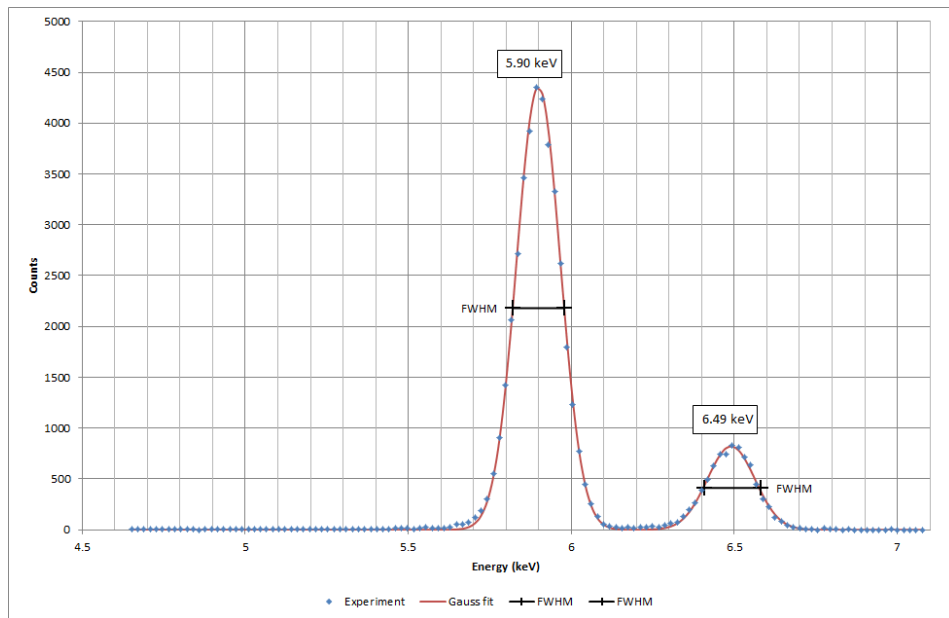


Figure 10.5.: Detector breadboard test data with a gaussian fit curve (linear y-axis).

### 10.3. Electronics Engineering Model

The electronics engineering model (EM) is the first model with flight-like electronics. Its main purpose is to test the circuitry together with the detector and to improve the layout for the final design iteration.

The power supply board now incorporates the converters for all required voltages, including the detector high voltage supply. The main board comprises the whole signal processing chain from analogue to digital. The detector is connected to the main board with a flexible flat cable. Both boards are four layer PCBs manufactured with the same high standards as the qualification and flight model PCBs.

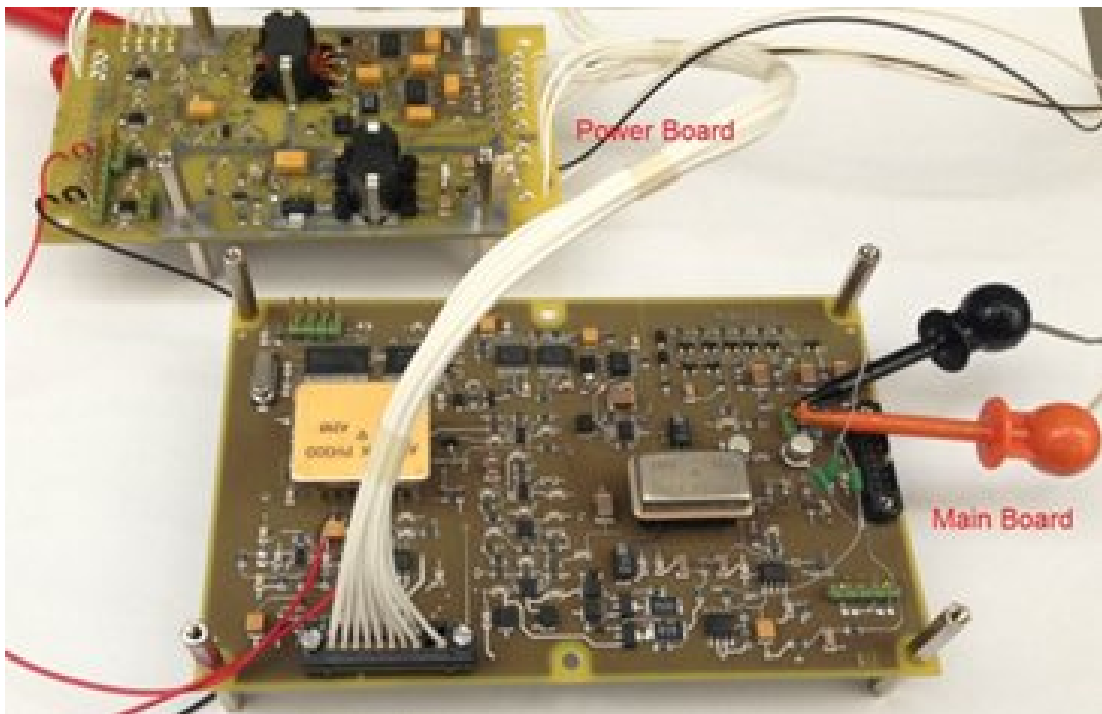


Figure 10.6.: Electronics EM boards during testing.

# 11. Conclusion

Within the scope of this work, a fully functional miniature X-ray telescope has been designed. The design has been verified so that the telescope can successfully fulfill its scientific mission. The  $\mu$ ROSI project, started in early 2008, is still not completely finished. However, most of the project goals have been accomplished.

- The structural design has been verified by vibration testing.
- The final design of the telescope is complete.
- The detector has been tested successfully with the BB electronics.
- The thermal design has been verified by analysis.
- The hardware for the thermal control subsystem has been developed, manufactured and tested successfully.
- The electronics design has been verified by functional testing.
- The manufacturing of the mirror shells has been completed including the self-developed mandrel polishing process.
- The mirror properties have been verified by X-ray testing one sample mirror shell.

The manufacturing of the mirror shells was one of the most important milestones in this project. Attaining the surface smoothness corresponding to the ultra short wavelength of X-rays requires an elaborate polishing process (section 7.4). The polishing of the eROSITA mandrels is carried out by the company Media Lario Technologies. However, in order to reduce time and costs, the polishing process has been successfully established at the MPE by Elias Breunig (Breunig, 2011a, diploma thesis).

The X-ray measurement of the sample mirror shell #06 (section 7.5) was the final verification of the surface quality. Although the surface roughness of the mandrels has been verified beforehand by optical (VIS) measurements, the results of these measurements can never replace the “real” X-ray test due to the huge difference in wavelength between VIS and X-ray. Thus, the X-ray test finally

## *11. Conclusion*

---

proved that the polishing process at the MPE and the following e-forming at Media Lario delivered good mirror shells.

The structure of the  $\mu$ ROSI telescope (chapter 8) was designed as a lightweight aluminium structure milled from a monolithic block. This design was the result of a trade-off analysis and structural FEM analysis conducted by Elias Breunig (Breunig, 2011b). A structural qualification model has been manufactured and tested on the vibration table. For the test, all subsystems were simulated by mass dummies that were mounted to the structure at their designated interfaces. The test showed that the structure itself has sufficient load capability to support all subsystems under the specified test conditions. However, two design improvements were implemented as a result of this test campaign:

1. The mounting of the electronics PCB has been relocated to the side walls instead of the cover. This was necessary to avoid resonance effects between the cover and the PCB and the decision to use two separate PCBs with a dedicated power board instead of a single PCB.
2. The material of the four M5 satellite interface screws has been changed from stainless steel A2-70 to high strength titanium alloy TiAl6V4 in order to increase the screw torque and the interface contact pressure. Helicoil thread inserts and additional spring washers support this effort.

The  $\mu$ ROSI thermal control subsystem (chapter 9) is another key element that is essential for the detector performance. With the specifically developed latent cold storage (LCS) the system is capable of effectively compensating huge temperature difference as they are experienced in a low Earth orbit (LEO) keeping the detector temperature stable at  $-15^{\circ}\text{C}$ . All components are working passively with a minimum of electrical power and without any consumables ensuring an unlimited life time. The novelty is not the use of a phase change material as a thermal capacitor, but the temperature range it has been designed for. As far as my research has revealed, this LCS is the first phase change capacitor for temperatures below  $0^{\circ}\text{C}$  designed for a space mission. The LCS can be used for any device in a LEO that requires a cold and stable temperature, like star trackers or optical sensors for Earth observation. The LCS can be easily scaled in size to meet the requirements of any other device.

The heat pipe used in the thermal control subsystem uses the same cross section and manufacturing process developed by myself for the eROSITA cameras. The eROSITA CCD camera is operated even at a much lower temperature of  $-95^{\circ}\text{C}$ , so that the heat pipe is filled with ethane as a working fluid. Although the

---

eROSITA heat pipes have undergone extensive testing, operating the  $\mu$ ROSI heat pipe successfully in space prior to the eROSITA launch would add the TRL 7<sup>1</sup>. The extra confidence is much appreciated, because the testing of the eROSITA camera cooling system with its seven cameras, two radiators and a total number of 13 heat pipes has proven to be extremely difficult on ground due to gravity effects (Fürmetz, 2012).

The  $\mu$ ROSI electronics (chapter 10) has been developed specifically for the needs of the SDD detector. In order to operate the SDD in single-photon counting mode, the electronics needed to provide analogue signal processing capabilities as well as digital data handling and housekeeping.

The electronics follows a modular design philosophy featuring a power supply board and a main board. The power supply is critical for the detector performance as it provides the high voltage for the detector. The analogue signal processing and data handling is located on the main board. This setup allowed for design iterations on the analogue section while reusing the power supply. Consequently, the third electronics breadboard model BB3 has been tested successfully with a detector and a radioactive X-ray source. This test proved that the complete subsystem comprising the electronics and the detector is capable of delivering the required energy and timing resolution.

Currently, there is work in progress and more things to do in order to prepare the  $\mu$ ROSI telescope ready for flight:

- Integrate the mirror shells into the mirror spider and conduct X-ray test of the integrated mirror module.
- Finalize electronics EM testing.
- Redesign electronics QM and FM, if required (depending on EM test results).
- Conduct X-ray test with EM electronics and detector.
- Conduct thermal balance and cycling test with the integrated thermal control subsystem.
- Assemble and test the telescope QM with qualification test levels (functional test, vibration test, thermal test, X-ray test).
- Assemble and test the telescope FM with acceptance test levels.
- Integrate the telescope and test with the satellite.

---

<sup>1</sup>System prototype demonstration in a space environment, compare table A.3

## *11. Conclusion*

---

These activities are presumably finished in autumn 2013. The telescope then is ready to be integrated into the Max-Valier Satellite. After integration and testing the satellite with the telescope at the MPE, the satellite can be shipped to the launch site. The launch is scheduled for April 2014 with a VEGA rocket from Kourou.

The  $\mu$ ROSI EM and QM models remain at the MPE and are later used in X-ray test facilities for measuring spectra. The EM does not have the same cooling system for the detector as the QM and the flight model, as it can be cooled by a chiller that is already used in the test facilities for various purposes.

The preliminary simulation conducted in section 5.3 suggests that the  $\mu$ ROSI is capable of meeting its primary scientific objective of measuring spectra of at least 100 X-ray sources during its all-sky survey. However, the simulation is based on the ROSAT all-sky survey data and the images produced by  $\mu$ ROSI will yield different results. Besides the higher angular resolution of the ROSAT images, the ROSAT PSPC detector had a superb background rejection whereas  $\mu$ ROSI excels in spectral resolution. With the good time resolution of the detector,  $\mu$ ROSI will be able to resolve some bright transient sources, and, perhaps also measure the O<sub>2</sub> in the upper Earth atmosphere.

# A. Appendices

## A.1. Thermal Modeling

### Thermal capacity

$$\dot{Q} = m \cdot C_p \cdot \frac{dT}{dt} \quad (\text{A.1})$$

$$\Rightarrow T = \int \frac{\dot{Q}}{m \cdot C_p} dt \quad (\text{A.2})$$

### Thermal conductivity

$$\dot{Q}_{1 \rightarrow 2} = k (T_1 - T_2) = \frac{\lambda \cdot A}{l} (T_1 - T_2) \quad (\text{A.3})$$

### Ambient radiation

$$\dot{Q}_{1 \rightarrow 2} = \sigma F_{1 \rightarrow 2} A_1 \varepsilon_1 (T_1^4 - T_2^4) \quad (\text{A.4})$$

### Surface to surface radiation

$$\dot{Q}_{1 \rightarrow 2} = \sigma F_{1 \rightarrow 2} A_1 \left( \frac{1}{\varepsilon_1} + \frac{1}{\varepsilon_2} - 1 \right)^{-1} (T_1^4 - T_2^4) \quad (\text{A.5})$$

## Phase Change Material Modeling

The phase change material (PCM) used in the latent cold storage needs to be modelled precisely to predict the behaviour of the resulting temperatures. Three different states have to be modeled: solid, liquid and phase transition. The PCM temperature is composed of partial temperatures:

$$T_{PCM} = T_s + T_l + T_m \quad (\text{A.6})$$

where  $T_{PCM}$  is the total temperature of the phase change material,  $T_s$  is the partial temperature of the solid phase,  $T_l$  of the liquid phase and  $T_m$  is the PCM's melting temperature.

## A. Appendices

---

The internal energy stored in the PCM is obtained by

$$U = Q = m (\Delta h \cdot x + c_{p,s} \cdot T_s + c_{p,l} \cdot T_l) \quad (\text{A.7})$$

where  $x \in [0 \dots 1]$  is the fraction of the melted phase in the PCM. The time derivative of  $U$  then yields

$$\dot{Q} = m \left( \Delta h \frac{dx}{dt} + c_{p,s} \frac{dT_s}{dt} + c_{p,l} \frac{dT_l}{dt} \right) \quad (\text{A.8})$$

Table A.1 shows the value ranges for different states. The internal energy level  $U$  in this model equals zero when  $x = 0$ . That is the case when the PCM is completely frozen and at melting temperature.

	Solid	Phase transition	Liquid
$T_s$	$< 0$	0	0
$T_l$	0	0	$> 0$
$T_{PCM}$	$< T_m$	$= T_m$	$> T_m$
$x$	0	$0 \dots 1$	1
$U$	$< 0$	$> 0$	$> 0$

Table A.1.: Value ranges for different states in PCM modeling.

## A.2. Spectral Lines

Table A.2 lists spectral lines of some elements in the soft X-ray bandwidth.

z-Number	Element	K <sub>α1</sub>	K <sub>β1</sub>	L <sub>α1</sub>	L <sub>β1</sub>
6	C	0.277			
7	N	0.3924			
8	O	0.5249			
12	Mg	1.25360	1.3022		
13	Al	1.48670	1.55745		
14	Si	1.73998	1.83594		
25	Mn	5.89875	6.49045	0.6374	0.6488
29	Cu	8.04778	8.90529	0.9297	0.9498
47	Ag	22.16292	24.9404	2.98431	3.15094

Table A.2.: X-ray emission lines of selected elements in *keV* (values from Bearden, 1967, published on <http://www.med.harvard.edu>).

### **A.3. Technology Readiness Levels**

Table A.3 lists the technology readiness levels (TRL) as they are defined unanimously by NASA (Mankins, 1995) and ESA (ESA, 2012a). TRLs can be used for assessing the maturity of any kind of technology, e.g. components, software, materials or manufacturing processes.

TRL	Description
1	Basic principles observed and reported
2	Technology concept and/or application formulated
3	Analytical & experimental critical function and/or characteristic proof-of-concept
4	Component and/or breadboard validation in laboratory environment
5	Component and/or breadboard validation in relevant environment
6	System/subsystem model or prototype demonstration in a relevant environment (ground or space)
7	System prototype demonstration in a space environment
8	Actual system completed and “Flight qualified” through test and demonstration (ground or space)
9	Actual system “Flight proven” through successful mission operations

Table A.3.: Technology Readiness Levels as defined by NASA (Mankins, 1995) and ESA (ESA, 2012a).

## A.4. Parts List

Table A.4.: μROSI parts list. Subsystems and subassemblies are emphasized with bold font.

Level	Number	Part Name	Material	Mass	Qty
[1]	<b>554-0000-000</b>	<b>μROSI</b>		<b>2.4596 kg</b>	<b>0</b>
[1.1]	<b>554-1000-000</b>	<b>Structure</b>		<b>0.6465 kg</b>	<b>1</b>
[1.1.1]	554-1100-001	Optical-Bench	AW-6061-T6	0.6446 kg	1
[1.1.1.1]	Böllhoff 4130 104 0006	Helicoil M4x1.5d	CuSN6	kg	0
[1.1.2]	DIN_7-3_m6_x_10	Zylinderstift_3_m6_x_10	VA		5
[1.2]	554-1200-001	Cover	AW-6061-T6	0.1556 kg	1
[1.3]	<b>554-2000-000</b>	<b>Detector-Assembly</b>		<b>0.0502 kg</b>	<b>1</b>
[1.3.1]	554-2000-001	Filter-Foil	Polyimid	0 kg	1
[1.3.2]	554-2100-001	Detector-Mounting	AW-6061-T6	0.0028 kg	1
[1.3.3]	554-2100-002	Detector-Shroud	AW-6061-T6	0.0104 kg	1
[1.3.4]	554-2100-003	Filter-Cap	AW-6061-T6	0.004 kg	1
[1.3.5]	554-2100-004	Retention-Ring	AW-6061-T6	0.0033 kg	1
[1.3.6]	554-2100-005	Venting-Light-Seal	AW-6061-T6	0.0011 kg	1
[1.3.7]	554-2300-000	Drift-Chamber-Complete		0.0148 kg	1
[1.3.7.1]	554-2300-001	SDD	Kupfer	0.0119 kg	1
[1.3.7.2]	554-5300-101	Flexlead-Cable	Polyimid	0.0015 kg	1
[1.3.7.3]	Harwin_M80-4001405	Harwin_M80-4001405		0.0013 kg	1
[1.3.8]	554-2300-002	SDD-Dummy	AW-6061-T6	0.0119 kg	1
[1.3.9]	O-Ring_15.0x2.0	O-Ring_15.0x2.0	VITON	0.0003 kg	1
[1.3.10]	Scheibe_ISO_7089_2	Scheibe_ISO_7089_2	VA	0 kg	3
[1.3.11]	ISO_14580_M2x3_A2-70	Zylinderschraube_Torx_M2x3	A2-70	0.0002 kg	3
[1.3.12]	ISO_14581_M2x8_A2-70	Senkschraube_Torx_M2x8	A2-70	0.0002 kg	4
[1.4]	<b>554-3000-000</b>	<b>Mirror</b>		<b>0.5312 kg</b>	<b>1</b>
[1.4.1]	554-3200-000	Mirror-Module		0.5501 kg	1
[1.4.1.1]	554-3100-000	Mirror-Shells		0.3905 kg	1
[1.4.1.1.1]	554-3100-001	Mirror-Shell-01	Nickel	0.053 kg	1
[1.4.1.1.2]	554-3100-002	Mirror-Shell-02	Nickel	0.0506 kg	1
[1.4.1.1.3]	554-3100-003	Mirror-Shell-03	Nickel	0.0483 kg	1
[1.4.1.1.4]	554-3100-004	Mirror-Shell-04	Nickel	0.0461 kg	1
[1.4.1.1.5]	554-3100-005	Mirror-Shell-05	Nickel	0.044 kg	1
[1.4.1.1.6]	554-3100-006	Mirror-Shell-06	Nickel	0.0419 kg	1
[1.4.1.1.7]	554-3100-007	Mirror-Shell-07	Nickel	0.02 kg	1
[1.4.1.1.8]	554-3100-008	Mirror-Shell-08	Nickel	0.019 kg	1
[1.4.1.1.9]	554-3100-009	Mirror-Shell-09	Nickel	0.0181 kg	1
[1.4.1.1.10]	554-3100-010	Mirror-Shell-10	Nickel	0.0173 kg	1
[1.4.1.1.11]	554-3100-011	Mirror-Shell-11	Nickel	0.0165 kg	1
[1.4.1.1.12]	554-3100-012	Mirror-Shell-12	Nickel	0.0157 kg	1
[1.4.1.2]	554-3401-002	Spider	Ti6Al4V	0.064 kg	1

continued on next page...

## A. Appendices

---

... continued from previous page

Level	Number	Part Name	Material	Mass	Qty
[1.4.1.2.1]	Böllhoff 4130 103 0045	Helicoil M3x1.5d	CuSN6	kg	0
[1.4.2]	554-3300-000	Baffle		0.0547 kg	1
[1.4.2.1]	554-3300-001	CFK-Rohr	CFRP	0.0451 kg	1
[1.4.2.2]	554-3300-002	Baffle-Flansch	TiAl6V4	0.0096 kg	1
[1.4.3]	554-3401-001	Mirror-Adapter	AW-6061-T6	0.0183 kg	1
[1.4.4]	Scheibe_ISO_7089_3	Scheibe_ISO_7089_3	A2-70	0.0001 kg	4
[1.4.5]	ISO_4762_M3x6	Zylinderschraube_M3x6	A2-70	0.001 kg	4
[1.5]	<b>554-4000-000</b>	<b>Thermal-Control-System</b>		<b>0.6886 kg</b>	<b>1</b>
[1.5.1]	554-0401-001	μROSI-HP	AW-6060	0.0265 kg	1
[1.5.2]	554-4100-001	Radiator-Plate	AW-6061-T6	0.1431 kg	1
[1.5.3]	554-4100-003	Detector-Kettle	PEEK-GF30	0.0915 kg	0
[1.5.4]	554-4100-004	Cooling-Interface	AW-6061-T6	0.0218 kg	1
[1.5.4.1]	Böllhoff 4130 104 0006	Helicoil M4x1.5d	CuSN6	kg	0
[1.5.5]	554-4100-005	Detector-Kettle-FM	PEEK-GF30	0.0919 kg	1
[1.5.6]	554-4300-000	LCS-Container	Cu / SS	0.35 kg	1
[1.5.7]	Scheibe_ISO_7089_4	Scheibe_ISO_7089_4	A2-70	0.0003 kg	16
[1.5.8]	Mutter_M_4_DIN_934	Mutter_M_4.DIN_934	VA		12
[1.5.9]	ISO_14581_M4x10_A2-70	Senkschraube_Torx_M4x10	A2-70	0.0013 kg	12
[1.5.10]	ISO_14581_M4x8_A2-70	Senkschraube_Torx_M4x8	A2-70	0.0011 kg	6
[1.5.11]	ISO_4762_M4x8	Zylinderschraube_M4x8	A2-70	0.0019 kg	8
[1.5.12]	Schnorr_Spannscheibe_D4	Schnorr_Spannscheibe_D4	X12CrNi17-7	0.0004 kg	12
[1.6]	554-4100-002	Bushing	PEEK	0.0003 kg	12
[1.7]	<b>554-5000-000</b>	<b>Electronics</b>		<b>0.1782 kg</b>	<b>1</b>
[1.7.1]	554-5100-000	Main-Board		0.0737 kg	1
[1.7.1.1]	554-5100-001	Main-Board-PCB	FR5	0.07 kg	1
[1.7.1.2]	Harwin_M80-5101405	Harwin_M80-5101405		0.0013 kg	1
[1.7.1.3]	Harwin_M80-5101005	Harwin_M80-5101005		0.0012 kg	1
[1.7.1.4]	Harwin_M80-5101805	Harwin_M80-5101805		kg	1
[1.7.2]	554-5500-000	Power-Board		0.0795 kg	1
[1.7.2.1]	554-5100-002	Cable-Pull-Relief	PEEK	0.004 kg	1
[1.7.2.2]	554-5500-001	Power-Board-PCB	FR5	0.0493 kg	1
[1.7.2.3]	554-5500-002	Power-Shielding	AW-6061-T6	kg	1
[1.7.2.4]	Harwin_M80-5100605	Harwin_M80-5100605		0.0011 kg	1
[1.7.3]	554-5300-000	Harness		0.0249 kg	1
[1.7.3.1]	554-5320-001	Soldered-Cable-Loop		kg	17
[1.7.3.2]	Harwin_M80-4000605	Harwin_M80-4000605		0.001 kg	1
[1.7.3.3]	Harwin_M80-4001005	Harwin_M80-4001005		0.0011 kg	1
[1.7.3.4]	Harwin_M80-4001805	Harwin_M80-4001805		kg	1
[1.7.3.5]	554-5311-000	Sat-Cable-1		kg	1
[1.7.3.6]	554-5312-000	Sat-Cable-2		kg	1
[1.7.3.7]	554-5313-000	Sat-Cable-3		kg	1
[1.7.3.8]	554-5314-000	Sat-Cable-4		kg	1
[1.7.3.9]	CVM_207252_P_9P	Stecker_D-Sub_P_9P		0.0118 kg	1
[1.7.3.10]	Ty-Rap_TC105	Ty-Rap_TC105	Aluminium	0.0007 kg	2

continued on next page...

#### A.4. Parts List

---

... continued from previous page

Level	Number	Part Name	Material	Mass	Qty
[1.7.3.11]	Ty-Rap_TC824-TB	Ty-Rap_TC824-TB	Aluminium	0.0007 kg	4
[1.8]	554-5000-001	Bushing_D7_D3.2_L5	AW-6060	0.0004 kg	12
[1.9]	Scheibe_ISO_7089_3	Scheibe_ISO_7089_3	A2-70	0.0001 kg	16
[1.10]	Scheibe_ISO_7089_4	Scheibe_ISO_7089_4	A2-70	0.0003 kg	18
[1.11]	Scheibe_ISO_7089_5	Scheibe_ISO_7089_5	VA	0.0004 kg	4
[1.12]	ISO_14581_M4x10_A2-70	Senkschraube_Torx_M4x10	A2-70	0.0013 kg	8
[1.13]	ISO_4762_M3x5	Zylinderschraube_M3x5	A2-70	0.0008 kg	4
[1.14]	ISO_4762_M3x12	Zylinderschraube_M3x12	VA	0.001 kg	8
[1.15]	ISO_4762_M3x16	Zylinderschraube_M3x16	VA	0.0014 kg	4
[1.16]	ISO_4762_M4x12	Zylinderschraube_M4x12	A2-70	0.002 kg	8
[1.17]	ISO_4762_M4x20	Zylinderschraube_M4x20	A2-70	0.003 kg	6
[1.18]	DIN-912_M5x20_Ti6Al4V	Zylinderschraube_M5x20	Ti6Al4V	0.005 kg	4
[1.19]	ISO-4762_M4x8_A2-70_gebohrt	Vakumschraube_M4x8	VA	0.0018 kg	4
[1.20]	Schnorr_Spannscheibe_D5	Schnorr_Spannscheibe_D5	X12CrNi17-7	0.0007 kg	4



# Bibliography

- Arianespace (2013). “Vega to launch MaxValier & Venta-1”. Presentation. OHB and Arianespace meeting at Le Bourget 2013 (cit. on p. 23).
- Bade, N., H. H. Fink, D. Engels, et al. (1995). “AGN from the ROSAT all-sky survey.” In: *Astronomy and Astrophysics Supplement* 110, p. 469 (cit. on p. 19).
- Bearden, J. A. (1967). “X-Ray Wavelengths”. In: *Review of Modern Physics*, pp. 86–99. URL: <http://www.med.harvard.edu/jpnm/physics/refs/xrayemis.html> (visited on 11/10/2012) (cit. on p. 165).
- Becker, W. and J. Truemper. “The X-ray luminosity of rotation-powered neutron stars.” In: *Astronomy and Astrophysics* (cit. on p. 18).
- Berghoefer, T. W., J. H. M. M. Schmitt, and J. P. Cassinelli (1996). “The ROSAT all-sky survey catalogue of optically bright OB-type stars.” In: *Astronomy and Astrophysics Supplement* 118, pp. 481–494 (cit. on p. 18).
- Bhardwaj, A., G. Randall Gladstone, R. F. Elsner, et al. (2007a). “First terrestrial soft X-ray auroral observation by the Chandra X-ray Observatory”. In: *Journal of Atmospheric and Solar-Terrestrial Physics* 69, pp. 179–187. DOI: [10.1016/j.jastp.2006.07.011](https://doi.org/10.1016/j.jastp.2006.07.011). eprint: [arXiv:astro-ph/0612261](https://arxiv.org/abs/astro-ph/0612261) (cit. on p. 18).
- Bhardwaj, A., R. F. Elsner, G. Randall Gladstone, et al. (2007b). “X-rays from solar system objects”. In: *Planetary and Space Science* 55. arXiv: [1012.1088 \[astro-ph.EP\]](https://arxiv.org/abs/1012.1088) (cit. on p. 17).
- Breunig, Elias (2011a). “Entwicklung und Betrieb des Superpolierprozesses für das Spiegelsystem des Röntgenteleskop  $\mu$ ROSI”. German. Diplomarbeit. Technische Universität München (cit. on pp. iii, 3, 89, 90, 159).
- (2011b). *Entwicklung und Qualifikation der optischen Bank des Röntgenteleskops  $\mu$ ROSI*. German. Semesterarbeit. Technische Universität München (cit. on pp. iii, 3, 109, 110, 112, 113, 160).
- Briel, U. G. and J. P. Henry (1993). “X-ray emission from a complete sample of Abell clusters of galaxies”. In: *Astronomy and Astrophysics* 278, pp. 379–390 (cit. on p. 19).
- Briel, U. G., B. Aschenbach, J Englhauser, et al., eds. (1996). *ROSAT User’s Handbook*. Max-Planck-Institut für extraterrestrische Physik. URL: <http://heasarc.gsfc.nasa.gov/docs/rosat/ruh/handbook/handbook.html> (visited on 04/15/2013) (cit. on pp. 55, 56, 58).

## Bibliography

---

- Burrows, C. J., R. Burg, and R. Giacconi (1992). “Optimal grazing incidence optics and its application to wide-field X-ray imaging”. In: *The Astrophysical Journal* 392, pp. 760–765. DOI: 10.1086/171479 (cit. on pp. 38, 39).
- Burwitz, V. and B. Menz (2013). Personal communication (cit. on p. 105).
- Burwitz, V., M. Bavadz, G. Paresci, et al. (2013). “In focus measurements of IXO type optics using the new PANTER x-ray test facility extension”. In: *Society of Photo-Optical Instrumentation Engineers (SPIE) Conference Series* (cit. on p. 40).
- Collon, M. J., R. Günther, M. Ackermann, et al. (2010). “Silicon pore x-ray optics for IXO”. In: *Society of Photo-Optical Instrumentation Engineers (SPIE) Conference Series* (cit. on p. 51).
- Dennerl, K. (2002). “Discovery of X-rays from Mars with Chandra”. In: *Astronomy and Astrophysics* 394, pp. 1119–1128. DOI: 10.1051/0004-6361:20021116. eprint: arXiv:astro-ph/0211215 (cit. on p. 17).
- Dennerl, K., V. Burwitz, J. Englhauser, et al. (2002). “X-rays from Venus discovered with Chandra”. In: *The High Energy Universe at Sharp Focus: Chandra Science*. Ed. by E. M. Schlegel and S. D. Vrtilek. Vol. 262. Astronomical Society of the Pacific Conference Series, p. 21 (cit. on p. 17).
- Dennerl, K., C. M. Lisse, A. Bhardwaj, et al. (2006). “First observation of Mars with XMM-Newton. High resolution X-ray spectroscopy with RGS”. In: *Astronomy and Astrophysics* 451, pp. 709–722. DOI: 10.1051/0004-6361:20054253 (cit. on p. 17).
- Dennerl, Konrad (2008). “Solar System Objects”. In: *The Universe in X-Rays*. Ed. by Joachim E. Trümper and Günther Hasinger. Astrophysics and Space Science Library. Berlin, Germany: Springer. ISBN: 978-3-540-34411-7 (cit. on p. 18).
- Eggert, T., P. Goldstrass, J. Kemmer, et al. (2003). “Analysis of background events in Silicon Drift Detectors”. In: *Nuclear Instruments and Methods in Physics Research A* 512, pp. 257–264. DOI: 10.1016/S0168-9002(03)01902-8 (cit. on p. 49).
- Englhauser, Jakob, ed. (2001). *The ROSAT X-Ray All-Sky Survey*. URL: <http://www.xray.mpe.de/cgi-bin/rosat-survey> (visited on 03/20/2013) (cit. on p. 26).
- ESA (2012a). *Strategic Readiness Level*. ESA. URL: <http://sci.esa.int/jump.cfm?oid=37710> (visited on 06/25/2013) (cit. on p. 166).
- (2012b). *XMM-Newton Users Handbook*. Ed. by E. Piconcelli. Issue 2.10. ESA: XMM-Newton SOC. URL: [http://xmm.esac.esa.int/external/xmm\\_user\\_support/documentation/](http://xmm.esac.esa.int/external/xmm_user_support/documentation/) (visited on 12/16/2012) (cit. on pp. 39, 40).
- Faghri, Amir (1995). *Heat Pipe Science and Technology*. Taylor & Francis Group. ISBN: 1-56032-383-3 (cit. on pp. 133, 134, 139–141, 143).

- Fleming, T. A., S. L. Snowden, E. Pfeffermann, et al. (1996). “Catalogue and luminosity function of white dwarfs detected in the ROSAT all-sky survey.” In: *Astronomy and Astrophysics* 316, pp. 147–154 (cit. on p. 18).
- Fortescue, P., J. Stark, and G. Swinerd (2003). *Spacecraft Systems Engineering*. Wiley. ISBN: 978-0-470-85102-9. URL: [http://books.google.de/books?id=\\_KCNCxYPUZgC](http://books.google.de/books?id=_KCNCxYPUZgC) (cit. on p. 1).
- Freyberg, M. J., B. Budau, W. Burkert, et al. (2008). “New technology and techniques for x-ray mirror calibration at PANTER”. In: *Society of Photo-Optical Instrumentation Engineers (SPIE) Conference Series* (cit. on p. 79).
- Friedrich, P., B. Aschenbach, C. Braig, et al. (2006). “Manufacturing of Wolter-I mirror segments with slumped glass”. In: *Society of Photo-Optical Instrumentation Engineers (SPIE) Conference Series* (cit. on p. 51).
- Fürmetz, M. (2012). “Design, Development and Verification of the eROSITA Thermal Control System”. Dissertation. Technische Universität München (cit. on pp. 3, 118, 135, 136, 141, 161).
- Fürmetz, M., J. Eder, P. Predehl, et al. (2008). “eROSITA Camera Low Temperature Thermal Control”. In: *38th International Conference on Environmental Systems*. SAE Technical Paper 2008-01-1957. DOI: 10.4271/2008-01-1957 (cit. on pp. 58, 121).
- Gatti, Emilio and Pavel Rehak (1983). “Semiconductor drift chamber: An application of a novel charge transport scheme”. In: *2nd Pisa Meeting on Advanced Detectors* (cit. on pp. 45, 48).
- Ghigo, M., S. Basso, F. Borsa, et al. (2012). “Development of high angular resolution x-ray telescopes based on slumped glass foils”. In: *Society of Photo-Optical Instrumentation Engineers (SPIE) Conference Series* (cit. on p. 51).
- Harris, D. E. (1990). *The Einstein Observatory Catalog of IPC X-ray Sources* (cit. on p. 8).
- Harrison, F. A., W. W. Craig, F. E. Christensen, et al. (2013). “The Nuclear Spectroscopic Telescope Array (NuSTAR) High-energy X-Ray Mission”. In: *The Astrophysical Journal* 770, 103, p. 103. DOI: 10.1088/0004-637X/770/2/103. arXiv: 1301.7307 [astro-ph.IM] (cit. on p. 14).
- Henke, B.L., E.M. Gullikson, and J.C. Davis (1993). “X-ray interactions: photoabsorption, scattering, transmission, and reflection at E=50-30000 eV, Z=1-92”. In: *Atomic Data and Nuclear Data Tables* 54.2, pp. 181–342. URL: [http://henke.lbl.gov/optical\\_constants/](http://henke.lbl.gov/optical_constants/) (cit. on pp. 75, 76).
- Hess, Victor F. (1912). “Über Beobachtungen der durchdringenden Strahlung bei sieben Freiballonfahrten”. In: *Physikalische Zeitschrift* 13, pp. 1084–1091 (cit. on p. 7).
- Hünsch, M., J. H. M. M. Schmitt, and W. Voges (1998). “The ROSAT all-sky survey catalogue of optically bright late-type giants and supergiants”. In: *As-*

## Bibliography

---

- Astronomy and Astrophysics Supplement* 127, pp. 251–255. DOI: 10.1051/aas:1998347 (cit. on p. 19).
- Hünsch, M., J. H. M. M. Schmitt, M. F. Sterzik, et al. (1999). “The ROSAT all-sky survey catalogue of the nearby stars”. In: *Astronomy and Astrophysics Supplement* 135, pp. 319–338. DOI: 10.1051/aas:1999169 (cit. on p. 19).
- Klingelhöfer, G., J. Brückner, C. D’Uston, et al. (2007). “The Rosetta Alpha Particle X-Ray Spectrometer (APXS)”. In: *Space Science Reviews* 128, pp. 383–396. DOI: 10.1007/s11214-006-9137-3 (cit. on p. 73).
- Lechner, P., C. Fiorini, A. Longoni, et al. (2004). “Silicon Drift Detectors for High Resolution, High Count Rate X-Ray Spectroscopy at Room Temperature”. In: *Advances in X-ray Analysis* 47, pp. 53–58 (cit. on pp. 49, 50).
- Lisse, C. M., K. Dennerl, J. Englhauser, et al. (1996). “Discovery of X-ray and Extreme Ultraviolet Emission from Comet C/Hyakutake 1996 B2”. In: *Science* 274, pp. 205–209. DOI: 10.1126/science.274.5285.205 (cit. on p. 17).
- Mankins, John C. (1995). *Technology Readiness Levels. A White Paper*. White Paper. NASA Advanced Concepts Office. URL: <http://www.hq.nasa.gov/office/codeq/trl/trl.pdf> (visited on 06/25/2013) (cit. on p. 166).
- Meidinger, N., S. Bonerz, H. W. Braeuninger, et al. (2003). “Frame store PN-CCD detector for the ROSITA mission”. In: *Society of Photo-Optical Instrumentation Engineers (SPIE) Conference Series* (cit. on p. 47).
- Menz, B., V. Burwitz, G. Hartner, et al. (2012). *PANTER X-Ray Measurements of Shell #06*. Measurement Report. Max-Planck-Institut für extraterrestrische Physik (cit. on pp. 94–96, 98, 99).
- Metzger, A. E., D. A. Gilman, J. L. Luthey, et al. (1983). “The detection of X rays from Jupiter”. In: *Journal of Geophysical Research* 88, pp. 7731–7741. DOI: 10.1029/JA088iA10p07731 (cit. on pp. 17, 18).
- Mitsuda, K., M. Bautz, H. Inoue, et al. (2007). “The X-Ray Observatory Suzaku”. In: *Publications of the Astronomical Society of Japan* 59, pp. 1–7 (cit. on p. 13).
- Orgler, Ludwig, Indulis Kalnins, and Lars Tiedemann (2009). “The challenging South Tyrolean “Max Valier” nano satellite with X-ray amateur telescope and AIS experiments”. In: *60th International Astronautical Congress*. Ed. by International Astronautical Federation. IAC-09.B4.6B.9 (cit. on pp. 1, 21, 22).
- Pavlinsky, M., R. Sunyaev, E. Churazov, et al. (2008). “Spectrum-Roentgen-Gamma astrophysical mission”. In: *Society of Photo-Optical Instrumentation Engineers (SPIE) Conference Series* (cit. on p. 15).
- Petrinec, S. M., D. L. McKenzie, W. L. Imhof, et al. (2000). “Studies of X-ray observations from PIXIE”. In: *Journal of Atmospheric and Solar-Terrestrial Physics* 62, pp. 875–888. DOI: 10.1016/S1364-6826(00)00035-3 (cit. on p. 18).

- Predehl, P., R. Andritschke, H. Böhringer, et al. (2010). “eROSITA on SRG”. In: *Society of Photo-Optical Instrumentation Engineers (SPIE) Conference Series* (cit. on p. 8).
- Revnivtsev, M., S. Sazonov, K. Jahoda, et al. (2004). “RXTE all-sky slew survey. Catalog of X-ray sources at  $|b| > 10^\circ$ ”. In: *Astronomy and Astrophysics* 418, pp. 927–936. DOI: 10.1051/0004-6361:20035798. eprint: arXiv:astro-ph/0402414 (cit. on p. 8).
- Ritter, H. and U. Kolb (2003). “Catalogue of cataclysmic binaries, low-mass X-ray binaries and related objects (Seventh edition)”. In: *Astronomy and Astrophysics* 404, pp. 301–303. DOI: 10.1051/0004-6361:20030330. eprint: arXiv:astro-ph/0301444 (cit. on p. 18).
- Rosati, P., S. Borgani, and C. Norman (2002). “The Evolution of X-ray Clusters of Galaxies”. In: *Annual Review of Astronomy and Astrophysics* 40, pp. 539–577. DOI: 10.1146/annurev.astro.40.120401.150547. eprint: arXiv:astro-ph/0209035 (cit. on p. 19).
- Rutherford, E., H. Geiger, and J. Harling (1908). “An Electrical Method of Counting the Number of  $\alpha$ -Particles from Radio-Active Substances”. In: *Royal Society of London Proceedings Series A* 81, pp. 141–161 (cit. on p. 7).
- Schmitt, J. H. M. M., S. L. Snowden, B. Aschenbach, et al. (1991). “A soft X-ray image of the moon”. In: *Nature* 349, pp. 583–587. DOI: 10.1038/349583a0 (cit. on p. 17).
- Sharma, S.D. and Kazunobu Sagara (2005). “Latent Heat Storage Materials and Systems: A Review”. In: *International Journal of Green Energy* 2.1, pp. 1–56. DOI: 10.1081/GE-200051299 (cit. on p. 126).
- Strüder, Lothar and Norbert Meidinger (2008). “CCD Detectors”. In: *The Universe in X-Rays*. Ed. by Joachim E. Trümper and Günther Hasinger. Astrophysics and Space Science Library. Berlin, Germany: Springer. ISBN: 978-3-540-34411-7 (cit. on p. 58).
- Tiedemann, Lars, Josef Eder, Maria Fürmetz, et al. (2008). “Thermal Storage at  $-80^\circ\text{C}$  for the eROSITA Telescope”. In: *38th International Conference on Environmental Systems*. SAE Technical Paper 2008-01-1955. DOI: 10.4271/2008-01-1955 (cit. on pp. 58, 121).
- Tiedemann, Lars, Maria Fürmetz, Peter Predehl, et al. (2013). “The development of  $\mu$ ROSI - Micro Röntgen Satellite Instrument”. In: *64th International Astronautical Congress*. Vol. 64. IAC-13-B4.2.6 (cit. on pp. 145, 146, 149).
- Trümper, Joachim E. and Günther Hasinger, eds. (2008). *The Universe in X-Rays*. Astrophysics and Space Science Library. Berlin, Germany: Springer. ISBN: 978-3-540-34411-7 (cit. on pp. 16, 17, 19, 34, 36, 47, 48).
- Ueda, Y., T. Takahashi, H. Inoue, et al. (1998). “Sky surveys with ASCA – Large Sky Survey”. In: *Astronomische Nachrichten* 319, p. 47 (cit. on p. 8).

## Bibliography

---

- van Miltenburg, J. Cees, Hana Gabrielová, and Květoslav Růžička (2003). “Heat Capacities and Derived Thermodynamic Functions of 1-Hexanol, 1-Heptanol, 1-Octanol, and 1-Decanol between 5 K and 390 K”. In: *Journal of Chemical & Engineering Data* 48, pp. 1323–1331 (cit. on p. 128).
- van Speybroeck, L. P. and R. C. Chase (1972). “Design Parameters of Paraboloid-Hyperboloid Telescopes for X-ray Astronomy”. In: *Appl. Opt.* 11.2, pp. 440–445. DOI: 10.1364/AO.11.000440. URL: <http://ao.osa.org/abstract.cfm?URI=ao-11-2-440> (cit. on p. 38).
- Ventspils High Technology Park (2012). *Latvia’s first satellite Venta-1*. URL: <http://www.vatp.lv/en/latvia-s-first-satellite-venta-1> (visited on 08/25/2013) (cit. on p. 23).
- Verbunt, F., W. H. Bunk, H. Ritter, et al. (1997). “Cataclysmic variables in the ROSAT PSPC All Sky Survey.” In: *Astronomy and Astrophysics* 327, pp. 602–613 (cit. on p. 18).
- Vernani, D., G. Borghi, G. Calegari, et al. (2011). “Performance of a mirror shell replicated from a new flight quality mandrel for eROSITA mission”. In: *Society of Photo-Optical Instrumentation Engineers (SPIE) Conference Series* (cit. on p. 106).
- Vikhlinin, A., B. R. McNamara, W. Forman, et al. (1998). “A Catalog of 200 Galaxy Clusters Serendipitously Detected in the ROSAT PSPC Pointed Observations”. In: *Astrophysical Journal* 502, p. 558. DOI: 10.1086/305951. eprint: [arXiv:astro-ph/9803099](https://arxiv.org/abs/astro-ph/9803099) (cit. on p. 19).
- Voges, W., B. Aschenbach, T. Boller, et al. (1999). “The ROSAT all-sky survey bright source catalogue”. In: *Astronomy and Astrophysics* 349, pp. 389–405. eprint: [arXiv:astro-ph/9909315](https://arxiv.org/abs/astro-ph/9909315). URL: <http://www.xray.mpe.mpg.de/rosat/survey/rass-bsc/> (cit. on pp. 8, 24, 26, 55).
- Voges, W., B. Aschenbach, T. Boller, et al. (2000). “ROSAT All-Sky Survey Faint Source Catalog (Voges+ 2000)”. In: *VizieR Online Data Catalog* 9029, p. 0. URL: <http://www.xray.mpe.mpg.de/rosat/survey/rass-fsc/> (cit. on p. 8).
- Watson, M. G. (2009). “ROSAT’s view of the X-ray sky. Commentary on: Voges W., Aschenbach B., Boller Th., et al., 1999, A&A, 349, 389”. In: *Astronomy and Astrophysics* 500, pp. 581–582. DOI: 10.1051/0004-6361/200912206 (cit. on p. 8).
- Willingale, R., G. Pareschi, F. Christensen, et al. (2013). “The Hot and Energetic Universe: The Optical Design of the Athena+ Mirror. An Athena+ supporting paper” (cit. on p. 51).
- Wolter, Hans (1952). “Spiegelsysteme streifenden Einfalls als abbildende Optiken für Röntgenstrahlen”. In: *Annalen der Physik* 445, pp. 94–114. DOI: 10.1002/andp.19524450108 (cit. on pp. 33, 35).

# **Curriculum**

Dipl.-Ing. Lars Tiedemann

LarsTiedemann@yahoo.de

## **Personal Information**

Name	Lars Tiedemann
Birth	12 October 1976 in Hamburg

## **Education**

2000 – 2006	Aerospace Engineering Studies Universität Stuttgart Degree: Diplom-Ingenieur
2006	Diploma Thesis “ <i>AdeSat - Structural Design of a Small Satellite</i> ” The University of Adelaide
2005	Study Thesis “ <i>Beobachtungs- und Kommunikationsbedingungen eines lunaren Kleinsatelliten</i> ” Institut für Raumfahrtssysteme, Universität Stuttgart
1997 – 2000	Vocational Training as Aircraft Mechanic DaimlerChrysler Aerospace Airbus GmbH, Hamburg
1986 – 1995	Gymnasium Corveystraße, Hamburg

## **Professional Experience**

2014 – present	Project Manager and Systems Engineer HPS GmbH, München
2007 – 2014	Mechanical Engineer High Energy Astrophysics Research Group Max-Planck-Institut für extraterrestrische Physik, Garching
2007	Software Engineer PHP/MySQL Mayflower GmbH, München
2005	Working Student Quality Management DaimlerChrysler AG, Stuttgart